# Quantifying the Stability of Ice Sheets During the Mid-Miocene Climatic Optimum

Sam Bradley

Supervised by Dr Caroline Lear and Professor Paul Pearson

Thesis Submitted for the Degree of Doctor of Philosophy

Cardiff University

September 2014

**DECLARATION**

This work has not been submitted in substance for any other degree or award at this or any other university or place of learning, nor is being submitted concurrently in candidature for any degree or other award.

Signed …… (candidate) Date ……

**STATEMENT 1**

This thesis is being submitted in partial fulfilment of the requirements for the degree of ……(insert MCh, MD, MPhil, PhD etc, as appropriate)

Signed …… (candidate) Date ……

**STATEMENT 2**

This thesis is the result of my own independent work/investigation, except where otherwise stated.
Other sources are acknowledged by explicit references. The views expressed are my own.

Signed …… (candidate) Date ……

**STATEMENT 3**

I hereby give consent for my thesis, if accepted, to be available for photocopying and for inter-library loan, and for the title and summary to be made available to outside organisations.

Signed …… (candidate) Date ……

**STATEMENT 4: PREVIOUSLY APPROVED BAR ON ACCESS**

I hereby give consent for my thesis, if accepted, to be available for photocopying and for inter-library loans **after expiry of a bar on access previously approved by the Academic Standards & Quality Committee.**

Signed …… (candidate) Date ……

**Acknowledgements**

"*Et Hoc Quoque Transibit*" - And this too shall pass. I chose this quote as the opening to my thesis for two reasons: one because it is something of a pun; I sincerely hope that this thesis will be granted a passing grade (edit: it did!). The second reason is to remind the next student that picks this thesis up that, no matter how hard it seems right now, their PhD will end. I hear the statistic is something like a 40% drop-out rate, but a 95% pass rate for those who stick it out, so stick it out.

To my parents: thank you for all of your support at every stage of this thesis. I would not have managed to cope without all of the "red cross food parcels" and washing up liquid you sent me.

To my supervisors, Carrie Lear and Paul Pearson: thank you for all of your patience, your comments, and your advice. I hope I was a better student than I felt I was.

To Sindia Sosdian, Elaine Mawby, and Kirsty Edgar: thank you for all of your help and conversation in the lab. To Sindia especially, thank you for getting the $\delta^{11}B$ data for me.

To Anabel and Sandra, the lab technicians at Cardiff University: thank you for all of your help and for your technical expertise. In a very real way, this thesis would not have been possible without you.

To the folk at the Bremen Core Repository: thank you for all of the sample material.

To my office mates (in alphabetical order): Stephanie Bates, Scott Butler, Miros Charidemou, Milly Deany, Rachel North, Kim Pyle, Maggi Simon, and Jamie Wilson, thank you for making these four years go by that much better. Whenever we were low on sugar, caffeine, or any other drug necessary for the completion of just one more day, there you were. From the bottom of my rapidly palpitating heart, I thank you.

Other thanks go out to Helen Beddow, Lynz Fox, Will Grey, Niels van Helmond, Rick Hennekam, Tuiri Konijnendijk and all the other wonderful people that attended the Urbino Summer School of Palaeoclimatology 2011, and ICP 2013. You guys have given me many happy memories, and many more happy times that were not recorded to memory.

Finally, to Talya: Thank you for all of the love and support that you gave me during this PhD. Sometimes you were all that kept me going.

**Commonly Used Abbreviations**

| | |
|---|---|
| AABW | Antarctic Bottom Water |
| ALK | Alkalinity |
| ANDRILL | ANtarctic geological DRILLing program |
| BFAR | Benthic Foraminiferal Accumulation Rate |
| BWT | Bottom Water Temperature |
| *C.* | *Cibicidoides* |
| $C_{org}$ | Organic Carbon |
| DIC | Dissolved Inorganic Carbon |
| DSDP | Deep Sea Drilling Program |
| EAIS | East Antarctic Ice Sheet |
| EOCT | Eocene-Oligocene Climate Transition |
| E-P | Evaporation - Precipitation |
| *G.* | *Globogerinoides* |
| IODP | Integrated Ocean Drilling Program |
| IPCC | Intergovernmental Panel on Climate Change |
| ITCZ | Intertropical Convergence Zone |
| ka | Thousand years before present |
| kyr | Thousand years (duration) |
| Ma | Million years before present |
| mbsf | Meters Below Sea Floor |
| mbsl | Meters Below Sea Level |
| mcd | Meters Composite Depth |
| MMCO | Mid-Miocene Climatic Optimum |
| MMCT | Mid-Miocene Climate Transition |
| Myr | Million years (duration) |
| NADW | North Atlantic Deep Water |
| *O.* | *Oridorsalis* |
| ODP | Ocean Drilling Program |
| OMB | Oligocene-Miocene Boundary |
| *P.* | *Pyrgo* |
| $pCO_2^{ATM}$ | Partial-pressure of $CO_2$ in the atmosphere |
| PP | Primary Productivity |
| PPFI | Physical Property Frequency Informed (age model) |
| ppmv | Parts per mil (thousand) by volume |
| psu | Practical Salinity Unit |
| SI | Stomatal Index |
| SSS | Sea Surface Salinity |
| SST | Sea Surface Temperature |
| VPDB | Vienna Pee Dee Belemnite |
| V-SMOW | Vienna Standard Mean Ocean Water |
| WAIS | West Antarctic Ice Sheet |
| XCB | Extended Core Barrel |

| | |
|---|---|
| $\Delta[CO_3^{2-}]$ | Carbonate saturation state ($[CO_3^{2-}]_{in\ situ} - [CO_3^{2-}]_{at\ saturation}$) |
| $\delta^{18}O_{sw}$ | $\delta^{18}O$ of sea water, a proxy for ice volume |
| $\delta^{18}O_{ssw}$ | $\delta^{18}O$ of surface sea water, a proxy for salinity |
| $[CO_3^{2-}]_{in\ situ}$ | Concentration of $CO_3^{2-}$ in sea water being measured |
| $[CO_3^{2-}]_{sat}$ | Maximum potential concentration of $CO_3^{2-}$ at saturation |
| $[measurement]_G$ | Any element ratio or stable isotope $\delta$-notation followed by subscript-G indicates that it refers to that value in *G. trilobus* |
| $[measurement]_M$ | As $[measurement]_G$, but in *C. mundulus* |
| $[measurement]_O$ | As $[measurement]_O$, but in *O. umbonatus* |

**Summary**

The Cenozoic represents the transition from the greenhouse world of the Cretaceous to the ice house world of today. Nonetheless, it was not a steady linear trend from an ice free world to an ice house, and there were several reversals along the way. One such reversal was the Mid Miocene Climatic Optimum (MMCO, 14-17 Ma).

Material from the Ocean Drilling Program Site 926 on Ceara Rise in the Equatorial Atlantic Ocean is used to examine two intervals within the MMCO from 16.4-15.9 Ma and 15.7-15.3 Ma. Stable isotopes and trace element ratios in two species of benthic foraminifera, *Cibicidoides wuellerstorfi*, and *Oridorsalis umbonatus*, and one planktonic foraminifer, *Globigerinoides trilobus* are used to reconstruct multiple climatological parameters at 2-4 kyr resolution.

Paired Mg/Ca and $\delta^{18}O$ measurements from the benthic species examined suggest that sea level varied by as much as 40m during the MMCO. Sea level variability was accompanied by changes in sea surface salinity, as measured using $\delta^{18}O$ and Mg/Ca from *G. trilobus*, which suggests that the Intertropical Convergence Zone (ITCZ) was responding to high-latitude forcing centred upon the Northern Hemisphere. The implication is that significant Northern Hemisphere ice sheets were present during the Middle Miocene, some 13 Ma before their currently held date of inception during the Pliocene.

These changes in sea level were accompanied by large changes in benthic and planktonic carbonate saturation states ($\Delta[CO_3^{2-}]$), which are inferred to be representative of changes to global alkalinity and dissolved inorganic carbon. Changes in global export productivity, as evidenced by benthic foraminiferal accumulation rates and the planktonic-benthic gradient of $\delta^{13}C$, are inferred to be controlling the carbon cycle and atmospheric $pCO_2^{ATM}$ during the MMCO. The ITCZ is also inferred to be controlling primary productivity at Ceara Rise.

Additionally, the relationship between multiple trace element/Ca ratios and $\Delta[CO_3^{2-}]$ are examined using core-tops taken from the Norwegian Sea. The relationship between Mg/Ca and $\Delta[CO_3^{2-}]$ in *C. wuellerstorfi* is confirmed by expanding the available holothermal data. Mg/Ca in the benthic species *Pyrgo murrhina* appears to respond exclusively to changes in $\Delta[CO_3^{2-}]$, and the relationship of U/Ca in *P. murrhina* to $\Delta[CO_3^{2-}]$ is the opposite of that seen in *C. wuellerstorfi* and *O. umbonatus*.

## CONTENTS

**LIST OF FIGURES**

**LIST OF TABLES**

# 1 INTRODUCTION

Little attention has been paid to warming intervals in the Cenozoic outside of the modern day to the Pliocene, and the Palaeocene and Eocene. Just as the present is key to understanding the past, so too is the past the key to understanding the future. Analyses of warming intervals that are analogous to modern climate are essential for predictive work in understanding what is to come in the not-too-distant future. Studies of Palaeocene and Eocene hyperthermals (e.g., Bohaty et al., 2009; Bowen, 2013; Carozza et al., 2011; Tripati and Elderfield, 2005; Zachos et al., 2008) are useful to give an idea of what the world might be like under much higher atmospheric $CO_2$ concentrations ($pCO_2^{ATM}$), but give no indication of what the transition to that world might be like as those intervals have no ice in either hemisphere to melt. The ice sheets play a major role in Earth's climate through increasing the Earth's albedo, keeping sea levels low, and locking up methane within permafrost.

Looking towards deglaciations in the Pliocene and Pleistocene has merit, but $pCO_2^{ATM}$ was between 180 and 240ppmv (van de Wal et al., 2011; Zhang et al., 2013); lower than today's levels of just above 400ppm (IPCC, 2013). Ice volumes in the Northern Hemisphere were far greater, with the Eurasian, Siberian, and Laurentide ice sheets sitting on top of Eurasia, Siberia and the North American continent, respectively (Lisiecki and Raymo, 2005; Miller et al., 2005; Woodard et al., 2014). Therefore deglaciations at those times are not directly applicable to what we may experience in the next 100-1000 years. What is needed is an interval with conditions between that of the Pliocene and the Eocene to provide something of a road-map from where we are now to the extreme conditions represented by the Eocene hyperthermals. The Miocene (25-5 Ma) exists temporally and climatologically between the extremes represented by the Pliocene and the Eocene, and so may offer us that map.

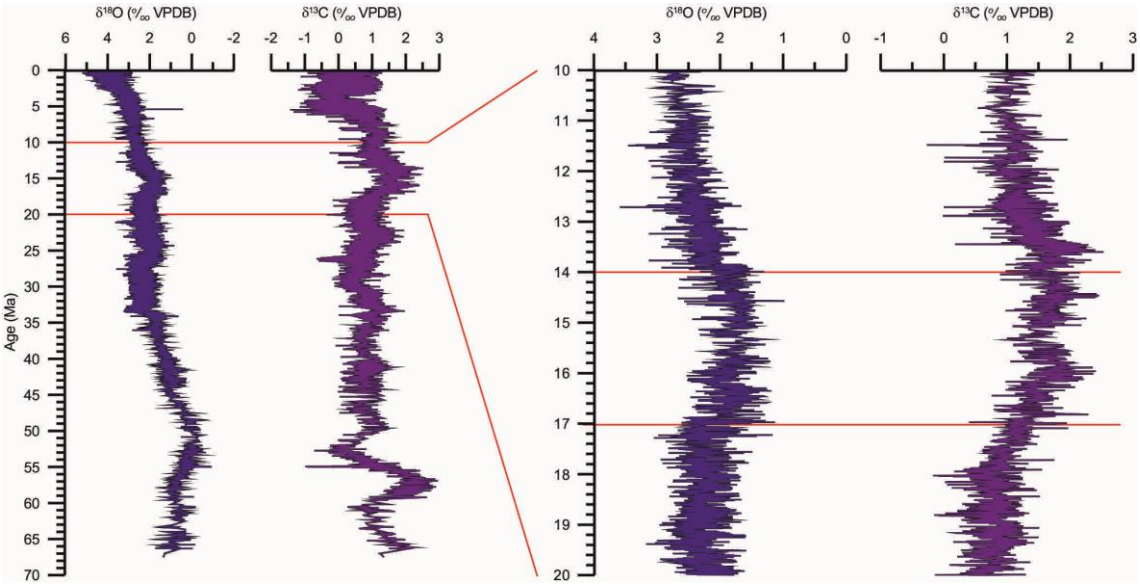


**Figure 1 – Global deep sea composite oxygen and carbon isotope record of the Cenozoic, data taken from Zachos et al. (2001). The MMCO is outlined in red.**

## 1.1 The Mid Miocene Climatic Optimum

The Mid Miocene Climatic Optimum (MMCO, 17-14 Ma, Figure 1) is a geologically brief period of elevated temperatures and stands above the general background of Cenozoic cooling(Zachos et al., 2001). It presents an ideal interval for this study. $pCO_2^{ATM}$ by both recent geochemical estimates (Foster et al., 2012; Greenop et al., 2014; Zhang et al., 2013) and by analysis of leaf stomatal indices (Kürschner and Kvaček, 2009; Retallack, 2002) was analogous to the modern value; estimates fall between 300 and 500ppmv (c.f. the modern value of ~400ppmv; IPCC, 2013). Ice volumes (sea level) during the MMCO are thought to be lower (higher) than the modern day, as evidenced by the presence of southern beech tree and *nothofagus* grass pollen near the Antarctic continental margin (Warny et al., 2009), but nonetheless there still may have been some at least ephemeral ice in the Northern Hemisphere, as evidenced by ice rafted debris (IRD) on the Lomonosov Ridge (St John, 2008).

### *1.1.1 Palaeoclimate Records of the MMCO*

Analysis of sea levels in the Miocene have focused primarily on the Middle Miocene Climate Transition (MMCT, 14.2-13.8 Ma; e.g., Flower and Kennett, 1994; Holbourn et al., 2010; Holbourn et al., 2007; Holbourn et al., 2004; Lewis et

al., 2007; Shevenell et al., 2004; Shevenell et al., 2008), a period of cooling and ice-growth. Studies on the MMCO have tended towards low-resolution ice-proximal sedimentological records from the ANDRILL sites (e.g., Fielding et al., 2011; Passchier et al., 2011), or come from more terrestrially-based records of floral and faunal assemblages (Böhme, 2003; Warny et al., 2009). Other records have focussed on the increased weathering associated with the warmer temperatures and higher $pCO_2^{ATM}$ (Wan et al., 2009). John et al. (2011) identified eight intervals of eustatic sea level change between 18 and 9 Ma from sequence stratigraphic analyses, however they focus on the sea level fall associated with the MMCT.

#### *1.1.1.1 Bottom Water Temperature*

Bottom water temperature (BWT) estimates across the MMCO either include long-term, and low resolution records (e.g., Lear et al., 2000), or become lower resolution at the MMCO due to coring gaps, or similar (Shevenell et al., 2008). Shevenell et al. (2008) estimates bottom water temperatures around 16Ma at between 3 and 6°C at the Southern Ocean ODP Site 1171, however the record is patchy and low resolution between 15 and 16 Ma. Lear et al. (2010) covers from 16.8 Ma to 11.5 Ma, and so captures the very end of the MMCO warming, but their BWT estimates between 17 and 15 Ma show ($\Delta[CO_3^{2-}]$-corrected) temperatures from Mg/Ca in *O. umbonatus* of 9-11°C at the subtropical ODP Site 761 on the Wombat Plateau.

#### *1.1.1.2 Sea Surface Temperature*

Sea surface temperature (SST) estimates have been made using various proxy methodologies and at varying latitudes. A number of estimates have been made across the MMCT, and some extend into the latest parts of the MMCO. LaRiviere et al. (2012) have made estimates from alkenone records, and show SSTs in the subtropical East Pacific of ~27°C (ODP Site 1010) and ~23°C in the Northeast Pacific (ODP 1021). Similarly, estimates of SST from foraminiferal

Mg/Ca subtropical South China Sea show temperatures of 28-30°C at ~15.5 Ma (ODP Site 1146, Holbourn et al., 2010). Estimates from the SST estimates in the Southern Ocean at 16 Ma vary between ~16 – 18°C from foraminiferal Mg/Ca (Shevenell et al., 2004). Ice-proximal records from Prydz bay palynological assemblages (Warny et al., 2009) give SST ranges between -2.1 to 29.6°C and 11.5-29.2°C, depending on the palynomorph taxa examined, and so SSTs at this high latitude probably varied seasonally between -2.1 and 11.5 °C during the MMCO. More directly relevant to this study is the work of Zhang et al. (2013), conducted at Ceara Rise ODP Site 925, whose $TEX_{86}$ and $U^{k'}_{37}$ data suggest a tropical Atlantic SST of between 28°C and 30°C. It is worth noting that the 15-25Ma is about the only period of their 40 Ma study where the two proxies are in good agreement, though this is likely due to a changing seasonal bias in one or both proxies. Similar results were obtained by Rousselle et al. (2013) using $U^{k'}_{37}$ from IODP Site U1338 in the Equatorial Pacific Ocean.

#### *1.1.1.3 Ice volume*

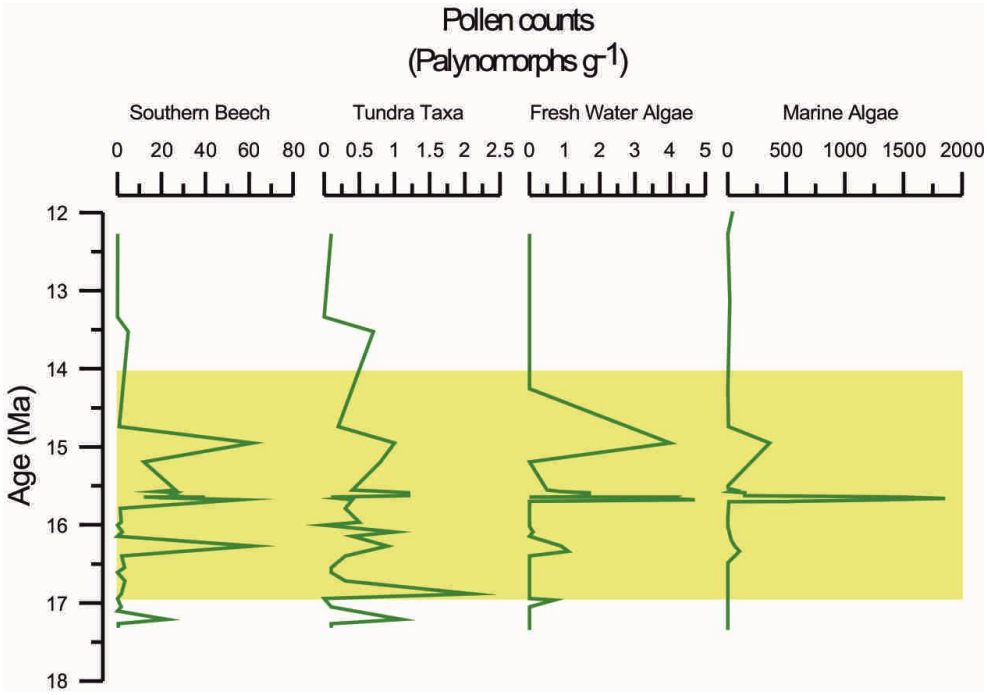


**Figure 2 – Palynological results from Warny et al. (2009). Land plants and fresh water algae on Antarctica is key evidence of reduced ice volume during the MMCO.**

A number of modelling efforts have been made that study ice volume across the MMCO (Goldner et al., 2014; Herold et al., 2012; Justino et al., 2014; You et al., 2009), but few geochemical estimates have been made to support or inform them. One study of $\delta^{18}O$ across the MMCO suggests that sea levels rose by 20-60m at that time (Pekar and DeConto, 2006), which is consistent with a warming and deglaciation. Sedimentological studies have focused on IRD at ice-proximal sites, with IRD records suggesting sea ice minima in Antarctica at 16.5-16.3 and 15.7-15.6 Ma (Passchier et al., 2011). The West Antarctic ice sheet is suggested to be very dynamic across the MMCO, with glacially proximal (large ice sheets) conditions at the current location of the Ross Sea ice shelf between 17.3 and 16.7Ma, turning to distal (smaller ice sheets) conditions from 16.7-16.5Ma, followed by a gradual trend towards more proximal conditions from 16.5 to 14.5 Ma (Fielding et al., 2011). These are borne out by palynological records from near the Ross Shelf (Warny et al., 2009) that show increases in land plants on the Antarctic continent at around 17.2 Ma and 15.7-15.5 Ma, and one spike in pollen in between (not dated, Figure 2).

#### *1.1.1.4 $pCO_2^{ATM}$*

$pCO_2^{ATM}$ estimates across the MMCO are far more numerous and easy to come by, not least because of the attention that has been paid to obtaining long-term records of $pCO_2^{ATM}$ for the Cenozoic in recent years (e.g., Pagani et al., 2005; Pearson and Palmer, 2000; Zhang et al., 2013), though a number of records have also focused on the MMCO (Foster et al., 2012; Kürschner and Kvaček, 2009) to resolve the discrepancy found in early records between the warm and, apparently, low-$CO_2$ Miocene found by Pearson and Palmer (2000) and Pagani et al. (2005). It is worth noting that this discrepancy has more-or-less been resolved by studies conducted after the Pagani et al. (2005) alkenone-based $pCO_2^{ATM}$ reconstruction.

Current estimates of $pCO_2^{ATM}$ during the MMCO are between 300 and 500 ppmv (Figure 3). These values are well agreed upon between different proxy

estimates, including stomatal densities of *Laurophyllum pseudoprinceps, Ocotea hradekensis,* and *Laurus abchasica* leaves (280-520 ppmv; Kürschner and Kvaček, 2009), $\delta^{11}B$ of *G. trilobus* (300-500 ppmv during the peak of the MMCO; Foster et al., 2012), and $\delta^{13}C$ of $C_{37}$-$C_{39}$ ethyl and methyl ketones (350-550 ppmv; Zhang et al., 2013). A recent, and far higher resolution study (Greenop et al., 2014) suggest that variability of $pCO_2^{ATM}$ may have been between 200 and 800 ppmv on 100ka timescales across the MMCO. $pCO_2^{ATM}$ from calcitic palaeosols of Miocene age in the Railroad Canyon, Idaho, USA, show a similar range of values, suggesting that $pCO_2^{ATM}$ during the MMCO was highly variable (Retallack, 2009).

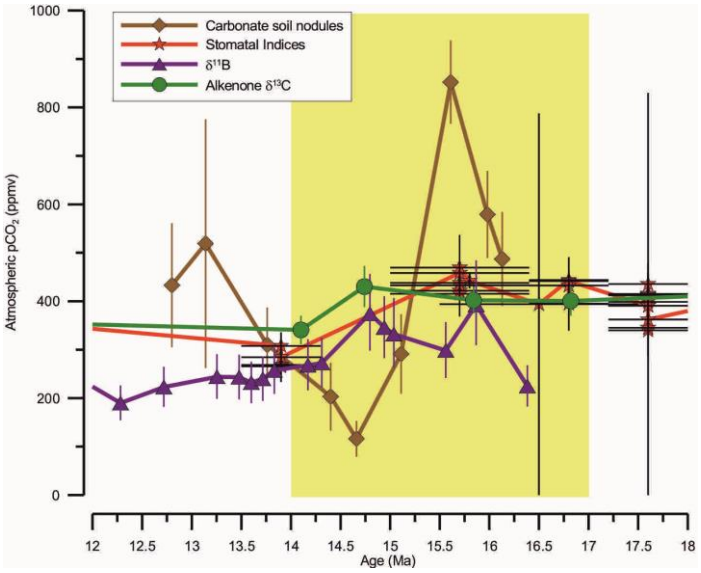


**Figure 3 – $pCO_2^{ATM}$ estimates throughout the MMCO. Brown squares are from analyses of carbonate soil nodules (Retallack, 2009). Red stars show stomatal indices.(Kürschner and Kvaček, 2009)Purple triangles show data from $\delta^{11}B$ (Foster et al., 2012). Green circles are from $\delta^{13}C$ of alkenones (Zhang et al., 2013).**

### *1.1.1.5 Sea Surface Salinity*

Sea surface salinity (SSS) is a key climatological parameter intimately tied with evaporation and precipitation rates, and more directly the difference between the two (E-P; Bingham et al., 2010; Bingham et al., 2012; Yu, 2011). E-P at the equator is strongly tied to the position of the intertropical convergence zone (ITCZ; Arbuszewski et al., 2013), which is in turn linked to the volume of ice sheets and temperature of the Southern and Northern Hemispheres (Chiang

et al., 2003; Chiang and Bitz, 2005; Xie and Philander, 1994). It is clear, then, that at near-equatorial sites, such as Ceara Rise, that information about SSS can give information about the movement of the ITCZ with respect to the ice sheets. SSS changes in palaeoclimate records are difficult to quantify because of the lack of direct and independent proxies for it. The closest available proxy for SSS is planktonic $\delta^{18}O$, which is also affected by $\delta^{18}O$ of sea water (itself a function of salinity, temperature, and ice volume), and SST. Nonetheless estimates of SSS during the Miocene have been made, and first order approximations suggest that it is highly variable (Holbourn et al., 2010; Rousselle et al., 2013; Shevenell et al., 2004).

### *1.1.2 MMCO Summary*

It is clear from the brief review above that the MMCO is an understudied interval in the Cenozoic, and moreover one which would welcome high-resolution geochemical analyses to allow for quantification of the MMCO climatic conditions. Many extant geochemical studies either skip the MMCO to focus on the MMCT (e.g., Holbourn et al., 2007), or include it only as part of a low resolution, long-term study (e.g., Lear et al., 2000; Zachos et al., 2001; Zachos et al., 2008). This study aims to re-address that balance somewhat by providing a high resolution, mutli-proxy, focused and holistic look at intervals within the MMCO. In doing so it is hoped that this will provide real insight into a dynamic palaeoclimatological interval with enormous relevance to modern-day global climate changes.

## 1.2 Core Top Benthic Foraminifer Trace Metal Geochemistry

### *1.2.1 Mg/Ca and $\Delta[CO_3^{2-}]$*

Foraminiferal Mg/Ca was first hypothesised to be affected by the saturation state of sea water ($[CO_3^{2-}]_{in\ situ} - [CO_3^{2-}]_{at\ saturation}$; $\Delta[CO_3^{2-}]$) by Martin et al. (2002), though other authors quickly came to the same conclusions (e.g., Lear et al., 2004; Marchitto and deMenocal, 2003; Skinner et al., 2003). The link between

$\Delta[CO_3^{2-}]$ and foraminiferal Mg/Ca was first formalised by Elderfield et al. (2006), who corrected a global coretop Mg/Ca study to a uniform temperature of 3°C and compared the residual data to the $\Delta[CO_3^{2-}]$ of the sites that data were acquired from. They found a small, but significant sensitivity of Mg/Ca in *Cibicidoides wuellerstofi* (*C. wuellerstorfi*) to $\Delta[CO_3^{2-}]$ of ~0.0086 mmol $mol^{-1}$ μmol $kg_{sw}^{-1}$. This has massive implications for Mg/Ca palaeothermometry as estimates of ice volume changes from $\delta^{18}O$ require an independent thermometer to deconvolve the temperature and $\delta^{18}O_{sw}$ signals from foraminiferal $\delta^{18}O$. It also helps to explain many strange anomalies, such as ice-growth across the Eocene-Oligocene Climate Transition (EOCT) without an apparent cooling (Coxall et al., 2005; Lear et al., 2000; Lear et al., 2004). Since then , a number of studies have been conducted to further constrain and correct foraminiferal Mg/Ca for variations in $\Delta[CO_3^{2-}]$ (Bryan and Marchitto, 2008; Dawber and Tripati, 2012a; Lear et al., 2010; Yu and Elderfield, 2007, 2008). Despite this, there is much work still to be done in both expanding the number of species examined for $\Delta[CO_3^{2-}]$ effects on their geochemistry, and in searching for a reliable and independent proxy for $\Delta[CO_3^{2-}]$ to allow Mg/Ca to be corrected.

#### *1.2.1.1 Mg/Ca in O. umbonatus versus C. wuellerstorfi*

One potential method to at least confirm the veracity of temperature trends inferred from foraminiferal Mg/Ca is to compare records derived from infaunal and epifaunal species. Infaunal species exist in permanently $CO_3^{2-}$ under-saturated conditions within pore waters and so appear to be less sensitive to changes in $\Delta[CO_3^{2-}]$, but still reflect changes in BWT (Elderfield et al., 2010). *Oridorsalis umbonatus* (*O. umbonatus*) is one such species that tends to live infaunally (Murgese and De Deckker, 2005; Rathburn and Corliss, 1994), and moreover is a commonly used foraminifer for palaeooceanographic work (e.g., Coxall and Wilson, 2011; Dawber and Tripati, 2012b; Lear et al., 2000; Lear et al., 2010; Lear et al., 2003; Tripati and Elderfield, 2005). Confirmation that it has a lower sensitivity to changes in $\Delta[CO_3^{2-}]$, as well as the addition of other species-

specific calibrations to the palaeoceanographer's arsenal, would be of great benefit to palaeoceanography.

#### *1.2.1.2 U/Ca*

Currently calibrated geochemical proxies for $\Delta[CO_3^{2-}]$ include B/Ca (Brown et al., 2011; Dawber and Tripati, 2012a; Foster, 2008; Rae et al., 2011; Yu and Elderfield, 2007; Yu et al., 2010b), Sr/Ca (Dawber and Tripati, 2012a; Raitzsch et al., 2010; Rosenthal et al., 2006), and U/Ca (Keul et al., 2013; Raitzsch et al., 2011). Of those, U/Ca is calibrated for only three species: *C. wuellerstorfi* (also referred to as *Planulina wuellerstorfi*), *C. mundulus* (Raitzsch et al., 2011), and *Ammonia sp.* (Keul et al., 2013). U/Ca appears to show a strong, negative, and linear relationship with $\Delta[CO_3^{2-}]$ (Keul et al., 2013; Raitzsch et al., 2011), and expansion upon the effect of $\Delta[CO_3^{2-}]$ upon foraminiferal U/Ca would be beneficial. Uranium precipitation in seawater is strongly related to oxygenating bottom water conditions (Anderson, 1982; Boiteau et al., 2012; Francois et al., 1993; McManus et al., 2005), but Mn precipitation is predominant under oxygenating conditions (Boyle, 1983; Calvert and Pedersen, 1996; Chun et al., 2010; Mangini et al., 2001) and so analysis of both Mn/Ca and U/Ca can rule out these effects.

### *1.2.2 Morphotype effect on Mg/Ca*

One key conclusion of Rae et al. (2011) was that B/Ca is not only different between species (specifically *C. mundulus* and *C. wuellerstorfi*), but also between species morphotypes. *C. mundulus* and *C. wuellerstorfi* both have two morphotypes: the species *sensu stricto* and the species *variant* and the sensitivity of B/Ca to changes in $\Delta[CO_3^{2-}]$ is different for the different morphotypes. In addition to this, planktonic foraminiferal Mg/Ca can show slightly different relationships to temperature depending on coiling direction (e.g., Cleroux et al., 2008), though not in all cases (e.g., Duckworth, 1977) and occasionally even show different ecological behaviour (e.g., Lombard et al., 2009). One study that

is worth a cursory look, therefore, is if sinistral and dextral benthic foraminifera are sufficiently different morphotypes to show different relationships between their trace element/Ca ratios and the conditions in which they grew. A culturing experiment on *Ammonia tepida* by De Nooijer et al. (2014) suggests not, but this remains to be seen in core-tops, as sinistral and dextral foraminifera may occupy a slightly different ecological niche.

## 1.3 The Intertropical Convergence Zone (ITCZ)

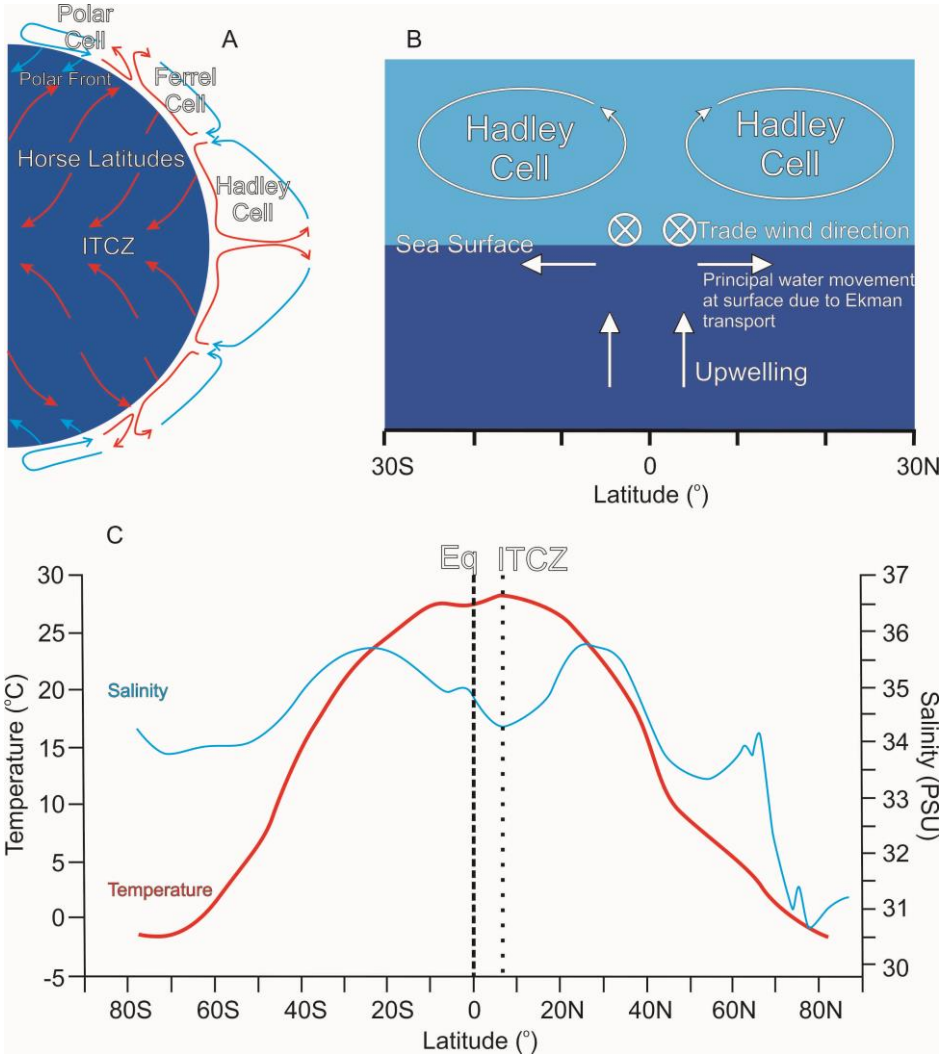


**Figure 4 – Schematic of the ITCZ. A) The position of the wind cells relative to one another on the globe and principal directions of the trade winds. B) The effect of Hadley Cell circulation on sea surface currents and upwelling. C) Mean Sea Surface Temperature (red) and salinity (blue) distribution with latitude (Levitus, 1982). The mean position of the ITCZ (dotted line labelled ITCZ) can be seen as a maximum in temperature and a minimum in salinity. Its position relative to the equator (dashed line labelled Eq) is shown.**

In the northern hemisphere, rising air at the equator eventually reaches equilibrium and flows northwards. Once it cools enough it sinks in the Horse latitudes (30-35$^{o}$N) and the air flows southwards back towards the equator, forming the trade winds (e.g: Karnauskas and Ummenhofer, 2014; Stachnik and Schumacher, 2011). This circulation forms the Hadley wind cell and is one of three such cells in each hemisphere. The other cells (Figure 4a) are the Polar Cell, and the Ferrell Cell (e.g:Huang and McElroy, 2014).. At Earth's surface the Hadley Cells are associated with Northerly winds in the Northern Hemisphere and Southerly winds in the Southern Hemisphere. The ITCZ is the region of the globe near to the equator at which the two Hadley Cells converge (Philander et al., 1996; Xie and Philander, 1994; Xie and Saito, 2001).

Due to Earth's rotation, Coriolis forces deflect the Northerly winds to the right (left) in the Northern (Southern) Hemisphere (Figure 4a). The effect of this is that to the north and the south of the ITCZ the Trade Winds that transport air towards the equator associated with the Hadley Cells are deflected to become Easterlies. These drive the currents in the surface ocean and, due to Coriolis forcing once again, the primary Ekman transport direction is away from the equator (Figure 4b). This divergence of water masses forces the upwelling of cold, deep, nutrient rich waters to the surface producing a zone of high productivity and low salinity (Figure 4b).

Due to the asymmetrical distribution of the continents about the equator the Northern Hemisphere is warmer than the Southern Hemisphere. As a result, the mean position of the ITCZ is ~5$^{o}$N of the equator (Figure 4c), though it varies on multiple timescales from seasonal (e.g., Bingham et al., 2010; Bingham et al., 2012; Kaandorp et al., 2005), to glacial-interglacial, (e.g., Arbuszewski et al., 2013; Sepulcre et al., 2011; Tachikawa et al., 2014) up to Myr (e.g., Armstrong and Allen, 2011; Hofmann and Wagner, 2011; Hyeong et al., 2014). The position of the ITCZ over land is far more dynamic due to the lower heat capacity of land compared to the sea, and it is not considered here. The principal control over the position of the ITCZ is the temperature contrast between the Southern

and Northern Hemispheres and cross-equatorial energy transport (Bischoff and Schneider, 2014; Broccoli et al., 2006; Chiang et al., 2003; Chiang and Bitz, 2005; Xie and Philander, 1994). As the Northern Hemisphere cools (warms), relative to the Southern, the ITCZ will move south (north) towards the Equator (North Pole). Changes in the mean temperature of a hemisphere relative to the other can have a strong effect on the position of the ITCZ, which can be seen in the geological record as changes in salinity at near-equatorial ocean sites (Arbuszewski et al., 2013; Armstrong and Allen, 2011; Holbourn et al., 2014; Holbourn et al., 2010; Hyeong et al., 2014; Schmidt and Spero, 2011). A change in ice volume in one hemisphere will therefore move the ITCZ away from that hemisphere (Broccoli et al., 2006; Chiang and Bitz, 2005). Analysis of how $\delta^{18}O$ of sea water, which is affected by global ice volumes, and how sea surface salinity co-vary should give an indication of the location of any changes in ice volume if a position of an ocean site relative to the ITCZ can be assumed.

## 1.4 Sites used in this Thesis

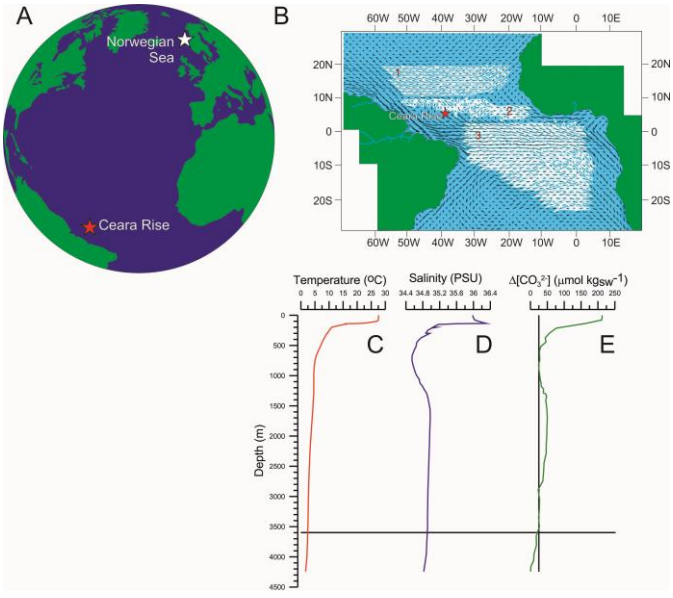


**Figure 5: Location of the sites used in this thesis. A) Location of Ceara Rise (red star) and the Norwegian Sea (white star). B) Location of Ceara Rise in the Atlantic (Red star) and the principal ocean currents (highlighted regions. Arrow lengths show the relative strength and direction of the ocean currents) 1- the North Equatorial Current (Bischof et al., 2004b); 2 – The North Equatorial Counter-Current (Bischof et al., 2004a); 3 – The South Equatorial Current (Bonhoure et al., 2004). Principal hydrography of the water column at Ceara Rise is shown in; C – temperature. D – Salinity, E- $\Delta[CO_3^{2-}]$. Data from GEOSECS Site 40 and Lewis and Wallace (1998).**

A more detailed outline of the sites examined will be used in the relevant chapters. Sites in the Norwegian Sea used for the core top calibrations will be described in Chapter 3, and the geology of Ceara Rise will be described in Chapter 4. Nonetheless, the Norwegian Sea is a marginal sea off the coast of Norway (Figure 5a) and is notable due to its approximately holothermal bottom waters (Elderfield et al., 2006; Jordan, 2008). This feature allows it to be used for core-top calibrations that need to be independent of changes in temperature. Ceara Rise is a bathymetric high in the Western Equatorial Atlantic (Figure 5a) that was the target of the Ocean Drilling Program's (ODP) Leg 154 and contains sediments from the modern day to the Eocene (Shipboard Scientific Party, 1995a).

Ceara rise sits just to the South of the North Equatorial Counter Current (NECC, Figure 5b2) and to the North of the South Equatorial Current (SEC, Figure 5b3). The SEC transports around 17-26 Sv of warm (~26$^{o}$C, ±2$^{o}$C dependant on season) waters from the subtropics towards Ceara Rise (Bonhoure et al., 2004) and extends down to around 100m depth. Beneath that, the eastward-flowing equatorial under-current follows the approximate depth of the thermocline and brings cooler (~20$^{o}$C) waters to the surface, forced by Ekman-driven divergence at the equator.

The NECC (Figure 5b2) is a seasonal current that is highly subject to wind-forcing and is strongest during austral winter when the SEC is also at its strongest (Bischof et al., 2004a). The influence of subtropical cells, which connect the subtropics to the surface equatorial currents via equatorward flow at the thermocline, brings a tongue of cold (<15$^{o}$C) waters that are eventually upwelled. At other times, the region is dominated by the Northern Equatorial Current (NEC, Figure 5b1). The NEC brings relatively warm (24-32$^{o}$C, from boreal winter to summer, respectively) with a mean transport of ~8.5 Sv from the north-western coast of Africa (Bischof et al., 2004b).

## 1.5 Outline

Chapter 2: Methods, will outline the methods used in this study and examine the reproducibility of the data obtained herein.

In Chapter 3: Core-Top Calibration of Trace Metal Ratios of Benthic Foraminifera from the Norwegian Sea, this study will first examine core top samples from the Norwegian Sea for Mg/Ca, Li/Ca, B/Ca, and U/Ca in *C. wuellerstorfi*, *O. umbonatus*, and *Pyrgo murrhina* (*P. murrhina*) against changes in $\Delta[CO_3^{2-}]$. In addition, the coiling direction of *C. wuellerstorfi* will be examined for differences in the above trace element ratios between the sinistral and dextral forms.

Following that the findings of that chapter will be used in Chapter 4: Mid-Miocene ITCZ Changes in Response to Northern Hemisphere Ice Sheet Growth. Temperature, ice volume and salinity will be examined across two intervals in the MMCO to examine climate variability and infer movements of the ITCZ during that period. A hypothesis for a deglaciation centred on the Northern Hemisphere and accompanying evidence for that will be presented.

Chapter 5: Carbon Cycling During the MMCO, will present further evidence for movement of the ITCZ by examining changes in proxies for productivity. The reliability of temperature changes inferred in Chapter 4 will be examined by looking at changes in $\Delta[CO_3^{2-}]$. In addition, estimates of $\Delta[CO_3^{2-}]$ and $pCO_2^{ATM}$ will be presented and the changes in global carbon cycling that they represent will be explored.

Chapter 6: Synthesis and Conclusions, will conclude this study, and provide a summary of the key findings with reference to the research questions presented above.

# 2 METHODOLOGY

## 2.1 Introduction

The processing of the sediment for running on an inductively coupled plasma mass spectrometer (ICP-MS) is comprised of five phases, which will be summarised herein. The first phase is the washing of the raw sediment through 63 μm mesh sieves to separate the sand-size fraction (>63 μm) and free up the individual foraminifera for picking. The second phase is to pick the foraminifera and to sort for species and size fraction. The third phase is to crush the individuals to open up the chambers and facilitate the cleaning. The fourth phase is to clean the crushed foraminifera to remove contaminants such as clays, oxides and organic material (Boyle and Keigwin, 1985/1986). Finally, the foraminifera are dissolved and the solutions are diluted prior to analysis by ICP-MS (Rosenthal et al., 1999).

Several small tests have been performed over the course of the washing and cleaning process to test the efficacy of each phase. These include experiments to examine the techniques used in washing the sediment, and experiments to assess the optimal wash time of the sample introduction system during analysis, the reproducibility of the element ratio analyses and the long-term precision of the ICP-MS analyses. The results of these tests are detailed here.

Finally, the climate parameters examined, geochemical proxies used, and the calibrations used to convert one to the other are outlined. An explanation of each and justification for their use are provided where appropriate.

## 2.2 Sample Preparation

### *2.2.1 Washing*

The purpose of this phase is to disaggregate the sediment to free the individual foraminifera for picking and to calculate the percentage coarse fraction by weight. The raw sediment was removed from its bag and soaked overnight in 15 MΩ de-ionised water (DI $H_2O$) in a labelled and sealed 60 ml glass jar. While the sediment was soaking, it was placed on a spinner to gently assist the disaggregation.

Subsequently, the jars were slowly emptied into a 63 μm sieve. A garden sprayer was used to gently spray the sediment with 15 MΩ DI $H_2O$ in order to wash away the <63 μm fraction. The <63 μm material was washed into a labelled bag so that it could be dried and weighed. The >63 μm material was labelled and left to dry in the oven at 40°C. Once dry, they were put into vials and weighed.

The material from ODP Site 926 is relatively consolidated and can easily take up to 15 L of DI $H_2O$ per sample to be washed through properly. To save on time, and to protect the foraminifera from being leached by the mildly acidic DI $H_2O$, the sediment was only washed through with 2 L before stopping the washing process. Anything more than this was too likely to damage the foraminifera and removed progressively less and less of mud fraction.

### *2.2.2 Picking*

The purpose of this phase is to separate out individual species of foraminifera within a given size fraction. This allowed single-species analyses to be used to ensure that vital effects are accounted for in the final data. The >63 μm material is sieved into >355 μm, 250-355 μm and 150-250 μm size fractions. The size fractions to be used were picked using a fine artists' brush that has been dampened in 15 MΩ DI $H_2O$.

### *2.2.3 Crushing*

The purpose of this phase is to open up the individual chambers of the foraminifera so that the cleaning phase can remove contaminants more thoroughly. It is a delicate operation as crushing too much makes the foraminifers' test material prone to being siphoned off during the cleaning, whereas crushing too little can leave contaminants inside the test.

Around 20 individuals between 250 and 355 μm were crushed for a single sample. When there is not enough material, fewer foraminifera are used per sample. No fewer than three individuals were used for a given analysis. The

work area was wiped down with 15 MΩ DI $H_2O$ and the foraminifera to be crushed were placed on a clean glass slide using a clean artists' brush damped with fresh DI $H_2O$. The foraminifera were placed in two rows with larger individuals in one row and the smaller individuals in the other. A second clean glass slide was lowered onto the foraminifera and then pressed down to crack the foraminifers' tests. Placing the foraminifera in two rows allowed the top glass slide to rest on the tests evenly to ensure that no foraminifers are over or under-crushed. The crushed foraminifera are put into individually labelled, acid-cleaned micro-centrifuge tubes.

### *2.2.4 Trace Metal Cleaning*

The purpose of this step is to remove contaminants that could interfere with the trace metal ratio signals. The methodology is the cadmium-cleaning protocol using a reducing step adapted from Boyle & Keigwin (1985) and has been modified based on the results of other publications (Barker et al., 2003; Martin and Lea, 2002; Pena et al., 2005), though it differs from that used in Barker et al. (2003) due to the use of an oxide removal reducing step. This is included because the full suite of trace metals were analysed on each sample. The full process is provided in the appendices (Section 8.1). The same method was used for both benthic and planktonic foraminifera.

### *2.2.5 Analysis*

#### *2.2.5.1 Stable isotopes*

Samples were split after crushing for stable isotope analysis and analysed on a ThermoFinnigan MAT252 with online sample preparation using an automated Kiel III carbonate device at Cardiff University. The long term-precision of the in-house standard is better than 0.09 ‰ in $\delta^{18}O$ and better than 0.06 ‰ in $\delta^{13}C$ ($1\sigma$). Results are reported relative to Vienna Pee Dee Belemnite (VPDB). Larger samples were further split to bring the sample weights in between 50 and 100 μg and each split was run separately.

| | Mg/Ca | | Sr/Ca | | B/Ca | | Li/Ca | | U/Ca | | Mn/Ca | |
|---|---|---|---|---|---|---|---|---|---|---|---|---|
| | Mean ratio (mmol $mol^{-1}$) | Precision (1σ) | Mean ratio (mmol $mol^{-1}$) | Precision (1σ) | Mean ratio (μmol $mol^{-1}$) | Precision (1σ) | Mean ratio (μmol $mol^{-1}$) | Precision (1σ) | Mean ratio (nmol $mol^{-1}$) | Precision (1σ) | Mean ratio (μmol $mol^{-1}$) | Precision (1σ) |
| CS1 | 1.19 | 0.0080 | 0.44 | 0.0027 | 14.6 | 1.19 | 5.78 | 0.26 | 4.85 | 0.19 | 28.4 | 0.53 |
| CS2 | 6.81 | 0.033 | 1.66 | 0.0099 | 219 | 5.20 | 43.2 | 1.74 | 29.3 | 0.85 | 196 | 8.89 |
| *C. mundulus* | 1.39 | 0.13 | 1.15 | 0.04 | 125 | 5.62 | 13.8 | 0.71 | 19.8 | 3.07 | 407 | 63.9 |
| *O. umbonatus* | 1.87 | 0.14 | 0.93 | 0.027 | 32.9 | 9.89 | 14.0 | 0.93 | 34.3 | 8.75 | 585 | 143 |
| *G. trilobus* | 3.71 | 0.10 | 1.23 | 0.028 | 69.0 | 4.34 | 12.6 | 0.60 | 46.7 | 6.75 | 672 | 50.8 |

**Table 1 – Mean element/Ca ratios and precision for consistency standards and foraminifera examined in this study. The precision of the standards reflects analytical precision. The precision for the foraminifera reflects sample reproducibility, and is the mean 1σ taken from samples run multiple times (between 2 and 4 times) using different individuals from the same samples.**

*2.2.5.2 Trace elements*

Samples were cleaned and analysed for trace metal composition as described above and in in the appendices (Section 8.1). Samples were analysed on a Thermo Element XR ICP-MS at Cardiff University. Sample [Ca] were between 1 and 4 mmol $mol^{-1}$, and where they were above 4 mmol $mol^{-1}$ they were diluted down to 4 mmol $mol^{-1}$ by further addition of trace-metal pure (Optima) 4 mM $HNO_3$.

Mg/Ca analyses by ICP-MS are strongly affected by matrix effects (Lear et al., 2002; Rosenthal et al., 1999). Matrix matching of samples was performed by analysing a diluted aliquot of each sample for its calcium concentration. Individual standards of the same calcium concentration were produced for each sample, and analysed in pairs by ICP-MS. A "blank" solution, comprising the same acids used for sample dissolution and dilution was analysed in between six samples. The isotope intensities of the blank solution were subtracted from the isotope intensities of the samples. Where the sample intensities were less than five times that recorded in the blank solution, the results for that element/Ca ratio were discarded.

Sample results were then screened for contaminants by examining the Al/Ca, Fe/Ca, and Mn/Ca ratios. Where Al/Ca was greater than 100 μmol $mol^{-1}$, or Fe/Ca, and/or Mn/Ca were greater than 1000 μmol $mol^{-1}$ it was assumed that the cleaning had not been thorough enough and so all data were discarded for that sample.

*2.2.5.3 Long term precision*

Long-term precision was analysed using two consistency standards (CS1 & CS2) during each run. The two standards are mixed and maintained at Cardiff University and are run at a concentration of 4mM Ca. They are compared to the multi-element calibration standard (MCS) that is used throughout each run. During 2012 the standard lab procedure was that each user would maintain

their own set of consistency standards to prevent cross-contamination between users. In 2013, the procedure was changed so that all users take from a centrally maintained batch of consistency standards to ensure consistency between users' runs. There is no clear change between 2012 and 2013 to suggest that this compromised the standards' consistency

Long term precision for Mg/Ca ratios in CS1 (Figure 6a) and CS2 (Figure 7a) were both high. In the cases of both standards, the standard deviations represent less than 1% of the mean, and the ranges represent around 2% of the mean (Table 1). Variations in Mg/Ca between samples are real, and not down to analytical error within the mass spectrometer.

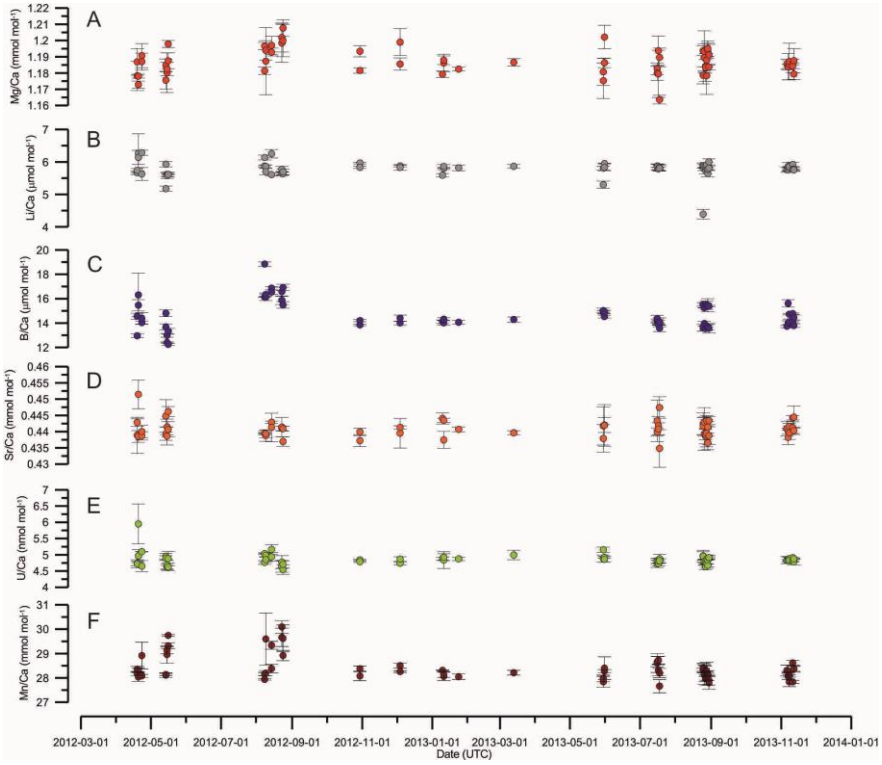


**Figure 6 – Measured trace metal ratios of Consistency Standard CS1 over time. A) Mg/Ca. B) Li/Ca. C) B/Ca. D) Sr/Ca. E) U/Ca. F) Mn/Ca Error bars show one standard deviation.**

The long-term precision for Li/Ca is 4% of the mean (1σ) for CS1 and 3% of the mean for CS2 (Table 1). Long term precision for B/Ca, was within 10% of the mean for CS1 and within 2% of the mean for CS2. The relatively poor long-term precision for B/Ca in CS1 results from the very low B/Ca ratios for this particular standard (14.6 µmol $mol^{-1}$, Table 1).

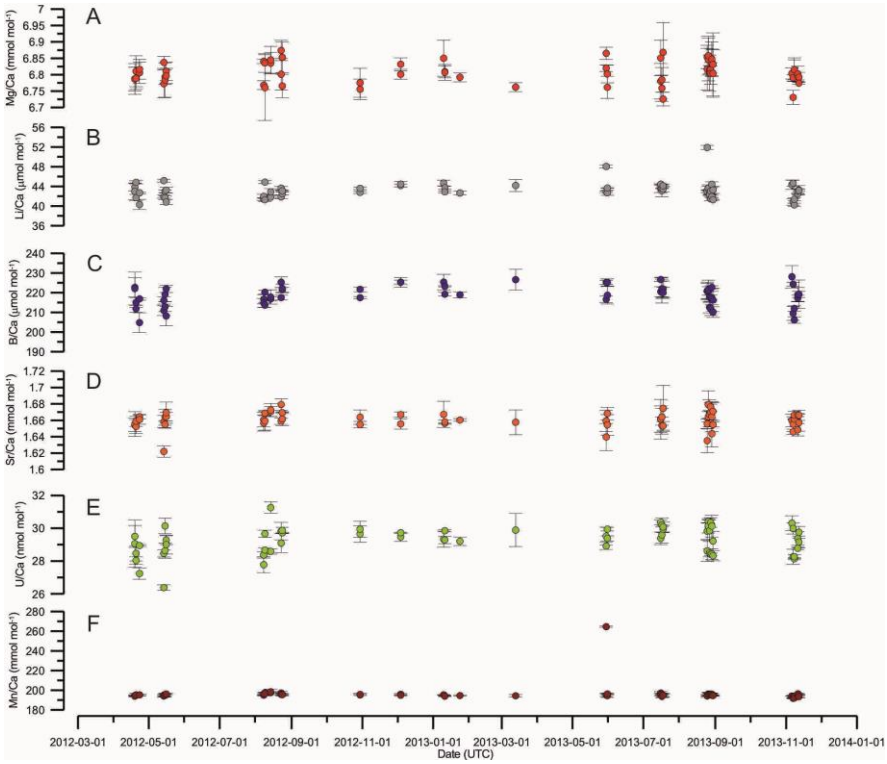


**Figure 7 – Measured trace metal ratios of Consistency Standard CS2 over time. A) Mg/Ca. B) Li/Ca. C) B/Ca. D) Sr/Ca. E) U/Ca. F) Mn/Ca. Error bars show one standard deviation,**

## 2.3 Tests

### *2.3.1 Reproducibility of foraminiferal trace metal data*

In order to assess sample reproducibility, a monospecific sample of 400 individuals of the planktonic foraminifera *Neogloboquadrina pachyderma* was picked from a core-top sediment sample JR 179BC 492 Y 0-1cm from the Southern Ocean. These were crushed together and the resultant material was mixed up to ensure that the results were as homogenous as possible and separated out into 20 samples, in a similar manner to the same test performed by Barker et al. (2003). These 20 samples were cleaned using the method of Barker et al. (2003).

In general, the sample reproducibility for Mg/Ca, Li/Ca and B/Ca is good (Figure 8). Ignoring samples 7 and 17, the Mg/Ca data are normally distributed, with a 1σ standard deviation of 0.042 around a mean of 0.639 mmol $mol^{-1}$. This means the 95% confidence interval for the natural variability of Mg/Ca is ± 0.084 mmol mol-1, or ± ~13%. For Li/Ca, the 1σ is 0.433, with a mean of 16.04 µmol

$mol^{-1}$. This equates to the 95% confidence of natural variability being ± 0.866, or ± ~5%. For B/Ca, the 1σ is 2.292 around a mean of 48.62 μmol $mol^{-1}$. The 95% confidence interval of natural variability is ± 4.584 or ± ~9%. The lower reproducibility values for Li/Ca and B/Ca is due the low concentrations of Li and B in *N. pachyderma*, which meant that the isotope intensities were less than ten times that of the blank solution. Species with higher Li/Ca and B/Ca ratios will have higher levels of reproducibility, as observed by comparing the precision of the two different consistency standards.

Samples 7 and 17 show elevated values of Mg/Ca, Li/Ca and B/Ca and have thus been discarded as anomalous. Sample 17 also shows elevated Al/Ca (Figure 8g) and Fe/Ca (Figure 8f) which suggests that the clay removal step was less effective than for other samples (Barker et al., 2003). Similarly, the Mn/Ca (Figure 8h) is elevated for samples 3, 7 and 17 which suggests that the reducing step was not as effective as it should have been for these samples. This is supported by the Fe/Ca (Figure 8f) results for samples 3 and 17, which may suggest that the problem, for those samples at least, lies in the crushing stage rather than with the cleaning; if all the chambers were not opened sufficiently, then contaminants on the inside of the chambers will not have been removed properly.

### *2.3.2 Experiment to determine the optimum wash time*

A series of standards and acids were run in sequence to determine the optimum length of the wash time. Standards were used to contaminate the probe before each wash cycle and then a 0.5M $HNO_3$ solution was analysed for the full suite of trace metals. The wash time was set at 2 minutes, 3 minutes, 4 minutes, 5 minutes and 6 minutes. Standards were run at Ca concentrations of 1mM, 2mM, 3mM, and 4mM to assess how the washout time varied with concentration.

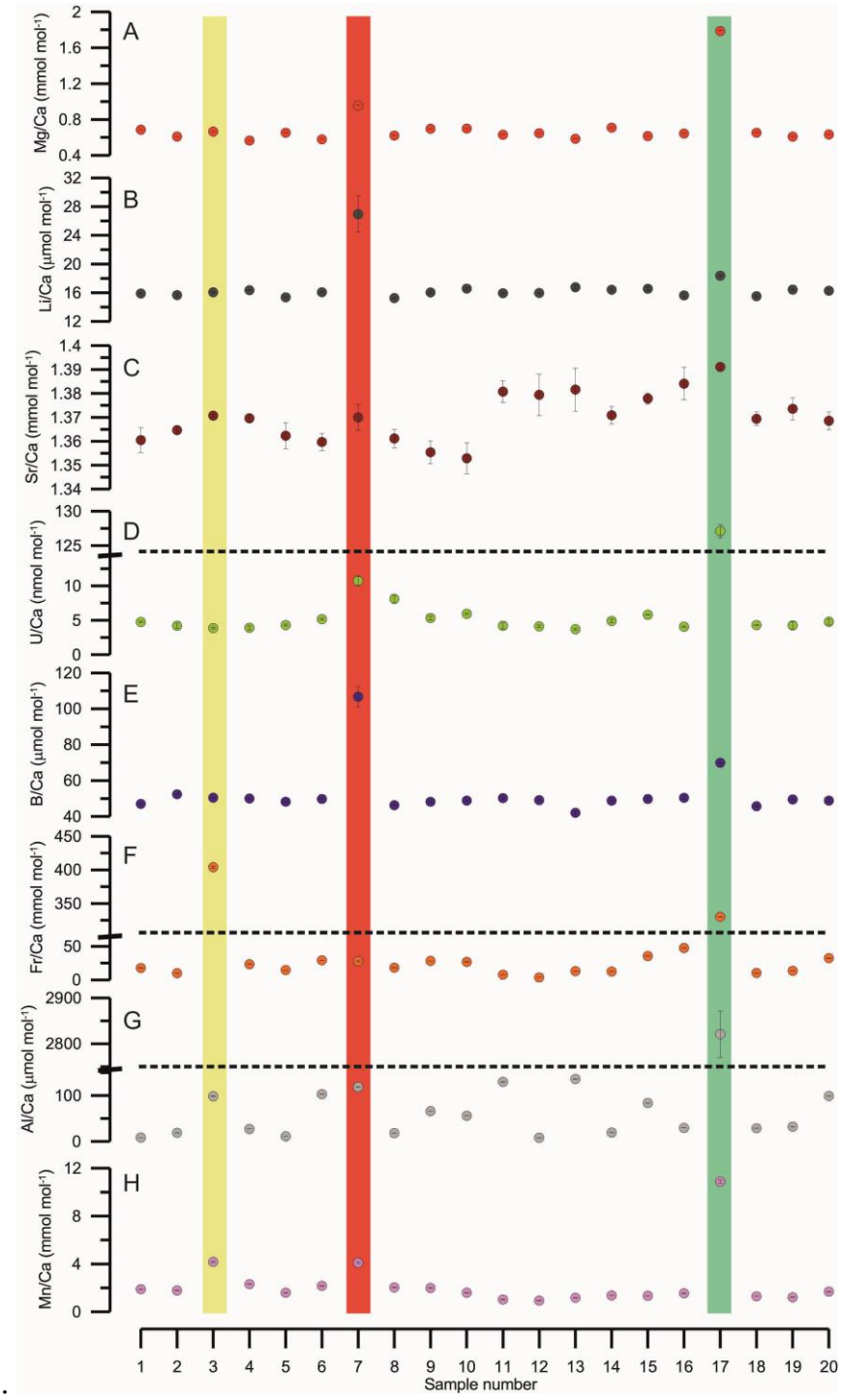


**Figure 8 – Measured element/calcium ratios from the sample reproducibility test. Error bars represent the 1σ of multiple measurements on the same sample made by the ICP-MS, and as such are an underestimate of the total error. A) Mg/Ca. B) Li/Ca. C) Sr/Ca. D) U/Ca. E) B/Ca. F) Fe/Ca. G) Al/Ca. H) Mn/Ca. In general the samples show element/Ca values of around the same value, which would be expected, however there are notable exceptions. Sample 3 is highlighted as a yellow circle. Sample 7 is highlighted as a red triangle. Sample 17 is highlighted as a green square. Where a break in the y axis is necessary, a dashed line has been put across the graph to make it clear which points are above and below the break. Error bars show one standard deviation. Where no error bars are visible, the error bars are smaller than the size of the points.**

It seems, however that increasing the wash time between two and six minutes has an insignificant effect on the measured concentrations of the acid

sample (Figure 9). The major effect appears to loosely be the concentration of the preceding standard. Nevertheless a wash time of 4 minutes was chosen for samples in this thesis as a compromise between the observed lack of effect and any unforeseen effects that may not have been accounted for.

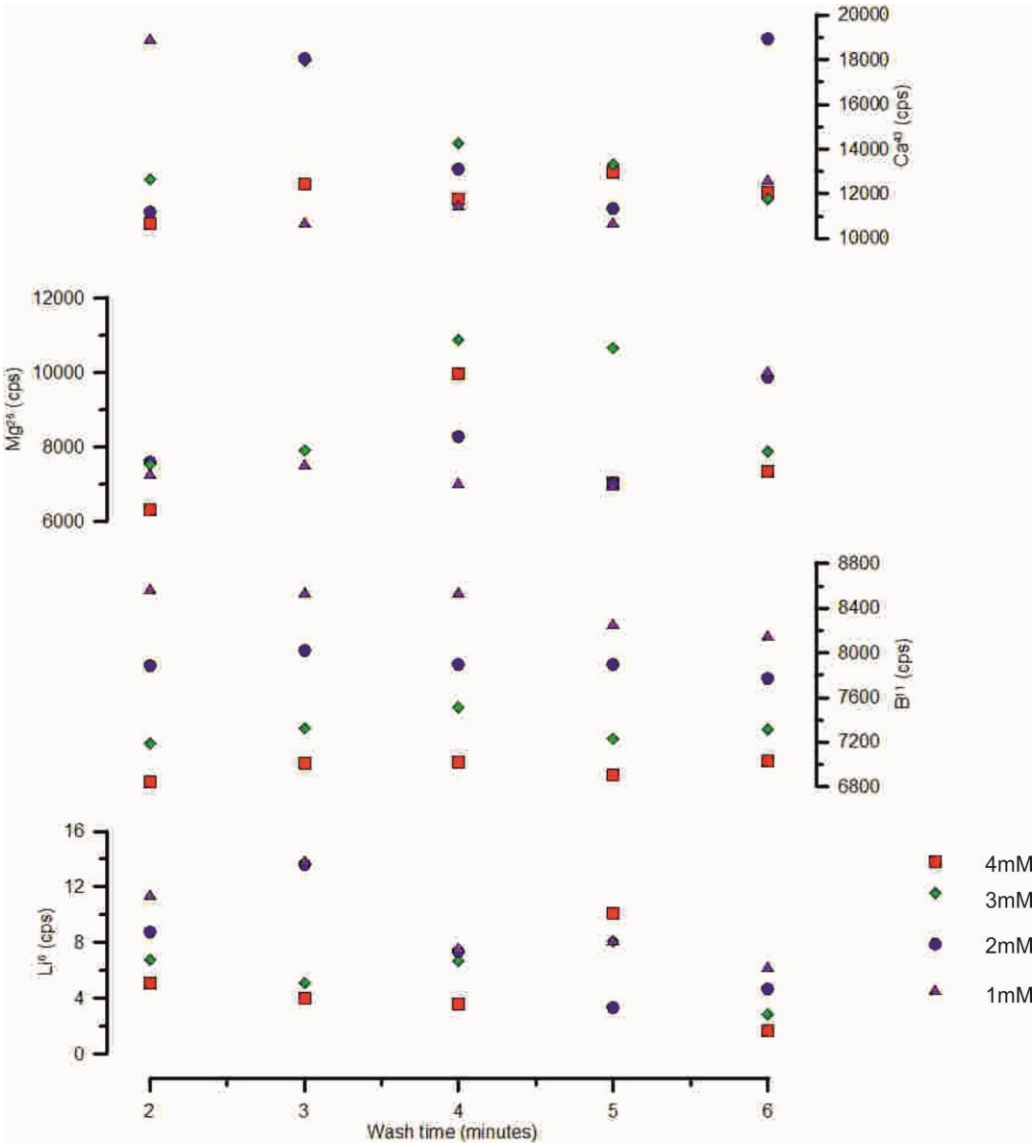


**Figure 9 – The effect of wash time on background signal intensity. [Ca] of the standard preceding the analysed acid sample is differentiated as follows: red square: 1 mM. Green diamond: 2 mM. Blue circle: 3 mM. Pink triangle: 4 mM.**

## 2.4 Site Selection

Several DSDP, ODP and IODP sites were reviewed for this study. Sites were selected based on the quality of preservation and the sedimentation rate. As the aim of the study is to produce high resolution records, sites with a sedimentation rate of less than 10 m $Ma^{-1}$ were discounted. Because the depth of

burial tends to adversely affect the quality of preservation a compromise had to be reached. Sites on the short list included IODP Site 154-U1334, and ODP Sites 154-925, 154-926, and 184-1148.

IODP Site 154-U1334 (equatorial Pacific Ocean, 4.8 km water depth) was the preferred Site for this project. It consists primarily of nannofossil ooze and has a sedimentation rate through the Miocene of approximately 13 m $Ma^{-1}$ (Pälike et al., 2009). Preservation of benthic foraminifera is described as good (though not glassy), and planktonics as medium to good. Oceanographically, U1334 is situated in the middle of the world's largest ocean basin and so is well situated to make inferences about global changes. At the time of starting this project, material from U1334 was still under moratorium and so unavailable for use. On 10$^{th}$ October 2010 it had come off of moratorium, however this project had the potential to conflict with ongoing work, and so U1334 was deemed best avoided.

ODP Site 184-1148 (northern South China Sea, 2.1 km water depth) consisted of primarily clayey nannofossil ooze, which I had hoped would bode well for foraminiferal preservation (Wang et al., 2000). In addition the sediment accumulation rate was between 11 and 17 m $Ma^{-1}$ during the Miocene. Unfortunately planktonic foraminiferal preservation is listed as moderate to poor and benthic foraminifera are hardly mentioned at all except as being "few to abundant". From an oceanographic perspective, the South China Sea may be too restricted to allow for any inferences about global oceanographic changes that would have occurred as a result of any variability in the size of the global ice volume, and so ODP Site 1148 was rejected.

ODP Sites 154-925 and 154-926 (Ceara Rise, western equatorial Atlantic Ocean, 3 km and 3.6 km water depth respectively) both contain relatively complete Miocene sections, though 926 is the more complete of the two. Both cycle between nannofossil ooze and nannofossil ooze with clay, and both show moderate to good preservation of benthic foraminifera and poor to moderate preservation of planktonics, though preservation is better in 925. Sedimentation

rates in 925 and 926 throughout the Miocene are reported as being between 11 and 12 m $Ma^{-1}$, respectively. Recovery of Miocene sediments in Site 925 was poorer than that of 926, and there are significant coring gaps over areas of interest to this study. Conversely, 926 hole B showed more than 100% core recovery throughout both intervals of interest. For this reason, Site 926 was chosen for this study.

## 2.5 ODP Site 926 Age Model

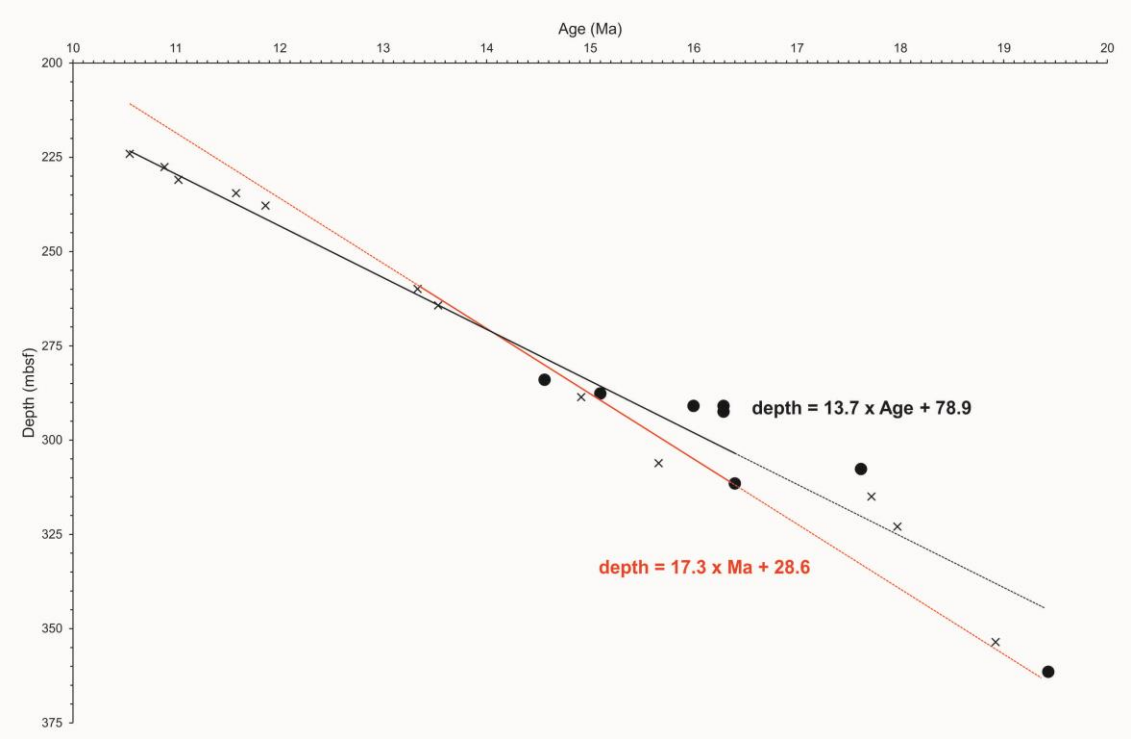


**Figure 10 – ODP Site 926 age model. A) Original age model based purely on biostratigraphic data (black line), and revised age model incorporating results from physical property frequency analysis (Figure 11, see text for details). Solid lines show the range of the calculated linear age model, dotted line project the age model forwards and backwards. Crosses show age datums based on nannofossils, circles based on planktonic foraminifera (Shipboard Scientific Party, 1995c; Wade et al., 2011).**

ODP Site 926 has strong biostratigraphic age control in general, but unfortunately the core material suffered from magnetic overprinting, and so it has no magnetostratigraphic age control. Sites on Ceara Rise show strongly cyclic bands of alternating light and dark sediment and material of Oligocene and Early Miocene age have been orbitally tuned (Pälike et al., 2004), however that tuning stops below the intervals being studied. Based on biostratigraphic data, the intervals being studied show a sedimentation rate of approximately

9.4 m $Ma^{-1}$. A hiatus is postulated in material from site 926 between 15.5 and 17.7 Ma based on magnetic susceptibility data (Shackleton et al., 1999), however biostratigraphic data suggest continuous sedimentation until at least 16.4 Ma (P.N. Pearson, pers. comm., 2012). The initial age model was produced by fitting a regression through the biostratigraphic data (Figure 10). The foraminiferal biostratigraphic depth datums from Pearson and Chaisson (1997) were assigned ages from Wade et al. (2011), and the nannofossil biostratigraphic depth datums from Raffi et al. (2006)

The physical properties measured on board when the core was collected were analysed to determine their dominant frequencies of variability. As the biostratigraphic data suggest that the sedimentation rate stays constant between 10 and 16.4 Ma, the data from this extended interval was examined to improve the fidelity of the spectral analysis. In order to perform the spectral analyses, a combination of REDFIT (Schulz and Mudelsee, 2002) and Analyseries (Paillard et al., 1996) were used. The advantage of the REDFIT program is that, aside from running on a windows machine without requiring an emulator, it calculates 95% and 99% confidence intervals for each spectrum it calculates. The advantage of Analyseries is that it is far more user-friendly and can easily perform other functions. For this study, calculation of spectra and confidence intervals was performed with REDFIT, and all other functions were done using Analyseries.

Bulk density (Figure 11a) shows four prominent (>99% confidence) frequencies. Magnetic susceptibility (Figure 11b) shows five prominent frequencies. Only the frequency with a period of 23.5 ka bares any resemblance to a known orbital cycle (Earth's precession cycle). It is interesting to note that the second-most prominent frequency with a period of 52.1ka would have a period of approximately 41ka if the sedimentation rate were around 17.5 m $Ma^{-1}$. In previous analyses of the periodicity present in ODP Site 926 from 17.9-26.5 Ma, the obliquity cycle of 41ka was found to be the most prominent signal (Pälike et al., 2006a). Cyclicity in the colour reflectance of the core also shows a

range of periodicities with different frequencies more or less prominent depending on which colour reflectance metric is being examined. B* (Figure 11c, strength of reflectance in the blue or yellow parts of the visible light spectrum) shows seven prominent frequencies. L* (Figure 11d, the lightness of the core) shows eight prominent frequencies. A* (Figure 11e red-green reflectance) shows four prominent frequencies. The different frequencies and their associated periods are shown in appendix 2 (Section 8.2).

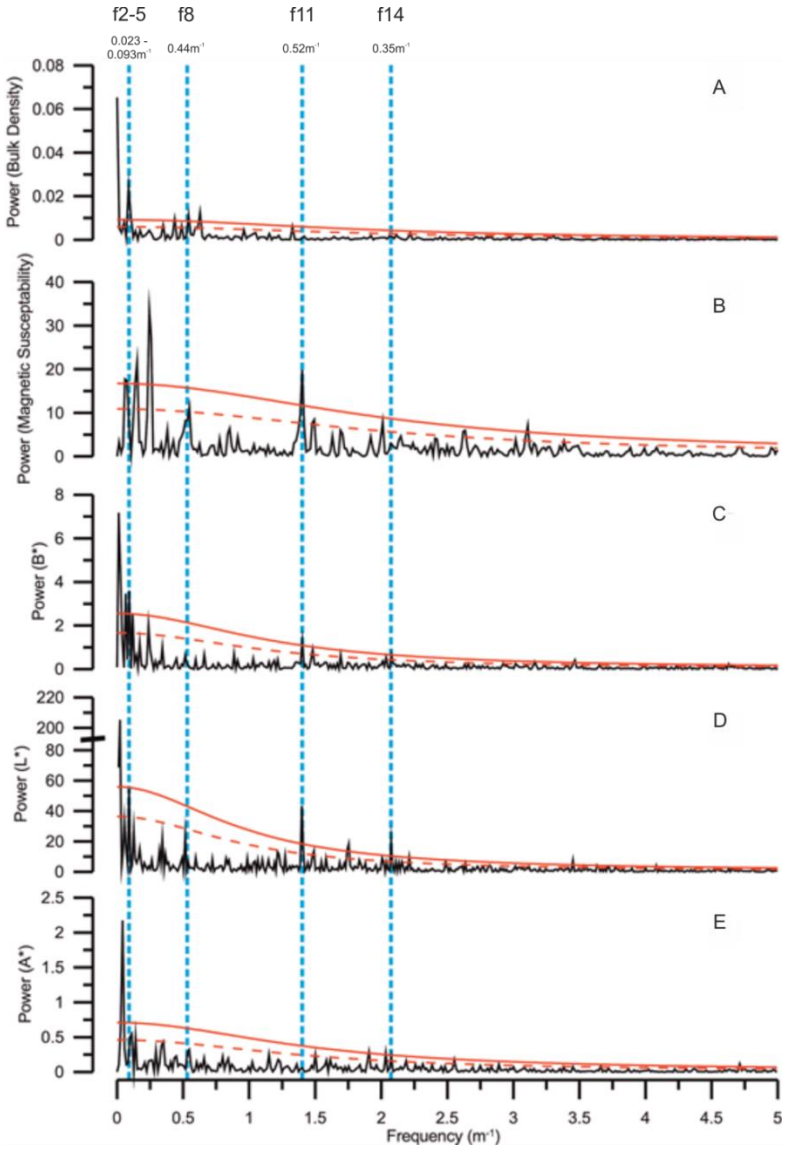


**Figure 11 – Comparison of the dominant frequencies present in different physical properties of the sediment in 926 of Early to Mid-Miocene age (~1.5-16.5 Ma). A) Bulk Density, B) Magnetic Susceptibility, C) B* (yellow-blue reflectance), D) L* (lightness), and E) A* (red-green reflectance).**

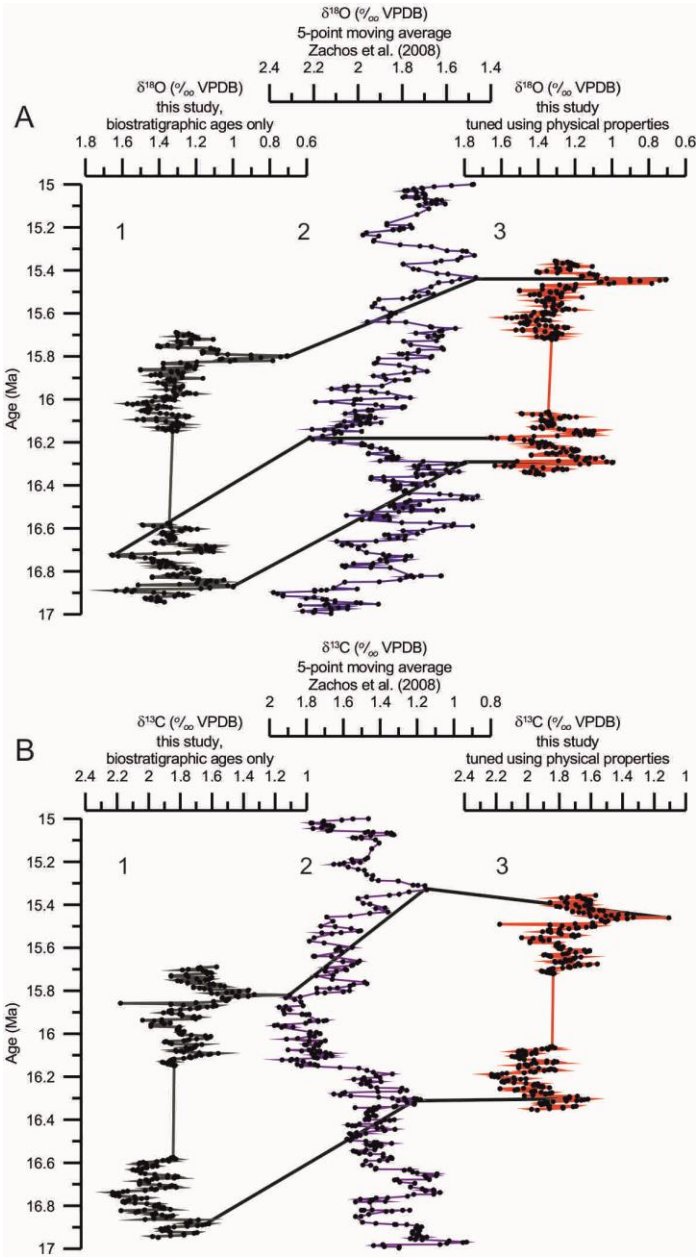


**Figure 12 – Comparison of biostratigraphy-only age model to PPFI age model. A) Comparison of $\delta^{18}O$ in bio-stratigraphy only (1), Zachos et al 2008's record (2), and PPFI age model (3). B) Comparison of $\delta^{13}C$ in biostratigraphy only (1), Zachos et al 2008's record (2), and PPFI age model (3).**

Of all the frequencies only those labelled f11 and f14 (Table 6 in appendix 2, Figure 11; numbers refer to frequencies identified in physical property measurements, appendix 2, section 8.2) are shared across more than 2 of the physical properties. Assuming the linear sedimentation rate derived from the biostratigraphic age model, their periods are around 52 ka and 35 ka, respectively (Figure 11). Assuming the f11 (52kyr) signal actually represents the ~41 kyr obliquity cycle implies a revised linear sedimentation rate between 225 and 300 mbsf of ~17.3m $Ma^{-1}$, which is still consistent with the biostratigraphic

age data (Figure 10). In this scenario the f14 signal has a revised period of around 26 kyr, which may correspond to orbital precession. This assumption allows a new age model, which is dubbed "physical-property frequency informed" (PPFI) to be estimated (Figure 10, red line).

Comparison of the stable isotopes obtained in this study to the revised multi-site benthic $\delta^{18}O$ stack of Zachos et al. (2008) using both the biostratigraphy-only and PPFI age models reveals a far better agreement using the latter age model (c.f. Figure 12a1, a2, and a3). This agreement holds less true for $\delta^{13}C$, however the record at this time is derived primarily from Deep Sea Drilling Program (DSDP) Site 588 in the Western Equatorial Pacific (Shipboard Scientific Party, 1982; Zachos et al., 2008). Given the potential differences in $\delta^{13}C$ between the Atlantic and Pacific Oceans, differences in $\delta^{13}C$ between this record and the one from Zachos et al. (2008) may be expected.

## 2.6 Proxies used in this study

### *2.6.1 Temperature*

Palaeotemperature can be calculated in a number of ways using various proxies, including $TEX_{86}$ (Kim et al., 2008; Kim et al., 2010; Leider et al., 2010; Powers et al., 2004; Schouten et al., 2007), floral and faunal assemblage transfer functions (Chapman et al., 1996; Feldberg and Mix, 2002; Kucera et al., 2005; Mix et al., 1999; Ortiz and Mix, 1997), $\delta^{18}O$ of biogenic calcite (Erez and Luz, 1982; Kroopnic.P et al., 1972; Marchitto et al., 2014; O'Neil et al., 1969; Shackleton and Kennett, 1975), and Mg/Ca of foraminiferal calcite (Bryan and Marchitto, 2008; Dekens et al., 2002; Groeneveld and Filipsson, 2013; Healey et al., 2008; Lea et al., 1999; Lear, 2007; Lear et al., 2000; Lear et al., 2002; Marchitto et al., 2007; Rosenthal et al., 1997; Rosenthal et al., 2000; Tisserand et al., 2013; Yu and Elderfield, 2008).

Organic proxies such as $TEX_{86}$ suffer from concerns over seasonal bias which may not have been constant through time and requires that sufficient organic material be preserved to study. $\delta^{18}O$ of foraminiferal calcite does not suffer from

this shortcoming, however $\delta^{18}O$ of calcite is also affected by the $\delta^{18}O$ of the seawater that calcite was precipitated in, which is also a function of ice volume and local salinity (Cooke and Rohling, 2001). In this study foraminiferal Mg/Ca was used to calculate bottom water and sea surface temperatures.

The relationship of Mg/Ca with temperature in inorganic calcite is exponential and well defined (Katz, 1973; Oomori et al., 1987), however in biogenic calcite the temperature sensitivity relationship is stronger, may be more linear in form, and is heavily dependent on the organism being examined. So-called "vital effects" necessitate genus, or even species-level separation of taxa and individual calibrations. There are numerous calibrations for foraminiferal Mg/Ca with temperature in both benthic (e.g., Elderfield et al., 2006; Healey et al., 2008; Lear et al., 2002; Marchitto et al., 2007) and planktonic species (e.g., Anand et al., 2003; Dekens et al., 2002; McConnell and Thunell, 2005; Nurnberg, 2000; von Langen et al., 2005).

In cold, deep waters with low levels of carbonate saturation, benthic foraminiferal Mg/Ca is also affected by the carbonate saturation state, the difference between $[CO_3^{2-}]$ of the sea water and the $[CO_3^{2-}]$ required for saturation ($\Delta[CO_3^{2-}]$). Surface-dwelling planktonic foraminifera live in carbonate-saturated waters and so a $\Delta[CO_3^{2-}]$ effect on the Mg/Ca ratio of their tests does not need to be considered. Temperature estimates derived from planktonic foraminifera are more reflective of local conditions, however, and are less useful than benthic foraminifera for making estimates of global conditions.

#### *2.6.1.1 Bottom Water Temperature Variations*

In this study, I rely on $\delta^{18}O$ and Mg/Ca, with additional support from Li/Ca. The calibration used to estimate temperature changes from Mg/Ca is from the work of Lear et al. (2002). (1):

$$Mg/Ca = 0.867e^{0.109T} \quad \textbf{(1)}$$

This calibration was chosen in preference to others available due to its broad temperature range and use of multiple *Cibicidoides* species. Species specific calibrations (e.g., Healey et al., 2008; Marchitto et al., 2007) either suffered from effects other than temperature on the Mg/Ca ratio (e.g. $\Delta[CO_3^{2-}]$) or were not appropriate to *C. mundulus* or *Oridorsalis umbonatus* (*O. umbonatus*).

Benthic foraminiferal Mg/Ca is affected by bottom water $\Delta[CO_3^{2-}]$ as well as changes in temperature, and so temperature estimates made based on Mg/Ca need to either rule out or take into account the $\Delta[CO_3^{2-}]$ conditions (Elderfield et al., 2006; Lear et al., 2010). Li/Ca is also affected by $\Delta[CO_3^{2-}]$ and temperature, although Li/Ca decreases with increasing temperature (Bryan and Marchitto, 2008; Dawber and Tripati, 2012a; Hall and Chan, 2004; Lear et al., 2010; Lear and Rosenthal, 2006). Li/Ca in *O. umbonatus* is less variable than in *C. mundulus* (Section 4.4.2), which I have interpreted as being a result of *O. umbonatus*' infaunal habit; living immersed in sediment pore waters as opposed to direct contact with bottom waters is likely to have buffered it from large changes in $\Delta[CO_3^{2-}]$, hence its Li/Ca signal is more stable (Mawbey and Lear, 2013). This would imply that the Mg/Ca temperature record derived from *C. mundulus* is less reliable due to the stronger effect that changes in $\Delta[CO_3^{2-}]$ have the potential to have had. None the less, the Mg/Ca in *O. umbonatus* and Mg/Ca in *C. mundulus* records show many of the same features and agree on the timings and magnitude of changes in temperature. As a result it seems likely that *C. mundulus* was mainly above the threshold $\Delta[CO_3^{2-}]$ for changes in $\Delta[CO_3^{2-}]$ to impact Mg/Ca. Corresponding B/Ca and Sr/Ca can be used to support this interpretation (chapter 5) .

*2.6.1.2 Near-Surface Water Temperature*

Temperatures from the near-surface were calculated using Mg/Ca from *G. trilobus* ($Mg/Ca_G$). *G. trilobus* is an extant planktonic foraminifera that first occurs at around 22.96-22.90 Ma (Shackleton et al., 1999; Wade et al., 2011). Nonetheless, it is poorly represented in core-top calibrations and so the calibrations for *Globogerinoides sacculifer* were used instead. *G. sacculifer* also has the advantage of having an empirically-derived H value (0.41), which allows correction for changes in sea water Mg/Ca and to account for vital effects in the partitioning of Mg into the foraminiferal test (Evans and Müller, 2012). The core-top calibrations of Dekens et al. (2002) and Nurnberg (2000) are identical to within error and the calibration of Dekens et al. (2002) was used here (2):

$$\boldsymbol{Mg/Ca = 0.37e^{0.09T}} \quad \textbf{(2)}$$

The multi-specific Mg/Ca temperature calibration of Anand et al. (2003) differs in both the pre-exponential constant and the exponent by more than double and almost half, respectively. This equation has not been used partly because of its disagreement with the other two, and partly because of the nature of the calibration, which is based on sediment trap, rather than core-top samples.

*2.6.1.3 Correcting for changes in seawater Mg/Ca*

Temperatures were corrected for past variations in the Mg/Ca of seawater ($Mg/Ca_{sw}$) using the model of Stanley and Hardie (1998) as it agrees with proxy estimates from around the same time (e.g., Coggon et al., 2010). A past seawater Mg/Ca of 3.1 mol $mol^{-1}$ was used in conjunction with the modern day value of 5.2 mol $mol^{-1}$. In addition to this, vital effects on the partitioning of $Mg^{+}$ into foraminiferal calcite was taken into account using the method of Evans and Müller (2012). An H value of 0.44 for *C. mundulus* was used (Evans and Müller,

2012). Because the residence time of $Ca^{2+}$ in the oceans is ~1 Ma, $Mg^{+}$ is ~3Ma (Broecker and Peng, 1982) and the duration of each of the two study intervals is no greater than 600 kyr, there will not be any consequential changes in oceanic Mg/Ca. In addition, the major temperature changes are corroborated by simultaneous changes in Li/Ca, and $\delta^{18}O$, and appear in multiple species records.

In order to calculate an absolute temperature from Mg/Ca, the $Mg/Ca_{sw}$ at the time must be known. The assumption made in many previous studies to calculate this (e.g., Foster et al., 2012; Lear et al., 2000) is that (3):

$$\boldsymbol{Mg/Ca_{foram} = \frac{Mg/Ca_{sw}^{t=t}}{Mg/Ca_{sw}^{t=0}} \times Be^{AT}} \quad \textbf{(3)}$$

Where B and A are empirically derived constants unique to individual species. This assumes that the relationship between $Mg/Ca_{foram}$ and $Mg/Ca_{sw}$ is linear. It was shown by Segev and Erez (2006) and Hasiuk and Lohmann (2010) that a better approximation for the relationship between $Mg/Ca_{foram}$ and $Mg/Ca_{sw}$ is (4):

$$\boldsymbol{Mg/Ca_{foram} = F \times Mg/Ca_{sw}^{H}} \quad \textbf{(4)}$$

Where F and H are empirically derived and are unique for individual species, and $Mg/Ca_{sw}$ is the Mg/Ca of sea water, such that (5):

$$\boldsymbol{Mg/Ca_{foram} = \frac{F \times Mg/Ca_{sw}^{t=t^H}}{F \times Mg/Ca_{sw}^{t=0^H}} \times Be^{AT}} \quad \textbf{(5)}$$

Where t=0 is in the modern ocean and t=t is in the ocean during the time period being studied. This can be rearranged as (6):

$$Mg/Ca_{foram} = \frac{B}{Mg/Ca_{sw}^{t=0^H}} \times Mg/Ca_{sw}^{t=t^H} e^{AT} \quad \textbf{(6)}$$

Evans and Müller (2012) point out that in order to calculate $\delta^{18}O_{sw}$ for a sample using coupled $\delta^{18}O$ and Mg/Ca measurements, four values need to be constrained: $Mg/Ca^{t=t}{}_{sw}$, and H as well as $Mg/Ca_{foram}$, and $\delta^{18}O_{foram}$. Assuming an ice free world has a $\delta^{18}O_{sw}$ of between -0.9‰ and -1.2‰ (Lear et al., 2000) has allowed them to estimate the H of *O. umbonatus* as being between 0.44 and 0.48, though they have also made the assumption that the model estimate of $Mg/Ca_{sw}$ at 49 Ma by Stanley and Hardie (1998) is correct. It is worth noting that they calculated H using $\delta^{18}O_{sw}$ of -0.9‰ as well, giving a value between 0.52 and 0.54 for $H_{O.\ umbonatus}$. Despite the uncertainties associated with determining H, the Evans and Müller (2012) estimate of 0.44 is used here to calculate absolute BWT from *C. mundulus* Mg/Ca records.

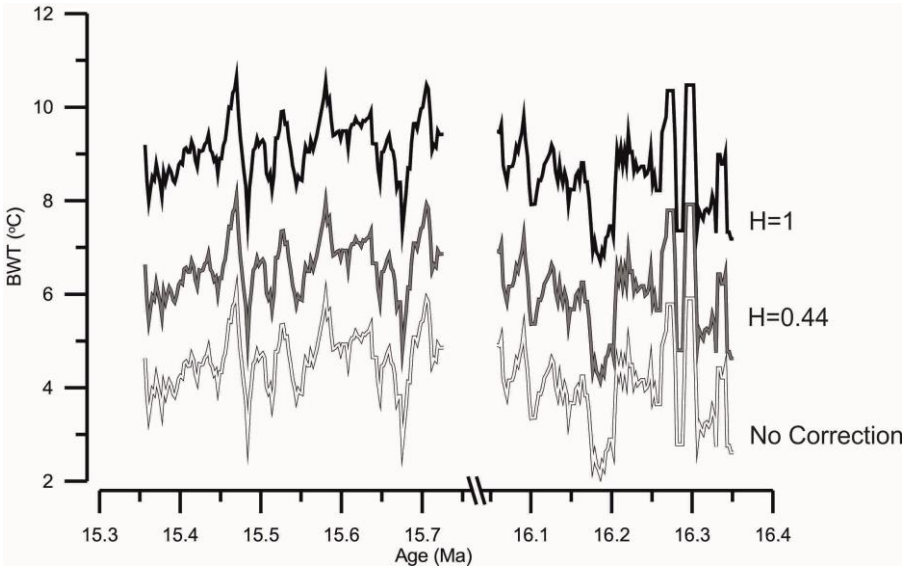


**Figure 13 – Comparison of different bottom water temperatures obtained when differing values of H are assumed. H = 1 assumes a linear relationship between seawater Mg/Ca and foraminiferal Mg/Ca. H=0 assumes Mg/Ca from foraminifers does not need to be corrected for secular changes in seawater Mg/Ca. H=0.44 is the value calculated for *O. umbonatus* by Evans and Müller (2012). Despite there being large changes in the absolute value of temperature obtained, there is no difference in the relative change in temperature in each record.**

The modelled estimate of Miocene (16 Ma) seawater Mg/Ca of Stanley and Hardie (1998) (~3.1 ± 0.5 mol $mol^{-1}$) was used as this model agrees well with proxy data from the same time (Coggon et al., 2010; Evans and Müller, 2012; Fantle and DePaolo, 2006; Horita et al., 2002; Lowenstein et al., 2001). Of note is the fact that the relative changes in temperature do not change if H is changed or if no correction is applied at all (Figure 13). This means that uncorrected or even incorrectly corrected Mg/Ca temperature estimates are still useful in showing relative changes on timescales less than the residence time of Mg in sea water.

Correcting the temperature estimates assuming that H=1 (i.e.: a linear response of foraminiferal test Mg/Ca to changes in Mg/Ca of seawater) results in 5°C higher bottom water temperatures when compared to the uncorrected temperature estimates and ~4°C higher than estimates assuming H=0.44 (Figure 13). Bottom water temperature estimates of between 8 and 10°C are higher than previous estimates of bottom water temperatures during the MMCO (Lear et al., 2000; Shevenell et al., 2008), but fall in line with the temperatures reported by Foster et al. (2012). The difference between the uncorrected temperature and H=0.44 is ~1°C.

### *2.6.2 Sea Level/Ice Volume*

Changes in global ice volume can be estimated from changes in benthic $\delta^{18}O_{sw}$ (e.g., Lear et al., 2008; Lear et al., 2000). The *Cibicidoides spp.* temperature versus $\delta^{18}O$ calibration of Marchitto et al. (2014) was used to calculate $\delta^{18}O_{sw}$ (7):

$$(\boldsymbol{\delta^{18}O_c - \delta^{18}O_{sw} + 0.27}) = \boldsymbol{-0.245T + 0.0011T^2 + 3.58} \quad \textbf{(7)}$$

Where T is the temperature in °C, $\delta^{18}O_{sw}$ is the $\delta^{18}O$ of the ambient sea water (relative to SMOW) and $\delta^{18}O_c$ is the $\delta^{18}O$ of the foraminiferal carbonate. I use temperatures derived from $Mg/Ca_M$ and $\delta^{18}O_c$ from *C. mundulus* to calculate

$\delta^{18}O_{sw}$. Calculating surface $\delta^{18}O_{sw}$ was done in a similar manner, but using Mg/Ca and $\delta^{18}O$ derived from *G. trilobus*, and the equation of O'Neil et al. (1969) (8):

$$\boldsymbol{T = 16.9 - 4.38(\delta^{18}O_c - (\delta^{18}O_{sw} - 0.27)) + 0.1(\delta^{18}O_c - (\delta^{18}O_{sw} - 0.27))^2} \quad \textbf{(8)}$$

*G. trilobus* is a suitable species for estimates of surface conditions as it is surface dwelling (Be and Hutson, 1977), well-studied in terms of its geochemistry (e.g., Anand et al., 2003; Dekens et al., 2002; Nurnberg, 2000), and persists from the modern into the earliest Miocene (Shackleton et al., 1999; Wade et al., 2011).

Benthic $\delta^{18}O_{sw}$ is then subtracted from the planktonic $\delta^{18}O_{sw}$ on the assumption that benthic $\delta^{18}O_{sw}$ is primarily controlled by ice volume and that planktonic $\delta^{18}O_{sw}$ is controlled by both ice volume and surface salinity changes. The resultant $\delta^{18}O$ of the surface sea water ($\delta^{18}O_{ssw}$) is assumed to reflect surface salinity.

### *2.6.3 Saturation State*

Carbonate saturation state ($\Delta[CO_3^{2-}]$) is a key component of the global carbon cycle. It is defined as the difference between the measured $[CO_3^{2-}]$ *in situ* and $[CO_3^{2-}]$ at saturation and is an indication of the tendency of $CaCO_3$ to dissolve (Broecker and Peng, 1982). $[CO_3^{2-}]$ at saturation in the ocean is estimated by (9):

$$\boldsymbol{[CO_3^{2-}]_{saturation} = 90e^{0.16(z-4)}} \quad \textbf{(9)}$$

Where Z is the water depth in km (Broecker and Peng, 1982). $\Delta[CO_3^{2-}]$ is therefore estimated by (10):

$$\Delta[CO_3^{2-}] = [CO_3^{2-}]_{in\ situ} - [CO_3^{2-}]_{saturation}$$

**(10)**

Positive numbers indicate oversaturation, negative numbers indicate under-saturation. Changes in $\Delta[CO_3^{2-}]$ below a threshold of ~25 μmol $kg_{sw}^{-1}$ (Elderfield et al., 2006) appear to affect foraminiferal Mg/Ca enough to mask the signal caused by changes in temperature and so quantifying $\Delta[CO_3^{2-}]$ is important for palaeothermometry.

There are several geochemical proxies that can be used when estimating saturation state. Those that have been used in this study are Sr/Ca (Dawber and Tripati, 2012a; Raitzsch et al., 2010; Rathmann and Kuhnert, 2008; Rosenthal et al., 2006), U/Ca (chapter 3, this thesis; Keul et al., 2013; Raitzsch et al., 2011), and B/Ca (Dawber and Tripati, 2012a; Rae et al., 2011; Yu and Elderfield, 2007; Yu et al., 2010b).

#### *2.6.3.1 Sr/Ca*

Foraminiferal Sr/Ca ratios have been used in several calibration studies to quantify changes in $\Delta[CO_3^{2-}]$ (Dawber and Tripati, 2012a; Raitzsch et al., 2010; Rathmann and Kuhnert, 2008; Rosenthal et al., 2006). Sr/Ca is problematic in this regard, though, as it is also affected by temperature (Cleroux et al., 2008; Dawber and Tripati, 2012a; Mortyn et al., 2005). Foraminiferal Sr/Ca also reflects variations in seawater Sr/Ca, but the long residence times of Sr (~10 Myr) and Ca (~1 Myr) in seawater means this is not a significant issue in this study.

Estimates of benthic $\Delta[CO_3^{2-}]$ using Sr/Ca are made in this thesis using the calibration of Dawber and Tripati (2012a) as it is specific to *Oridorsalis umbonatus* (11):

$$\boldsymbol{Sr/Ca = 0.00207(\pm 0.0003)\Delta[CO_3^{2-}] + 0.8764(\pm 0.0072)}$$

***(11)***

*2.6.3.2 U/Ca*

U/Ca offers a new alternative for bottom water $\Delta[CO_3^{2-}]$ reconstructions (chapter 3, this thesis; Keul et al., 2013; Raitzsch et al., 2011). This proxy is similarly beset by problems, not least of which is its inclusion in authigenic coatings on foraminiferal calcite, and its close association with redox conditions below the sediment-water interface (Boiteau et al., 2012; Chun et al., 2010; Francois et al., 1993; Mangini et al., 2001; McManus et al., 2005). As it stands, much more work needs to be conducted upon U/Ca before it can be reliably used as an indicator of carbonate saturation conditions at the sea floor. In this thesis I attempt to use it in conjunction with Mn/Ca as an indicator of sea-floor redox conditions.

*2.6.3.3 B/Ca*

A global core-top study suggests that benthic foraminiferal B/Ca also correlates well with $\Delta[CO_3^{2-}]$, with $R^2$ values of ~0.8 in the two *Cibicidoides* species studied here (C. mundulus and C. wuellerstorfi, Yu and Elderfield, 2007). This study is noteworthy in that they used foraminifera from multiple ocean basins with very different oceanographic profiles and yet still found a strong correlation between B/Ca and $\Delta[CO_3^{2-}]$. Yu and others have successfully applied foraminiferal B/Ca to changes in $[CO_3^{2-}]$ across the last glacial maximum (Yu et al., 2010a; Yu and Elderfield, 2007; Yu et al., 2008). None the less, Rae et al. (2011) caution against relying too heavily on B/Ca due to its sensitivity to vital effects that becomes apparent even at the species morphotype level (c.f. *C. wullerstorfi sensu stricto, C. wullerstorfi var., C. mundulus var.,* and *C. mundulus sensu stricto*).

Estimates of $\Delta[CO_3^{2-}]$ used using B/Ca are made using the equation of Yu and Elderfield (2007) as it is specific to *Cibicidoides mundulus* (12):

$$\boldsymbol{B/Ca = 0.69(\pm 0.072)\Delta[CO_3^{2-}] + 119.1(\pm 2.62)} \quad \textbf{(12)}$$

*2.6.3.4 $pCO_2^{ATM}$*

Boron is useful in other capacities within geochemical analyses of foraminiferal calcite. $\delta^{11}B$ is used as a proxy for pH and is used in conjunction with other carbonate-system parameters to calculate $CO_2$ (e.g., Foster et al., 2012; Greenop et al., 2014). Boron exists in sea water as boric acid ($B(OH)_3$) and the borate ion ($B(OH)_4^-$), related by the acid-base equilibrium (13):

$$\boldsymbol{B(OH)_3 + 2H_2O \leftrightarrow B(OH)_4^- + H_3O^+} \quad \textbf{(13)}$$

The equilibrium constant of this reaction ($K_B^*$) is $10^{-8.6}$, $pK_B^*$ is 8.6 in seawater of 25°C, 35 salinity and at atmospheric pressure (Dickson, 1990), the proportions of the two major boron-containing species should vary with ocean pH (typically ~8) (Rae et al., 2011). This is the basis for the $\delta^{11}B$ pH proxy, and it works on the assumption that it is exclusively the $B(OH)_4^-$ ion that is incorporated into foraminiferal calcite, (Rae et al., 2011). The seawater carbonate system is defined by six variables: alkalinity, $pCO_2^{ATM}$ , pH, total dissolved inorganic carbon, $[CO_3^{2-}]$, and $[HCO_3^-]$, but has only two degrees of freedom. If two of the variables plus temperature, pressure, and salinity are known, then the rest of the variables can be estimated (e.g., Foster et al., 2012; Pearson et al., 2009).

Boron exists as two stable isotopes in sea water: $^{11}B$ (~80%) and $^{10}B$ (~20%), expressed as a ratio $\delta^{11}B$ relative to the NIST 951 standard (Catanzaro et al., 1970) such that (14):

$$\boldsymbol{\delta^{11}B = \left[\left(\frac{^{11}B/^{10}B_{sample}}{^{11}B/^{10}B_{NIST951}}\right) - 1\right] \times 1000} \quad \textbf{(14)}$$

$\delta^{11}B$ of modern seawater is 39.61 ‰ (Foster et al., 2010b; Rae et al., 2011). Isotopic fractionation exists between $B(OH)_4^-$ and $B(OH)_3$ so that $^{11}B$ is concentrated in $B(OH)_3$. The proportions of $B(OH)_4^-$ and $B(OH)_3$ vary with ocean pH however the overall $\delta^{11}B$ of seawater does not. The $\delta^{11}B$ of each species therefore varies with pH, and as B(OH)4- is the species incorporated into foraminiferal carbonate, the $\delta^{11}B$ of that carbonate will reflect ocean $\delta^{11}B$ and thus pH (Rae et al., 2011)

In this study, five samples were chosen for boron isotope analysis at NOC conducted by S. Sosdian and R. Greenop. $pCO_2^{ATM}$ calculations follow Greenop et al. (2014).

### *2.6.4 Productivity*

#### *2.6.4.1 $\delta^{13}C$*

There are many proxies for productivity, one of which is $\delta^{13}C$ of planktonic foraminiferal calcite. Preferential uptake of the lighter carbon isotope, $^{12}C$, causes marine organic matter to have heavily depleted $\delta^{13}C$ values of ~-20 to -23‰ (Cooke and Rohling, 2001). As a result, the remaining inorganic carbon, primarily $HCO_3^-$, is very depleted in $^{12}C$ and calcium carbonate formed from that reservoir reflects that. As a result, all else being equal, heavier $\delta^{13}C$ of planktonic carbonate reflects increased primary productivity (PP).

Remineralisation of organic matter at depth results in the depleted $\delta^{13}C$ signal re-equilibrating with $HCO_3^-$ and so a signal relatively enriched in $^{12}C$ occurs in carbonates formed at depth. If the rate of remineralisation in the deep ocean increases, this may result in an increased gradient between surface and deep $\delta^{13}C$, and so surface-deep $\Delta\delta^{13}C$ has been suggested to reflect local productivity.

In regions of upwelling, the isotopically light remineralised carbon may be brought back to the surface, complicating interpretation of $\delta^{13}C$ records. Furthermore, benthic $\delta^{13}C$ records can also be affected by changing water masses as well as numerous other factors (see Cooke and Rohling, 2001 for a

comprehensive treatment of the controls on δ13C). Nevertheless, there are some intervals where carbon isotope records have been used to explain global cooling via high productivity and burial of excess organic carbon, (e.g., post-MECO (middle Eocene climatic optimum) (Spofforth et al., 2010), and the post- MMCO Monterey interval (Flower and Kennett, 1993; Raymo, 1994)).

#### *2.6.4.2 BFAR*

Interpretation of $\delta^{13}C$ can be aided by benthic foraminiferal accumulation rate (BFAR), a semi-quantitative measure of productivity. BFAR has been used to estimate export productivity in many palaeoclimatological studies, and serve as a useful guide to the amount of organic matter reaching the sea floor as it provides a good food source for benthic communities (Berger and Wefer, 1990; Diester-Haass et al., 2011; Herguera, 2000). Usually all tests >150 μm are used, however only foraminifera above >250 μm were counted here, as these were the specimens being used for geochemical analysis. The sedimentation rate used was the same as that used to calculate the age model for the record: 1.73cm $ka^{-1}$. Dry bulk densities were taken from Shipboard Scientific Party (1995c). Calculation of BFAR (in tests $cm^{-2}$ $ka^{-1}$) was done using the following equation (15):

$$\boldsymbol{BFAR = \frac{DBD \times n}{S}} \quad \textbf{(15)}$$

Where DBD is the dry bulk density of the sediment, n is the number of benthic foraminiferal tests >250 μm in size and S is the sedimentation rate in cm $ka^{-1}$

# 3 CORE-TOP CALIBRATION OF TRACE METAL RATIOS OF BENTHIC FORAMINIFERA FROM THE NORWEGIAN SEA

Foraminiferal Mg/Ca is sensitive to changes in the carbonate saturation state of sea water ($\Delta[CO_3^{2-}]$) as well as temperature. Quantifying the effect of $\Delta[CO_3^{2-}]$ on Mg/Ca as well as other trace element/Ca ratios such as Li/Ca, B/Ca, and U/Ca will help to remove the effect of $\Delta[CO_3^{2-}]$ on estimates of temperature derived from this proxy. The benthic foraminiferal species: *Cibicidoides wuellerstorfi*; *Oridorsalis umbonatus;* and *Pyrgo murrhina* from the Norwegian Sea were analysed. A suite of multiple element/Ca ratios were collected from each species using an inductively-coupled mass spectrometer at Cardiff University. The Norwegian Sea is unique in that its waters below ~1500m are almost holothermal at around -1°C, allowing changes in $\Delta[CO_3^{2-}]$ to be analysed independently of temperature. The sensitivity of Mg/Ca in *C. wuellerstorfi to changes in* $\Delta[CO_3^{2-}]$ was found to be ~0.0077 mmol $mol^{-1}$ $\mu mol^{-1}$ $kg_{sw}^{-1}$, which is similar to results obtained in other studies. Mg/Ca in *P. murrhina* was found to show very little or no sensitivity to changes in temperature below 2°C, but shows potential as a temperature-independent recorder of changes in $\Delta[CO_3^{2-}]$. Additionally U/Ca shows negative sensitivity to changes in $\Delta[CO_3^{2-}]$ in all species analysed except *P. murrhina*.

### 3.1 Introduction

Reconstructions of palaeooceanographic conditions require use of proxies in order to estimate past physical climatic conditions. Magnesium/Calcium (Mg/Ca) ratios of benthic foraminiferal tests are used as a proxy for deep ocean temperatures (e.g., Lear et al., 2000; Lear et al., 2002). In order to calibrate Mg/Ca for use as a palaeothermometer, modern analogues to ancient species are found and their test chemistry analysed and compared to the conditions under which their tests precipitated. The temperature at which inorganic calcite precipitates can effect a change in the ratio of magnesium to calcium within the calcite lattice (Burton and Walter, 1991). The same can be said for biogenically precipitated calcite, however the Mg/Ca ratio is strongly affected by the type of organism being studied (e.g., Chave, 1954). The sensitivity of the Mg/Ca ratio to changes in temperature can vary between the species being studied, making species-specific calibrations very important for analyses of changes in palaeotemperature (Healey et al., 2008; Lear et al., 2002).

Foraminiferal Mg/Ca is sensitive to changes in bottom water $CO_3^{2-}$ saturation state ($\Delta CO_3^{2-} = [CO_3^{2-}]_{in\ situ} - [CO_3^{2-}]_{saturation}$), especially below 3°C (Elderfield et al., 2006) and at saturation states below ~25 $\mu mol/kg_{sw}$ (Healey et al., 2008; Yu and Elderfield, 2008). The partitioning of Mg into $CaCO_3$ is affected by changes in the $\Delta[CO_3^{2-}]$ (Lear et al., 2004; Lear et al., 2002; Rosenthal et al., 2006). This can give a misleading temperature signal across intervals where the $\Delta[CO_3^{2-}]$ has changed dramatically, such as the EOT (Lear et al., 2000; Lear et al., 2004). As the intervals being studied include significant changes in global ice volume, $\Delta[CO_3^{2-}]$ may be variable due to the links between sea level & the global carbon cycle (Merico et al., 2008).

*Oridorsalis umbonatus* (*O. umbonatus*) is a common benthic foraminifer that originated in the late Cretaceous, ~86 Ma (Kaiho, 1998). It is a cosmopolitan species that can tolerate a broad depth range within the sediment, can be found living between 0 and 4cm, and can tolerate conditions with low oxygenation and limited food supply (Rathburn and Corliss, 1994). Conversely, *O.*

*umbonatus* has also been found in cold, well oxygenated bottom waters (Murgese and De Deckker, 2005), though its preference for nutrient-poor waters is well documented. Its habit as a shallow-infaunal species makes it an ideal companion to trace metal studies of palaeoclimate with epifaunal species. Due to its infaunal habit *O. umbonatus'* test chemistry may reflect pore water rather than bottom water conditions. One advantage of this is that its Mg/Ca signal may be sheltered from changes in the bottom-water $\Delta[CO_3^{2-}]$ (Mawbey and Lear, 2013). *O. umbonatus* has been used multiple times in studies of deep-sea palaeotemperatures due to its relative abundance and longevity (Lear et al., 2000; Lear et al., 2010; Lear et al., 2003; Tripati et al., 2005). Lear et al. (2003) used *O. umbonatus* in conjunction with *Cibicidoides wuellerstorfi* (*C. wuellerstorfi*) and *Cibicidoides mundulus* (*C. mundulus*) from ODP Site 926 in the Atlantic and ODP Site 806 in the Pacific. They note that the Mg/Ca ratio of *O. umbonatus* behaves more similarly to *C. mundulus* in their Atlantic record and more similarly to *C. wuellerstorfi* in their Pacific record. They speculate that this is to genetic differences between *O. umbonatus* individuals in either basin.

*C. wuellerstorfi* is an epibenthic foraminifera that evolved between 16.1 and 15.7 Ma (Thomas, 2007; Thomas and Vincent, 1987). *C. wuellerstorfi* is one of the staple workhorses of benthic foraminiferal palaeoclimatology in the Neogene and has been used in numerous studies utilising stable isotopes and Mg/Ca to deconvolve ocean floor temperatures and global ice volume (Billups and Schrag, 2002; Lear et al., 2000; Lear et al., 2003). It lives on objects that stick out above the sediment-water interface to allow it to suspension feed (Thomas, 2007). Its presence in the modern ocean is associated with regions of high PP and high proportion of coarse sediment (Mackensen, 1987). Living on the sediment-water interface makes it ideal for recording the conditions present at the sea-floor because it is not sheltered, like *O. umbonatus*, from any changes that occur and changes in bottom water $\delta^{13}C$ are reflected almost 1:1 by changes in $\delta^{13}C$ in the test of *C. wuellerstorfi* (Cooke and Rohling, 2001, and references therein). The negative consequence of this is that its tests' Mg/Ca ratio may

therefore be vulnerable to large changes in $\Delta[CO_3^{2-}]$ at low levels of carbonate saturation state (e.g., Elderfield et al., 2006).

*Pyrgo murrhina* (*P. murrhina*) is a porcelaneous benthic (or miliolite) foraminifera less commonly used in palaeoceanographic studies. It occurs as far back as the Oligocene (Shipboard Scientific Party, 2002). In modern oceans it appears to thrive in cold (<2.5$^{o}$C), well oxygenated (>3.5ml $l^{-1}$) and oligotrophic conditions (Gudmundsson, 1998; Murgese and De Deckker, 2005). It has a relatively global modern day distribution, appearing in deep waters in the North Atlantic, in the Gulf of Mexico, and in the Pacific ocean (Gudmundsson, 1998), as well as in the Indian Ocean (Murgese and De Deckker, 2005). *P. murrhina* is noted as having an unusually high Mg/Ca ratio in its test (Boyle, 1983; Healey et al., 2008) and its Mg/Ca ratio shows high sensitivity to changes in bottom water temperature; between 1 and 3$^{o}$C it shows ~6.3 mmol $mol^{-1}$ $^{o}C^{-1}$ change in Mg/Ca, or in exponential calibrations it appears to show a 43% increase in its Mg/Ca ratio per 1$^{o}$C increase in temperature (Healey et al., 2008). This fact alone makes it appear as if it would be of great use as a palaeothermometer as a 1 mmol $mol^{-1}$ change in its test's Mg/Ca ratio could show <0.2$^{o}$C changes in temperature. Its potential use is hampered by its poor representation amongst core-top and culture trace-metal calibrations (Healey et al. (2008) being the only one available at time of writing) and its poor tolerance for temperatures much above 7$^{o}$C.

Numerous temperature calibrations using foraminiferal Mg/Ca have been performed on both planktonic (Anand et al., 2003; Lea et al., 1999; McConnell and Thunell, 2005; Skinner and Elderfield, 2005; von Langen et al., 2005) and benthic (Allison et al., 2010; Elderfield et al., 2006; Lear et al., 2002; Marchitto et al., 2007; Rosenthal et al., 1997; Segev and Erez, 2006; Yu and Elderfield, 2008) foraminiferal tests. Predictions based on thermodynamic calculations for pure mineral phases suggest that the Mg/Ca ratio of calcite will increase by around 3% per 1$^{o}$C increase in temperature between 0$^{o}$C and 30$^{o}$C (Koziol and Newton, 1995). The sensitivity of Mg/Ca to temperature determined from culture and

core-top studies of foraminiferal calcite suggests that Mg/Ca increases around 10% per 1°C increase in temperature (Lea et al., 1999; Rosenthal et al., 1997). Recent calibrations show no statistically significant hints that foraminiferal Mg/Ca responds exponentially to temperature (Bryan and Marchitto, 2008; Healey et al., 2008; Marchitto et al., 2007) even though this would be expected from thermodynamics and experiments involving abiogenic uptake of Mg into calcite (Koziol and Newton, 1995).

The differences in response, both between species and between biogenic and abiogenic uptake of Mg, of the Mg/Ca ratio in foraminiferal tests is affected by more than just simple thermodynamic processes, and that there may be some physiological component as well (Bentov and Erez, 2006; Elderfield et al., 2006; Lear et al., 2000; Lear et al., 2002; Rosenthal et al., 1997; Segev and Erez, 2006; Skinner and Elderfield, 2005). The difference in Mg/Ca ratios between species can give temperature discrepancies of as great as 5°C in samples from the same stratigraphic height (Skinner and Elderfield, 2005). This highlights the need for species specific Mg/Ca temperature calibrations.

The partitioning of Mg into $CaCO_3$ is also affected by changes in seawater $\Delta[CO_3^{2-}]$ of the ocean when $\Delta[CO_3^{2-}]$ is approximately <25 μmol $kg^{-1}$ (Elderfield et al., 2006; Lear et al., 2004; Lear et al., 2002; Rosenthal et al., 2006; Yu and Elderfield, 2008). This can give a misleading temperature signal across intervals where the $\Delta[CO_3^{2-}]$ has changed dramatically, such as the Eocene Oligocene Climate Transition (EOCT) (Lear et al., 2000; Lear et al., 2004). Changes in $\Delta[CO_3^{2-}]$ can mask the temperature signal in Mg/Ca, so it is important to constrain the magnitude of changes in $\Delta[CO_3^{2-}]$ when calculating palaeotemperatures.

Yu and Elderfield (2007) found an empirical relationship between B/Ca and $\Delta[CO_3^{2-}]$ of marine water. There are significant differences in the relationship between B/Ca and $\Delta[CO_3^{2-}]$ between species and, as was shown by Rae et al. (2011), between species morphotypes. Foraminiferal B/Ca as a proxy for seawater $\Delta[CO_3^{2-}]$ is still in its infancy. A global core-top study suggests that

benthic foraminiferal B/Ca correlates well with $\Delta[CO_3^{2-}]$, with $R^2$ values of ~0.8 in the two *Cibicidoides* species studied. (Yu and Elderfield, 2007). Their study included four species (*C. wuellerstorfi, C. mundulus, Uvigerina spp.* and *Hoeglundia elegans*), and it is noteworthy in that they used foraminifera from multiple ocean basins with very different oceanographic profiles and yet still found a strong correlation between B/Ca and $\Delta[CO_3^{2-}]$. Yu and others have successfully applied foraminiferal B/Ca to changes in $[CO_3^{2-}]$ across the last glacial maximum (Yu et al., 2010a; Yu and Elderfield, 2007; Yu et al., 2008). None the less, Rae et al. (2011) caution against relying too heavily on B/Ca due to its sensitivity to vital effects that becomes apparent even at the species morphotype level (c.f. *C. wuellerstorfi sensu stricto, C. wuellerstorfi var., C. mundulus var.,* and *C. mundulus sensu stricto*). This highlights a pressing need for new foraminiferal B/Ca core-top calibrations to expand the current range of species available for palaeo-$\Delta[CO_3^{2-}]$ reconstruction.

Another promising proxy for sea water $\Delta[CO_3^{2-}]$ is U/Ca . U is incorporated in the $CaCO_3$ lattice as uranyl tricarbonate ($UO_2(CO_3)_3^{4-}$), replacing both Ca and $CO_3$. Because $[UO_2CO_3]$ and $[UO_2(CO_3)_2^{2-}]$ both decrease with increasing $[CO_3^{2-}]$ in sea water, and U/Ca shows the same relationship, these species may substitute for $UO_2(CO_3)_3^{4-}$ in calcite (Keul et al., 2013; Russell et al., 2004). It was noted that U/Ca varied with Mg/Ca ratios in sediments on the Sierra Leone Rise in the Equatorial Eastern Atlantic, and in the Caribbean sea (Russell et al., 1996). At the time, this was hypothesised to represent a temperature dependence on U/Ca, as a $\Delta[CO_3^{2-}]$ dependence on Mg/Ca was not considered or was discounted. A culture study of *Orbulina universa* and *Globigerina bulloides* indicated that U/Ca in planktonic foraminifera decreases by 25% for every 100 $\mu mol\ kg_{sw}^{-1}$ increase in $[CO_3^{2-}]$ (Russell et al., 2004). U/Ca also shows a strong dependence on test-size. This is thought to be related to the fact that larger foraminifera grow at a faster rate and so are less able to discriminate between ions that they incorporate into their tests (Ni et al., 2007). Ni et al. (2007) also

observed variations in U/Ca between sites with similar [$CO_3^{2-}$], and so they suggest that other factors may influence U/Ca.

Benthic foraminiferal U/Ca shows a linear relationship over a range of $\Delta[CO_3^{2-}]$ from -10 to 40 μmol $kg_{sw}^{-1}$ with a sensitivity of -0.27 and -0.30 nmol $mol^{-1}$ $\mu mol^{-1}$ $kg_{sw}^{-1}$ in *C. wuellerstorfi* and *C. mundulus*, respectively (Raitzsch et al., 2011). The linear appearance of the relationship is attributed to the narrow range of $\Delta[CO_3^{2-}]$ over which the study was conducted. The $R^2$ values (0.58 for *C. wuellerstorfi* and 0.65 for *C. mundulus*) of the calibrations given by Raitzsch et al. (2011) are taken as an indication that only some of the trends seen can be explained as reflecting changes in bottom water $\Delta[CO_3^{2-}]$, and that therefore there must be some other factor, or factors, controlling U/Ca ratios in benthic foraminifera.

One potential other factor that affects U/Ca ratios is the concentration of U in authigenic coatings on foraminiferal tests. Authigenic U is added to sediments when soluble U(IV) from pore waters is reduced to insoluble U(VI) and precipitates out (Boiteau et al., 2012). The enrichment of U in sediments is limited by the flux of U from the overlying water column, which is in turn determined by the availability of oxygen, and the rate of supply of organic carbon to the sea floor (Barnes and Cochran, 1990). Elevated U/Ca values (>~70 nmol $mol^{-1}$) at 23.2 to 23 Ma from ODP Sites 926 and 929 were interpreted to be from an authigenic source due to the lack of any corresponding change in other $\Delta[CO_3^{2-}]$ proxies (Mawbey and Lear, 2013).

### *3.1.1 Study Site- the Norwegian Sea*

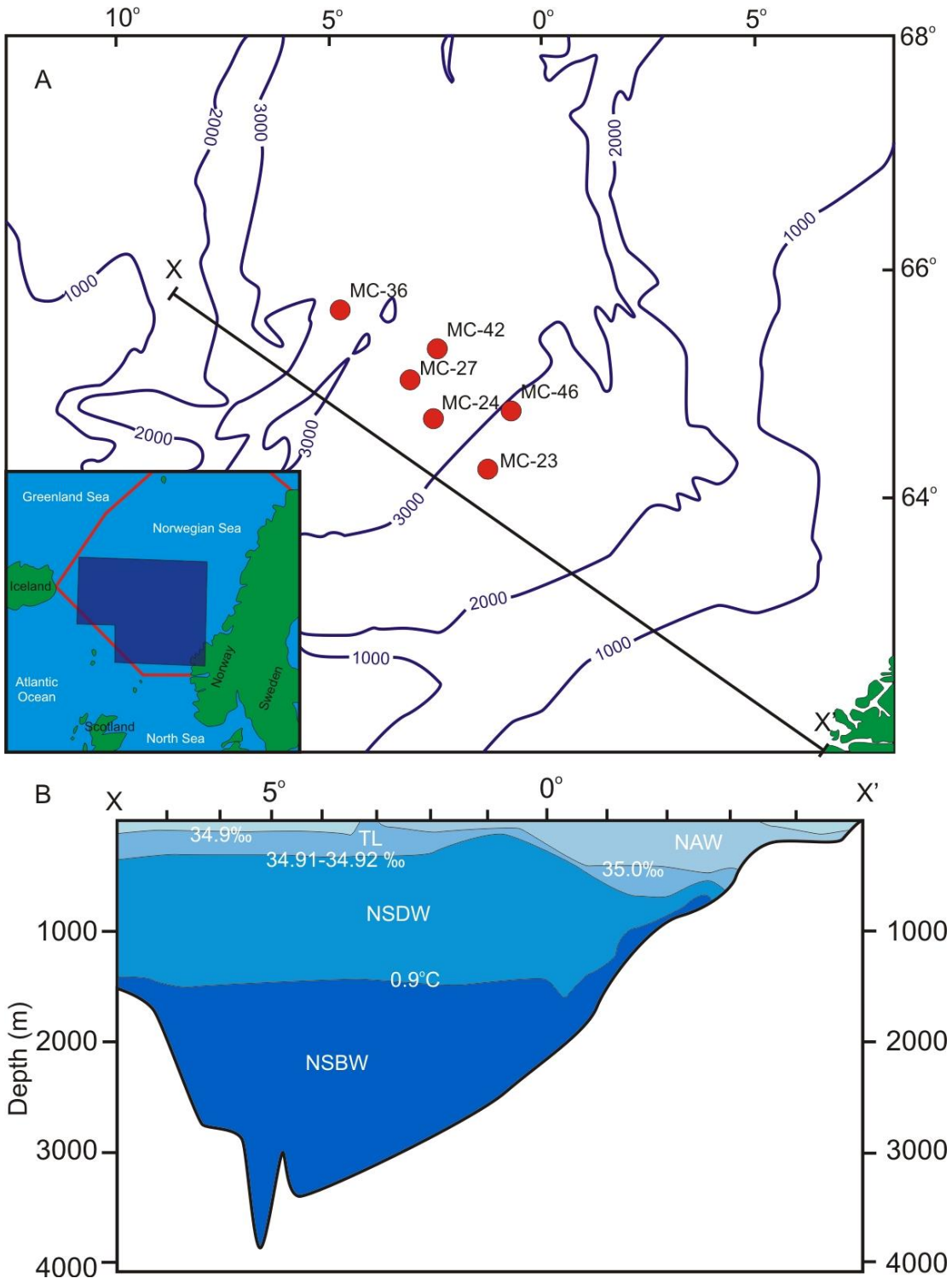


**Figure 14 – Location and oceanography of the Norwegian Sea. A) The study area. Sites are labelled with red circles. (PIP – the location of the Norwegian Sea bounded in red and the study area in dark blue in relation to it). B) Oceanography of the Norwegian Sea. NAW = North Atlantic Water. TL = Transition Layer. NSDW = Norwegian Sea deep water. NSBW = Norwegian Sea Bottom Water. Adapted from Mackensen et al., 1985. The location of study sites was taken from the Knorr KNR-177II Cruise**

This study uses benthic foraminifera collected from the Norwegian Sea, which is a marginal sea in the North Atlantic Ocean (Figure 14A). It is bounded

to the east by the west coast of Norway, to the north by the southern tip of Spitsbergen and to the west by the eastern tip of Iceland (International Hydrographic Organisation, 1953). Its average depth is around 2000m, though it is ~3800m at its deepest point.

There are four primary water masses that fill the Norwegian Sea basin: North Atlantic Water (NAW) sits above the continental slope and bathes the Norwegian Coast in highly saline (>35‰) waters to a depth of around 500 m in waters that are between 6 and 14°C. below that is a layer of transitional water (TL) that forms a boundary between NAW and the homohaline (~34.91‰) Norwegian Sea Deep Water (NSDW). The NSDW itself goes down to a depth of ~1500m, though the TL and the NSDW are between them only 200m thick on near the continental margin as the Norwegian Sea Bottom Waters (NSBW) are depressed upwards by the permanent pycnocline. The bottom of the Norwegian Sea and the continental slope to a minimum of 600m depth is bathed in NSBW (Mackensen et al., 1985). The water mass is almost homothermal at ~-1°C, which makes it a useful study area to investigate the effects of $\Delta[CO_3^{2-}]$ on the chemistry of foraminiferal tests independently of temperature.

The temperatures below 2000m in the Norwegian Sea vary between -0.76°C and -0.86°C, with the warmer temperatures at the deeper depths (Figure 15). Based on the linear temperature calibration of Healey et al. (2008) for Mg/Ca ratios in *C. wuellerstorfi* this could account for a 0.05 mmol $mol^{-1}$ change in the Mg/Ca ratios, or ~0.01 mmol $mol^{-1}$ using the equation of Lear et al. (2002). The instrumental error on individual measurements is around <1%, which will account for variation in Mg/Ca ratios of around 0.02 mmol $mol^{-1}$. Typical sample reproducibility is around ±0.04 mmol $mol^{-1}$ (Chapter 2), which suggests that variations in Mg/Ca due to variation in bottom water temperatures may not be discernible in these samples. In addition, bottom water salinity does not vary appreciably, however the increasing water depth means that $\Delta[CO_3^{2-}]$ below 2000m varies between 34.8 and 7.2 μmol $kg_{sw}^{-1}$ (Figure 15). Therefore,

changes in Mg/Ca and other element/Ca ratios seen in the foraminiferal tests will most likely to be due to changes in bottom water $\Delta[CO_3^{2-}]$ (Lear and Rosenthal, 2006).

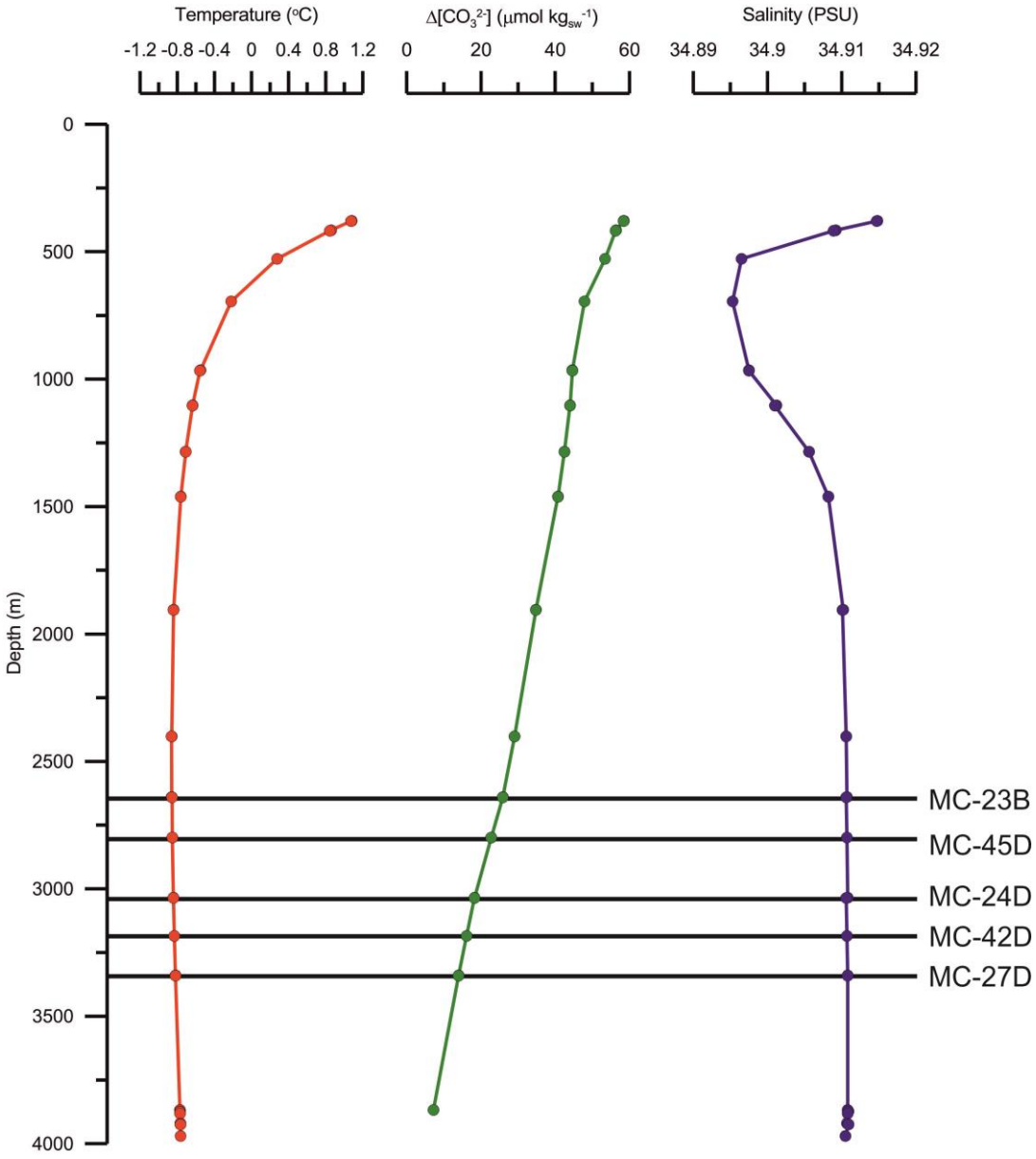


**Figure 15 – Profile of bottom water conditions in the Norwegian Sea. Hydrographic data taken from the R/V Knorr cruises (Johnson et al., 2003). Sites used in this study are shown as horizontal lines and are labelled.**

### *3.1.2 Core samples*

Samples were collected during the KN177-2 (R/V Knorr) cruise in 2004 using a multicore. The samples span a range of water depths from 2641m to 3341m. Water temperature varied at each site from -0.82 to -0.86°C and $\Delta[CO_3^{2-}]$ varies from site to site between 13.96 mmol $kg_{sw}^{-1}$ to 25.88 mmol $kg_{sw}^{-1}$ (Figure 15, Table

2). Salinity at the Norwegian sea sites was at a constant 34.91 PSU, and so variations in salinity will not affect the results shown here (Jordan, 2008). Samples are not true core-tops but instead come from a depth of 2-4 cm. The local sedimentation rate is low (~2cm $kyr^{-1}$) and so modern bottom water conditions are used. Carbonate saturation was corrected for anthropogenic $CO_2$ emissions in the manner of Jordan (2008) using the estimates of anthropogenic $CO_2$ of Sabine et al. (2004). $\Delta[CO_3^{2-}]$ was calculated for each site using the $CO_2$SYS macro for excel (Lewis and Wallace, 1998). Foraminiferal abundances were very high, and so not all foraminifera in a given sample were picked to be run. In general, 40 individuals were run for each species in the 150-250 μm size fraction, 20 individuals in the 250-355 μm size fraction, and 10 individuals in the >355 μm size fraction, with the exception of *P. murrhina*, which was much more massive than other foraminifera and so only 5 individuals were run in each sample.

| Latitude | Longitude | Core | Water depth (m) | Temperature (°C) | Salinity (PSU) | $[CO_3^{2-}]$ | $\Delta[CO_3^{2-}]$ |
|---|---|---|---|---|---|---|---|
| 64 02.717 N | 001 12.37 W | MC-23 | 2641 | -0.86 | 34.91 | 98.8 | 25.88 |
| 64 33.9111 N | 000 43.4230 W | MC-45 | 2799 | -0.85 | 34.91 | 97.6 | 22.76 |
| 64 30.239 N | 002 34.02 W | MC-24 | 3036 | -0.84 | 34.91 | 96.0 | 18.25 |
| 65 06.1803 N | 002 24.9242 W | MC-42 | 3185 | -0.83 | 34.91 | 95.8 | 16.15 |
| 64 50.9691 N | 003 50.0797 W | MC-27 | 3341 | -0.82 | 34.91 | 95.7 | 13.96 |

**Table 2 – Hydrography of the sample sites used in this study.**

| Core | *C. wuellerstorfi* 150-250 μm | | *C. wuellerstorfi* 250-355 μm | | *C. wuellerstorfi* >355 μm | | *O. umbonatus* 150-250 μm | *P. murrhina* >355 μm |
|---|---|---|---|---|---|---|---|---|
| | *Sin* | *Dex* | *Sin* | *Dex* | *Sin* | *Dex* | | |
| MC-23 | 40 | 40 | 20 | 20 | 10 | 10 | 40 | 5 |
| MC-45 | 40 | 40 | 20 | 20 | 10 | 10 | 40 | 5 |
| MC-24 | 40 | 40 | 20 | 20 | 10 | 10 | 40 | 5 |
| MC-42 | 40 | 40 | 20 | 20 | 10 | 10 | 40 | 5 |
| MC-27 | 40 | 40 | 20 | 20 | 10 | 10 | 35 | 4 |

**Table 3 – Number of individual foraminifera picked and run for each size fraction**

### *3.1.3 Sample preparation*

For information on sample preparation, please see methodology chapter 2 and Appendix 1 – Cleaning procedure. A modified version of the Cd-cleaning procedure of Boyle and Keigwin (1985/1986) was used.

## 3.2 Results and Discussion

### *3.2.1 Trace metal composition of different size fractions of benthic foraminifera*

Samples were picked from the 150-250 μm, 250-355 μm, and >355 μm size fractions. Mg/Ca ratios in *C. wuellerstorfi* in the 150-250 μm size fraction (n=10) vary between 0.22 and 1.33 mmol $mol^{-1}$ (mean = 0.51 mmol $mol^{-1}$). Mg/Ca ratios in the 250-355 μm size fraction (n=15) in *C. wuellerstorfi* vary between 0.90 and 1.40 mmol $mol^{-1}$ (mean = 0.99 mmol $mol^{-1}$). In the >355 μm size fraction (n=13) Mg/Ca varies between 0.89 μmol $mol^{-1}$ and 2.33 μmol $mol^{-1}$ (mean = 1.18 μmol $mol^{-1}$). Li/Ca in the 150-250 μm size fraction varies between 14.52 and 18.53 μmol $mol^{-1}$ (mean= 15.65 μmol $mol^{-1}$). In the 250-355 μm size fraction Li/Ca ratios vary between 13.20 μmol $mol^{-1}$ and 14.77 μmol $mol^{-1}$ (mean = 14.07 μmol $mol^{-1}$). In the >355 size fraction Li/Ca varies between 10.53 and 14.63 μmol $mol^{-1}$ (mean = 13.08 μmol $mol^{-1}$). In the 150-250 μm size fraction B/Ca varies between 181.62 and 203.78 μmol $mol^{-1}$ (mean= 192.81 μmol $mol^{-1}$). B/Ca ratios in the 250-355 μm size fraction vary between 175.99 and 212.63 μmol $mol^{-1}$ (mean = 200.69 μmol $mol^{-1}$). In the >355 μm size fraction B/Ca ratios vary between 181.01 and 212.31 μmol $mol^{-1}$ (mean = 198.68 μmol mol) (Figure 16).

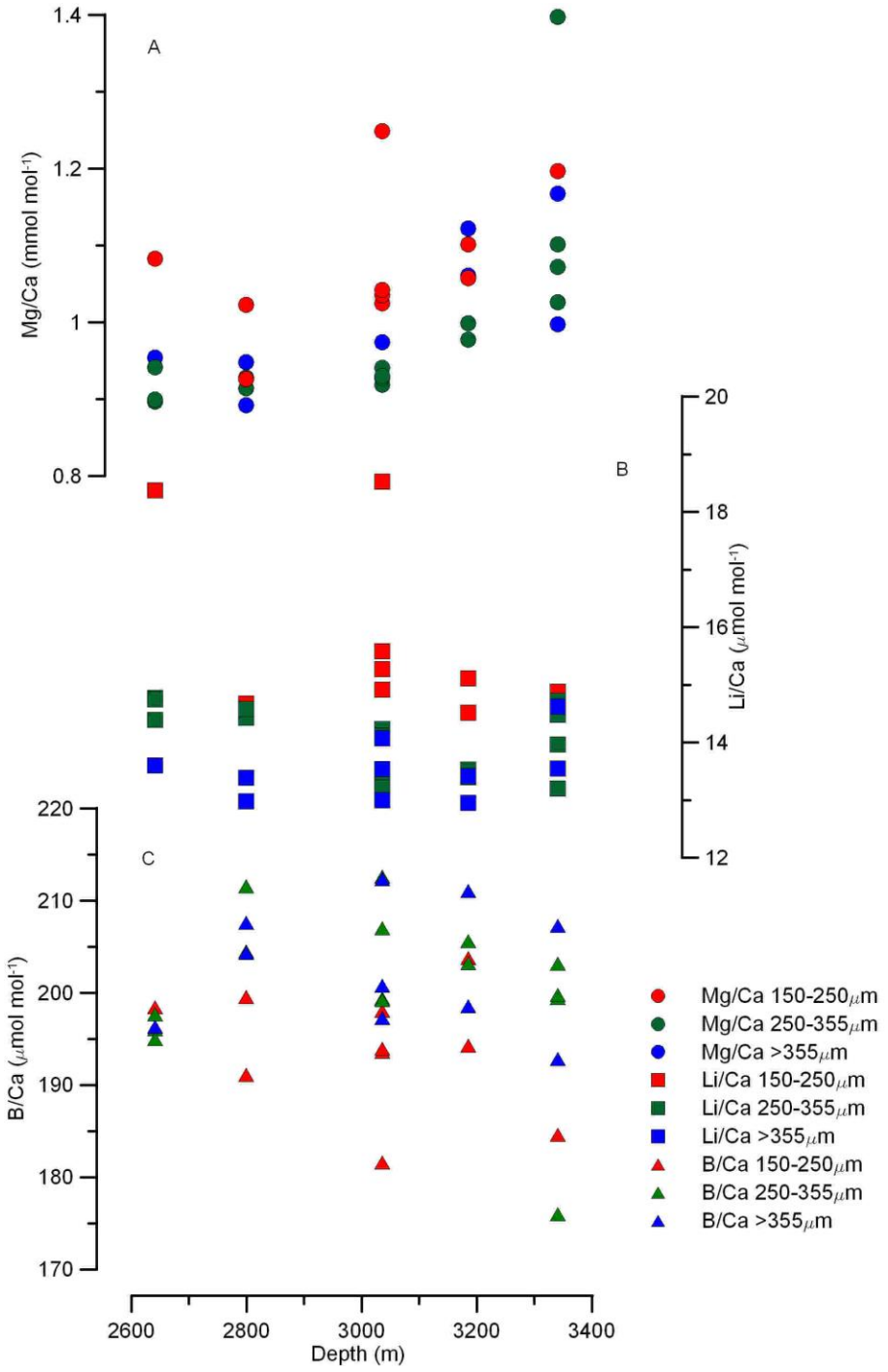


**Figure 16 –Comparison of trace metal ratios between different size fractions of samples of *C. wuellerstorfi* from a water depth transect from the Norwegian Sea. Charts show Mg/Ca (A, circles, top), Li/Ca (B, squares, middle), and B/Ca (C, triangles, bottom) split into three size-factions, 150-250 µm (red), 250-355 µm (green) and >355 µm (blue).**

Mg/Ca, Li/Ca and B/Ca across all size fractions all appear to cluster together with no clear trend in Element/Calcium ratios with increasing size, though there is some hint that the 150-250 µm size fraction has higher Mg/Ca and lower Li- and B/Ca than either the 250-355 or the >355 µm size fractions (Figure 16). This may be an artefact of the small sample size, however an independent

samples Kruskal-Wallis Test suggests that the element/Ca results for different size fractions are significantly ($p<0.05$) different (Mg/Ca $p=0.041$, Li/Ca $p=0.000$, B/Ca $p=0.020$). This suggests that where possible, a single, narrow size fraction should be used for trace metal analysis. In this thesis (chapters 4 and 5) the 250-355µm size fraction was used.

### *3.2.2 Coiling direction*

Due to the abundance of *C. wuellerstorfi* in the samples from the Norwegian Sea, the species was separated into its sinistrally and dextrally coiled forms to determine whether coiling direction may affect the Mg/Ca ratios in benthic foraminifera, as can be seen in planktonic foraminifera (Cleroux et al., 2008). There is evidence that species morphotype can affect trace metal ratios in benthic foraminifera (Rae et al., 2011). Samples were split and run in three size fractions (Section 3.2.1), however the data have been collated and analysed as a single dataset here.

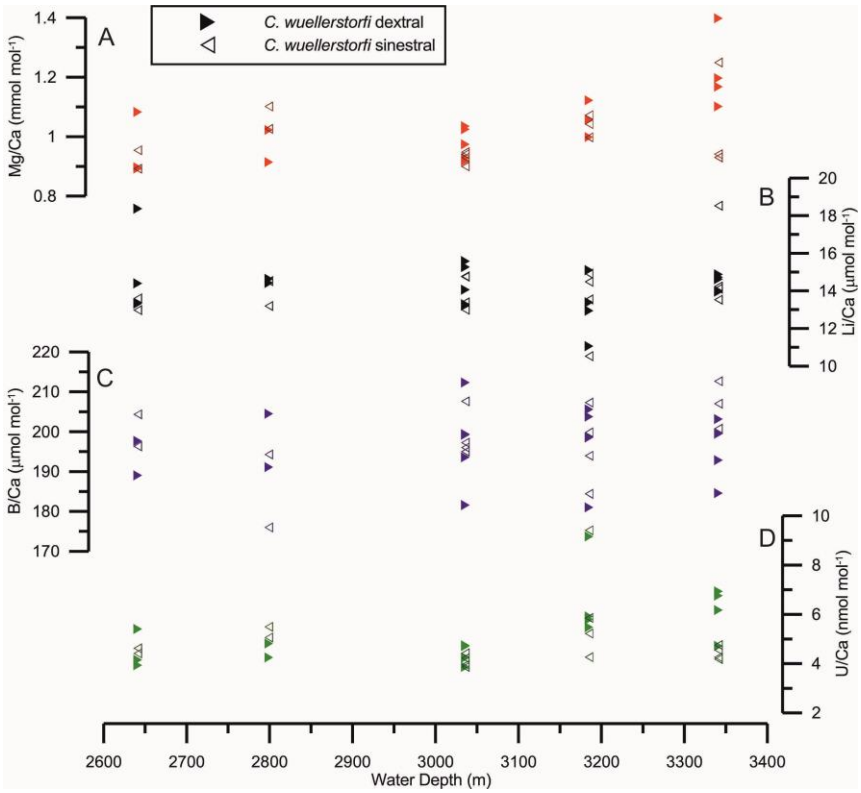


**Figure 17 – Comparison between dextrally coiled (right-pointing closed triangles) and sinistrally coiled (left-pointing open triangles) *C. wuellerstorfi* from the Norwegian Sea. A) Mg/Ca, B) Li/Ca. C) B/Ca. D) U/Ca.**

Mg/Ca ratios in sinistrally and dextrally coiled *C. wuellerstorfi* vary between 0.89 and 2.11 mmol $mol^{-1}$ (mean=1.04, n=20) and between 0.89 and 2.33 mmol $mol^{-1}$ (mean=1.11, n=18), respectively. Li/Ca ratios in sinistrally and dextrally coiled *C. wuellerstorfi* vary between 10.53 and 18.53 mmol $mol^{-1}$ (mean=14.01, n=20) and between 11.06 and 18.37 mmol $mol^{-1}$ (mean=14.29 n=18) respectively. B/Ca ratios in sinistrally and dextrally coiled *C. wuellerstorfi* vary between 175.99 and 212.63 mmol $mol^{-1}$ (mean=199.91, n=20) and 181.01 and 212.31 mmol $mol^{-1}$ (mean=196.33, n=18) respectively (Figure 17). There is no significant difference between the trace metal geochemistry of the two forms (at $p<0.05$), so they therefore have not been separated for analysis in this thesis (chapters 4 and 5).

### *3.2.3 Trace metal composition of benthic foraminifera from a Norwegian Sea water depth transect*

#### *3.2.3.1 C. wuellerstorfi*

The Mg/Ca ratio in *C. wuellerstorfi* in the 150-250 μm size fraction varies between 0.93 mmol $mol^{-1}$ and 1.2 mmol $mol^{-1}$ over the temperature range of -0.86°C to -0.82°C and a $\Delta[CO_3^{2-}]$ range of 13.96 and 25.88 μmol $kg_{sw}^{-1}$. Li/Ca varies between 14.52 and 18.37 μmol $mol^{-1}$. The B/Ca ratio varies between 181.62 and 203.78 μmol $mol^{-1}$. U/Ca varies between 3.87 and 5.91 nmol $mol^{-1}$ (Figure 18, left hand side). The Mg/Ca ratio in *C. wuellerstorfi* in the 250-355 μm size fraction varies between 0.90 and 1.10 mmol $mol^{-1}$ over the same temperature and $\Delta[CO_3^{2-}]$ range as other size fractions. Li/Ca varies between 13.20 and 14.77 μmol $mol^{-1}$ and B/Ca varies between 175.99 and 112.63 μmol $mol^{-1}$. U/Ca varies between 3.93 and 6.94 nmol $mol^{-1}$ (Figure 18, centre graphs). The Mg/Ca ratio in *C. wuellerstorfi* in the >355 μm size fraction varies between 0.89 and 1.17 mmol $mol^{-1}$ over the same temperature and $\Delta[CO_3^{2-}]$ range as the other size fractions. Li/Ca varies between 12.95 and 14.63 μmol $mol^{-1}$ and B/Ca varies between

192.86 and 112.31 μmol mol$^{-1}$. U/Ca varies between 3.86 and 9.16 nmol mol$^{-1}$ (Figure 18, right hand side).

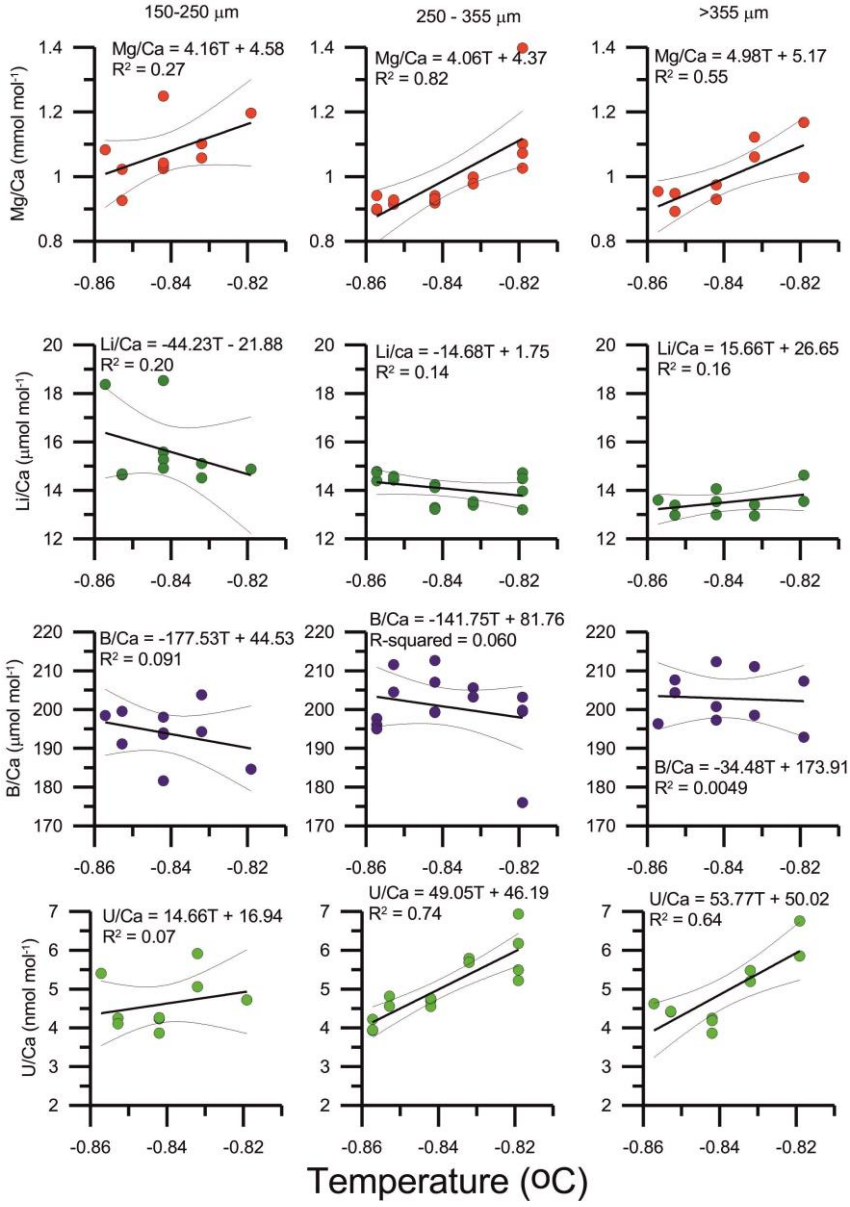


**Figure 18 – Trace element data for *C. wuellerstorfi* from the Norwegian Sea plotted against bottom water temperature. Graphs are organised to show the 150-250 μm size fraction in the left hand column, 250-355 μm in the middle column, and >355 size fraction in the right hand column. Mg/Ca ratios are shown on the first row, Li/Ca ratios in the second row, B/Ca ratios on the third row, and U/Ca on the fourth row. The upper and lower 95% confidence intervals for each line of best fit are shown as thin black lines above and below each line of best fit.**

*C. wuellerstorfi* Mg/Ca shows a positive trend with temperature in all size fractions (Figure 18) and a negative trend with bottom water $\Delta[CO_3^{2-}]$ (Figure 19). Li/Ca ratios show a very poor correlation with both temperature and $\Delta[CO_3^{2-}]$, as does B/Ca. The sensitivity of Mg/Ca to temperature at the 250-355 μm size fraction (the size fraction with the strongest linear fit with temperature)

is ~4 mmol $Mol^{-1}$ $^{o}C^{-1}$ change in temperature. This is a far higher sensitivity to changes in temperature than other studies (e.g., Healey et al., 2008, ~0.3 mmol $mol^{-1}$ $^{o}C^{-1}$; Lear et al., 2002, 0.109 mmol $mol^{-1}$ $^{o}C^{-1}$; Martin et al., 2002, ~0.4 mmol $mol^{-1}$ $^{o}C^{-1}$). Equations for the linear and exponential fits of the data with temperature can be found in Table 4. Equations with $\Delta[CO_3^{2-}]$ can be found in Table 5. Errors on the coefficients of the equations given in brackets represent 2σ. Of all the size fractions of *C. wuellerstorfi* analysed, the 250-355 μm fraction shows the lowest scatter and highest $R^2$ values.

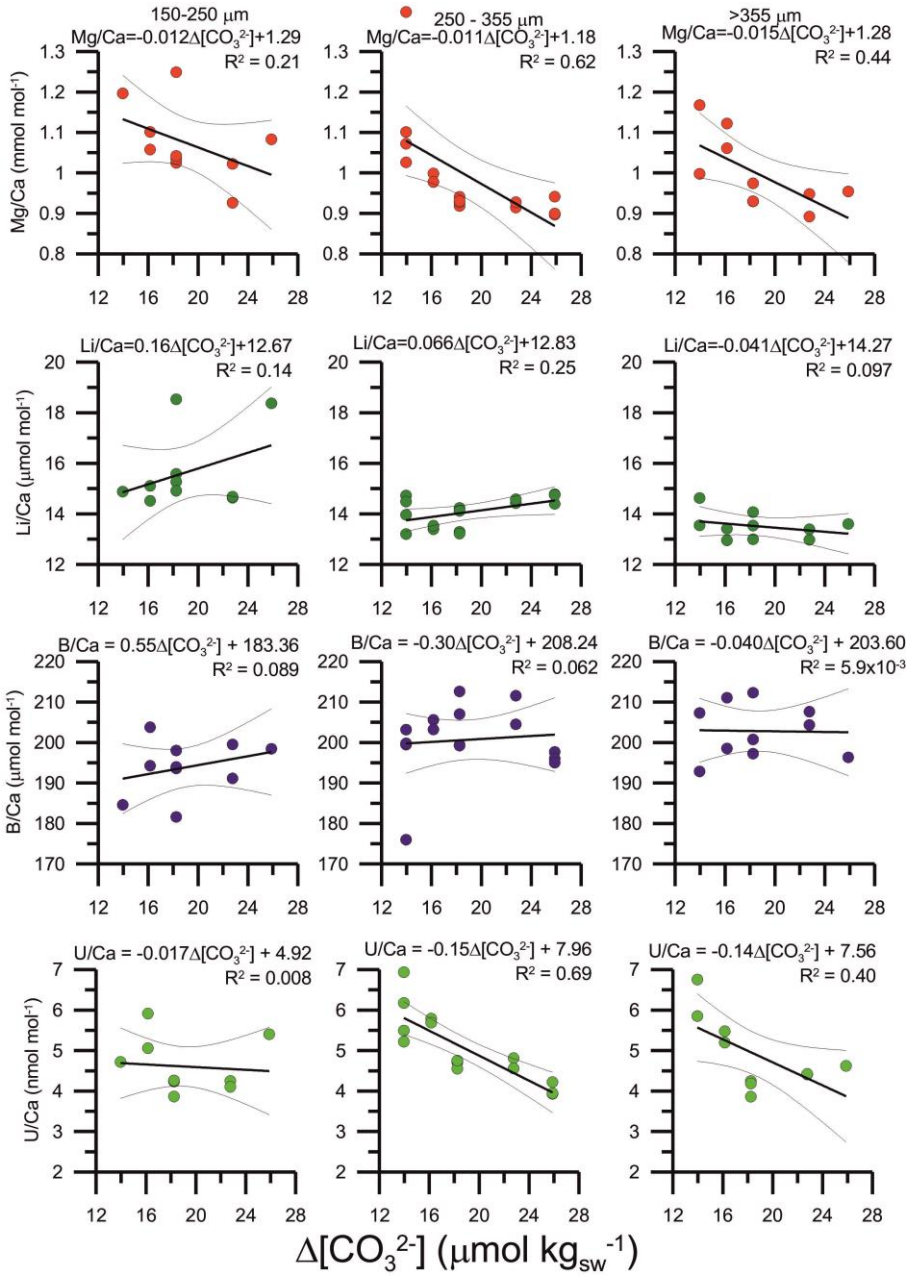


**Figure 19 - Trace element data for *C. wuellerstorfi* from the Norwegian Sea plotted against bottom $\Delta[CO_3^{2-}]$. Graphs are organised in the same manner as Figure 18.**

| Mg/Ca versus temperature calibration equations | | | | | | | | |
|---|---|---|---|---|---|---|---|---|
| Species | Size Fraction | | Linear Equation | | | Exponential Equation | | |
| | | n | m | c | $R^2$ | B | A | $R^2$ |
| *C. wuellerstorfi* | 150-250 µm | 10 | 4.16 (± 4.84) | 4.58 (± 4.08) | 0.27 | 27.98 (±102.01) | 3.87 (± 4.42) | 0.28 |
| | 250-355 µm | 15 | 4.06 (± 1.10) | 4.37 (± 0.93) | 0.82 | 30.52 (± 27.89) | 4.12 (± 1.09) | 0.83 |
| | >355 µm | 13 | 4.98 (± 3.20) | 5.17 (± 2.68) | 0.55 | 59.20 (± 153.65) | 4.87 (± 3.09) | 0.55 |
| *O. umbonatus* | 150-250 µm | 5 | 7.43 (± 31.68) | 7.21 (± 26.40) | 0.07 | 5026 (± $151x10^3$) | 10.25 (± 35.93) | 0.10 |
| *P. murrhina* | >355 µm | 8 | -28.48 (± 44.39) | -16.97 (±18.73) | 0.22 | 0.236 (± 1.28) | -4.02 (±6.48) | 0.20 |
| Li/Ca versus temperature calibration equations | | | | | | | | |
| *C. wuellerstorfi* | 150-250 µm | 10 | -44.23 (± 65.87) | -21.88 (± 55.42) | 0.20 | 1.64 (± 5.55) | -2.65 (± 4.02) | 0.20 |
| | 250-355 µm | 15 | -14.68 (± 20.57) | 1.75 (± 17.26) | 0.14 | 5.84 (± 7.23) | -1.05 (± 1.48) | 0.13 |
| | >355 µm | 13 | 15.66 (± 25.10) | 26.65 (± 21.06) | 0.16 | 34.72 (± 53.46) | 1.126 (± 1.83) | 0.16 |
| *O. umbonatus* | 150-250 µm | 5 | 334.6 (± 332.8) | 298.7 (± 277.4) | 0.57 | $5.47x10^6$ (±$72.4x10^6$) | 15.05 (± 15.87) | 0.55 |
| *P. murrhina* | >355 µm | 4 | 7.85 (± 16.284) | 7.46 (± 31.23) | 0.10 | 53.13 (± 926.91) | 4.18 (± 20.65) | 0.076 |
| B/Ca versus temperature calibration equations | | | | | | | | |
| *C. wuellerstorfi* | 150-250 µm | 10 | -177.5 (± 397.8) | 44.53 (± 334.7) | 0.091 | 88.02 (± 153.2) | -.094 (2.07) | 0.093 |
| | 250-355 µm | 15 | -141.8 (± 310.6) | 81.76 (± 260.7) | 0.060 | 107.12 (± 143.5) | -0.75 (± 1.60) | 0.063 |
| | >355 µm | 13 | -34.48 (± 348.9) | 173.9 (± 292.8) | 0.005 | 174.07 (±251.2) | -0.182 (± 1.72) | 0.006 |
| *P. murrhina* | >355 µm | 8 | 48.12 (± 555.2) | 20.65 (± 657.9) | 0.001 | 243.33 (± 4340) | 2.51 (± 21.14) | 0.009 |
| U/Ca versus temperature calibration equations | | | | | | | | |
| *C. wuellerstorfi* | 150-250 µm | 10 | 14.66 (± 39.08) | 16.94 (± 32.90) | 0.07 | 64.95 (± 440.98) | 3.16 (± 8.09) | 0.07 |
| | 250-355 µm | 15 | 49.05 (±15.97) | 46.19 (± 13.40) | 0.74 | $15.7x10^3$ (± $38.2x10^3$) | 9.61 (± 2.91) | 0.77 |
| | >355 µm | 13 | 53.77 (± 28.35) | 50.02 (± 23.79) | 0.64 | $25.5x10^3$ (± $122x10^3$) | 10.22 (± 5.69) | 0.57 |
| *O. umbonatus* | 150-250 µm | 5 | 250.6 (± 116.3) | 215.5 (± 96.89) | 0.86 | $56.82x10^{12}$ (± $490.1x10^{12}$) | 35.80 (± 10.35) | 0.80 |
| *P. murrhina* | >355 µm | 5 | -69.45 (±41.54) | -100.9 (± 49.54) | 0.85 | 0.049 (± 0.14) | -6.84 (± 3.35) | 0.85 |

**Table 4 – Table of calibrations of element/Ca ratios versus temperature from this study. The values in the linear equation section are given in the form Mg/Ca = Temperature x m + c. Values in the exponential equation section are given in the form Mg/Ca = B exp (A x Temperature). $R^2$ is the correlation coefficient. Uncertainties given are 2x the standard error.**

| Mg/Ca versus $\Delta[CO_3^{2-}]$ calibration equations | | | | | | | | |
|---|---|---|---|---|---|---|---|---|
| Species | Size Fraction | | Linear Equation | | | Exponential Equation | | |
| | | n | m | c | $R^2$ | B | A | $R^2$ |
| *C. wuellerstorfi* | 150-250 µm | 10 | -0.012 (± 0.016) | 1.29 (±0.31) | 0.37 | 1.31 (± 0.37) | -0.011 (± 0.014) | 0.22 |
| | 250-355 µm | 15 | -0.011 (± 0.0060) | 1.18 (± 0.10) | 0.62 | 1.20 (± 0.12) | -0.011 (± 0.006) | 0.63 |
| | >355 µm | 13 | -0.015 (± 0.012) | 1.28 (± 0.23) | 0.44 | 1.31 (± 0.29) | -0.015 (± 0.012) | 0.45 |
| *O. umbonatus* | 150-250 µm | 5 | -0.046 (± 0.16) | 1.779 (± 2.742) | 0.09 | 2.70 (± 8.40) | -0.061 (0.19) | 0.13 |
| *P. murrhina* | >355 µm | 8 | 0.11 (± 0.13) | 4.902 (± 2.75) | 0.30 | 5.15 (± 2.06) | 0.015 (± 0.02) | 0.29 |
| Li/Ca versus $\Delta[CO_3^{2-}]$ calibration equations | | | | | | | | |
| *C. wuellerstorfi* | 150-250 µm | 10 | 0.18 (± 0.19) | 11.90 (± 3.71) | 0.34 | 12.46 (±2.83) | 0.011 (± 0.012) | 0.33 |
| | 250-355 µm | 15 | 0.066 (± 0.062) | 12.83 (± 1.21) | 0.25 | 12.87 (± 1.12) | 0.005 (± 0.004) | 0.25 |
| | >355 µm | 13 | -0.041 (± 0.88) | 14.27 (± 1.64) | 0.10 | 14.26 (± 1.74) | -0.003 (± 0.006) | 0.09 |
| *O. umbonatus* | 150-250 µm | 5 | -1.67 (± 1.88) | 47.49 (± 31.23) | 0.51 | 67.63 (± 101.3) | -0.075 (±0.09) | 0.49 |
| *P. murrhina* | >355 µm | 4 | 1.81 (± 1.97) | -0.012 (± 0.098) | 0.031 | 1.75 (± 2.26) | -0.0059 (± 0.064) | 0.016 |
| B/Ca versus $\Delta[CO_3^{2-}]$ calibration equations | | | | | | | | |
| *C. wuellerstorfi* | 150-250 µm | 10 | 0.55 (± 1.25) | 183.36 (± 24.20) | 0.09 | 183.31 (± 23.16) | 0.003 (± 0.006) | 0.09 |
| | 250-355 µm | 15 | 0.183 (± 1.04) | 197.21 (± 20.25) | 0.01 | 196.65 (± 20.48) | 0.001 (± 0.006) | 0.011 |
| | >355 µm | 13 | -0.04 (± 1.18) | 203.60 (± 22.44) | $6x10^{-4}$ | 203.37 (± 22.50) | $1.6x10^{-4}$ (±0.006) | $4x10^{-4}$ |
| *P. murrhina* | >355 µm | 8 | 33.53 (± 43.05) | -0.14 (± 2.11) | 0.003 | 35.58 (± 49.16) | -0.010 (± 0.068) | 0.014 |
| U/Ca versus $\Delta[CO_3^{2-}]$ calibration equations | | | | | | | | |
| *C. wuellerstorfi* | 150-250 µm | 10 | -0.017 (±0.13) | 4.92 (± 2.60) | 0.08 | 4.88 (± 2.48) | -0.004 (± 0.026) | 0.09 |
| | 250-355 µm | 15 | -0.154 (± 0.058) | 7.96 (± 1.11) | 0.69 | 8.91 (± 1.74) | -0.031 (±0.010) | 0.74 |
| | >355 µm | 13 | -0.142 (± 0.12) | 7.56 (± 2.37) | 0.40 | 7.96 (± 3.72) | -0.027 (± 0.024) | 0.37 |
| *O. umbonatus* | 150-250 µm | 5 | -1.30 (± 0.67) | 28.17 (± 11.22) | 0.83 | 140.30 (± 261.9) | -0.188 (± 0.112) | 0.79 |
| *P. murrhina* | >355 µm | 5 | 10.02 (± 4.42) | 0.28 (± 0.23) | 0.65 | 10.69 (± 3.27) | 0.019 (± 0.019) | 0.64 |

**Table 5 - Table of calibrations of element/Ca ratios versus $\Delta[CO_3^{2-}]$ from this study. The values in the linear equation section are given in the form Mg/Ca = $\Delta[CO_3^{2-}]$ x m + c. Values in the exponential equation section are given in the form Mg/Ca = B exp (A x $\Delta[CO_3^{2-}]$). $R^2$ is the correlation coefficient. Uncertainties given are 2x the standard error.**

### *3.2.4 Mg/Ca and Δ[$CO_3^{2-}$] in C. wuellerstorfi*

Elderfield et al. (2006) performed a study on Mg/Ca ratios in *C. wuellerstorfi* and put forward an initial calibration for Mg/Ca ratios against Δ[$CO_3^{2-}$]. This study included data from the Norwegian Sea which is directly comparable to the data presented here. The temperatures of the sites studied by Elderfield et al. (2006) vary between -1.15 and -0.77°C and the Δ[$CO_3^{2-}$] of the sites vary between 27.66 and 61.15 μmol $kg_{sw}^{-1}$. The range of Mg/Ca values obtained by Elderfield et al. (2006) (1.0 to 1.5 mmol $mol^{-1}$ for the >250 μm size fraction) is similar to that observed here (0.9 to 1.4 mmol $mol^{-1}$ for the 250-355 μm size fraction). Combining the Norwegian Sea data set from Jordan (2008) Elderfield et al. (2006) and the data from this study shows a weak correlation between Mg/Ca and Δ[$CO_3^{2-}$] (16), Figure 20).

$$\boldsymbol{Mg/Ca = 0.0074 \pm 0.0014 \times \Delta\left[CO_3^{2-}\right] + 0.88 \pm 0.041 \ (R^2 = 0.39)} \quad \textbf{(16)}$$

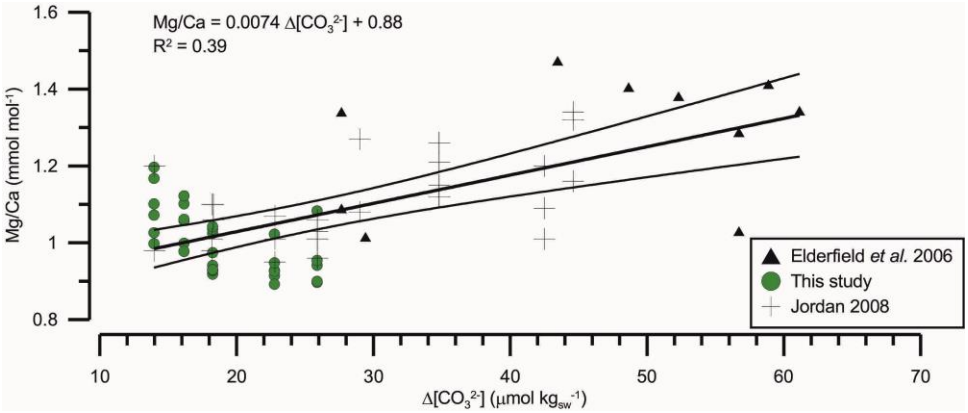


**Figure 20 – Mg/Ca versus Δ[$CO_3^{2-}$] in *C. wuellerstorfi* from the Norwegian sea only. Data from this study is in green circles, data from Elderfield et al. (2006) is in black triangles, data from Jordan (2008) is shown as black crosses. The Δ[$CO_3^{2-}$] of the sites used in this study are lower than any of the sites used in Elderfield et al. (2006), which allows us to make an extended Norwegian Sea only calibration.**

The reproducibility of measurements of Mg/Ca test (Figure 8) gave a standard error of the mean of 0.010 mmol $mol^{-1}$. Taking this equation in the general from of Mg/Ca = m Δ[$CO_3^{2-}$] + c, and the errors of each term as $\sigma_{term}$, the total error of Δ[$CO_3^{2-}$] ($\sigma_{\Delta[CO32-]}$) is given by equation (17:

$$\sqrt{\left(\frac{\sqrt{\left(\sigma_{Mg/Ca}{}^2\right)+\left(\sigma_c{}^2\right)}}{Mg/Ca-c}\right)^2+\left(\frac{\sigma_m}{m}\right)^2}=\frac{\sigma_{\Delta[CO_3^{2-}]}}{\Delta[CO_3^{2-}]} \quad \textbf{(17)}$$

Where $\sigma_c$ = 0.041; $\sigma_m$ = 0.0014; and $\sigma_{Mg/Ca}$ = 0.010, and m = 0.0074; and c = 0.88. For values of $\Delta[CO_3^{2-}]$ above 90 μmol $kg_{sw}^{-1}$, the % error obtained from equation (17 on a given estimate of $\Delta[CO_3^{2-}]$ from equation (16 is around 19%. Estimates of $\Delta[CO_3^{2-}]$ below 90 μmol $kg_{sw}^{-1}$ have greater % uncertainties. This translates to a temperature uncertainty from Mg/Ca estimates of ~12% of the calculated value (in this study, temperature ranges calculated for benthic foraminifera are between ~4°C and 8°C, so uncertainties from this alone are between ~0.5-0.9°C).

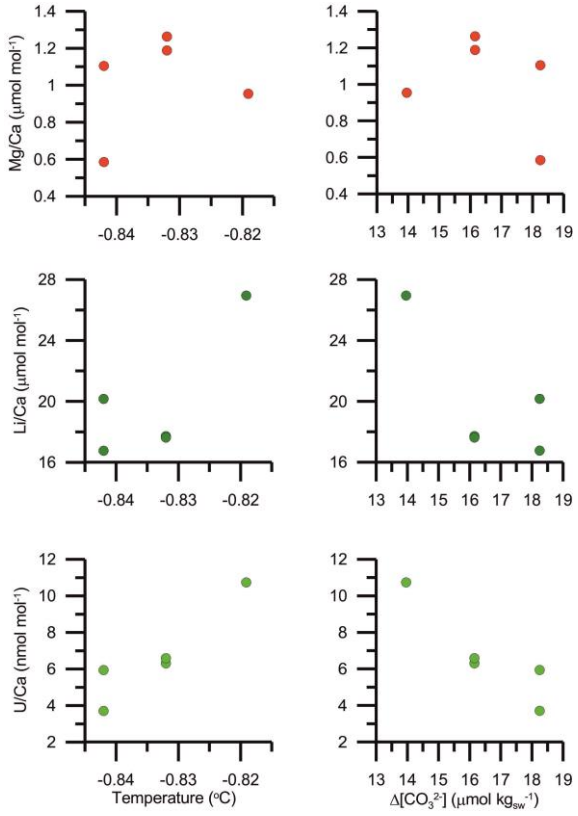


**Figure 21 – *O. umbonatus* Mg/Ca (top two graphs), Li/Ca (middle two graphs), and U/Ca (bottom two graphs) ratios versus temperature (left hand side) and $\Delta[CO_3^{2-}]$ (right hand side). Low boron levels in *O. umbonatus* made analyses of the boron concentration indistinguishable from the blank, and so B/Ca ratios have been excluded.**

The slope of the linear equation agrees with those given in other sources (Elderfield et al., 2006; Healey et al., 2008) and has the advantage that it is from core-top Mg/Ca data that has not been temperature-corrected. In addition, the apparent negative trend of Mg/Ca with $\Delta[CO_3^{2-}]$ obtained from the dataset in this study appears to reverse when combined with the Norwegian Sea data from Elderfield et al. (2006) somewhere between 19 and 26 μmol $kg_{sw}^{-1}$, which agrees with the ~25 μmol $kg_{sw}^{-1}$ threshold hypothesised by Elderfield et al. (2006). It is difficult to narrow down the exact point at which the trend reverses further due to the broad spread of the data. None the less, if a broader range of $\Delta[CO_3^{2-}]$ were covered either side of 25 μmol $mol^{-1}$, it may be possible to produce two linear trends and see at what $\Delta[CO_3^{2-}]$ they intersect.

### *3.2.5 O. umbonatus*

Mg/Ca ratios in *O. umbonatus* in this dataset vary between 0.58 and 1.26 mmol $mol^{-1}$ over the temperature range -0.84 to -0.82°C and the $\Delta[CO_3^{2-}]$ range 13.96 to 18.25 μmol $kg_{sw}^{-1}$ (Figure 21). Li/Ca varies over the range 16.76 – 26.95 μmol $mol^{-1}$ over the same temperature and $\Delta[CO_3^{2-}]$ range. B/Ca ratios are not shown due to the low concentration of boron in *O. umbonatus'* tests making [B] almost indistinguishable from the blank. However, U/Ca ratios vary between 3.71 and 10.74 μmol $mol^{-1}$ over the same temperature range.

Mg/Ca in infaunal *O. umbonatus* from the Norwegian Sea is slightly higher than expected for the temperature if the linear calibration of Healey et al. (2008) is extrapolated to cold temperatures, but similar to the expected temperature using the exponential calibrations of Healey et al. (2008) and Lear et al., (2002) (Figure 22a). The calibration of Mg/Ca with temperature for *Cibicidoides spp.* by Lear et al. (2002) predicts an Mg/Ca value of ~0.9 mmol $mol^{-1}$ at ~-1°C. This is similar to the *O. umbonatus* data seen here, and may suggest that *O. umbonatus*

exists above the $\Delta[CO_3^{2-}]$ threshold at these sites, despite the <25 μmol $kg_{sw}^{-1}$ $\Delta[CO_3^{2-}]$ recorded. Whether this is due to its shallow infaunal habit or due to the threshold for *O. umbonatus* being less than the 25 μmol $mol^{-1}$ proposed by Elderfield et al. (2006) remains to be seen. Plotting *O. umbonatus* Mg/Ca from the combined dataset against $\Delta[CO_3^{2-}]$ suggests a strong relationship between the two (Figure 22b), however as $\Delta[CO_3^{2-}]$ and temperature co-vary, it is difficult to know whether the Mg/Ca is varying due to changes in temperature or $\Delta[CO_3^{2-}]$.

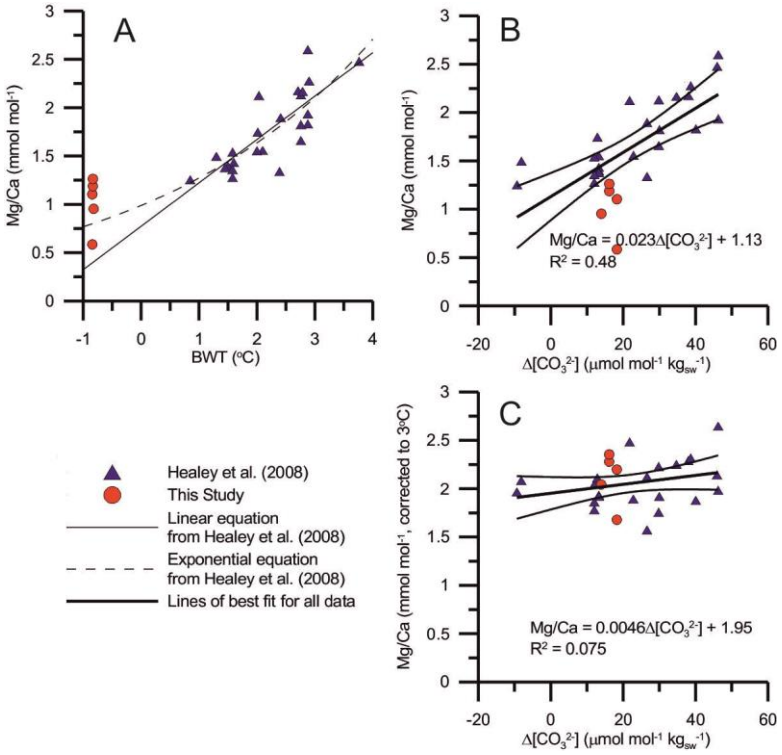


**Figure 22 – Mg/Ca in *O. umbonatus* from the Norwegian Sea (red circles, this study) and from a global coretop study (Healey et al., 2008, blue triangles). A) Mg/Ca versus bottom water temperature (BWT). Shown for comparison are the lines of best fit for the linear (solid line) and exponential (dashed line) temperature calibrations for the Healey et al. (2008) data. B) Mg/Ca versus bottom water $\Delta[CO_3^{2-}]$. C) Mg/Ca corrected to 3°C using the exponential temperature calibration of Healey et al. (2008) versus bottom water $\Delta[CO_3^{2-}]$. $\Delta[CO_3^{2-}]$ data was obtained from the closest GEOSECS station.**

One thing that is clear if the Norwegian Sea data is added to a more global dataset (Elderfield et al., 2006; Healey et al., 2008) is that the data from *C. wuellerstorfi* plots well outside of the expected trend of Mg/Ca with temperature (Figure 23a), whereas *O. umbonatus* is far closer to being in line with data from other sites (Figure 23b). The sensitivity of *O. umbonatus* to changes in $\Delta[CO_3^{2-}]$

when corrected to 3°C for temperature is also far lower than that of *C. wuellerstorfi* (Figure 24). This provides more evidence that, even if Mg/Ca in *O. umbonatus* is not completely immune to changes in $\Delta[CO_3^{2-}]$, it is at least more resistant to them than *C. wuellerstorfi*. In addition, the Norwegian Sea *O. umbonatus* appear to plot outside of the range of the majority of the other samples' from Healey et al. (2008) (Figure 11B). Correcting the Mg/Ca values to 3°C (Figure 22c) using the equation of Elderfield et al. (2006) results in a very poor trend of Mg/Ca with $\Delta[CO_3^{2-}]$ (Figure 11C), which is consistent with the work of Brown et al. (2011)which suggests a reduced impact of bottom water saturation state on the trace metal geochemistry on this species.

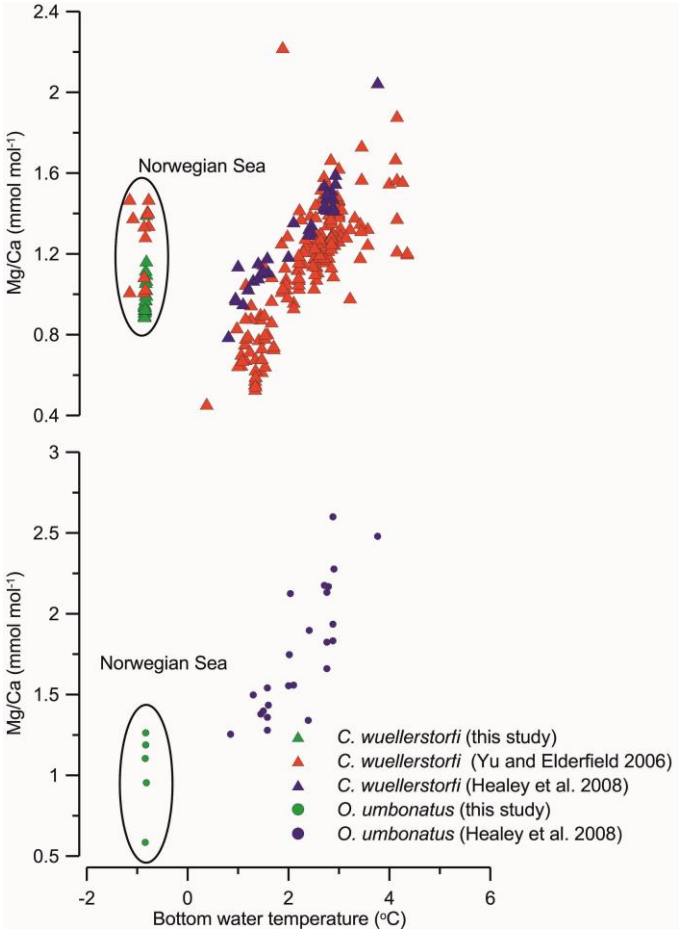


**Figure 23 –** ***C. wuellerstorfi*** **Mg/Ca (A, triangles) and** ***O. umbonatus*** **Mg/Ca (B, circles) versus temperature. C.** ***wuellerstorfi*** **from the Norwegian Sea (circled) do not plot in line with data from other basins, whereas it appears that** ***O. umbonatus*** **from the same region does.**

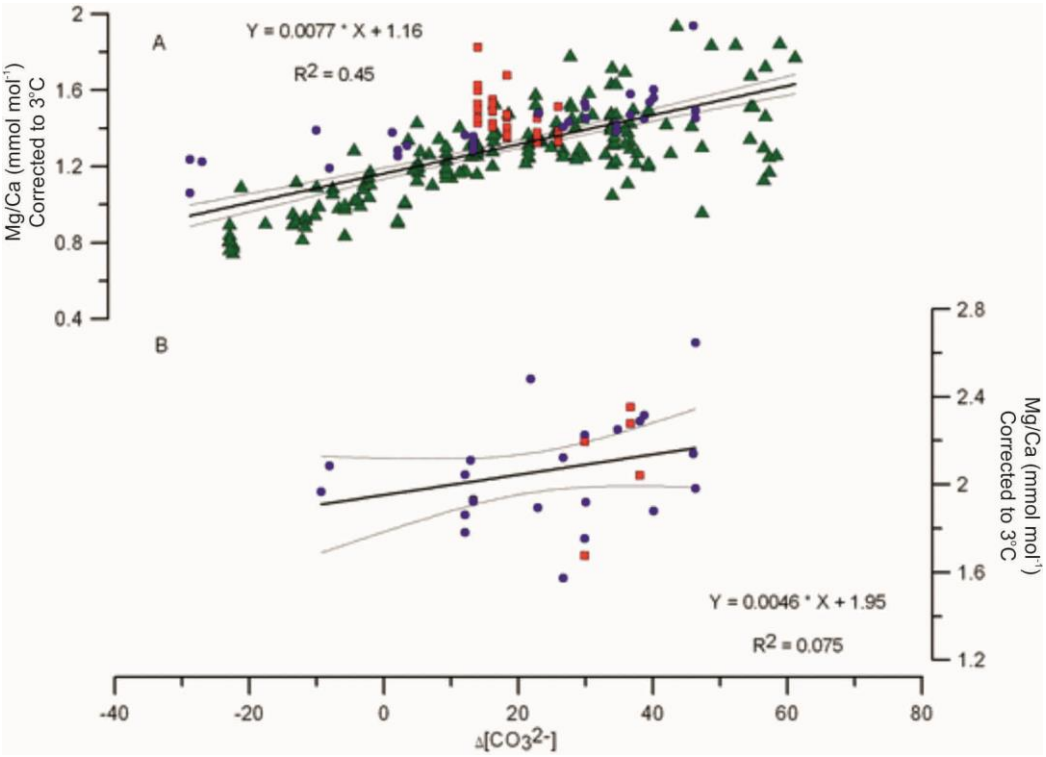


**Figure 24 – The effect of $\Delta[CO_3^{2-}]$ on Mg/Ca for C. *wuellerstorfi* (A) and *O. umbonatus* (B). The data in this plot have been normalised to 3°C using the temperature calibration of Elderfield et al. (2006, C. wuellerstorfi) and Healey et al. (2008, O. umbonatus) to remove the effect of temperature on Mg/Ca. Data are from Yu and Elderfield (2008, green triangles), Healey et al. (2008, blue circles) and from this study (red squares). Lines above and below the lines of best fit show the 95% confidence interval for those lines.**

The studies of Tisserand et al. (2013), and Dawber and Tripati (2012a) include analyses of *O. umbonatus* with $\Delta[CO_3^{2-}]$, however they use the cleaning protocol of Barker et al. (2003), which does not include a reducing step, and so their data has not been used here for direct comparisons. Rathmann and Kuhnert (2008) have also performed a similar study, but used laser ablation to ionise spots of their *O. umbonatus'* tests, rather than using a whole-test approach as in this and other studies. Nevertheless, Dawber and Tripati (2012a) find a sensitivity of 0.0122 (± 0.0016) mmol $mol^{-1}$ $\mu mol^{-1}$ $kg_{sw}^{-1}$ for *O. umbonatus* Mg/Ca with $\Delta[CO_3^{2-}]$, using a larger dataset corrected for differences in cleaning methods to bring all data in line with their oxidative cleaning, compared with this dataset's 0.0229 (± 0.0046) mmol $mol^{-1}$ $\mu mol^{-1}$ $kg_{sw}^{-1}$. The sensitivities are only slightly dissimilar at the 1σ level, and are within error of each other at the 2σ level, despite the differences in cleaning protocols used. They have not

corrected their data for changes in temperature, however the range in temperatures covered by their study is only 2.5°C (compared to this study's 0.04°C) and the range in $\Delta[CO_3^{2-}]$ values covered by their study is 67 μmol $kg_{sw}^{-1}$ (compared to this study's 8 μmol $kg_{sw}^{-1}$ for samples containing *O. umbonatus*), so they argue that applying a correction to account for temperature variability is not necessary.

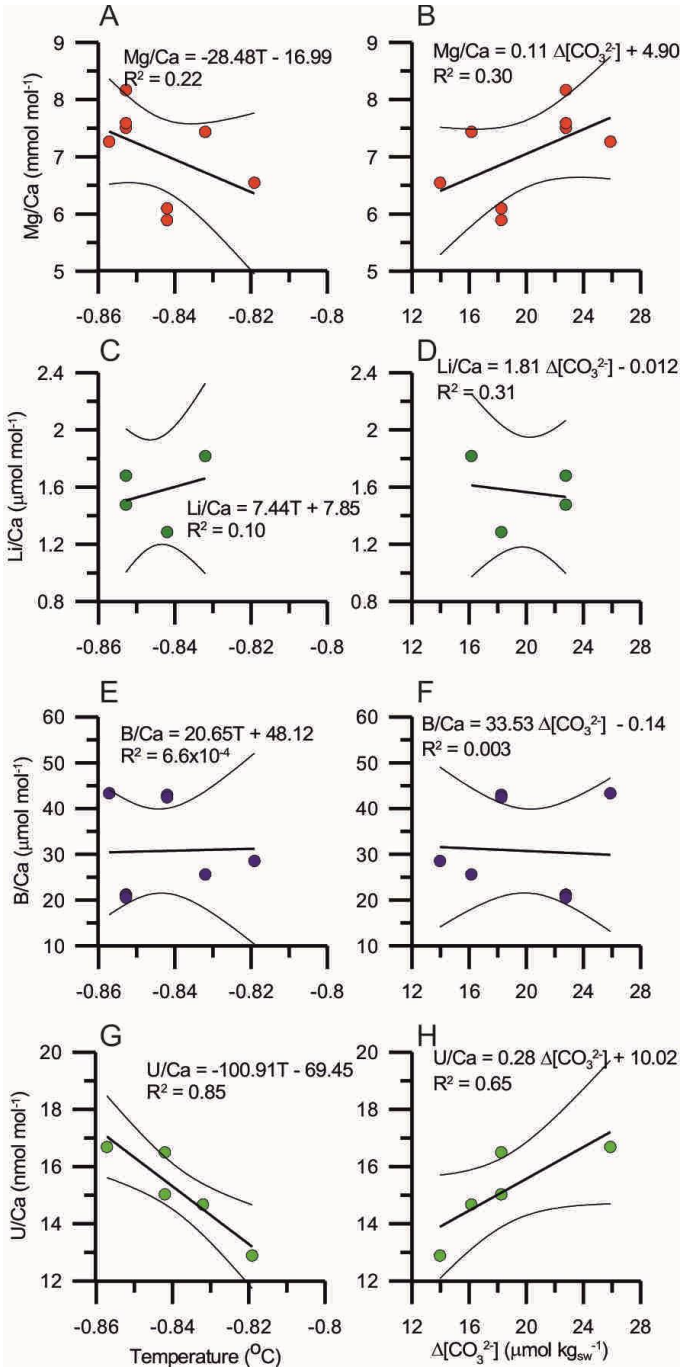


**Figure 25 – Trace metal ratios in *P. murrhina* versus temperature (left hand graphs) and $\Delta[CO_3^{2-}]$ (right hand graphs). Mg/Ca (A & B), Li/Ca (C & D), B/Ca (E & F) and U/Ca (G & H).**

*O. umbonatus* lives in the top 4cm of sediment (Rathburn and Corliss, 1994) and as such is sheltered from any large swings in $\Delta[CO_3^{2-}]$. It essentially lives in its own equilibrated bubble of pore waters (Elderfield et al., 2006; Rathmann and Kuhnert, 2008). This will make *O. umbonatus* useful for confirming that major trends in Mg/Ca in palaeoclimate records are caused by changes in temperature and not by changes in $\Delta[CO_3^{2-}]$. However, due to *O. umbonatus* living anywhere within the top 4cm of sediment, it would be unwise to use *O. umbonatus* to confirm the timing of trends in records sampled at resolutions higher than 4cm due to the potential for overlap between *O. umbonatus* specimens of different ages.

### *3.2.6 Pyrgo murrhina*

*Pyrgo murrhina* is a porcelaneous foraminifer, and as such has a test made from high Mg-calcite, as opposed to the hyaline tests of *C. wuellerstorfi* and *O. umbonatus*. Mg/Ca ratios in *P. murrhina* in this dataset vary between 5.89 and 8.17 mmol $mol^{-1}$ over a temperature range of ~0.04°C (Figure 25a), and a range of $\Delta[CO_3^{2-}]$ of ~12 μmol $kg_{sw}^{-1}$ (Figure 25b). Li/Ca ratios vary between 1.11 and 1.82 μmol $mol^{-1}$ over the same range of temperatures (Figure 25c) and $\Delta[CO_3^{2-}]$ (Figure 25d). B/Ca varies between 20.51 and 43.32 μmol $mol^{-1}$ (Figure 25e & f) and U/Ca between 11.23 and 16.69 nmol $mol^{-1}$ (Figure 25g & h).

The exponential and linear relationships for the trace element/Ca ratios versus temperature can be found in Table 4. The exponential and linear relationships for the same ratios versus $\Delta[CO_3^{2-}]$ can be found in Table 5. Given the very low range of temperatures observed, any apparent correlation with temperature is likely to instead reflect a correlation with another factor, such as $\Delta[CO_3^{2-}]$. For example, the correlation of U/Ca with temperature is over such a narrow range as to be meaningless, despite the good $R^2$ value (0.85) for both the linear and exponential equations (Table 4 & Table 5).

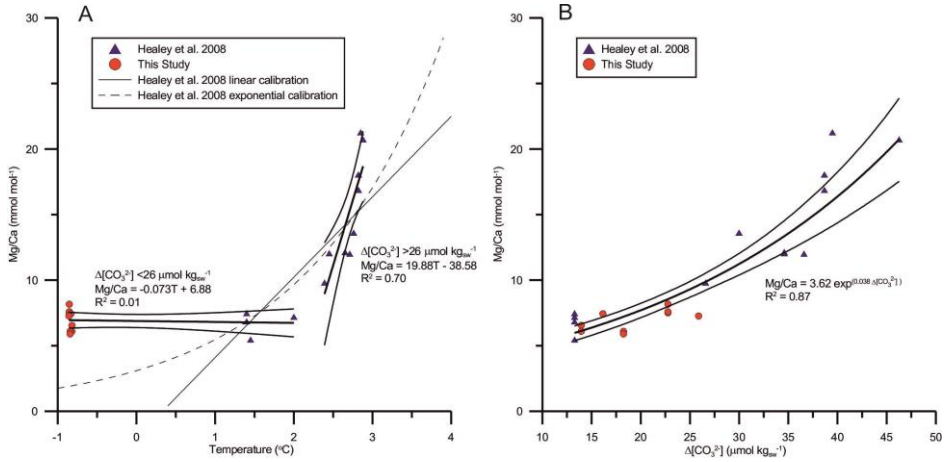


**Figure 26 – Mg/Ca versus temperature and $\Delta[CO_3^{2-}]$ in *P. murrhina*. A) This study's data (red circles) plotted with the data of Healey et al. (2008, blue triangles). Lines of best fit have been plotted through data from sites with <26 μmol $kg_{sw}^{-1}$ $\Delta[CO_3^{2-}]$ and through data from sites with >26 μmol $kg_{sw}^{-1}$ $\Delta[CO_3^{2-}]$. It appears there is an enormous difference in the way the different groups respond to changes in temperature. Also shown are the lines of best fit from the exponential (thin dashed line) and linear (thin solid line) calibrations of Healey et al. (2008). B) The same data plotted against $\Delta[CO_3^{2-}]$. For the sites used by Healey et al. (2008)**

Combining this study's data set with the data of Healey et al. (2008) reveals that below ~2°C Mg/Ca in the tests of *P. murrhina* ceases responding to changes in temperature; the Mg/Ca values of samples from the Norwegian Sea at ~-1°C are very similar to the Vema Channel samples analysed by Healey et al. (2008) between 1 and 2°C (Figure 26A). It also appears that above ~2°C, the sensitivity of *P. murrhina*'s test's Mg/Ca ratios to temperature dramatically increases. This threshold in temperature corresponds with a threshold in $\Delta[CO_3^{2-}]$ of ~26 μmol $kg_{sw}^{-1}$, which is coincidentally close to the threshold of 25 μmol $kg_{sw}^{-1}$ in *C. wuellerstorfi*'s Mg/Ca ratios proposed by Yu and Elderfield (2008). The result is that in waters with $\Delta[CO_3^{2-}]$ of <26 μmol $kg_{sw}^{-1}$ there is no discernible change in Mg/Ca ratios with changes in temperature, and in waters with $\Delta[CO_3^{2-}]$ of >26 μmol $kg_{sw}^{-1}$ in which a 1°C change in temperature can effect almost a 20 mmol $mol^{-1}$ change in Mg/Ca. An alternate explanation is that there is an exceptionally strong $\Delta[CO_3^{2-}]$ effect at low (<26 μmol $kg_{sw}^{-1}$) $\Delta[CO_3^{2-}]$ values, though this seems less likely. In addition, the data from the Norwegian Sea fall well outside of the values predicted by extrapolating out the linear and exponential equations based on material from the Vema Chanel (Figure 26A).

Plotting the same Mg/Ca data against bottom water $\Delta[CO_3^{2-}]$ results in a different story (Figure 26B). The data appears to follow an exponential regression (18):

$$\boldsymbol{Mg/Ca = 3.62 \pm 0.64 \exp^{(0.038 \pm 0.0066 \times \Delta[CO_3^{2-}])} (R^2 = 0.87)} \quad \textbf{(18)}$$

For completeness, the linear calibration equation is (19):

$$\boldsymbol{Mg/Ca = 0.423 \pm 0.086 \Delta[CO_3^{2-}] - 0.38 \pm 2.36 \ (R^2 = 0.83)} \quad \textbf{(19)}$$

The data from this study neatly covers the interval between $\Delta[CO_3^{2-}]$ values of 15 and 25 μmol $kg_{sw}^{-1}$ that was absent from the record of Healey et al. (2008). The data from this study also are from waters almost 2°C colder than those from the Vema Channel, and yet despite this they still fall in line with the other data. This may indicate that *P. murrhina* represents a foraminifera with test Mg/Ca ratios far more sensitive to changes in $\Delta[CO_3^{2-}]$ than it is to changes in temperature.

The Li/Ca and B/Ca in *P. murrhina* show practically no sensitivity to changes in either temperature or $\Delta[CO_3^{2-}]$ (Figure 25). U/Ca is the exception (Figure 25g & h), and shows a positive relationship with $\Delta[CO_3^{2-}]$, whereas the relationship is negative in *C. wuellerstorfi* and *O. umbonatus*. This is unprecedented among foraminiferal U/Ca (c.f. Keul et al., 2013; Raitzsch et al., 2011).

### *3.2.7 U/Ca as a potential proxy for seawater saturation state*

In this dataset, *C. wuellerstorfi* and *O. umbonatus* U/Ca show a strong negative trend with increasing $\Delta[CO_3^{2-}]$ (Figure 19, Figure 21, Table 5). This relationship has been seen in other studies (Keul et al., 2013; Raitzsch et al., 2011), though this is the first holothermal core-top study to examine this relationship. Curiously, *P. murrhina* shows the opposite trend (Figure 26, Figure 27e & f,

Table 5). No other studies have examined the relationship of U/Ca in *P. murrhina*, and so there is currently no basis for comparison to tell if this signal is representative of the response of *P. murrhina's* U/Ca ratio to $\Delta[CO_3^{2-}]$, or merely unique to specimens from the Norwegian Sea.

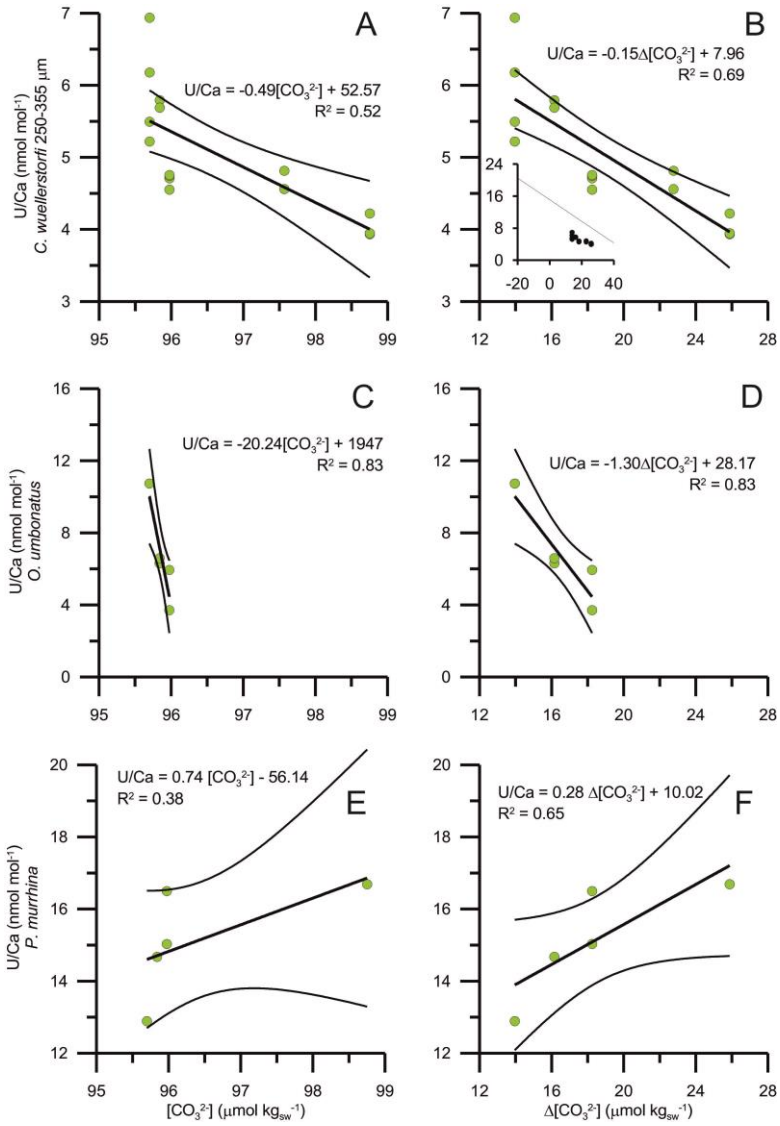


**Figure 27 – Comparison of U/Ca ratios in the three species examined in this study. Graphs on the left show U/Ca against $[CO_3^{2-}]$, whereas graphs on the right show U/Ca versus $\Delta[CO_3^{2-}]$. A & B show U/Ca from *C. wuellerstorfi*, B – inset) the line of best fit from Raitzsch et al. (2011), and the data from this study. Axes are the same as in B, but cover the range of values reported in Raitzsch et al. (2011). C & D) *O. umbonatus*, E & F) *P. murrhina*.**

It has been suggested that U/Ca may reflect the concentration of carbonate ions in seawater ($[CO_3^{2-}]$, Keul et al., 2013) rather than $\Delta[CO_3^{2-}]$. With the exception of *O. umbonatus*, the stronger relationship in this study is seen between U/Ca and $\Delta[CO_3^{2-}]$ (c.f. Figure 27 a with b, c with d, and e with f). This

conforms with the pattern seen in Raitzsch et al. (2011). However, there is a large off-set between the trends seen in *C. wuellerstorfi* in Raitzsch et al. (2011) and in this study (Figure 27b). The sensitivity of U/Ca to changes in $\Delta[CO_3^{2-}]$ was found to be -0.27 (± 0.04) nmol $mol^{-1}$ μmol $kg_{sw}^{-1}$ by Raitzsch et al. (2011) in *C. wuellerstorfi* (named as *Planulina wuellerstorfi* in their study). This is nearly twice as sensitive as that found in this study (-0.154 [± 0.058] nmol $mol^{-1}$ μmol $kg_{sw}^{-1}$, 250-355 μm size fraction), however it is also very nearly within error and so the higher sensitivities obtained here may just be a result of the narrow range. The y-intercept differ by a greater degree (15.1 ± 1.4, (Raitzsch et al., 2011) compared to 7.96 ±1.11, this study). The fact that temperature should show a positive relationship with U/Ca would serve to reduce the sensitivity reported in their study and their values are based on averaged intratest measurements using Laser Ablation ICP-MS (LA-ICP-MS). In addition, their samples were not cleaned in any way prior to analysis, and instead were pre-ablated for 1s to remove any surficial contamination. This study at least confirms that the negative correlation between U/Ca and $\Delta[CO_3^{2-}]$ seen in Raitzsch et al. (2011) in *C. wuellerstorfi* is real and not solely down to any correlation with temperature.

### 3.3 Conclusions

The data obtained here support a small effect of size fraction on element/Ca ratios, though perhaps not as great as other studies. Coiling direction does not affect element/Ca ratios in *C. wuellerstorfi* and so this species, at least, does not need to be separated by coiling direction when picking for trace-element analysis.

I have provided evidence to suggest that in a Norwegian Sea water depth transect Mg/Ca in *O. umbonatus* is less affected by changes in bottom water $\Delta[CO_3^{2-}]$ than *C. wuellerstorfi* and have hypothesised that this is either due to its shallow-infaunal habit, or due to a species specific difference in the threshold

$\Delta[CO_3^{2-}]$ below which Mg/Ca is heavily affected by changes in $\Delta[CO_3^{2-}]$. I have shown that the sensitivity of Mg/Ca to $\Delta[CO_3^{2-}]$ in *C. wuellerstorfi* is between 0.007 and 0.009 mmol $mol^{-1}$ $\mu mol^{-1}$ $kg_{sw}^{-1}$ by expanding the Norwegian Sea holothermal core-top calibration of Elderfield et al. (2006), and have shown that their estimate of 0.0088 mmol $mol^{-1}$ $\mu mol^{-1}$ $kg_{sw}^{-1}$ from a temperature-corrected global core-top analysis was accurate. I have provided evidence that Mg/Ca in *P. murrhina* may be unaffected by changes in temperature between -1 and 3°C and instead responds primarily to changes in $\Delta[CO_3^{2-}]$, at least between 10 and 50 $\mu mol\ kg_{sw}^{-1}$.

I have shown that foraminiferal U/Ca is still a promising proxy for $\Delta[CO_3^{2-}]$ when the whole test is analysed and the foraminifera have been reductively cleaned, though the sensitivity of changes in U/Ca to $\Delta[CO_3^{2-}]$ is lower than when compared with samples analysed with LA-ICP-MS (-0.154 compared to -0.27 nmol $mol^{-1}$ $\mu mol^{-1}$ $kg_{sw}^{-1}$). In addition, the absolute U/Ca values also appear lower. We show some evidence to suggest that U/Ca is a better proxy for $\Delta[CO_3^{2-}]$ than for $[CO_3^{2-}]$ in *C. wuellerstorfi*, *O. umbonatus*, and *P. murrhina*, however we find that U/Ca in the test of *P. murrhina* shows a positive correlation with $\Delta[CO_3^{2-}]$, whereas other species show a negative one. Analysis of whole-test U/Ca ratios need to be carried out under expanded ranges of $\Delta[CO_3^{2-}]$ and temperature conditions and with more species. Examining the trace element ratios of more miliolite foraminifera, such as *Quinqueloculina spp.*, may show similar trends to *P. murrhina* with temperature and $\Delta[CO_3^{2-}]$. Further analysis of *P. murrhina* specimens from other core-tops may confirm the trends seen here or may just help to confirm that it is unique to *P. murrhina* from the Norwegian Sea.

### *3.3.1 Future Work*

One potentially very useful application to which *P. murrhina* could be put is to culture it in temperature-controlled waters between 3 and 7°C. Taking the

temperature versus Mg/Ca calibrations of Healey et al. (2008), the changes in Mg/Ca between 1 and 3°C are nearly indistinguishable as being exponential or linear in form. However at 4°C, the exponential calibration equation predicts that the Mg/Ca ratio of *P. murrhina*'s test should be around 30 mmol $mol^{-1}$, whereas the linear equation predicts it should be around 23 mmol $mol^{-1}$. At 6°C, near the limits of where *P. murrhina* appears to thrive, the exponential and linear calibrations predict Mg/Ca ratios of ~94 and 36 mmol $mol^{-1}$, respectively. This difference is more than large enough to be discerned by ICP-MS and would provide a very useful insight into the processes by which this species controls the partitioning of Mg into its tests during formation of the calcite lattice.

Core-top material containing *Pyrgo murrhina* from a greater range of temperatures and carbonate saturation states need to be analysed to confirm this. The samples of Gudmundsson (1998) and Murgese and De Deckker (2005) from the Icelandic margin and Eastern Indian Ocean, respectively, represent two sample sets containing *P. murrhina*, as well as other miliolite foraminifera, that have already been collected and cover a broad (2-7°C) range of temperatures and differing $\Delta[CO_3^{2-}]$ regimes and would be suitable for further analysis. In addition, culture studies would vastly improve our understanding of how *P. murrhina* incorporates Mg and other trace metals into its test and under what conditions.

# 4 MID-MIOCENE ITCZ RESPONSE TO CHANGES IN THE NORTHERN HEMISPHERE ICE SHEETS

The Mid Miocene Climatic Optimum (MMCO) was a period of relative warmth between 17 and 14 Million years ago with reduced ice volumes compared to the modern day. Ceara Rise is a bathymetric high in the Western Equatorial Atlantic that shows sedimentation rates from 10-17m $Ma^{-1}$ during the MMCO allowing for high resolution analyses of climatological changes. Intervals from 15.35-15.72 and 16.06-16.36 Ma (±0.61 Ma for ages given) were analysed at 2ka resolution for foraminiferal Mg/Ca, $\delta^{18}O$, $\delta^{13}C$, as well as other trace element/Ca ratios in the benthic foraminifers *C. mundulus* and *O. umbonatus*, and the planktonic foraminifer *G. trilobus*. These were used to quantify temperature and $\delta^{18}O_{sw}$ changes in both the surface and deep ocean. Temperature varied by around 2-4°C during the MMCO, and sea levels also varied by up to 20-40 (±10)m. Changes in sea surface salinity occur coevally with changes in sea level and have been used to infer movement of the intertropical convergence zone (ITCZ). Northward movement of the ITCZ relative to Ceara Rise during a rise in sea level has been used to infer a reduction in ice volume centred on the Northern Hemisphere. This *a priori* implies the presence of ice sheets in the Northern Hemisphere during the MMCO some 13 Myr before they were thought to have appeared. Changes in productivity and the carbonate saturation state will be used in the next chapter to lend weight to the movements of the ITCZ implied herein.

## 4.1 Introduction

The Mid-Miocene Climatic Optimum (MMCO, Figure 28) was the warmest period in the past 35 Ma, lasting from around 17Ma to 14 Ma (Flower and Kennett, 1994; Holbourn et al., 2007; Zachos et al., 2001). The MMCO is associated with a ~1 ‰ excursion towards lower values of benthic foraminiferal $\delta^{18}O$, indicative of global warming and a reduction in global ice volume (Báldi, 2006; Holbourn et al., 2007; Zachos et al., 2001). Mean average annual temperatures are estimated to have been between 17 and 22°C in central Europe (Böhme, 2003), and >19°C in Southeast Asia (Zou et al., 2004) with global average temperatures approximately 6°C higher than today (e.g., Flower and Kennett, 1994). The peak warmth occurred ~15.7 Ma, based on palynological reconstructions and foraminiferal stable isotope measurements (Holbourn et al., 2007; Warny et al., 2009).

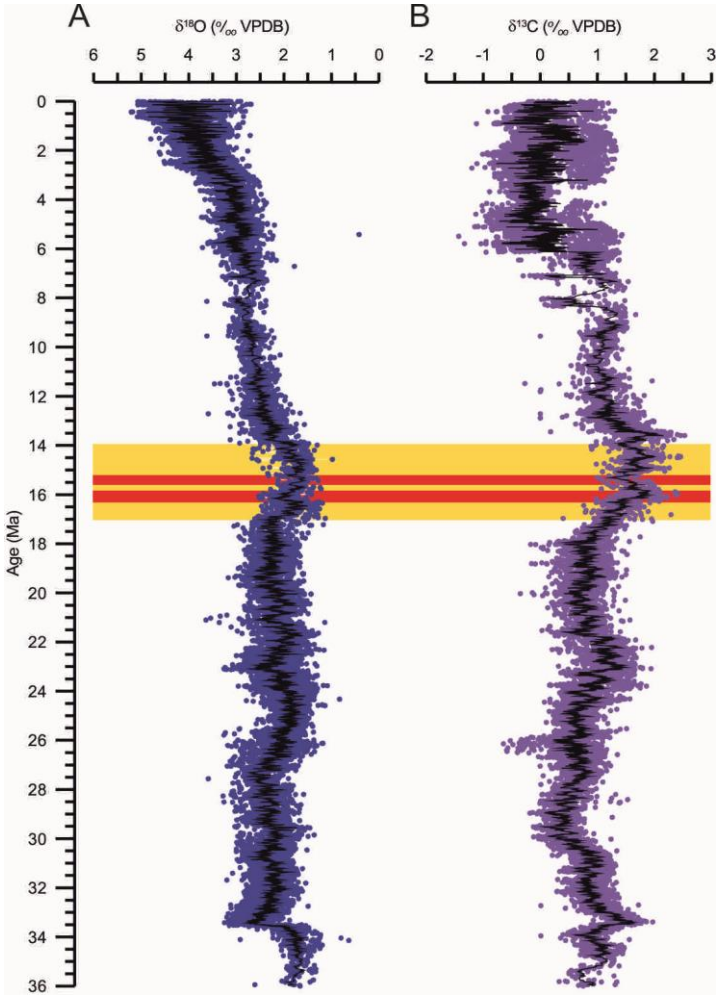


**Figure 28 – $\delta^{18}O$ (A) and $\delta^{13}C$ (B) from the last 36 Myr. The MMCO is highlighted in yellow. The intervals studied in this thesis are highlighted in red.**

This warmth is best modelled by elevated $pCO_2^{ATM}$. Stomatal index (SI) based estimates of $pCO_2^{ATM}$ suggests that values were as high as 500-600 ppm during peak warmth (Kürschner et al., 2008). Estimates by Retallack (2009) based on analyses of pedogenic calcite nodules suggests that $pCO_2^{ATM}$ may even have been as high as 800 ppm. More recent evidence from $\delta^{11}B$ by Foster et al. (2012) suggests that $pCO_2^{ATM}$ rose to around 400ppm (± 100 ppm), which is coincidentally around the same values as the modern $pCO_2^{ATM}$, and this is confirmed by recent, long-term single-site estimates based on alkenones by Zhang et al. (2013) of 400-500 ppm between 17 and 14 Ma and by a high-resolution (~36ka) study of $\delta^{11}B$ across the MMCO by Greenop et al. (2014). There is also evidence for increased weathering rates during the MMCO, which may be expected under greenhouse conditions (Wan et al., 2009). The increased $pCO_2^{atm}$ could be explained by the formation of major flood basalts in the USA, Central Europe and eastern China coincident with the onset of the MMCO (Foster et al., 2012; Hodell and Woodruff, 1994; Schwarz, 1997; Zou et al., 2004).

The location of ice volume retreat during the MMCO has always been assumed to have been centred on Antarctica, due in large part to the presence of southern beech and other temperate species on the Antarctic continent indicating reduced ice volumes (Warny et al., 2009), as well as the assumption that no major continental ice sheets appeared in the northern hemisphere until the Pliocene (Bartoli et al., 2005; Lunt et al., 2008; Pekar and DeConto, 2006; van de Wal et al., 2011; Zachos et al., 2001). None-the-less, more recent modelling studies on the thresholds for glacial inception in general (DeConto et al., 2008) and modelling of the MMCO specifically (Foster et al., 2010a; Herold et al., 2012; You et al., 2009) suggest that northern hemisphere ice sheets were possible. Evidence of ice-rafted-debris in the Northern Hemisphere at 18 and 16 Ma is strong evidence for the presence of at least ephemeral ice sheets (St John, 2008). Northern Hemisphere glaciation is inferred at the Oligocene-Miocene

Boundary (OMB, 23Ma) by tracking the ITCZ in the equatorial Pacific Ocean using the source of aeolian dust by way of $\varepsilon_{Nd}$ and $^{87}Sr/^{86}Sr$ ratios (Hyeong et al., 2014). Modelling of the Greenland Ice Sheet by Lunt et al. (2008) suggests that declining $pCO_2^{ATM}$ from ~400 ppmv to ~280 ppmv is sufficient to explain its inception, assuming Pliocene continental configurations.

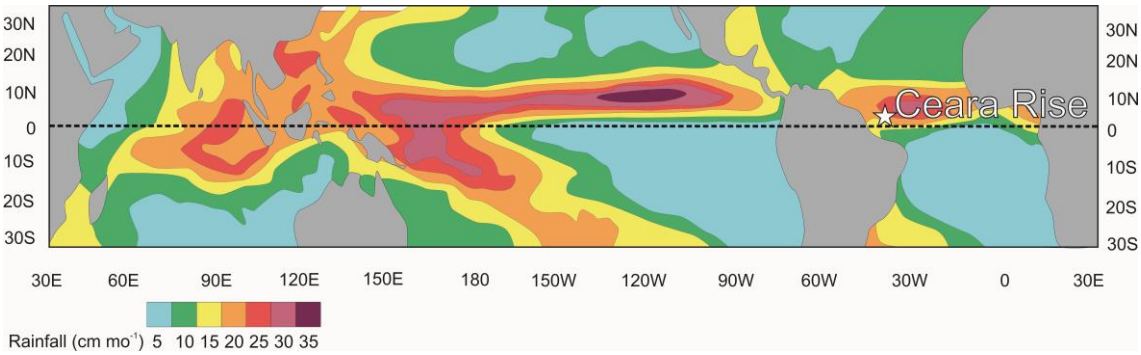


**Figure 29 – Monthly average rainfall rate near the equator, after Philander et al. (1996). The position of Ceara Rise in the Eastern Equatorial Atlantic has been marked on with a white star. The position of the ITCZ can be easily distinguished by the band of higher rainfall near to the equator.**

The presence and volume of ice at high latitudes in the Arctic and Antarctic can have significant effects on low latitude climate. One such effect is on the position of the intertropical convergence zone (ITCZ). The ITCZ is an area of increased precipitation caused by the ascending air currents associated with the equator and is a consequence of the convergence of the northern and southern Hadley cells. Today, its average annual position (Figure 29) is about 5°N of the equator (Philander et al., 1996), and this is caused by the rising air currents favouring the warmer hemisphere, as well as equatorial upwelling providing something of a cold-air barrier to further southern movement of the ITCZ (Xie and Philander, 1994). However as the ITCZ favours the warmer hemisphere, any increase (decrease) in average temperature or the decay (growth) of ice sheets on either the Northern or Southern Hemisphere will move the position of the ITCZ further into (away from) that hemisphere, and with it the associated reduced salinities and increased productivity. As Ceara Rise sits close to the southern boundary of the ITCZ, it will be very sensitive to relative changes in the position of the ITCZ; a decrease in surface salinity coupled with an increase

in productivity may be taken to mean a southerly movement of the mean position of the ITCZ, and if that is accompanied by a change in ice volume, a Northern or Southern Hemispherical locus of ice volume change can be inferred.

Calculating ice volume and sea level change during the MMCO is difficult due to the lack of good records. Ice-proximal ANDRILL records are either plagued by hiatuses caused by repeated advance and retreat of the ice margin (Davies et al., 2012), or come from regions where sedimentation is dominated by glacial, rather than biogenic, processes (Brachfeld et al., 2013; Passchier et al., 2011) which makes acquisition of long-term, high resolution geochemical palaeoclimate proxies difficult to obtain. Sedimentary facies analysis in the AND-2A core in McMurdo Sound suggests significant, yet brief ice retreat events occurred at 20.2-20.1, 19.6-19.3, 18.7-17.6, and 15.4 Ma. These are somewhat corroborated by palynological evidence of southern beech pollen, grasses and fresh water algae that suggests peak warmth occurred between 15.7 and 15.5 Ma, with smaller warm events occurring occasionally between 17.2 and 12.6 Ma (Warny et al., 2009). These records have the disadvantage that they can only give semi-quantitative estimates of ice extent (i.e.: bigger or smaller than today's), and cannot give estimates of the true magnitude of changes in global ice volume.

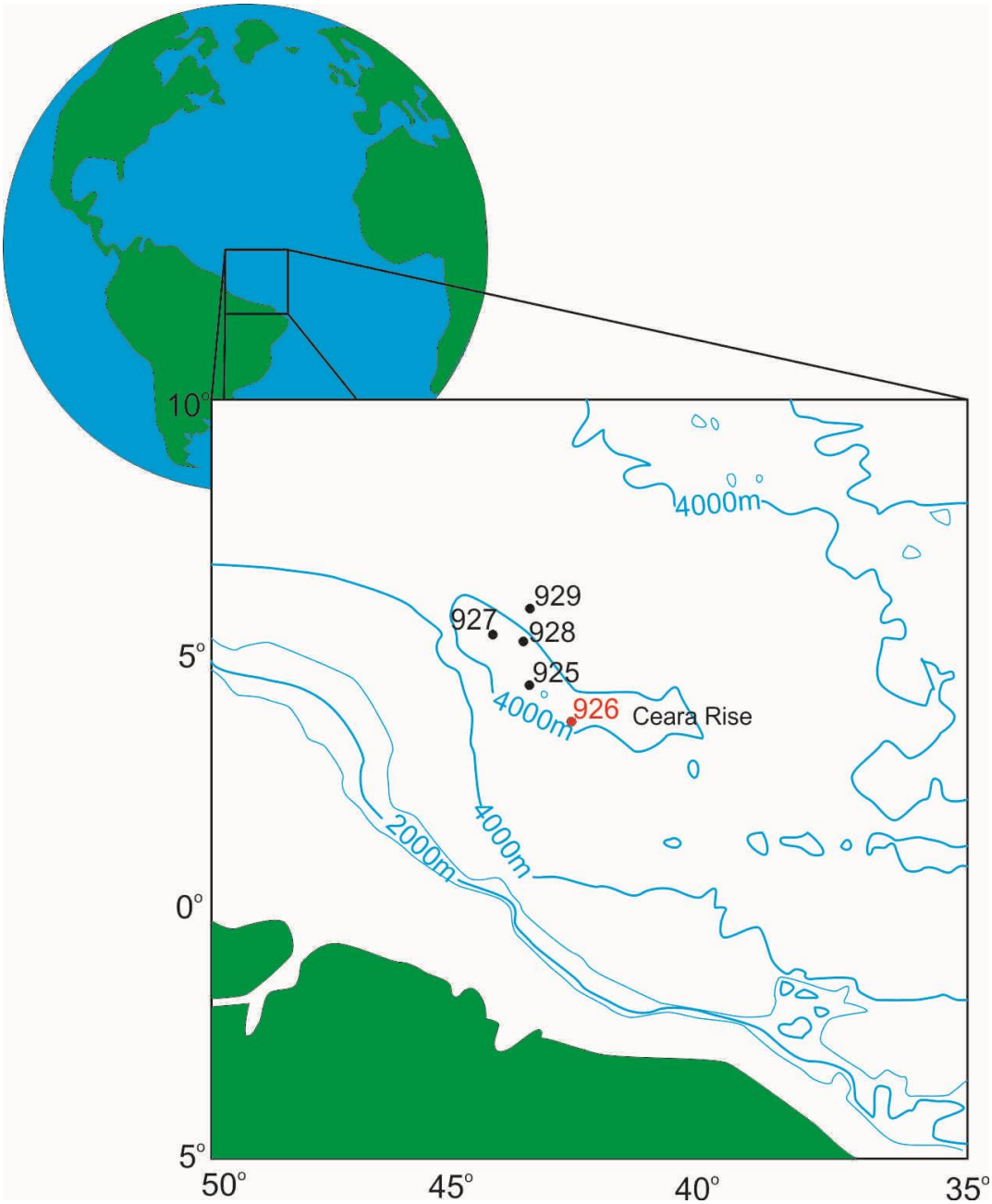


**Figure 30 – Location of Ceara Rise and of ODP Site 926. Also shown are the other drill sites from ODP leg 154 (adapted from Shipboard Scientific Party, 1995c).**

Geochemical proxy records from more distal sites broadly agree with these timings, though less so in specifics. The long term composite benthic foraminiferal $\delta^{18}O$ record of Zachos et al. (2008) shows the MMCO as occurring between ~17 and 14 Ma (

Figure 28). Peak warmth according to benthic $\delta^{18}O$ from Holbourn et al. (2007) and Lear et al. (2010) occurs at around 16 Ma, with a second peak in warmth at around 14.8 Ma before the decline in temperatures associated with

the Mid-Miocene climatic transition (MMCT). The $pCO_2^{ATM}$ record of Foster et al. (2012) agrees with these timings.

Here I present high resolution (~2-4 ka) benthic foraminiferal geochemical stable isotope and trace element/Ca ratio records from ODP Site 926 from two intervals (between ~15.2 and 15.6 Ma and between ~15.9 and 16.3 Ma,

Figure 28) that will help to constrain the variability of global ice volume during the MMCO. Furthermore, I present paired planktonic foraminiferal stable isotope and trace element/Ca ratio records from the samples. Reconstructed surface water conditions are interpreted in terms of a shift in the placement of the ITCZ which implies that ice growth and decay during the Miocene Climatic Optimum may not have been constrained to the southern hemisphere.

## 4.2 Methods

### *4.2.1 Sample location and acquisition*

Material for this study comes from ODP's Leg 154, site 926, located on Ceara Rise in the Western equatorial Atlantic (Figure 30). Ceara Rise is a bathymetric high that formed on the mid Atlantic ridge ~80 Ma and is draped in a thick (>1000 m) covering of sediment (Shipboard Scientific Party, 1995a). Ceara Rise has a minimum depth of around 2600 m below sea level, however sediments are thickest on areas 3000 m below sea level or deeper. The rationale for Leg 154 was to study the history of water flow and carbonate sedimentation and production in the Cenozoic. It was hoped that by drilling a depth transect across Ceara Rise, the history of interaction between North Atlantic Deep Water (NADW) and Antarctic Bottom Water (AABW) could be analysed. By assuming that the surface production of carbonate is constant over the area of Ceara Rise, the rates of dissolution of carbonate with water depth could also be studied by analysing differences in sedimentation rate between the sites. The shallowest Site drilled on Leg 154 was Site 925, which had a spud depth of ~3000 m below

sea level (mbsl), however core recovery in the Miocene and Oligocene suffered from large coring gaps that overlapped with intervals of interest to this study (Shipboard Scientific Party, 1995b). The next most shallow site, Site 927, had a depth of ~3300 mbsl, however evidence of sediment slumping at this site made it unsuitable for continuous high resolution sampling (Shipboard Scientific Party, 1995d) and so Site 926 was chosen.

Site 926 sits at a depth of ~3600 mbsl. Sedimentation rates are around 10 m $Ma^{-1}$ in the early-mid Miocene. This allows for a high resolution of ~1 sample every 4 ka to be achieved. The modern day carbonate saturation state of waters at ~3600 m depth in the western Atlantic is around 32 μmol $kg^{-1}$ (Broecker and Takahashi, 1978; King et al., 1997). Data from GEOSECS site 40 suggests that the modern bottom water temperature and saturation state at Ceara Rise is around 2.5°C and 35.9 μmol $kg_{sw}^{-1}$. This is above the suggested threshold of 25 μmol $kg^{-1}$ in which saturation effects significantly affect Mg/Ca ratios (Yu et al., 2008) and the palaeodepth of Site 926 during the Miocene was ~3400 m (Flower et al., 1997). None-the-less, there may still be significant changes in saturation state over the intervals being studied if the depth of the boundary between the relatively $CO_3^{2-}$ rich NADW and $CO_3^{2-}$ poor AABW changed vertically, or the CCD shoaled. Preservation of benthic foraminifera at Site 926 is described as moderate to good in sediments of Miocene age, though it becomes poorer down-core (Shipboard Scientific Party, 1995c). This is something of a trade-off due to the requirement of high sedimentation rates in order to achieve a high sample resolution.

All the sample material comes from two intervals from Site 926 Hole B. The intervals are from 293.76 to 300.15 mbsf (henceforth referred to as "the upper interval", 15.352 – 15.722 Ma) and 305.97 to 311.17 mbsf (henceforth referred to as "the lower interval", 16.059 – 16.360 Ma). 20cc of material was sampled at 4cm (~2.3ka) resolution to ensure a very high resolution record. The two intervals were designed to target ~16Ma and >17Ma in order to capture

snapshots of the climate before and after the warming associated with the MMCO, but inaccuracies in the preliminary age model prevented this (section 2.5).

All the sample material was acquired from hole 926B to obviate the risk of inducing uncertainty in relative ages by small mistakes in following a splice. The intervals taken from hole 926B have no major coring gaps (Figure 65 and Figure 66, Appendix 3, section 8.3) and were cored with an extended core barrel (XCB). The intervals sampled fall within the Lithologic Unit III, subunit IIIA, which has meter-scale cyclic changes from light grey nannofossil chalk with clay to greenish-grey clayey nannofossil chalk and carbonate content ranging from 80% to 60% (Shipboard Scientific Party, 1995c).

### *4.2.2 Age model*

The age model applied to the data is the one described in Methods chapter 2.

### *4.2.3 Sample analysis*

Samples were cleaned and analysed for trace metal composition as described in the appendices (Section 8.1). Samples of *Cibicidoides mundulus* (*C. mundulus*) were split after crushing for stable isotope analysis and analysed on a ThermoFinnigan MAT252 with online sample preparation, using an automated Kiel III carbonate device at Cardiff University. The long-term precision of the in-house standard is better than 0.09 ‰ in $\delta^{18}O$ and better than 0.06 ‰ in $\delta^{13}C$ (1 standard deviation). Results are reported relative to Vienna Pee Dee Belemnite (VPDB). Larger samples were further split to bring the sample weights in between 50 and 100 μg and each split was run separately.

### *4.2.4 Calculating temperature, $\delta^{18}O_{sw}$ and $\delta^{18}O_{ssw}$ from Mg/Ca and $\delta^{18}O$ records*

See Methodology chapter 2 for details. *C. mundulus* was used for the bulk of the benthic Mg/Ca paleothermometry and stable isotope work using the

temperature calibration of Lear et al. (2002). *C. mundulus* is predominantly an epifaunal benthic foraminifera (Rathburn and Corliss, 1994), though it may show some shallow infaunal behaviour (Hodell et al., 2001). The Mg/Ca temperature record was improved by the addition of $Mg/Ca_O$. $Mg/Ca_O$ was normalised to $Mg/Ca_M$ by taking the means of each record, finding the quotient (~0.73) of the two means and then correcting $Mg/Ca_O$ to $Mg/Ca_M$ by multiplication of the individual $Mg/Ca_O$ measurements by that quotient. $\delta^{18}O_M$ and $Mg/Ca_M$ was used to calculate $\delta^{18}O_{sw}$ using the $\delta^{18}O$ temperature calibration of Marchitto et al. (2014).

In order to find an absolute temperature, $Mg/Ca_M$ had to be corrected for both secular variations in Mg/Ca in seawater using the model of Stanley and Hardie (1998), which provided a value for Mg/Ca in sea water at 16Ma of 3.2 mol $mol^{-1}$. A correction was also applied for species specific vital effects on the partitioning of seawater Mg+ into foraminiferal calcite. In the absence of a *C. mundulus* specific H-value, a value of 0.44 was used (one of the estimates of H for *O. umbonatus*). It is worth noting that Evans and Müller (2012) produced a range of H-values between 0.44 and 0.54 for *O. umbonatus* based on differing assumptions, but the H-value used does not affect the relative temperature changes, and the difference in temperatures produced between those extremes was far less than the range of temperatures due to experimental error. Temperatures for *G. trilobus* were produced in a similar manner using the Mg/Ca calibration of Dekens et al. (2002), and an H-value of 0.41 (Evans and Müller, 2012)

## 4.3 Results

### *4.3.1 Coarse Fraction*

Coarse fraction weight percentage varies between 1% and 63%, with an average of 33%. The upper record is far more variable than the lower record and it possesses both the minimum and maximum values for both intervals

taken as a whole (Figure 31a). The upper record shows two frequencies significant at the 99% level at 4.66 $m^{-1}$ (12.4 kyr) and at 5.29 $m^{-1}$ (11.0 kyr, Figure 31c). There are also four more frequencies that are significant above the 95% level at 0.31 $m^{-1}$ (187 kyr), and 6.69 $m^{-1}$ (8.65 kyr).

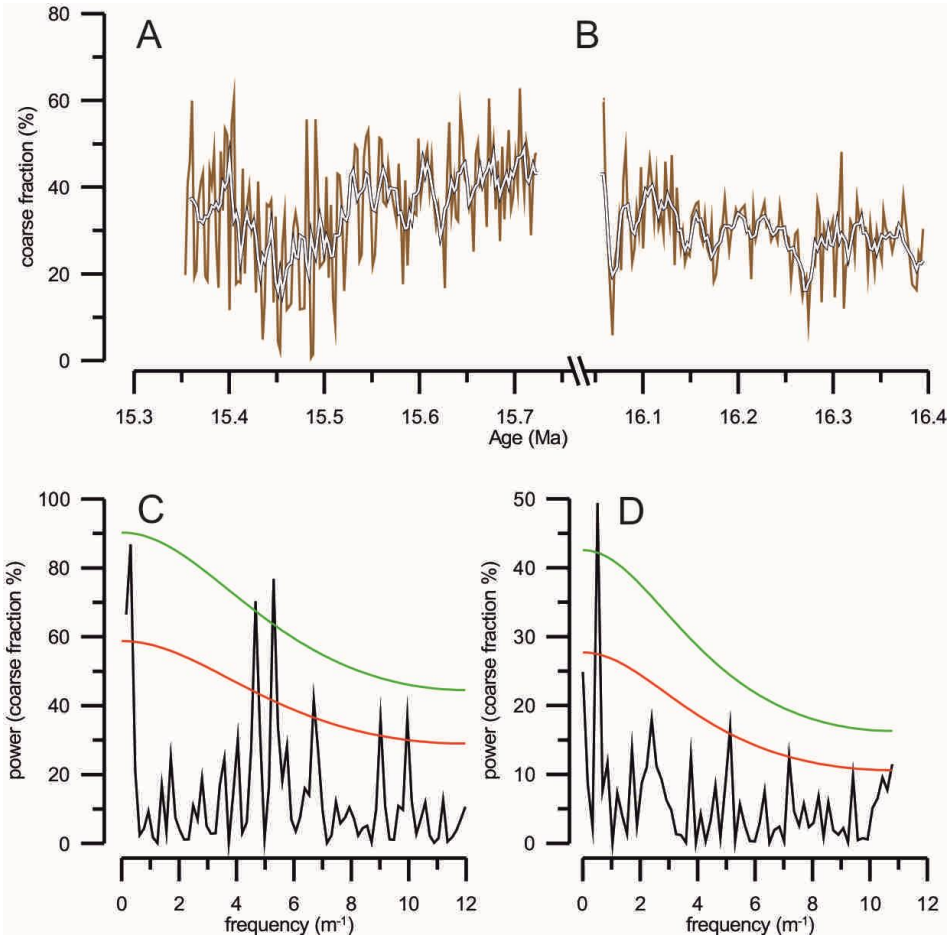


**Figure 31 – Coarse fraction percentage and cyclicity in the intervals used in this study. A) Coarse fraction percentage from the upper interval. The black line represents a 4 point symmetrical moving average. B) Coarse fraction percentage from the lower interval. C) Frequency analysis of the upper interval. The red line shows the 95% confidence interval, the green line shows the 99% confidence interval. D) Frequency analysis of the lower interval. The format is the same as C.**

The lower record varies between 6% and 49% (Figure 31b). It shows only one frequency that is distinguishable from red noise above the 99% confidence interval at 0.51 $m^{-1}$ (114 ka), and another two that are above the 95% confidence interval at 5.13 $m^{-1}$ (11.3 ka) and 7.18 $m^{-1}$ (8.06ka, Figure 31d). The upper record shows larger changes in course fraction weight percent at a higher frequency.

### *4.3.2 $\delta^{18}O$*

$\delta^{18}O$ in the planktonic foraminifera *G. trilobus* ($\delta^{18}O_G$) varies around a mean of -1.7 ‰, with a minimum of -2.3 ‰ and a maximum -0.96 ‰ (Figure 32a and b). Between 313 and 310.5 mbsf, $\delta^{18}O_G$ varies between around -1.8 ‰ and -1.4 ‰ around a mean of -1.6 ‰. At 310.5 mbsf $\delta^{18}O_G$ suddenly trends towards heavier values and peaks at -1.35‰. At 310 mbsf, $\delta^{18}O_G$ begins a long trend towards heavier values that peaks at a mean value of ~-1.3‰ at around 307.5 mbsf. This trend reverses and $\delta^{18}O_G$ returns to ~-1.7 ‰ within 50cm. At ~306.5 mbsf there appears to be a rapid increase to ~-1.2 ‰ followed by a rapid decline to ~-1.8‰ before the sampling gap at 306 mbsf.

Between 300 and 298 mbsf $\delta^{18}O_G$ appears to show a general trend towards heavier values from a mean value of around -2 ‰ to around -1.6 ‰. After that $\delta^{18}O_G$ varies more rapidly, between ~-2.1 ‰ and -0.96 ‰, and does not appear to show any particular strong or lasting trends. This increased variability is also seen in the $\delta^{18}O$ in the predominantly epifaunal (Rathburn and Corliss, 1994) *C. mundulus* ($\delta^{18}O_M$), and the wt% coarse fraction.

$\delta^{18}O_M$ varies between 0.43 and 1.86‰ (Figure 32c and d). Between 313 and 309mbsf, $\delta^{18}O_M$ varies between 1.0 and 1.6‰, however at ~309 mbsf it shows far less variability and instead begins a steady trend towards heavier values from ~1.2 ‰ to ~1.8‰ at 308 mbsf. This is followed by a marked decrease over ~16cm to ~0.9 ‰, though this settles back to a mean of around 1.2 ‰ at 307.5 mbsf, varying between 1.0 and 1.6 ‰ at 306mbsf. From 301 to 297.5 mbsf $\delta^{18}O_M$ remains within the same values as between 307.5 and 306 mbsf, however after that point it appears to vary much more and with a much higher frequency, mirroring the changes in variability in wt% coarse fraction and $\delta^{18}O_G$ that occur at around the same point. At around 295.5 mbsf $\delta^{18}O_M$ trends to lighter values, peaking at a mean of around 0.6 ‰. This falls back to around 1.2‰ by 294.5 mbsf and $\delta^{18}O_M$ once again varies between around 1.6‰ and 1.0 ‰.

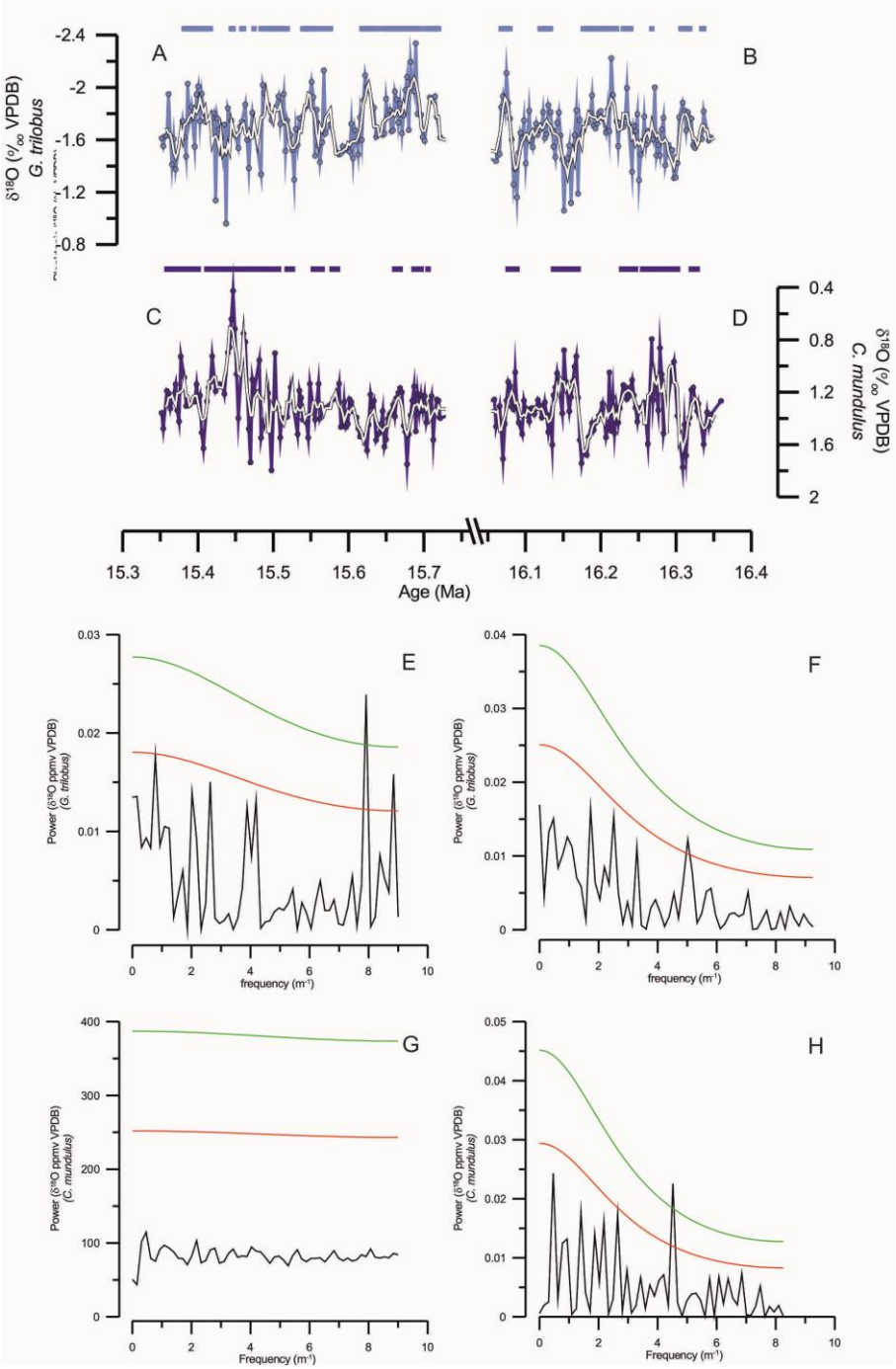


**Figure 32 – Foraminiferal $\delta^{18}O$ and frequency analysis from ODP Site 926. A and B) $\delta^{18}O$ from the planktonic foraminifer *G. trilobus* from the upper and lower intervals, respectively. C and D) $\delta^{18}O$ from the benthic foraminifer *C. mundulus* from the upper and lower intervals, respectively. The white lines in graphs A-D represent a 4 point symmetrical moving average. E and F) frequency analysis of the data from plots A and B, respectively. G and H) Frequency analysis of the data from plots C and D, respectively.**

Where the moving average falls below the overall mean $\delta^{18}O$ for both $\delta^{18}O_M$ and $\delta^{18}O_G$ has been marked with a blue line (Figure 32). This provides a qualitative, first-order indicator of periods that were warmer or more ice-free

than the average for the record as a whole. From this, it can be argued that the upper interval displays lighter $\delta^{18}O$ values than the lower and so represents a warmer climate.

$\delta^{18}O$ shows no consistent frequencies between records, with one frequency significant above the 99% confidence level in the upper interval in *G. trilobus* at ~8 $m^{-1}$ (~7 kyr period), and one in the lower interval at ~4.5 $m^{-1}$ (~13 kyr period). In general, variability in $\delta^{18}O$ shows no periodicity that is not distinguishable from red noise.

### *4.3.3 $\delta^{13}C$*

*C. mundulus* $\delta^{13}C$ ($\delta^{13}C_M$) in the lower interval varies between 0.91 and 2.31 (Figure 33d). The smoothed data vary between ~1.6 and ~2.2 ‰. This contrasts with the $\delta^{13}C$ in *G. trilobus* ($\delta^{13}C_G$) which varies between 2.1 and 3.8 ‰. There is one trend in $\delta^{13}C_G$ which stands out above the general background. Between 307.53 and 307.17 mbsf $\delta^{13}C_G$ decreases from 3.35 to 3.13 ‰ by 307.33 mbsf.

The carbon isotope records from the upper interval are far more variable. Between 300.11 and 298.15 mbsf, $\delta^{13}C_M$ follows a saw-tooth pattern, with a shallow trend towards lighter values, followed by a sharp increase (Figure 33c). From 300 to 299.35 mbsf, $\delta^{13}C_M$ trends towards lighter values from ~1.9 to ~1.6 ‰. There is then a sharp increase of ~0.2 ‰ from 299.35 to 299.23 mbsf. The second saw-tooth is smaller, with only ~0.15 ‰ trend towards lighter values over 0.6 m. At 298.79 mbsf $\delta^{13}C_M$ increases to 1.86 ‰ and then begins the third saw-tooth. The decrease associated with the start of the third and final saw-tooth in this set is steeper, its peak is more rounded, and the increase that follows is shallower than the other two. $\delta^{13}C_M$ decreases by 0.28‰ over 0.32 m and, rather than a sudden increase as with the first two cycles, it instead remains at ~1.6 ‰ for 0.2 m or so before increasing to around 1.8 ‰ by 298.11 mbsf. At 297.39 mbsf $\delta^{13}C_M$ increases to ~2.0 ‰ within 0.08m, then decreases to 1.7 ‰. Between 296.68 and 295.64 mbsf the smoothed $\delta^{13}C_M$ data decreases to

1.11 ‰ in a steady trend that is only broken between 296.32 and 296.04 mbsf where there is a sudden increase to 2.18 ‰. The raw data between 296.32 and the end of the record shows a great degree of variability. $\delta^{13}C_M$ varies between 0.94 and 2.45 ‰. $\delta^{13}C_G$ does not show the same saw-toothed variability as $\delta 13C_M$. Between 300.15 and 297.08 mbsf the smoothed $\delta^{13}C_G$ varies between ~2.92 and 3.36 ‰ on ~0.8m period. At 296.08 mbsf $\delta^{13}C_G$ decreases to 2.39 ‰. The minima in $\delta^{13}C_G$ coincides with the minima in $\delta^{13}C_M$. From 295.8 to 293.88 mbsf $\delta^{13}C_G$ varies between 2.39 and 294.8 ‰ (Figure 33a).

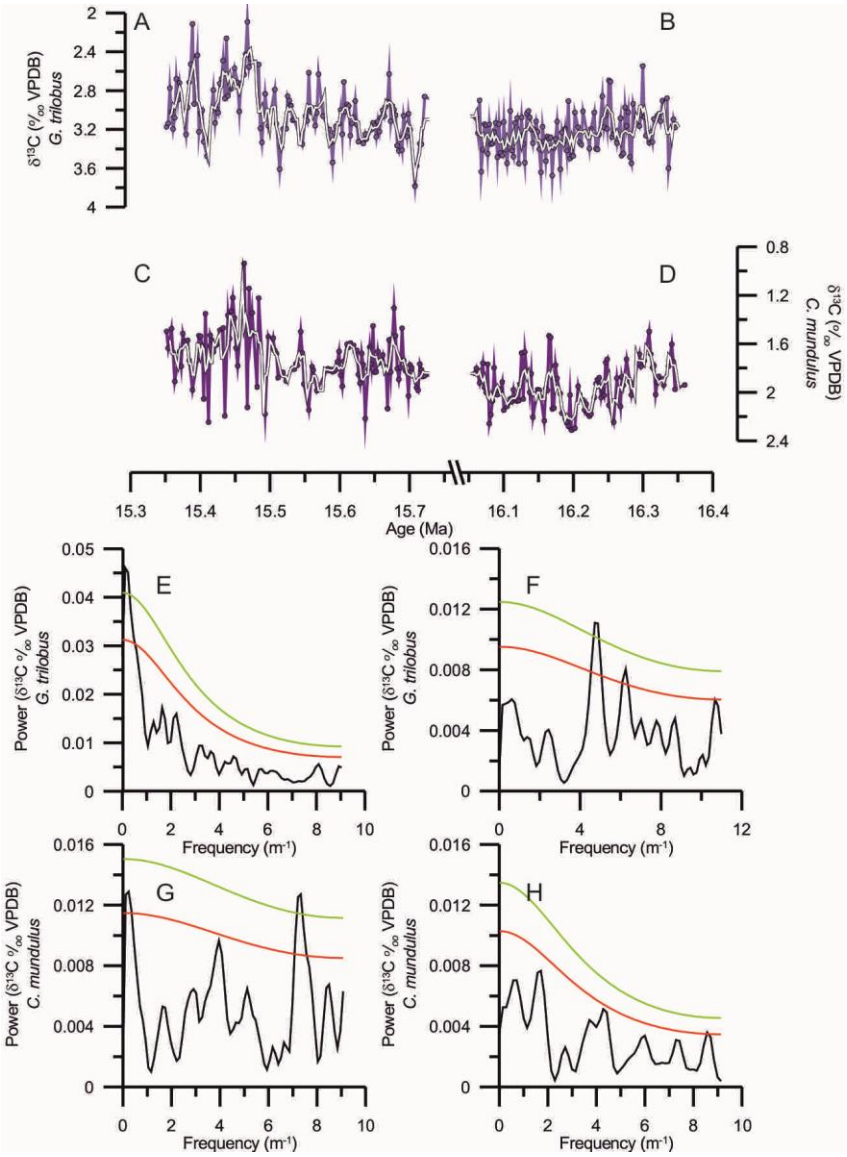


**Figure 33 - Foraminiferal $\delta^{13}C$ and frequency analysis from ODP Site 926. A and B) $\delta^{13}C$ from the planktonic foraminifer *G. trilobus* from the upper and lower intervals, respectively. C and D) $\delta^{13}C$ from the benthic foraminifer *C. mundulus* from the upper and lower intervals, respectively. The white lines in graphs A-D represent a 4 point symmetrical moving average. E and F) frequency analysis of the data from plots A and B, respectively. G and H) Frequency analysis of the data from plots C and D, respectively.**

$\delta^{13}C_M$ in the lower interval and $\delta^{13}C_G$ in the upper interval do not show significant cyclicity at orbital frequencies (Figure 33e & h). $\delta^{13}C_G$ in the lower interval shows only one significant peak at the 95% and 99% confidence levels at ~0.21m, which is equivalent to ~12ka (Figure 33f). At the 95% confidence level there is also a significant peak at 0.16m (~9.17ka). $\delta^{13}C_M$ in the upper interval (Figure 33g) shows a 99% significant peak at ~0.14m (~7.79ka) and a peak significant at the 95% confidence level of ~4.30m (~245ka).

### *4.3.4 Mg/Ca*

*G. trilobus* Mg/Ca ($Mg/Ca_G$) varies between 3.02 and 4.44 mmol $mol^{-1}$ with a mean of ~3.7 mmol/mol and $\sigma 1$ of 0.22 mmol $mol^{-1}$. $Mg/Ca_G$ begins at the base of the lower interval at around 3.80 mmol $mol^{-1}$, and shows a decline to around 3.50 mmol $mol^{-1}$ by 310.3 mbsf. The range of $Mg/Ca_G$ in the lower interval is between 3.4 and 3.8 mmol $mol^{-1}$, however there appears to be one deviation when the data are smoothed using a moving average; at around 310 mbsf $Mg/Ca_G$ shows a slight spike to ~4.0 mmol $mol^{-1}$. A similar spike is not seen in the benthic Mg/Ca or $\delta^{18}O$ records, however it does coincide with a similar maximum around the same time in $\delta^{18}O_G$. $Mg/Ca_G$ in the upper interval shows similar variability as in the lower interval. There is a maximum of ~4.4 mmol $mol^{-1}$ at approximately 295.7 mbsf which coincides with similar maxima in the benthic Mg/Ca records. There are no frequency peaks in either the upper or lower intervals that are significant to at least 95% (Figure 34g & h).

Mg/Ca in *C. mundulus* ($Mg/Ca_M$) is appears to vary more rapidly than $Mg/Ca_G$; its minima and maxima are 0.97 and 1.91 mmol $mol^{-1}$ around a mean of 1.39 mmol $mol^{-1}$ with a $\sigma 1$ of 0.17 mmol $mol^{-1}$. Between 313 and ~308.5 mbsf $Mg/Ca_M$ varies between 1.00 and 1.87 mmol $mol^{-1}$ and shows no discernible trends or cyclicity. At around 308.5 mbsf, $Mg/Ca_M$ appears to show a general

trend towards higher values, increasing from ~1.1 mmol $mol^{-1}$ at 308.5 mbsf to ~1.4 mmol $mol^{-1}$ at 306 mbsf, though superimposed on this trend are small fluctuations that reach approximately 0.1 mmol $mol^{-1}$ above or below the base trend.

The upper interval appears less noisy than the lower one, and shows more discernible trends and patterns. $Mg/Ca_M$ at 300 mbsf shows a decline from ~1.6 mmol $mol^{-1}$ to ~1.2 mmol $mol^{-1}$ at around 299.5 mbsf. $Mg/Ca_M$ fluctuates between these two extremes until around 296 mbsf, at which point it declines suddenly from ~1.4 mmol $mol^{-1}$ to 0.97 mmol $mol^{-1}$ before rebounding to 1.91 mmol $mol^{-1}$. A similar sudden change is also seen at around the same stratigraphic height in Mg/Ca in *O. umbonatus* ($Mg/Ca_O$). $Mg/Ca_M$ declines back to ~1.4 mmol $mol^{-1}$ by 295.5 mbsf and then shows a gradual decline to 1.3 mmol $mol^{-1}$, fluctuating between ~1.6 and 1.2 mmol $mol^{-1}$. There are two peaks in the upper interval (Figure 34i) significant to >95%; one at ~1.9 $m^{-1}$ (period of ~29.9 ka), and one at ~6.1 $m^{-1}$ (period of ~9.4ka). These do not correspond to any orbital frequencies.

Mg/Ca in *O. umbonatus* ($Mg/Ca_O$) varies around a mean of 1.87 mmol $mol^{-1}$, with $\sigma 1$ of 0.23 mmol $mol^{-1}$. $Mg/Ca_O$ is also somewhat noisy until around 309.5 mbsf although the general decrease between 311.5 and 310.5m is also seen as an increase in the benthic $\delta^{18}O_M$ and a decrease in the planktonic Mg/Ca record. From 309.5 to 306 mbsf $Mg/Ca_O$ fluctuates between 1.5 and 2.3 mmol $mol^{-1}$. In the smoothed data there appear to be three peaks in $Mg/Ca_O$ centred at ~307.6 mbsf, 307 mbsf, and 306.5 mbsf of ~2.1, 2.0, and ~2.2 mmol $mol^{-1}$ respectively. The middle peak shows a small fluctuation down to ~1.9 mmol $mol^{-1}$, however this is caused by one data point at ~1.5 mmol $mol^{-1}$ in the middle, and it is not clear if that is a real signal or noise. The lower interval has one frequency that stands out above the 99% confidence interval at 4.4 $m^{-1}$ (period of ~13.3 ka).

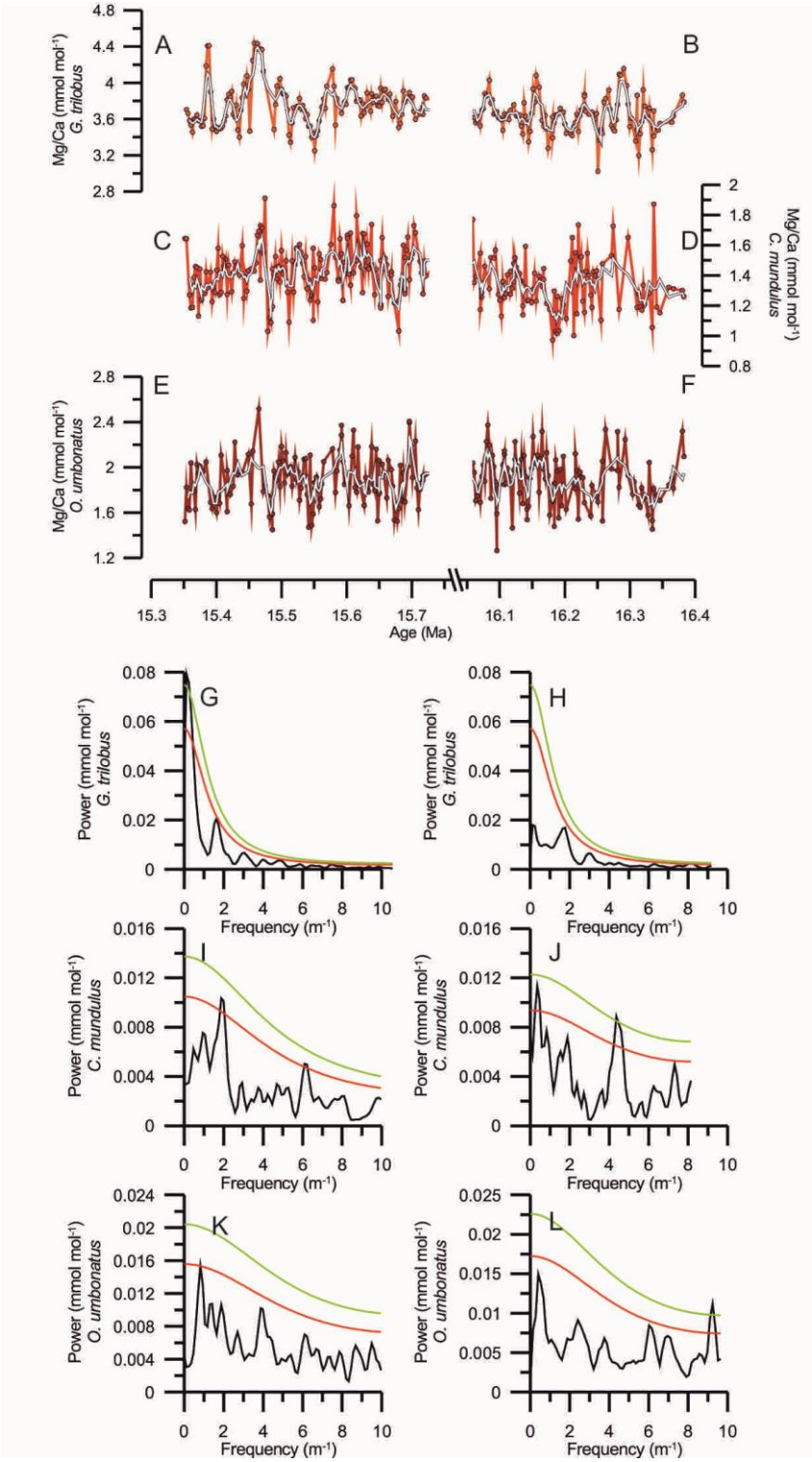


**Figure 34 – Mg/Ca in three species of foraminifera from site 926. A) Planktonic *G. trilobus* in the upper interval. B) *G. trilobus* in the lower interval. C) Epifaunal *C. mundulus* in the upper interval. D) *C. mundulus* in the lower interval. E) Shallow infaunal *O. umbonatus* in the upper interval. F) *O. umbonatus* in the lower interval. G & H) Frequency analysis of plots A and B, respectively. I & J) Frequency analysis of plots C & D, respectively. K & L) Frequency analysis of plots E & F, respectively. The white lines outlined in black show the symmetrical 4 point moving average of each record.**

In the upper interval, at 300 mbsf Mg/Ca$_O$ begins at around 1.8 mmol mol$^{-1}$ and rises quickly to ~2.2 mmol mol$^{-1}$, before falling to ~1.6 mmol mol$^{-1}$ at 299.5

mbsf. The smoothed Mg/Ca$_O$ data remain at around 1.8 mmol mol$^{-1}$ after that point, though the data fluctuate quickly between 1.7 and 2.2 mmol mol$^{-1}$. At 297.5 the smoothed Mg/Ca$_O$ record shows a slight dip to around 1.7 mmol mol$^{-1}$ and then a steady increase to ~1.9 mmol mol$^{-1}$ at ~296 mbsf. At that point, Mg/Ca$_O$ decreases to 1.6 mmol mol$^{-1}$ before recovering back to around 2.5 mmol mol$^{-1}$. A similar sudden change is also seen in Mg/Ca$_M$. From around 295.5 mbsf, Mg/Ca$_O$ fluctuates between 1.6 and 2 mmol mol$^{-1}$. Mg/Ca$_O$ has no frequencies significant above the 95% confidence interval that could be within orbital frequency ranges (Figure 34k & l).

### *4.3.5 Li/Ca*

Li/Ca in *G. trilobus* (Li/Ca$_G$) in the lower interval (Figure 35b) begins at around 13 μmol mol$^{-1}$, however it very quickly drops to a minima of 11.5 μmol mol$^{-1}$. The variability is lower in the benthic records, Li/Ca in *C. mundulus* (Li/Ca$_M$) and *O. umbonatus* (Li/Ca$_O$), detailed later, and the whole record shows a mean of 12.79 μmol mol$^{-1}$ and 2σ of 1.03 μmol mol$^{-1}$. The five-point moving average for the record begins with a steady increase from ~12 μmol mol$^{-1}$ to ~13 μmol mol$^{-1}$. This trend reverses over the next 1m and then there is the suggestion of a two-step increase from ~12 μmol mol$^{-1}$ to ~13.5 μmol mol$^{-1}$ from 310 mbsf to 309 mbsf. From ~309 to ~307.7 mbsf, Li/Ca$_G$ decreases from 13.5 μmol mol$^{-1}$ to ~12.5 μmol mol$^{-1}$, though again there is a hint that the decrease takes a stepped form. From there until 306 mbsf, Li/Ca$_G$ shows a general increase to ~13.5 μmol mol$^{-1}$, though it undergoes an interval of about 50cm in which it varies by ~0.6 μmol mol$^{-1}$.

The upper interval (Figure 35a) shows a general decrease from around 300.1 mbsf to 295.5 mbsf of ~1.75 μmol mol$^{-1}$. This takes the form of two steps, the first of which shows a decrease from 13.5 μmol mol$^{-1}$ to 12.2 μmol mol$^{-1}$ over ~1.1m. After this there is a slight rebound of ~0.5 μmol mol$^{-1}$ to 12.7 μmol mol$^{-1}$. At ~296.25 mbsf the second step begins and there is another decrease of ~1.1

μmol mol$^{-1}$ to ~11.6 μmol mol$^{-1}$ at 295.5 mbsf. At this point there is another increase and Li/Ca$_G$ settles around an average of 12.6 μmol mol$^{-1}$.

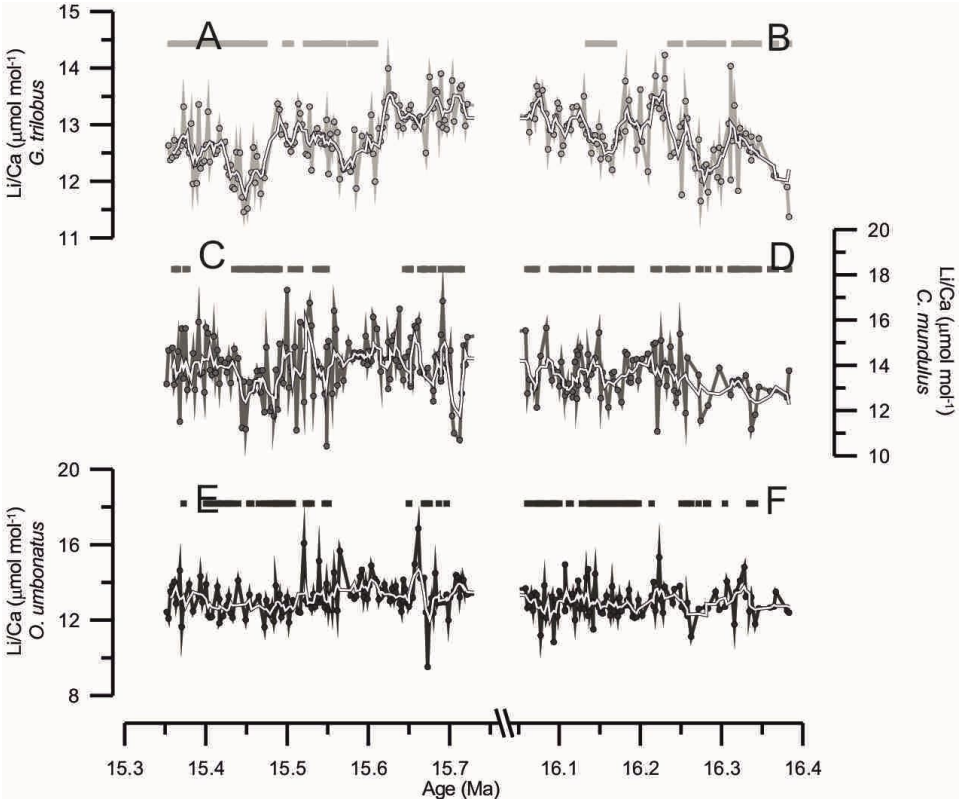


**Figure 35 – Li/Ca in three foraminiferal species from ODP Site 926. Li/Ca has an inverse relationship with temperature so the y-axies have been reversed to show higher temperatures at the top. A & B) show Li/Ca in *G. trilobus* in the upper and lower intervals, respectively. C & D) Li/Ca in *C. mundulus* in the upper and lower intervals. E & F) Li/Ca in *O. umbonatus* in the upper and lower intervals. The bars above each graph highlight regions where the symmetrical 4-point moving average (thick white line) is below the mean Li/Ca value for each record as a whole. This is to highlight regions where the Li/Ca suggests that the climate was warmer than the mean for the whole record.**

Li/Ca$_M$ is far noisier and far more variable than Li/Ca$_G$ or Li/Ca$_O$, and as a result it is difficult to see any definite trends or changes. The mean of the record is 13.82 μmol mol$^{-1}$, with a 2σ of 3.64 μmol mol$^{-1}$. The lower interval (Figure 35d) seems to show a general increase in Li/Ca$_M$ from ~12 μmol mol$^{-1}$ to ~14 μmol mol$^{-1}$. There are fluctuations in the moving average of this trend of ~1m in duration and <1 μmol mol$^{-1}$ in amplitude, but noise within the actual data makes it difficult to determine if they are real. The upper interval (Figure 35c) is not much better, though it appears to show a general increase of ~2 μmol mol$^{-1}$ followed by a decrease of approximately the same value. This is followed by a return to around 14 μmol mol$^{-1}$.

The mean value for the Li/Ca$_O$ record (Figure 35) is 13.95 μmol mol$^{-1}$ and 2σ is 27.82 μmol mol$^{-1}$. The values given here on in all refer to the five point moving average. From 312.4 mbsf to 311 mbsf Li/Ca$_O$ is around 12 - 12.5 μmol mol$^{-1}$. At 311mbsf Li/Ca$_O$ increases by 1.5 to 14 μmol mol$^{-1}$ over ~16cm. From 310.5 to 309 mbsf Li/Ca$_O$ decreases to around 12 μmol mol$^{-1}$ and then increases to 13.6 μmol mol$^{-1}$. Over ~60cm Li/Ca$_O$ increases to ~13 μmol mol$^{-1}$, where it remains until 306 mbsf. From 300 mbsf to 299 mbsf varies between 9.5 to 17 μmol mol$^{-1}$. The rest of the upper interval varies between 12.2 and 14.3 μmol mol$^{-1}$.

## 4.4 Discussion

### *4.4.1 Diagenesis*

Diagenetic effects may affect the geochemistry of foraminiferal carbonates, with some proxies and species being more sensitive to post-depositional changes than others (e.g., Edgar et al., 2013; Pearson et al., 2007; Sexton et al., 2006). In some situations paired Mg/Ca and Sr/Ca ratios can be a useful check for recrystallization processes as this tends to result in increased Mg/Ca and decreased Sr/Ca (Baker et al., 1982). However, Mg/Ca and Sr/Ca records also reflect different environmental parameters, which may co-vary through time. Mg/Ca and Sr/Ca in C. mundulus (Figure 36a & b) and in O. umbonatus (Figure 36c & d) do not covary, which suggests that Mg/Ca in the benthic species has not been altered by diagenesis.

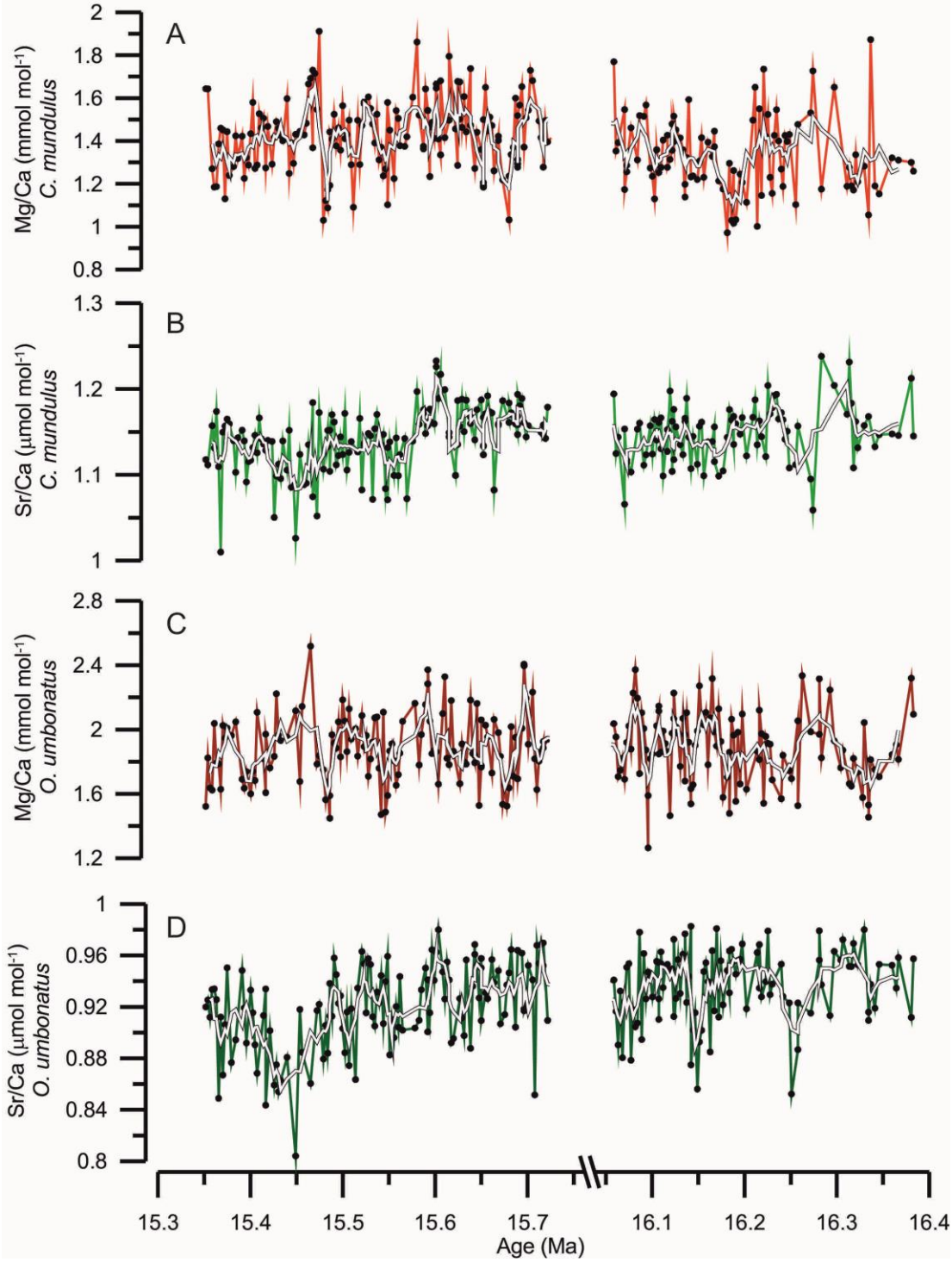


**Figure 36– Benthic foraminiferal Mg/Ca and Sr/Ca. A) Mg/Ca in *C. mundulus*. B) Sr/Ca in *C. mundulus*. C) Mg/Ca in *O. umbonatus*. D) Sr/Ca in *O. umbonatus***

Large changes seen in $Mg/Ca_M$ and $Mg/Ca_O$ are also seen in $Mg/Ca_G$, however $Mg/Ca_G$ does appear to very in opposition to Sr/Ca (Figure 37a & b). This may suggest that the $Mg/Ca_G$-derived temperatures are unreliable, however Sr/Ca from *G. trilobus* also bears a marked similarity to the B/Ca record

(chapter 5). As pH may have an effect on planktonic foraminiferal Sr/Ca (Lea et al., 1999; Russell et al., 2004), this likely indicates a decrease in pH (increase in $[H^+]$) associated with surface ocean warming rather than a diagenetic signal. In this thesis I therefore interpret the trace metal records primarily in terms of original test geochemistry. It is likely that the $\delta^{18}O$ of the planktonic foraminifera record will be biased to colder temperatures and contain a muted signal, but I assume the first order variations are preserved (Pearson et al., 2001). It is thought that benthic foraminiferal $\delta^{18}O$ is relatively robust to post-depositional diagenetic processes (Edgar et al., 2013).

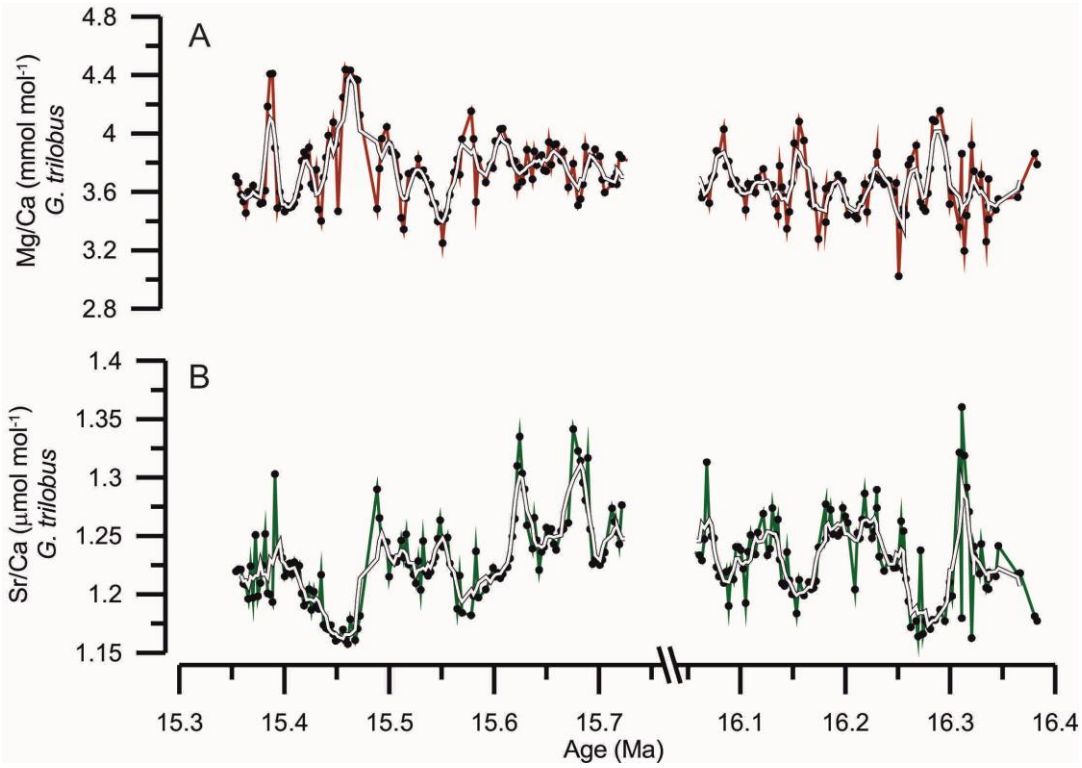


**Figure 37 - Planktonic foraminiferal Mg/Ca and Sr/Ca compared. A) Mg/Ca in *G. trilobus*. B) Sr/Ca in *G. trilobus*.**

### *4.4.2 Temperature changes, Ice Volume, and Salinity*

#### *4.4.2.1 Deep ocean temperature*

Ten intervals of distinct bottom water temperature (BWT) changes have been picked out of the record, and have been highlighted in Figure 38. BWT change 1 (T1) occurs from 16.32-16.27 Ma. Based on the smoothed data it is associated

with an increase in temperature of ~2°C. The BWT immediately begins to decrease into T2 (16.27 – 16.25 Ma), which is associated with a 2°C decrease. There is then a period of ~40ka of relatively stable BWT of ~6°C before T3 (16.21-16.18 Ma). T3 shows a general decrease of 2°C, though the temperature trend is over 30ka, as opposed to the <20ka of T2. The BWT again recovers during T4 (16.18-16.16 Ma) with another 2°C warming. T5 (16.10-16.07 Ma) appears to show between a 1.5 and 2°C pulse of slightly warmer BWT over the comparatively brief interval of 20-30ka.

T6 (15.70-15.67 Ma) shows a cooling of ~2.5-3°C, though this partially recovers in T7 (15.67-15.65 Ma) with a warming of ~2°C. There is then a period of ~80ka of relatively stable temperatures between ~6 and 7°C before T8 (15.57 – 15.53 Ma) shows another 2°C cooling. T9 (15.48 – 15.45 Ma) shows the most extreme BWT change in the record; the overall warming across T9 is ~2°C, in line with the other BWT changes, however T9 begins with a rapid (<20ka) drop of ~2°C followed by another rapid (~30ka) increase of ~4°C. This is immediately followed by T10 (15.45 – 15.43 Ma) in which BWT recovers to the levels it was at prior to T9 (~6°C).

The average magnitude of BWT changes in this record (in either direction) is ~2.4 °C, and occurs over ~30ka. This gives an average rate of change of ~0.08°C $ka^{-1}$, which is much slower than modern rates of change of BWT of ~0.03°C $decade^{-1}$, or 3°C $ka^{-1}$ (IPCC, 2013). This study is of far greater duration and far lower resolution than any modern study could reasonably expect to be, however, and it is impossible for this study to capture anything on a decadal timescale. Comparison to other palaeoclimate records of BWT changes of similar magnitude to those seen here, the warming at the end of Mi-1 was approximately 1.5°C over 100ka (0.015°C, $ka^{-1}$; Mawbey and Lear, 2013) and the warming associated with the PETM was approximately 4-5°C over <10ka (~0.4-0.5°C $ka^{-1}$; Kennett and Stott, 1991; Tripati and Elderfield, 2005). BWT changes in this record are of comparable magnitude, duration, and frequency to those

obtained from benthic foraminiferal Mg/Ca from Chatham Rise during the last 440kyr (Elderfield et al., 2010).

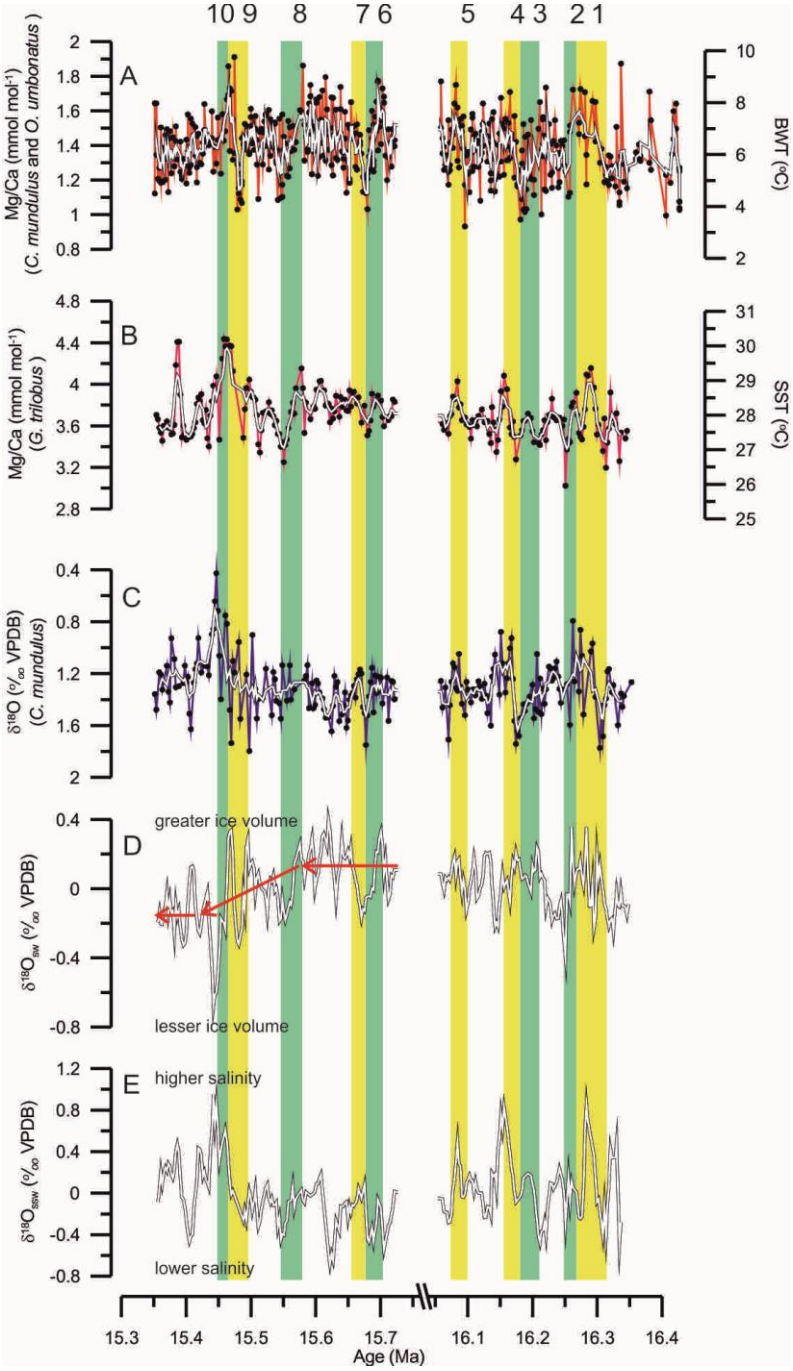


**Figure 38 – Changes in the primary temperature proxies across the studied intervals. Increases in temperature are highlighted in yellow, decreases highlighted in green and both have been numbered 1-10 for ease of reference in the text. A) Mg/Ca$_{M+O}$ and BWT. B) Mg/Ca$_G$ and SST. C) $\delta^{18}O_M$. D) $\delta^{18}O_{sw}$ E) $\delta^{18}O_{ssw}$. In A, Mg/Ca$_O$ has been corrected to be equivalent to Mg/Ca$_M$ by applying a correction factor of x0.74, calculated by comparing the means of both records. The temperature scale shown on D is calculated using the *Cibicidoides spp.* equation of Lear et al. (2002), and a value of H of 0.44 (Evans and Müller, 2012). The temperature scale on B is calculated using the *G. sacculifer* calibration of Dekens et al. (2002) and a value of H of 0.41 (Evans and Müller, 2012).**

#### 4.4.2.1.1 Statistical analysis of relationships in Figure 38

##### *4.4.2.1.1.1 Mg/Ca and $\delta^{18}O$*

The temperature changes identified in Figure 38 (highlighted regions 1-10) that have been used for discussion have been further analysed to examine their veracity. Figure 39c shows the gradient of the Mg/Ca record over a 5-point moving window. Where a warming is identified, the gradient should be positive, and where a cooling has been identified the gradient should be negative. The range of gradients thus examined is -0.21 – 0.30, suggesting that there are no changes greater than ~0.30 mmol $mol^{-1}$ $Ma^{-1}$. As it stands, there appears to be no strong correlation between a positive gradient and an identified warming interval and a negative gradient and an identified cooling interval.

Additionally, Figure 39d shows the Pearson's Rank coefficient for correlation between $\delta^{18}O$ and Mg/Ca. If both $\delta^{18}O$ and Mg/Ca are reflecting changes in temperature, we would expect some degree of consistent anticorrelation (-ve numbers). The range of Pearson's Rank coefficients is between 1 and -1, with a mean value of ~-0.11, suggesting that there is, on average, a slight anticorrelation between them but it is not consistent. The mean Pearson's value for the upper interval is ~-0.08 and ~-0.15 for the lower interval, but nothing stands out as showing a particularly or consistently strong correlation or anticorrelation. Both intervals in general still show a slight anticorrelation between $\delta^{18}O$ and Mg/Ca. In the absence of other information, it may be better to assume that Mg/Ca is being affected more by $\Delta[CO_3^{2-}]$ than by temperature. Estimates of changes in Sr/Ca and B/Ca in 5.4.1.2 suggest that $\Delta[CO_3^{2-}]$ was changing across the interval, and though the magnitude of the changes shown by the two proxies is not agreed upon, the timings of the changes are.

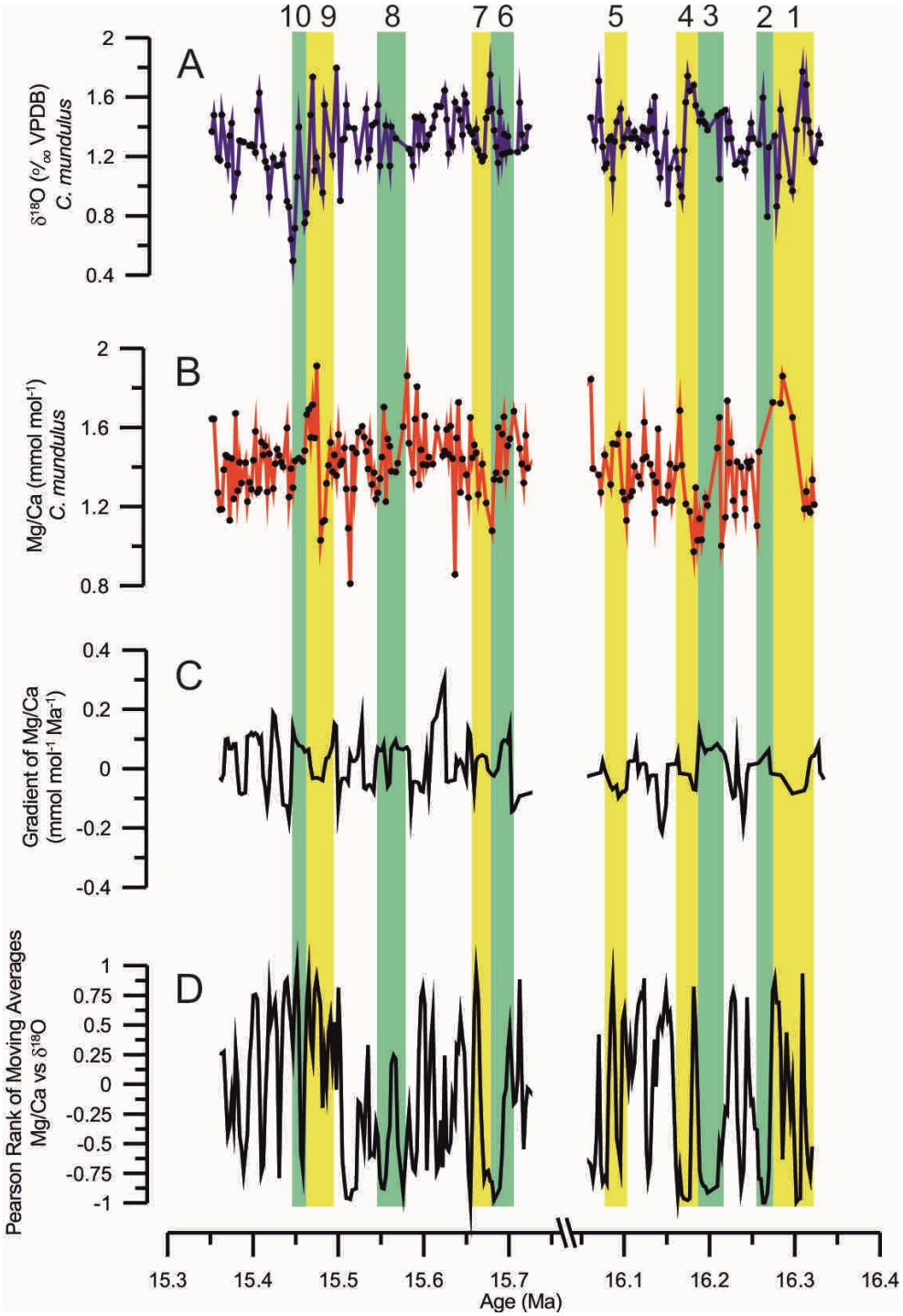


**Figure 39 – Statistical analysis of relationships between Mg/Ca and $\delta^{18}O$. A) $\delta^{18}O$ from *C. mundulus*. B) Mg/Ca from *C. mundulus*. C) Gradient of changes in Mg/Ca in mmol $mol^{-1}$ $Ma^{-1}$. 5-point moving window. D) Pearson's Rank correlation coefficient of Mg/Ca with $\delta^{18}O$. 1 is 1:1 positive correlation, -1 is a 1:1 anticorrelation. 5-point moving window of same-age pairs.**

*4.4.2.1.1.2 Ice Volume and Salinity*

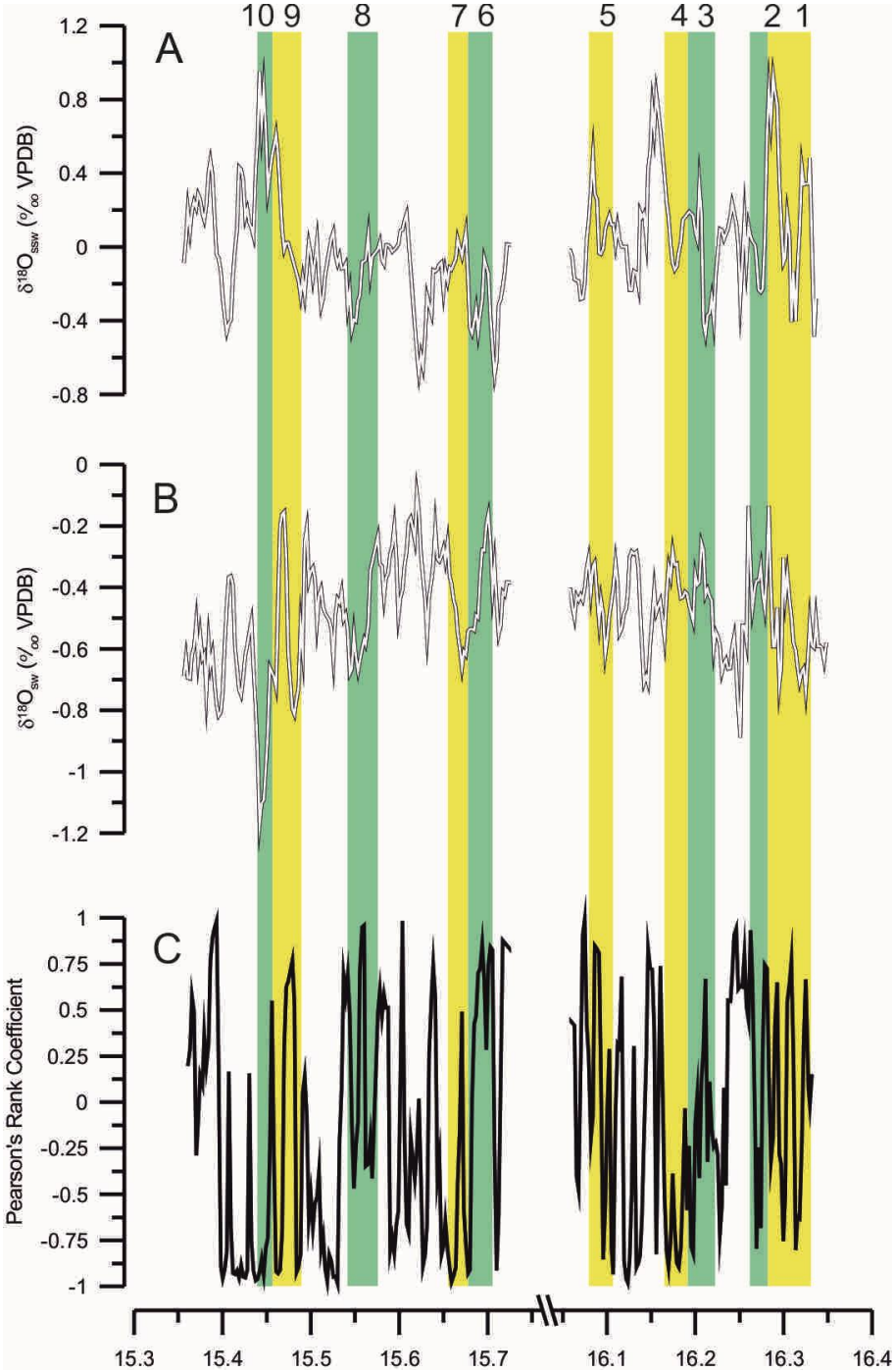


**Figure 40 – Examination of $\delta^{18}O_{sw}$ and $\delta^{18}O_{ssw}$. A) $\delta^{18}O_{sw}$. B) $\delta^{18}O_{ssw}$. Pearson's Rank Coefficient of $\delta^{18}O_{sw}$ and $\delta^{18}O_{ssw}$.**

Figure 40 shows the correlation between $\delta^{18}O_{sw}$ and $\delta^{18}O_{ssw}$ used to infer movement of the ITCZ. The mean Pearson's Rank coefficient is -0.13, and there appears to be good anticorrelation between $\delta^{18}O_{sw}$ and $\delta^{18}O_{ssw}$ around intervals 4 and 10. This suggests that there may be some veracity to the idea that $\delta^{18}O_{sw}$

and $\delta^{18}O_{ssw}$ are reflecting movements of the ITCZ at these intervals, but it is not clear.

#### *4.4.2.2 Sea Surface Temperature*

Large changes in sea surface temperature (SST, Figure 38b) do not occur as frequently as BWT, though the changes appear from the data to be smoother. T1 in BWT (Figure 38b) occurs coevally with an increase in SST of ~2.5-3°C, however the increase ceases at ~16.3 Ma before the end of T1 and begins a gradual decline of approximately the same size that ends at T2. This decline is punctuated by a slight rebound of ~0.5°C at the end of T2, though given the analytical uncertainty of Mg/Ca measurements amounts to ~ ±1°C, this is not particularly significant. Between T2 and T4 $Mg/Ca_G$ varies by ~0.5°C and the next large change is at T5, which is a transient warming of ~3°C, coeval with same warming in BWT (Figure 38a).

The next major temperature change evident in $Mg/Ca_G$ is a ~2.5-3°C cooling at T8, coeval with the same cooling in BWT. SST declines from ~29.5°C to 26.5°C over the duration of T8, though contrarily to BWT which then appears to experience a period of relative stasis between T8 and T9, SST appears to undergo a gradual increase to ~30°C by the end of T9. This trend is superimposed upon by 2 small fluctuations of ~1°C or so, though the raw data suggests that the rapid warming in T9 in SST is coeval with BWT, however the resolution of the SST drops a little at this point due to *G. trilobus*' absence from those samples, so the timing and magnitude of the minimum values at the start of T9 are uncertain. Nonetheless, the warming associated with T9 is also a transient one and the cooling of SST occurs with the same cooling in BWT of T10, albeit more gradually: the cooling associated with T10 ends around 15.42 Ma in SST rather than 15.43 in BWT.

*4.4.2.3 Ice volume*

Bottom water $\delta^{18}O$ ($\delta^{18}O_{sw}$) across this interval changes rapidly even in the smoothed record (Figure 38d), with the largest change being a decrease of ~1.2 ‰ in T9 & 10 (Figure 38d). This massive change appears to imply a rapid rise in sea level of between 100 and 120m, assuming a 10m change in eustatic sea level is equivalent to ~0.1 ‰ change in $\delta^{18}O$ (Fairbanks and Matthews, 1978; Miller et al., 2009; Pekar et al., 2002). This is in line with the largest estimates of sea level change during the Eocene-Oligocene climate transition (e.g., Coxall et al., 2005; Katz et al., 2008; Lear et al., 2008). The change across T9 & 10, however is much smaller. Ignoring the largest swings, which likely result from fliers in the raw Mg/Ca data, the mean change $\delta^{18}O_{sw}$ from the start of I8 to the end of I10 is ~0.3 ‰ (Figure 38c). This means the total sea level change is more likely to be a decrease of ~20 - 40m (Figure 41). This estimate was made using the $\delta^{18}O$ – sea level calibrations of Pekar et al. (2002), which estimates a mean sensitivity of ~0.34 ± 0.14‰ $10m^{-1}$. Error bars in Figure 41 reflect the uncertainty of ± 0.14‰ $10m^{-1}$ in that estimate. This is more consistent with previous estimates of sea level change during the MMCO (Pekar and DeConto, 2006). The $\delta^{18}O_{sw}$ becomes far more variable across the entirety of the shift; taking T8 (15.57-15.53 Ma) as the beginning of the trend towards reduced $\delta^{18}O_{sw}$ (and thus ice volume) this change in $\delta^{18}O_{sw}$ from +0.45 ‰ to +0.15 ‰ relative to the mean (‰ rttm) is "only" a change of -0.3 ‰. The next shift to higher values increases to +0.31‰ rttm by 15.58 Ma, and the next drop is down to -0.04 ‰ rttm by 15.55Ma: a change of -0.35 ‰. $\delta^{18}O_{sw}$ rebounds to ~+0.28 ‰ rttm by 15.53 Ma but there is a transient drop back to -0.08 ‰ rttm before it recovers by 15.50 Ma. At 15.50 Ma there is the first of two dramatic decreases in $\delta^{18}O_{sw}$: the first is to -0.36 ‰ rttm by 15.48 Ma (a change of -0.66 ‰), there is a recovery to +0.48 ‰ before the second dramatic drop to -0.60 ‰ rttm by 15.44 Ma. $\delta^{18}O_{sw}$ recovers to a new mean of around -0.14 ‰ rttm and the oscillations appear to begin to reduce in

size. This behaviour is also seen in the raw (uncorrected for temperature changes) $\delta^{18}O_M$ record (Figure 38c).

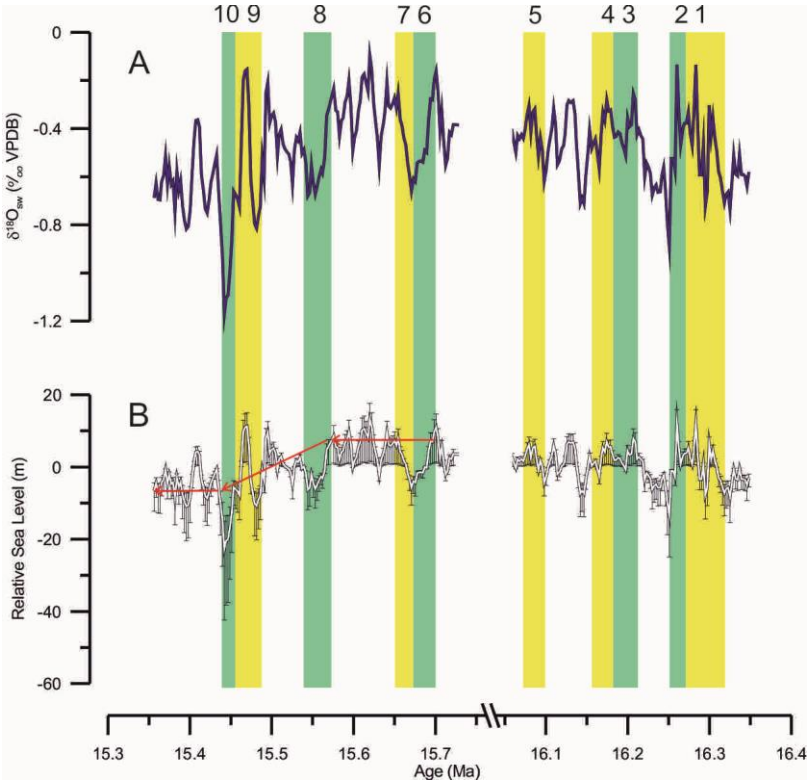


**Figure 41 – Changes in $\delta^{18}O_{sw}$ (A) and relative sea level (B). Sea level estimates are made using the methods of Pekar and DeConto (2006) and references therein.**

This pattern of increasing size of oscillations of ice sheets leading up to a more permanent new equilibrium state has been reflected in modelling studies of ice sheet behaviour (Calov and Ganopolski, 2005; DeConto and Pollard, 2003; Ganopolski et al., 2010; Zachos and Kump, 2005). This oscillatory behaviour is caused by rapid transitions in the forcing mechanisms (Zachos and Kump, 2005), and dampened by ice sheet hysteresis effects such as height mass balance feedback and albedo (Pollard et al., 2013). It is interesting to note that when Pollard et al. (2013) modelled this behaviour in an ice sheet growing in response to decreasing $CO_2$, their model run that assumed weathering was proportional to $CO_2$ (Donnadieu et al., 2006) did not display these oscillations. Their model run that assumed a nonlinearity between $CO_2$ consumption due weathering and atmospheric $pCO_2$ (Godderis et al., 2008) did show this behaviour, however.

This was primarily due to their modelled atmospheric $CO_2$ passing through the 0.5-1.5x pre-industrial level $pCO_2^{ATM}$ portion of Godderis et al. (2008)'s $CO_2$ weathering model in which $CO_2$ consumption *increases* with decreasing $pCO_2^{ATM}$. Taking pre-industrial $CO_2$ as 280ppmv, the modern (and MMCO) level of ~400ppmv falls just inside of that range. It is well worth noting that the models cited herein have focussed on Antarctic glaciations, whereas I have discussed what appears to be a deglaciation. As hysteresis plays a major role in the growth and decay of ice sheets (DeConto and Pollard, 2003; Oerlemans, 2002; Pollard and DeConto, 2005) it does not follow necessarily that their modelled findings hold true here.

#### *4.4.2.4 Sea Surface Salinity*

Sea surface salinity (SSS) can be taken as an indication of the difference between precipitation and evaporation (E-P) at a given location in the ocean, though it is also affected by the source waters, amount of ice melt (if proximal to an ice sheet), upwelling, and the amount of continental runoff. SSS responds primarily to E-P, rather than either evaporation (E) or precipitation (P) on their own (Bingham et al., 2010, 2012; Yu, 2011). Given this, changes in SSS in the open ocean can be used to infer changes in E-P, with increased (decreased) salinities suggesting positive (negative) values of E-P and favouring E (P) at the sample site. This does not hold true at sites with significant freshwater input from either melting ice sheets or riverine outflow. Given Ceara Rise's proximity to the modern equator, and given that it has not strayed more than $10^o$ away from it in the past 34 million years (estimate, based on calculations from www.serg.uncam.it), changes in SSS most likely reflect shifts in the position of the ITCZ (Arbuszewski et al., 2013). Evidence of upwelling from $\delta^{13}C$ that coincide with changes in SSS would be an indication of this.

Ceara Rise currently sits at the southern edge of the modern ITCZ in the Atlantic Ocean, so its position will make it very sensitive to changes in the

ITCZ's position (Figure 29). The position of the MMCO ITCZ relative to the Amazon-basin was sufficiently similar to today's to show similar magnitude changes in seasonal variability (Kaandorp et al., 2005), and so we can assume that the position of the ITCZ relative to Ceara Rise is also fairly similar to today's. The position of the ITCZ is nonetheless highly dynamic on geological timescales, and has been inferred to have been shifting steadily southwards, in the Western Pacific at least, for the past 27 Ma (Armstrong and Allen, 2011; Kim et al., 2006). The position of the ITCZ favours the warmer hemisphere (Chiang et al., 2003; Chiang and Bitz, 2005; Xie and Philander, 1994). Increases in ice volume in one hemisphere push the ITCZ towards the opposite hemisphere, so with all else being equal the result of northern hemisphere ice expansion would be a southerly movement of the ITCZ, as observed during glacial stages of the Pleistocene (Chang et al., 2012; Sepulcre et al., 2011; Ziegler et al., 2008).

Given Ceara Rise's position relative to the modern and paleo-ITCZ (Figure 42), it seems reasonable to assume changes in sea surface salinity are dominated by changes in the position of the ITCZ. This assumption has also been made by Arbuszewski et al. (2013), during the last glacial maximum in the Equatorial Atlantic; Holbourn et al. (2010), during the Middle Miocene, Western Equatorial Pacific; and Schmidt and Spero (2011), Caribbean and Western Equatorial Pacific during the past 350 ka. An increase in salinity can be assumed to be related to a northward movement of the ITCZ and a decrease in salinity can be assumed to be caused by a southward movement of the ITCZ. A change in SSS of 1 psu effect a change in $\delta^{18}O_{ssw}$ in the modern equatorial Atlantic of ~0.5‰ (Weldeab et al., 2006b). Changes in $\delta^{18}O_{ssw}$ of ~1.2‰ seen here would therefore equate to changes of surface salinity on the order of 2psu. SSS generally increases with decreasing latitude, however SSS declines from ~30° to the equator from ~36 psu to ~34 psu (Levitus, 1982). This decline in salinity is caused by upwelling and increased precipitation associated with the ITCZ, and

so at least part of the changes in $\delta^{18}O_{ssw}$ here can be assumed to be due to changes in SSS due to movement of the ITCZ.

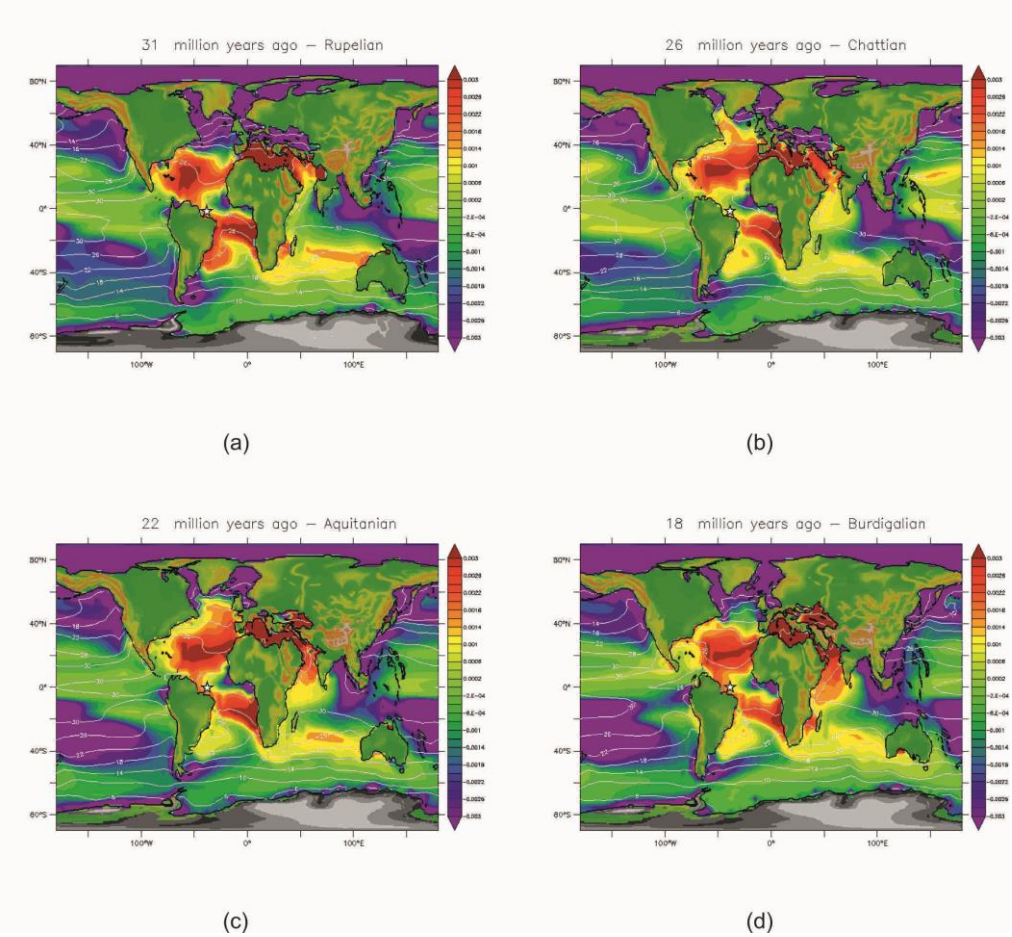


**Figure 42 – Annual modelled SSS during the Oligocene (a & b) and Early Miocene (c & d), after Lunt (D. Lunt, personal communication, 2014). Units are in (psu-35)/1000. The approximate position of Ceara Rise is shown on each figure with a white star. Ceara Rise sits very close to the southern boundary of the Atlantic ITCZ, making it very sensitive to changes in SSS**

Trends towards lighter values of $\delta^{18}O_{sw}$ occur coevally with trends towards heavier values of $\delta^{18}O_{ssw}$, and the inverse is also true (Figure 38a and b). This anti-correlation is also observed in the raw $\delta^{18}O$ records (Figure 43), demonstrating that this relationship is not an artefact caused by erroneous Mg/Ca-temperatures. This indicates that sea surface freshening occurs with increases in global ice volume, which is consistent with changes in ice volume centred on the Northern Hemisphere. Modelling of the MMCO by Herold et al. (2012) suggests that there was more sea ice in the North Atlantic during the MMCO than in the modern, though far less in the Arctic ocean proper, so

northern hemisphere glaciation at this time is possible, though the authors do note that they think the amount of sea ice they find is excessive.

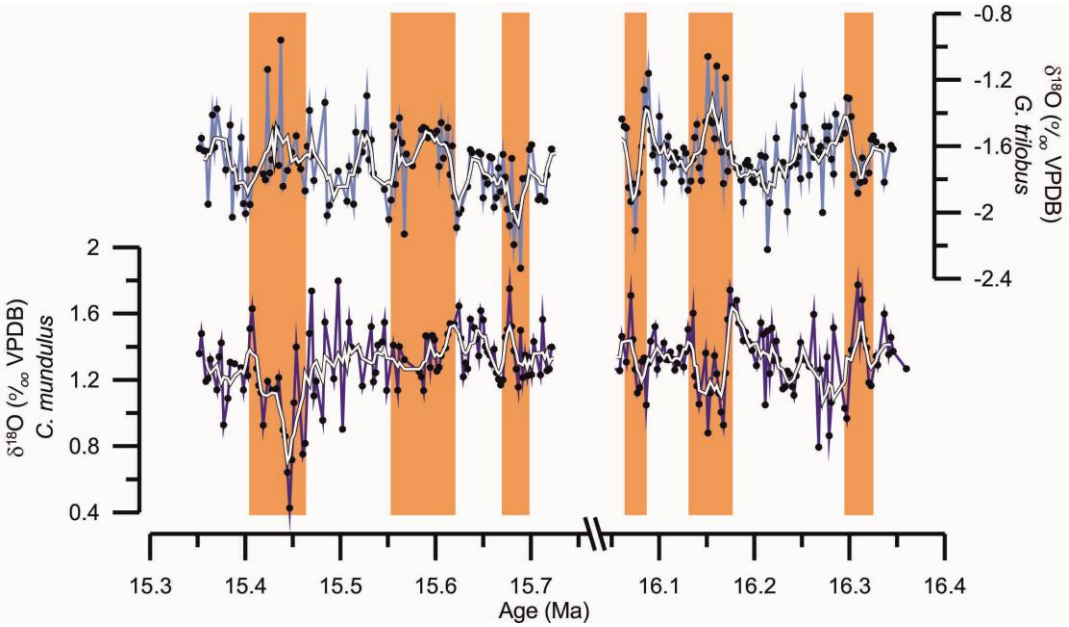


**Figure 43 – planktonic ($\delta^{18}O$ from *G. trilobus*, upper graph) and benthic ($\delta^{18}O$ from *C. mundulus*, lower graph) $\delta^{18}O$ compared. Highlighted regions show where planktonic $\delta^{18}O$ trends towards heavier values while benthic $\delta^{18}O$ trends towards lighter values (and *vice versa*)**

$\delta^{18}O_{ssw}$ varies quite dramatically in comparison to $\delta^{18}O_{sw}$ (Figure 38d), with regular shifts of ~1.2 ‰ in both the positive and negative direction. In the lower interval there are two periods of increased $\delta^{18}O_{ssw}$, which may be interpreted as increased SSS; one associated with T1 (0.8 ‰ rttm), and one associated with T4 (0.8 ‰ rttm). There are also minima at the start of T1 and at the start of T3 (both ~-0.4 ‰ rttm). The upper interval shows one interval of increased salinity associated with the end of T10 (0.8‰ rttm) as well as a minima in between T7 and T8 (-0.8 ‰ rttm). The shift in $\delta^{18}O_{ssw}$ associated with the largest changes in $\delta^{18}O_{sw}$ is that that occurs across T9-10. This implied increase in salinity also occurs coevally with a trend towards lighter $\delta^{13}C$ (Figure 44b), an increase in the lightness of the sediment (Figure 44c) and a minimum in benthic foraminiferal accumulation rate (a productivity proxy, Figure 44d). All of this points towards a reduction in productivity in the waters above Ceara Rise, which would imply a northern movement of the ITCZ. If the ITCZ is moving north in response to the drop in global ice volume implied by $\delta^{18}O_{sw}$ (Figure 38c), then some

component of the ice volume decrease may have occurred in the Northern Hemisphere: the position of the ITCZ favours the warmer hemisphere (Chiang et al., 2003; Chiang and Bitz, 2005; Xie and Philander, 1994), and changes in ice volume in either hemisphere are associated with which ever hemisphere experiencing the majority of the warming (Justino et al., 2014; Shakun and Carlson, 2010).

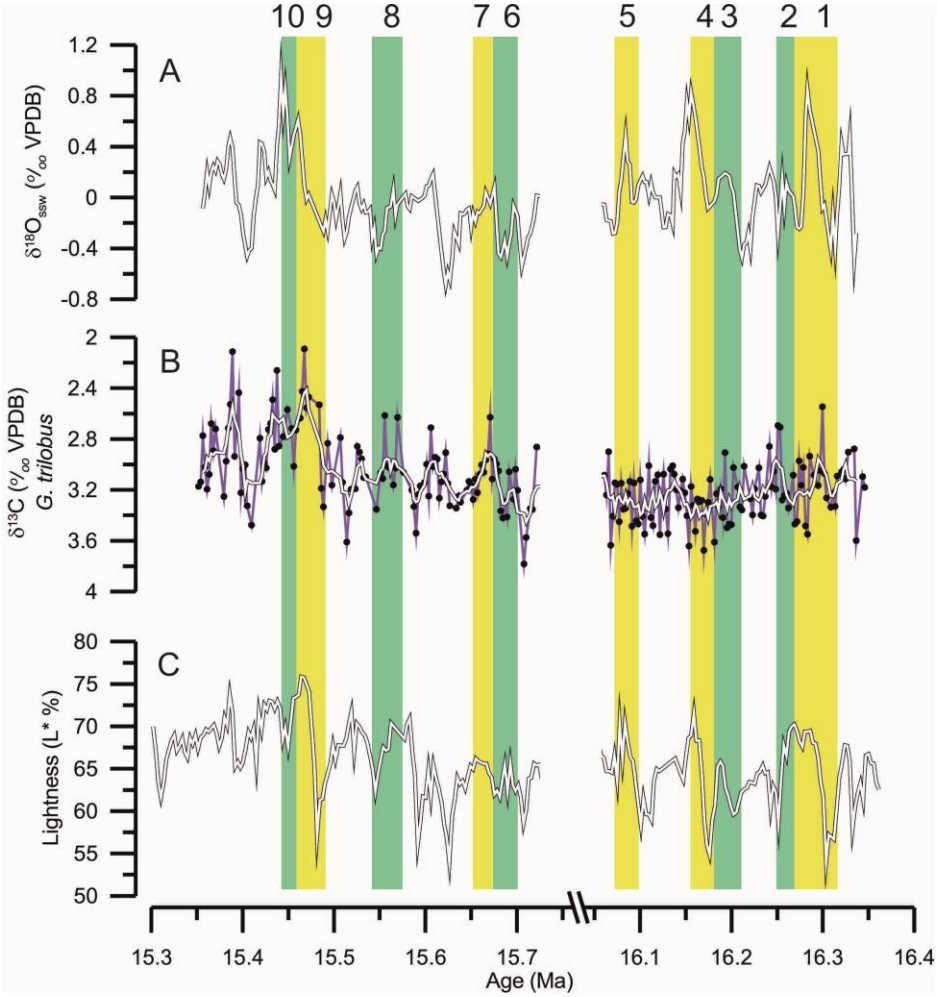


**Figure 44 - changes in productivity and surface salinity. A) $\delta^{18}O_{ssw}$, calculated by subtracting changes in $\delta^{18}O_{sw}$ (*C. mundulus*) from $\delta^{18}O_{sw}$ (*G. trilobus*). B) $\delta^{13}C_G$ C) L* reflectance, lightness of the sediment, related to clay content in site 926. Intervals are highlighted as in Figure 38.**

The presence of ice sheets in the northern hemisphere during the MMCO is potentially a contentious issue. There is evidence for maxima in ice-rafted debris in the Arctic Ocean at Lomonosov Ridge at ~18Ma and 14Ma, with a much smaller peak at ~16Ma that suggests that northern hemisphere ice-sheets were waxing and waning around this time (St John, 2008). Hyeong et al. (2014)

infer Northern Hemisphere Glaciation at the OMB by tracking the position of the ITCZ using the source of aeolian dust. In addition, the $pCO_2^{ATM}$ threshold for the initiation of Northern Hemisphere glaciation was estimated to be between 200 and 300ppmv by DeConto et al. (2008), which according to some estimates of $CO_2^{ATM}$ (Kürschner and Kvaček, 2009; Zhang et al., 2013) may have been reached at around 20Ma. Such thresholds are highly model dependant and changes in boundary conditions (such as topography or orbital configuration), or even fundamental but otherwise poorly defined constants (such as the lapse rate of ice), can lead to large changes in the threshold conditions for ice formation (Gasson et al., 2014). It is also prudent to point out that in the case of the stomatal index record by Kürschner and Kvaček (2009) 300ppmv is the minimum estimate of $pCO_2^{ATM}$ within the error of their stomatal index record, and for both records referenced above, 300 ppmv by 20 Ma is based on one data point. None the less, this may provide some evidence that the Mid-Miocene Climatic Optimum is worth much more extensive study as an analogue to the consequences of the modern $pCO_2^{ATM}$. The presence of even small ice-sheets in the northern hemisphere may mean that the Miocene was more like today than previously thought.

Greenop et al. (2014) cross-plot $pCO_2^{ATM}$ and $\delta^{18}O_{sw}$ for their records, a technique avoided in this thesis due to the small size of the $pCO_2^{ATM}$ record available. They identify two ice reservoirs during the MMCO, one highly dynamic and another more stable one and hypothesise that the more dynamic of the two represents the West Antarctic Ice Sheet (WAIS), and the more stable one the East Antarctic Ice Sheet (EAIS). If the ITCZ movements hypothesised here are correct, it may be the case that the more dynamic ice sheet was in the northern hemisphere. This does not exclude the possibility of the presence of the WAIS.

One possible alternative to Northern Hemisphere deglaciation causing a northward shift in the position of the ITCZ could be a Southern-Hemisphere-

only deglaciation associated with an increase in the transport of heat to the Northern Hemisphere. The position of the ITCZ is primarily controlled by the rate of cross-equatorial energy transport, in essence the difference in temperature between hemispheres (Bischoff and Schneider, 2014). Modelling of the MMCT suggests that one of the responses to glaciation was a warming of the surface waters of the southern ocean, primarily due to changes in the wind field in response to ice sheet growth bringing warmer waters towards the south pole (Knorr and Lohmann, 2014). It seems conceivable, therefore, that the reverse could also be true and a deglaciation of the southern hemisphere could result in its cooling and commensurate northward movement of the ITCZ. This is at odds, however, with geochemical data from both $\delta^{18}O$ (Majewski and Bohaty, 2010; Verducci et al., 2007) and Mg/Ca (Shevenell et al., 2004) that suggest the surface waters of the Southern Ocean cooled in response to the glaciation of the MMCT.

## 4.5 Conclusions

Bottom and surface water temperatures during the middle Miocene climatic optimum varied by around 3°C. Absolute temperature estimates from Mg/Ca are consistent with modelling estimates of palaeotemperatures.

Ice volume was dynamic during the MCO, with changes of around 20-40m of apparent eustatic sea level. Coeval with changes in sea level are SSS and productivity changes that can be tied to movement of the ITCZ relative to Ceara Rise. The ITCZ moved northwards during deglaciations, implying that changes in ice volume were focussed on the Northern Hemisphere. An alternative low-latitude explanation for the northward shift of the ITCZ could involve long-term changes in ENSO. However, while there may be a link between ENSO and Antarctic temperatures, there is no clear mechanism to explain a northward shift of the ITCZ in association with expansion of the Antarctic ice sheet. Therefore, the favoured explanation here is that Northern Hemisphere ice

sheets may have been present and responding to climatic changes across the MMCO. The location of Earth's continental ice sheets is crucial information in understanding Earth System Sensitivity, and the presence of Northern Hemisphere ice may significantly impact apparent climate variability recorded in marine oxygen isotope records. Clearly, further studies exploring the possibility of Neogene Northern Hemisphere Glaciation are required.

### *4.5.1 Future work*

Future work, as ever, needs to focus on improving calibrations and hence quantification of past temperatures and ice volume. Empirically-derived and at least genera-specific $Mg/Ca_{foram}$ versus $Mg/Ca_{sw}$ calibrations to determine H for different foraminifera would drastically improve estimates of absolute temperature, and may help to reduce the problem many models are having of reproducing proxy-derived temperatures.

In addition, a transect across the equatorial Atlantic targeting 14-18 Ma sediments to determine the relative timings of changes in sea surface salinity would help to constrain ITCZ movements during the MMCO. This would help to provide indirect evidence for changes in northern hemisphere glaciation at this time. More direct evidence would come from an interhemispheric comparison of records across the MMCO. An Antarctic deglaciation would result in enhanced warming of the Southern Hemisphere (Justino et al., 2014), whereas changes in ice volume centred on the Arctic would result in stronger changes in conditions in the Northern Hemisphere (e.g., Shakun and Carlson, 2010).

# 5 CARBON CYCLING DURING THE MMCO

In the previous chapter, coeval changes in salinity and ice volume inferred from changes in planktonic and benthic $\delta^{18}O_{sw}$ were used to imply a northward movement of the ITCZ in response to a rise in sea level. A salinity minimum and productivity maximum are associated with the ITCZ and so changes in primary productivity are inferred in this chapter to assist in tracking the movement of the ITCZ. Maxima in benthic foraminiferal accumulation rates occur coevally with salinity minima, which would be expected from the ITCZ's position being proximal to Ceara Rise. Mn/Ca and U/Ca respond to changes in oxidation state and so a hypothesis that Mn/U ratios could be used as a proxy for redox conditions is presented. Changes in Mn/U appear to follow changes in $\delta^{13}C$ and BFAR, which I believe warrants further investigation of this line of enquiry. Additionally, changes in Sr/Ca, and B/Ca are used to attempt to quantify changes in $\Delta[CO_3^{2-}]$, but while they agree on the general trend of changes, they do not agree on the magnitude. Changes in $\Delta[CO_3^{2-}]$ proxies appear to instead be coeval with changes in export productivity proxies, such as BFAR, and so may also be affected by changes in the position of the ITCZ.

## 5.1 Introduction

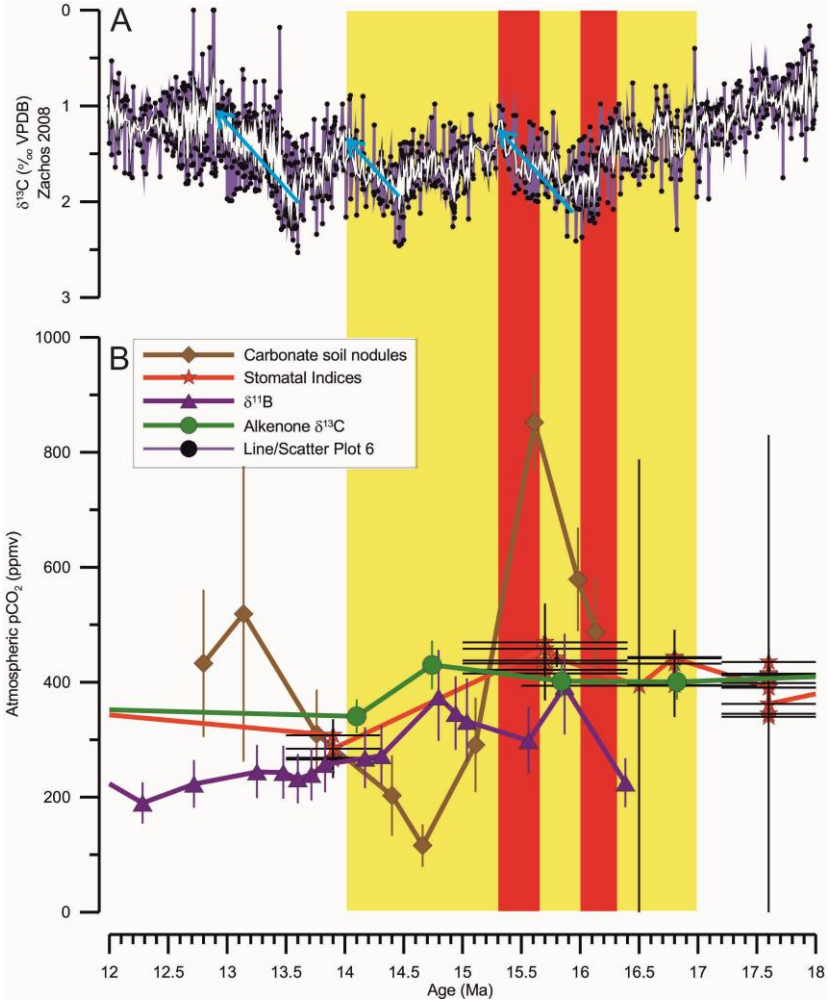


**Figure 45 – Benthic $\delta^{13}C$ (A) and $pCO_2^{ATM}$ (B) during the MMCO. The MMCO is highlighted in yellow, and the intervals examined in this thesis are highlighted in red. $\delta^{13}C$ is taken from (Zachos et al., 2008). Trends towards lighter $\delta^{13}C$ are highlighted with blue arrows. References for B are as Figure 3.**

The carbon cycle is one of the most complex climatological systems on the planet and a great deal of effort has been put into understanding how it has changed over Earth's history. There are many reservoirs for carbon on a global scale, the largest by far is the lithosphere (>$60x10^6$Gt in carbonates & $15x10^6$Gt in kerogens, Falkowski et al., 2000) though the most active reservoirs from a climatological perspective are the atmosphere (720Gt) and oceans (38,400Gt). Carbon exists in the atmosphere primarily as $CO_2$, and the concentration of $CO_2$ in the atmosphere ($pCO_2^{ATM}$) has a strong effect on global temperatures (IPCC, 2013). The effect of $pCO_2^{ATM}$ on global temperatures affects global ice volume (DeConto and Pollard, 2003; DeConto et al., 2008; Foster et al., 2012; Langebroek

et al., 2009; Monnin et al., 2001; Pollard and DeConto, 2005; Spofforth et al., 2010; Tripati et al., 2009), which in turn affects sea levels. The global temperature also affects precipitation patterns, and thus which areas are prone to aridity or flooding, as well as the frequency and intensity of storms. As many of the most populous cities in the world are on the coast, and with the expansion of global deserts and rapidly increasing population understanding how the carbon cycle works and how it affects the climate has never been more important.

The MMCO provides a potentially useful analogue to modern climate change. $pCO_2^{ATM}$ during the MMCO reached around 392 ±94 ppmv (Figure 45) by around 16Ma (Foster et al., 2012), though was found by Greenop et al. (2014) to vary between 250 and 500 ppmv between 16.5 and 15.5 Ma on an approximately 100 kyr timescale. The cause of this variability coincides with high latitude variations in climate during the MMCO, and appear to roughly coincide with periods of ice-sheet retreat observed in the sedimentary records of the ANDRILL cores (e.g., Fielding et al., 2011; Passchier et al., 2011; Warny et al., 2009). These $pCO_2^{ATM}$ levels are almost identical to the modern value of 400ppmv (as of time of writing). $pCO_2^{ATM}$ is controlled by a number of factors on multiple timescales, and similarly has its own effects on climate outside of its role as a greenhouse gas. On very long timescales (>$10^{5\text{-}6}$ years) $pCO_2^{ATM}$ is controlled by tectonic processes and weathering rates of silicates (Berner, 2006; Berner and Kothavala, 2001; Berner et al., 1983). On shorter timescales, its exchange with the surface ocean and its conversion to and subsequent burial as organic and inorganic carbon are more relevant to this thesis.

Chapter 3 dealt with the variability of global ice volume under these conditions, and the scope of this chapter is to examine contemporaneous carbon cycle dynamics. This chapter will include records reflecting changes in both the inorganic and organic carbon cycles.

### *5.1.1 The inorganic carbon cycle*

As the largest of the two climatologically active reservoirs the oceans play a key role in storing carbon, primarily as dissolved inorganic carbon (DIC). DIC refers to several carbon-containing species that maintain chemical equilibrium (20):

$$CO_{2(g)} \leftrightarrow [CO_{2_{(aq)}}] + H_2O_{(l)} \leftrightarrow [H_2CO_3] \leftrightarrow [H^+] + [HCO_3^-] \leftrightarrow 2[H^+] + [CO_3^{2-}] \quad \textbf{(20)}$$

In addition, ocean water alkalinity (ALK, the sum of negatively charged ions in solution, primarily $2[CO_3^{2-}]$, $[HCO_3^-]$, and $[B(OH)_4^-]$) plays a key role in regulating the proportion of the species of DIC available within a reservoir (Figure 46). For example, as ALK increases, the proportion of carbon present as $CO_2$ decreases in both seawater and, through the process of equilibration, the atmosphere (Sigman and Boyle, 2000).

Changes in $[CO_3^{2-}]$ in the ocean, often seen in sedimentary records as changes in the $CaCO_3$ content of oceanic sediments, are known to tie in with changes in high latitude climate (e.g., Coxall et al., 2005; Holbourn et al., 2014; Kender et al., 2014; Lear et al., 2004). At the Eocene Oligocene Climate Transition (EOCT, ~34 Ma), the drop in sea level associated with the inception of permanent ice sheets on Antarctica caused a significant change in the primary location of the deposition of $CaCO_3$ (Merico et al., 2008). The loss of a large swath of continental shelf oceans due to the ~70m (Katz et al., 2008; Pekar et al., 2002) drop in sea level caused a ~1km increase in the depth of the calcite compensation depth (CCD, Pälike et al., 2012).

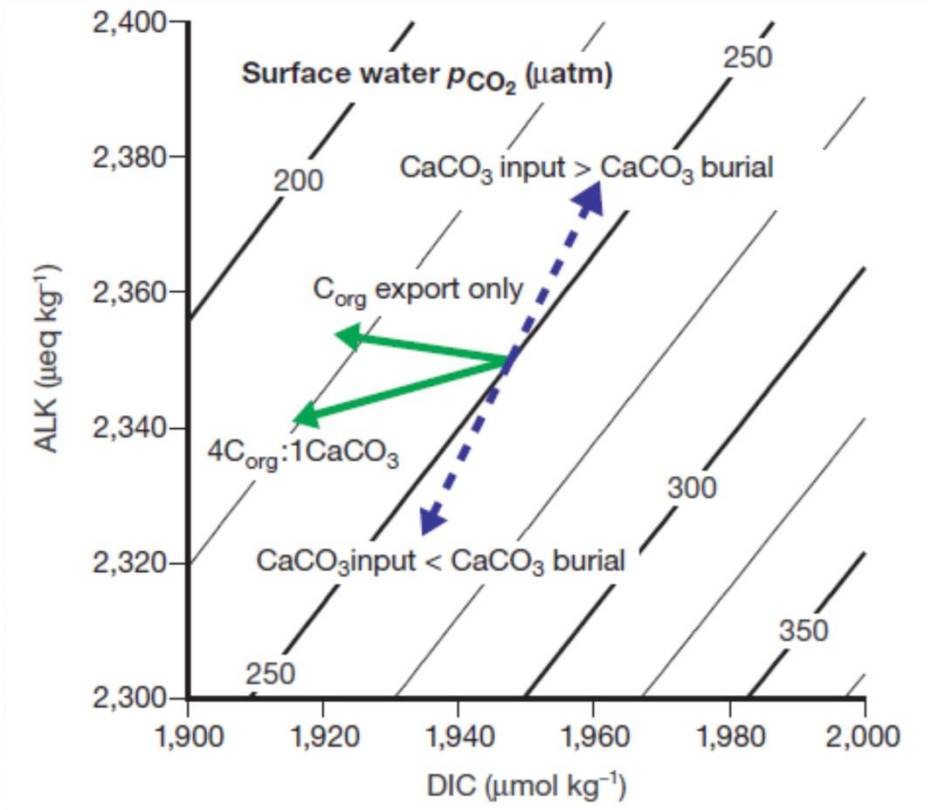


**Figure 46 – Relationship between DIC, ALK and $CO_{2(aq)}$. Taken from (Sigman and Boyle, 2000). The solid contours represent surface water $pCO_2$. Increases (decreases) in DIC relative to ALK will result in an increase (decrease) of $pCO_2^{ATM}$. The dashed lines represent imbalances from $CaCO_3$ inputs (typically from weathering). If the input of $CaCO_3$ is greater (less) than the amount bring buried, ALK increases (decreases) in a 2:1 ratio with DIC resulting in draw-down (release) of $CO_2$ from (to) the atmosphere. The solid arrows represent the effects of the burial of organic carbon either on its own, or in conjunction with the export of $CaCO_3$ caused by the growth and death of calcite producing organisms (typically in a 4:1 molar ratio in the tropical ocean). Both result in a drop in DIC and $CO_{2(aq)}$ (and thus a drawdown of $pCO_2^{ATM}$).**

$\Delta[CO_3^{2-}]$, or the carbonate saturation state is the difference between *in situ* $[CO_3^{2-}]$ and the $[CO_3^{2-}]$ required for saturation at a given temperature and pressure. Given that this study focuses on one site and examines intervals of a duration less than the residence time of Ca in the oceans (~1Ma), changes in $\Delta[CO_3^{2-}]$ can be assumed to reflect changes in $[CO_3^{2-}]$. Changes in seawater saturation state are expected to vary proportionally with changes in ALK and DIC (Sigman and Boyle, 2000). Therefore, assuming a relatively constant ocean carbon inventory within the study intervals, variations in seawater saturation state can be expected to be inversely proportional to those of $pCO_2$.

The controls on ocean [$CO_3^{2-}$] and DIC are manifold (Figure 46), but they boil down to weathering rates and the rate of supply and removal of $CaCO_3$ to or from the oceans (Armstrong and Allen, 2011; Coxall et al., 2005; Sigman and Boyle, 2000; Yu et al., 2010a), changes in ocean circulation (Sigman and Boyle, 2000; Yu et al., 2010a), changes in export productivity, changes in the $CaCO_3$/Corg rain rate of biogenic carbon and changes in sediment dissolution driven by organic matter remineralisation (Francois et al., 1997; Sigman and Boyle, 2000). Changes in $\Delta[CO_3^{2-}]$ during the MMCO will be examined in this thesis and the causes of these changes will be explored.

### *5.1.2 The organic carbon cycle*

Export productivity (the rate of transfer of organic carbon, or $C_{org}$, to the deep sea) is an important component of the carbon cycle as it is the primary means by which carbon is removed from the atmosphere and transferred to deep sea sediments. The export of $C_{org}$ from the surface to the deep oceans causes a decrease in $pCO_2^{ATM}$ both through the removal of carbon from the atmosphere, and by the removal of DIC from the surface ocean. This increases the proportion of ALK to DIC (Figure 46). The export of $CaCO_3$ with $C_{org}$, say from calcifying organisms, will also cause a net loss of $pCO_2^{ATM}$ at the molar ratios typical of low-latitude regions (1:4, Figure 46). Changes in the ratio of $CaCO_3$ to $C_{org}$ can affect the rate of drawdown of $pCO_2^{ATM}$. Reducing the ratio of $CaCO_3$ to $C_{org}$ being buried increases the rate of drawdown by leaving a greater proportion of ALK in the surface ocean, allowing for more dissolution of $CO_2$, and by reducing $CaCO_3$ burial, which increases whole ocean ALK (Sigman and Boyle, 2000).

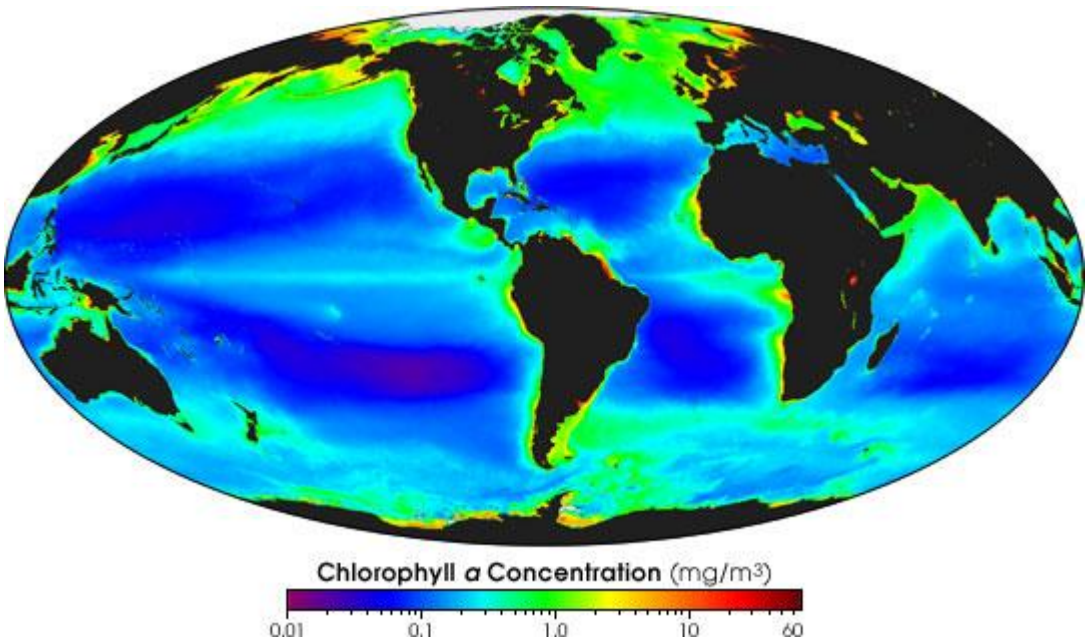


**Figure 47 – Global chlorophyll-a concentrations in the surface ocean, taken from (Ichoku, 2004). The band of high chlorophyll near to the equator is caused by upwelling associated with the ITCZ.**

While the ratio of $CaCO_3$ to $C_{org}$ being buried can affect $pCO_2^{ATM}$ through changes in ALK and DIC, the rate of primary productivity (PP) can also affect global $pCO_2^{ATM}$. Dissolved $CO_2$ is taken up by primary producers in the surface ocean to produce organic carbon through photosynthesis. Once the organisms that live in the surface die, a small fraction of the organic matter sinks to the deep ocean where they are either remineralised, dissolved, and upwelled back to the surface to be re-cycled, or they are buried. Upwelling of nutrient rich water results in high biological PP, which can be seen in modern oceans through global maps of surface water chlorophyll concentrations (Figure 47).

High PP is associated with zones of upwelling, as cold, nutrient-rich bottom waters are brought to the surface. Upwelling tends to be focused on the west coast of continents (or eastern edge of the oceans, depending on your perspective) as the predominant wind direction forces Ekman transport away from the continental shelf. In order to compensate for this surface transport of waters away from the coast, deep waters are upwelled and so a region of high PP is produced. The ITCZ is similarly associated with upwelling as the trade winds force Ekman transport away from the equator, and so the ITCZ typically

shows higher PP and lower sea surface salinities (SSS) than the surrounding ocean. This can be seen in Figure 47 as a band of higher chlorophyll near to the equator and in Figure 29 as a band of higher rainfall.

As Ceara Rise's position is just south of the modern (Figure 29) and palaeo-ITCZ (Figure 42), changes in the position of the ITCZ relative to Ceara Rise will be associated with changes in PP. Specifically, if the ITCZ becomes proximal to Ceara Rise, PP will increase, and as it becomes more distal PP will drop. The ITCZ's position favours the warmer hemisphere (Broccoli et al., 2006; Chiang et al., 2003; Chiang and Bitz, 2005; Philander et al., 1996). Any warming of the Northern Hemisphere relative to the Southern will push the ITCZ further north and cause an increase in SSS and a reduction in PP (Ichoku, 2004).

## 5.2 Methods

### *5.2.1 Reconstructing variations in export productivity*

#### *5.2.1.1 Benthic foraminiferal accumulation rates (BFAR)*

See Chapter 2 (Methodology) for a full explanation of the BFAR productivity proxy and how it has been calculated. BFAR is useful as an indication of PP. Benthic foraminiferal tests >250 μm were counted, and their abundance multiplied by the mass accumulation rate to give an indication of the rate of accumulation of benthic foraminifera. The assumption is that higher rates of accumulation of benthic foraminifera are associated with increased nutrient supply from the surface, and thus BFARs are indicative of PP (Berger and Wefer, 1990; Diester-Haass et al., 2011; Herguera, 2000)

#### *5.2.1.2 Changes in bottom water redox state*

Oxygen is used by both animals and aerobic bacteria in respiration. As such where there are more respiring organisms, oxygen utilisation will increase. This can have the effect of reducing the free oxygen available if it is not replenished faster than it is used and so in regions of high PP bottom waters can become deprived of oxygen (Algeo et al., 2013; Filipsson et al., 2011; Groeneveld and

Filipsson, 2013; Hallberg, 2004). The oxygenation state of bottom waters is difficult to determine from geochemical records, with most records relying on the presence of high concentrations of organic carbon (Calvert and Pedersen, 1996; Spofforth et al., 2010), though at best this gives a sort of digital presence/absence indication of bottom water oxygen. Both manganese (Calvert and Pedersen, 1996; Chun et al., 2010; Mangini et al., 2001) and uranium (Anderson, 1982; Boiteau et al., 2012; Francois et al., 1993; Mangini et al., 2001; McManus et al., 2005) concentrations in the water are dependent on the level of oxygen and their concentrations have been used to trace past variations in redox state (Boiteau et al., 2012; Calvert and Pedersen, 1996; Chun et al., 2010; Francois et al., 1993; Mangini et al., 2001). Below I propose that Mn/U ratios may also be used to gain additional insight into past redox variations.

#### *5.2.1.3 $\delta^{13}C$*

Organic carbon forms a key component of the carbonate system and PP within an ecosystem and transport of that organic carbon to the sea floor is a key sink for atmospheric $CO_2$. PP is controlled primarily by the supply of nutrients to the photic zone of the water column where primary producers are able to photosynthesise, and where consumers are able to predate upon them. There are many proxies for PP, one of which is $\delta^{13}C$ of planktonic foraminiferal calcite. Preferential uptake of the lighter carbon isotope, $^{12}C$, causes marine organic matter to have heavily depleted $\delta^{13}C$ values of ~-20 to -23‰ (Cooke and Rohling, 2001). As a result, the remaining inorganic carbon, primarily $HCO_3^-$, is very depleted in $^{12}C$ and calcium carbonate formed from that reservoir reflects that. As a result, all else being equal heavier $\delta^{13}C$ of planktonic carbonate can reflect increased productivity, however upwelling of the $^{12}C$-enriched bottom waters can reduce the $\delta^{13}C$ of the surface waters and disguise the productivity signal. As has been previously stated, upwelling and PP are closely linked and so care needs to be taken when interpreting $\delta^{13}C$ as a productivity proxy.

The difference between surface and deep ocean $\delta^{13}C$ has been used to give an indication of the efficiency of the biological pump (Broecker and Peng, 1982; Hilting et al., 2008). Increased gradients between the surface and the deep ocean reflect a more efficient transfer of organic carbon to the deep sea from the surface, which can indicate increased export productivity and increased burial of carbon (Cooke and Rohling, 2001; Corfield and Cartlidge, 1992). This can have the effect of reducing DIC and drawing down $pCO_2^{ATM}$.

### *5.2.2 Reconstructing variations in seawater carbonate saturation state ($\Delta[CO_3^{2-}]$)*

#### *5.2.2.1 Sr/Ca*

Foraminiferal Sr/Ca ratios have been used in several calibration studies to quantify changes in $\Delta[CO_3^{2-}]$ (Dawber and Tripati, 2012a; Raitzsch et al., 2010; Rathmann and Kuhnert, 2008). Sr/Ca can be problematic in this regard, though, as it is also affected by temperature (Cleroux et al., 2008; Dawber and Tripati, 2012a; Mortyn et al., 2005; Rosenthal et al., 2006). The inverse relationship between Sr/Ca and Mg/Ca (Figure 36 and Figure 37) suggests that, in this record at least, temperature is not the dominant control on foraminiferal Sr/Ca variations.

#### *5.2.2.2 U/Ca*

U/Ca offers a very new alternative to other geochemical proxies for bottom water $\Delta[CO_3^{2-}]$ (chapter 3, this thesis; Keul et al., 2013; Raitzsch et al., 2011). This proxy is similarly beset by problems, not least of which is its inclusion in authigenic coatings on foraminiferal calcite, and hence its close association with redox conditions below the sediment-water interface (Boiteau et al., 2012; Chun et al., 2010; Francois et al., 1993; Mangini et al., 2001; McManus et al., 2005). As it stands, much more work needs to be conducted upon U/Ca before it can be reliably used as an indicator of carbonate saturation conditions at the sea floor,

though in this chapter I attempt to use it in conjunction with Mn/Ca as an indicator of sea-floor redox conditions.

#### *5.2.2.3 B/Ca*

A global core-top study suggests that benthic foraminiferal B/Ca also correlates well with $\Delta[CO_3^{2-}]$, with $R^2$ values of ~0.8 in the two *Cibicidoides* species studied (C. mundulus and C. wuellerstorfi, Brown et al., 2011; Yu and Elderfield, 2007). These studies are noteworthy in that they used foraminifera from multiple ocean basins with very different oceanographic profiles and yet still found a strong correlation between B/Ca and $\Delta[CO_3^{2-}]$. Yu and others have successfully applied foraminiferal B/Ca to changes in $[CO_3^{2-}]$ across the last glacial maximum (Yu et al., 2010a; Yu and Elderfield, 2007; Yu et al., 2008). None the less, Rae et al. (2011) caution against relying too heavily on B/Ca due to its sensitivity to vital effects that becomes apparent even at the species morphotype level (c.f. *C. wullerstorfi sensu stricto, C. wullerstorfi var., C. mundulus var.,* and *C. mundulus sensu stricto*).

The resulting $\Delta[CO_3^{2-}]$ record will be put into context with the climate parameters presented in Chapter 4.

## 5.3 Results

### *5.3.1 $\delta^{13}C$ and $\delta^{18}O$*

These records are previously described in Chapter 4 (Mid-Miocene ITCZ Response to Changes in the Northern Hemisphere Ice Sheets).

### *5.3.2 U/Ca*

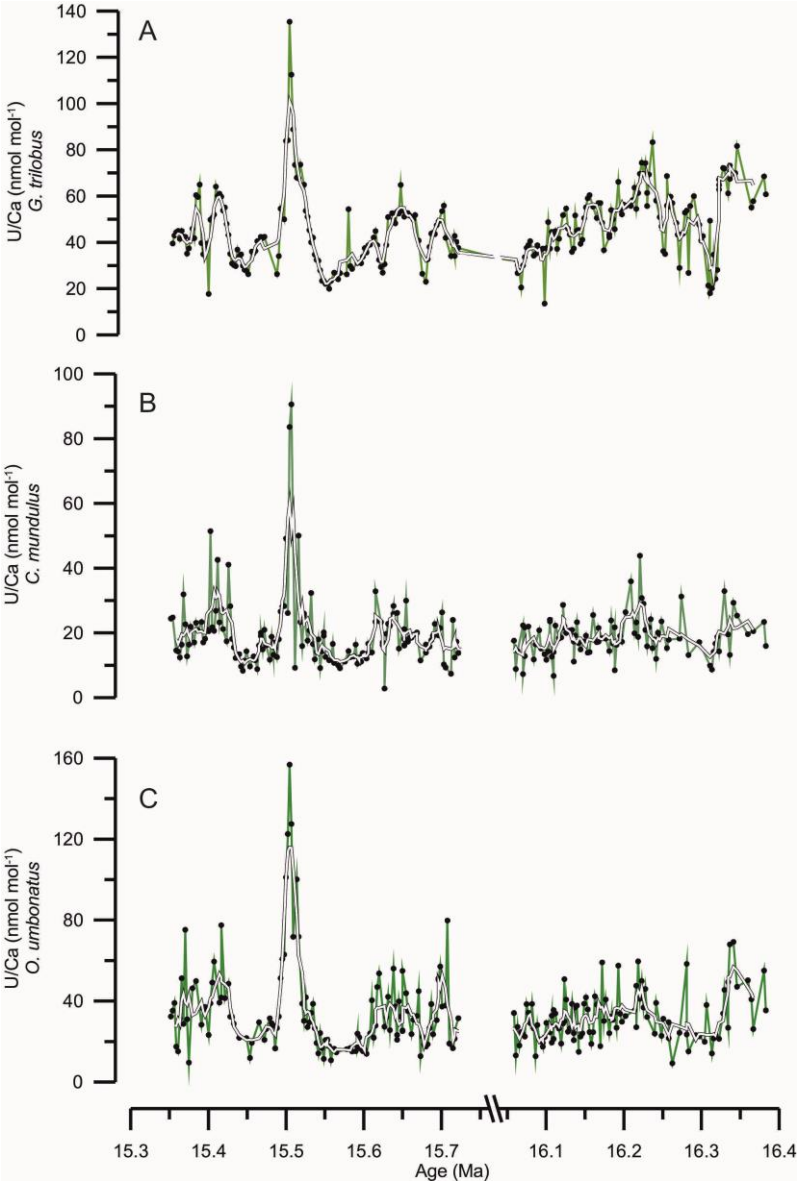


**Figure 48 – U/Ca at site 926. A)** ***G. trilobus*****. B)** ***C. mundulus*****. C)** ***O. umbonatus*****.**

#### *5.3.2.1 G. trilobus*

U/Ca in *G. trilobus* (Figure 48a $U/Ca_G$) has a minimum value of 13.5 nmol $mol^{-1}$ and a maximum value of 135 nmol $mol^{-1}$. However, the data are skewed towards lower values, with a mean of 46.7 nmol $mol^{-1}$, and $\sigma 1$ of 16.7 nmol $mol^{-1}$. In the lower interval, between 16.40 Ma and 16.32 Ma U/Ca is around 55 nmol $mol^{-1}$, however at 16.32 Ma there is a sudden drop to ~20.1 nmol $mol^{-1}$. From 16.32 Ma to 16.23 Ma there is a general increase to U/Ca of around 69.3 nmol $mol^{-1}$, though superimposed on this increase are ~0.02 Myr oscillations with an

amplitude of ~30 nmol $mol^{-1}$. From 16.23 Ma to ~16 Ma U/Ca generally decreases to ~30 nmol $mol^{-1}$, though there are again oscillations of similar period but with an amplitude of ~20 nmol $mol^{-1}$.

$U/Ca_G$ in the upper interval is ~34.1 nmol $mol^{-1}$ from 15.72 to 15.64 Ma, however this stability is interrupted by a large oscillation with a period of ~0.06 Ma and an amplitude of ~24 nmol $mol^{-1}$. At 15.64 Ma there is a decrease until 15.55Ma to 19.9 nmol $mol^{-1}$. At this point, U/Ca increases rapidly to 135.4 nmol $mol^{-1}$ at 15.51 Ma. There is a sudden drop to ~26.3 nmol $mol^{-1}$ by 15.49 Ma. From here, U/Ca stays at around 26.3 nmol $mol^{-1}$ until 15.43 Ma where there is another sudden increase to ~60.1 nmol $mol^{-1}$ at 15.41 Ma. U/Ca then undergoes a quick oscillation until 15.38 Ma with an amplitude of ~40 nmol $mol^{-1}$ and then finishes the record settled on ~41.5 nmol $mol^{-1}$.

#### *5.3.2.2 C. mundulus*

U/Ca in *C. mundulus* (Figure 48b, $U/Ca_M$) has a minimum value of 7.9 nmol $mol^{-1}$ and a maximum value of 90.6 nmol $mol^{-1}$. The mean of the data is 19.8 nmol $mol^{-1}$, and $\sigma 1$ is 9.8 nmol $mol^{-1}$. In the lower interval between 16.4 and 16.3Ma U/Ca is ~19.6 nmol $mol^{-1}$, however there is a decrease at ~16.3Ma to ~9.9 nmol $mol^{-1}$. There is a general increase in the data from 16.3 Ma to 16.2 Ma from 8.7 nmol $mol^{-1}$ to an average value of ~36 nmol $mol^{-1}$. There is then a swift decline from 16.2 Ma back to ~20 nmol $mol^{-1}$. Around 16.14 Ma there is a slight increase in $U/Ca_M$ which peaks at ~25 nmol $mol^{-1}$ at 16.12 Ma, though there is another gradual decline back to around 20 nmol $mol^{-1}$.

The upper interval shows a very general increase from 15.72 Ma to 15.64 Ma of ~16.0 to 25.8 nmol $mol^{-1}$, though superimposed on this are large swings of U/Ca with magnitudes equal to the magnitude of the overall decrease. U/Ca drops to ~12.9 nmol $mol^{-1}$ at 15.60 Ma where it remains until ~15.53 Ma. At this point it increases rapidly to 90.6 nmol $mol^{-1}$ by 15.51 Ma, and then decreases to ~13.2 nmol $mol^{-1}$ by 15.48 Ma. At 15.44 Ma U/Ca shows rapid oscillations with a

period of ~0.03 Myr and an amplitude of ~30 nmol $mol^{-1}$, it then settles at ~15.40 Ma at ~18.19 nmol $mol^{-1}$.

### *5.3.3 O. umbonatus*

The mean for U/Ca in *O. umbonatus* ($U/Ca_O$, Figure 48c) is 34.3 nmol $mol^{-1}$. The σ1 for the record is 20.1 nmol $mol^{-1}$. $U/Ca_O$ in the lower interval starts at ~16.4 nmol $mol^{-1}$, and decreases to 14.1 nmol $mol^{-1}$ at 16.33 Ma. $U/Ca_O$ then has a mean of ~34.4 nmol $mol^{-1}$ for the majority of the lower interval, with small oscillations with amplitudes between ~10 and ~30 nmol $mol^{-1}$.

The upper interval is far more variable and much more interesting. U/Ca goes through large oscillations around a mean of ~31.5 nmol $mol^{-1}$ from 15.72 to 15.62 Ma with a period of ~0.09 Ma and an amplitude of ~30 nmol $mol^{-1}$. At 15.62 nmol $mol^{-1}$ it almost flatlines around 16.2 nmol $mol^{-1}$ until 15.56 Ma, where there appears to be a stepped-increase to 30.21 nmol $mol^{-1}$ at 15.52 Ma, followed by a rapid jump to 156.8 nmol $mol^{-1}$ at 15.51 Ma. There is a rapid decrease to ~16.6 nmol $mol^{-1}$ by 15.49 Ma. $U/Ca_O$ stays at around a mean of 21.83 nmol $mol^{-1}$ until 15.44 Ma when there is another rapid increase to 77.5 nmol $mol^{-1}$ at 15.51 Ma, followed by another decrease to 23.2 nmol $mol^{-1}$ at 15.4 Ma. $U/Ca_O$ then oscillates between 9.58 and 75.1 nmol $mol^{-1}$ until the end of the record.

### *5.3.4 B/Ca*

#### *5.3.4.1 G. trilobus*

The mean for B/Ca in *G. trilobus* ($B/Ca_G$, Figure 49a) is 69 μmol $mol^{-1}$, with σ1 of 4 μmol $mol^{-1}$. B/Ca in *G. trilobus* shows very little difference between the two intervals. Taken separately, the upper interval shows a mean of 68 μmol $mol^{-1}$ (std. error of 0.3 μmol $mol^{-1}$) and σ1 of 3 μmol $mol^{-1}$. The lower interval has a mean of 70 μmol $mol^{-1}$ (std. error of 0.4 μmol $mol^{-1}$) and σ1 of 5 μmol $mol^{-1}$. The lower interval perhaps shows a general trend of increasing B/Ca from a mean of ~68 μmol $mol^{-1}$ at 16.33 Ma to ~72 μmol $mol^{-1}$ at ~16.0 Ma. Superimposed on

that, the moving average brings out a long, broad oscillation with a period of ~0.06 Myr and an amplitude of ~5 μmol mol$^{-1}$.

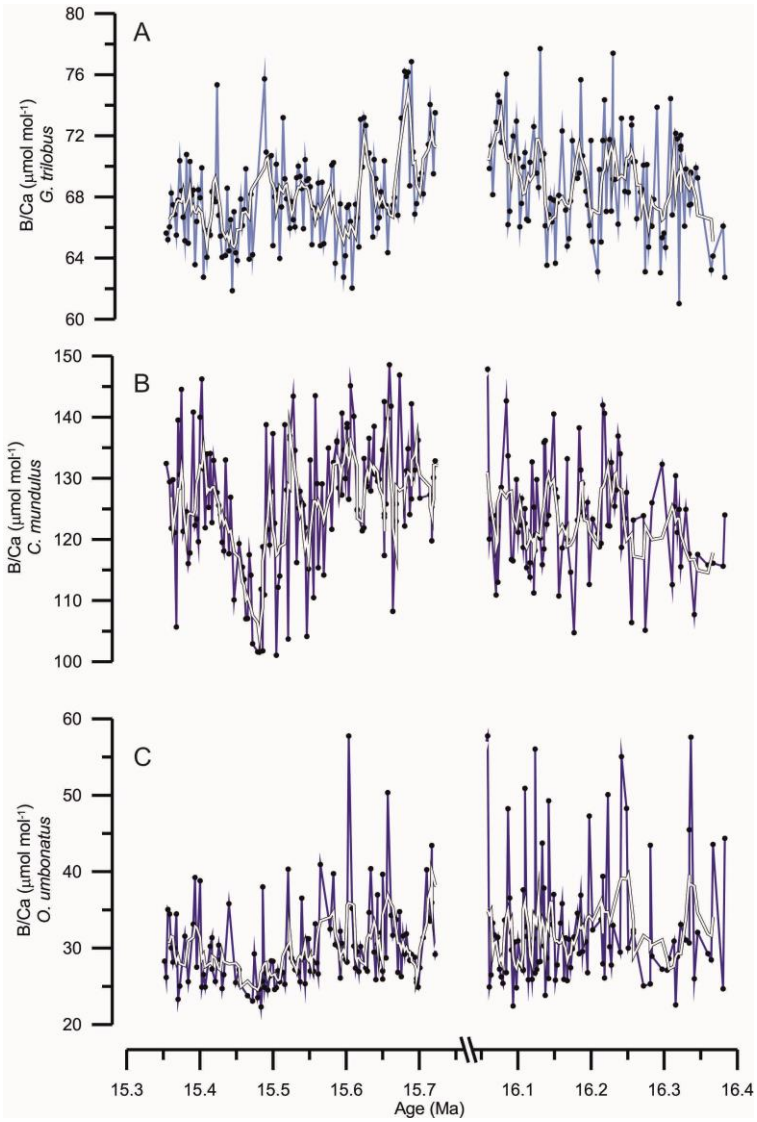


**Figure 49 – B/Ca in Site 926. Values that fall σ2 outside of the mean have been excluded to reduce the variability. A) *G. trilobus*. B) *C. mundulus*. C) *O. umbonatus*.**

The upper interval perhaps shows slightly more in the way of trends and features. There is a general decrease from 15.72 to 15.62 Ma of 72 μmol mol$^{-1}$ to 67 μmol mol$^{-1}$. This is interrupted by two pulses of increased B/Ca at 15.70 Ma and 15.65 Ma of ~8 μmol mol$^{-1}$ each. There is then a general increase to ~71 μmol mol$^{-1}$ by 15.49 Ma, followed by a rapid drop to ~64 μmol mol$^{-1}$ by 15.43 Ma. $B/Ca_G$ then recovers with a rapid increase to ~75 μmol mol$^{-1}$ at 15.42 Ma before dropping back to ~66 μmol mol$^{-1}$ at 15.40 Ma, around which it remains until the end of the record.

#### *5.3.4.2 C. mundulus*

The mean for B/Ca in *C. mundulus* ($B/Ca_M$, Figure 49b) is 125 μmol $mol^{-1}$, with a σ1 of 12 μmol $mol^{-1}$. The lower interval shows no particular clear trends and instead oscillates between ~105 μmol $mol^{-1}$ and ~142 μmol $mol^{-1}$ with no clear pattern or rhythm. This continues into the upper interval, until there is a very clear and marked decrease from around 15.54 Ma from a mean of ~127.9 μmol $mol^{-1}$ to ~100 μmol $mol^{-1}$ at 15.45 Ma.

#### *5.3.4.3 O. umbonatus*

B/Ca in *O. umbonatus* ($B/Ca_O$, Figure 49c) has a mean of 33 μmol $mol^{-1}$ with a σ1 of 16 μmol $mol^{-1}$. Given that σ1 is nearly 50% of the mean, the variability in $B/Ca_O$ is too high to discern any trends, although the minima in *C. mundulus* B/Ca appears to correspond to a minima in *O. umbonatus* B/Ca at ~15.5 Ma. The boron concentration in most *O. umbonatus* samples was <5x that of the blank, and so the data are not shown.

### *5.3.5 Mn/Ca*

#### *5.3.5.1 G. trilobus*

The mean of Mn/Ca in *G. trilobus* ($Mn/Ca_G$, Figure 50a) is 673 μmol $mol^{-1}$ and the σ1 is 85 μmol $mol^{-1}$. In the lower interval, $Mn/Ca_G$ starts at around 731 μmol $mol^{-1}$. There is a drop at 16.33 Ma to 384 μmol $mol^{-1}$, which then recovers to around 705 μmol $mol^{-1}$ by 16.28 Ma. $Mn/Ca_G$ then stays around a mean of 716 μmol $mol^{-1}$ for the remainder of the lower interval. Oscillations around that mean have an amplitude of between ~150 and 300 μmol $mol^{-1}$.

The upper interval shows similar variability, though the mean for the interval is lower at ~635 μmol $mol^{-1}$. There are no overtly clear trends, though from ~15.57 Ma to 15.49 Ma there appears to be a decrease followed by a recovery that appears similar to the same feature seen in $B/Ca_M$ (Figure 49b).

The lowest point of that decrease is ~390 μmol mol$^{-1}$, but this is one point on its own, and it is not clear if it is a flier. The recovery to higher values of $Mn/Ca_G$ is ended by ~15.42Ma with a value of ~707 μmol mol$^{-1}$, and this is followed by a gradual decrease to ~594 μmol mol$^{-1}$ by the end of the record.

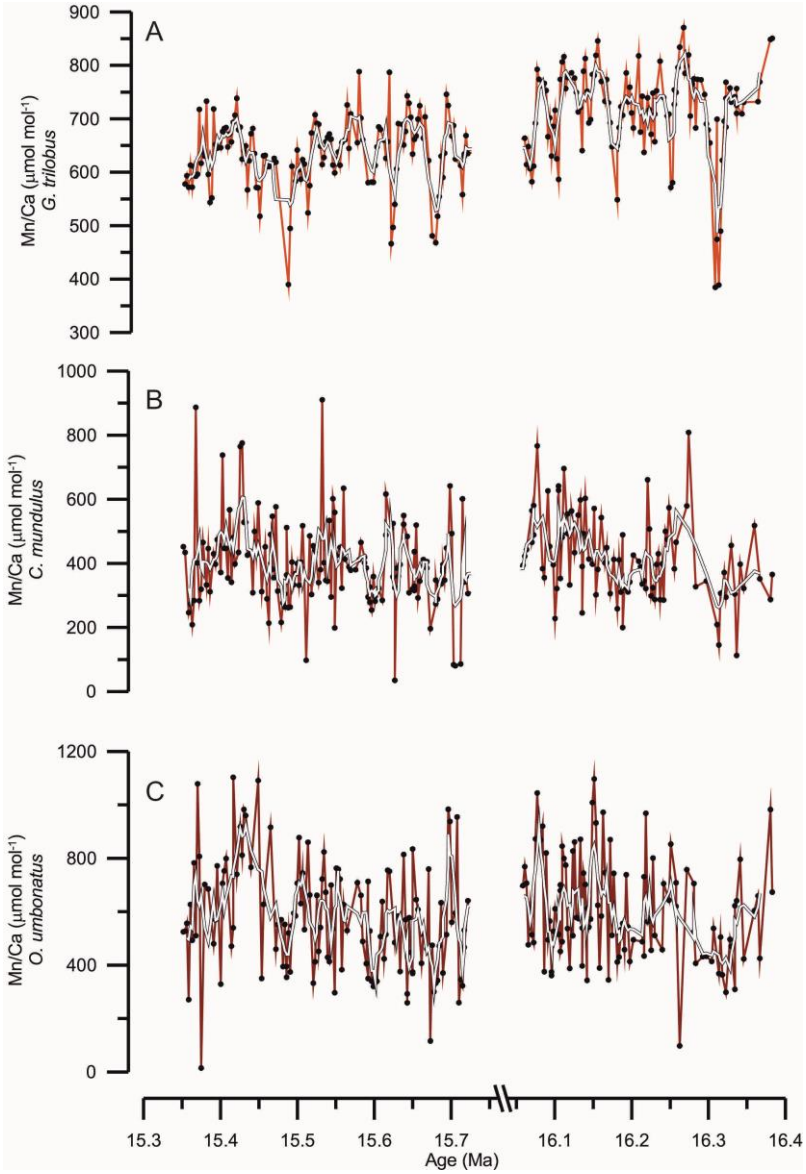


**Figure 50 – Mn/Ca in Site 926. A) *G. trilobus*. B) *C. mundulus*. C) *O. umbonatus*.**

### *5.3.5.2 C. mundulus*

The mean for Mn/Ca in *C. mundulus* ($Mn/Ca_M$, Figure 50b) is 407 μmol mol$^{-1}$, and σ1 is 129 μmol mol$^{-1}$. There are perhaps four broad trends visible in $Mn/Ca_M$. The first begins at ~16.33 Ma with a rapid increase in $Mn/Ca_M$ from ~295 to a maximum of ~809 μmol mol$^{-1}$ by 16.27 Ma. This is followed by a quick, but relatively steady decrease to ~342 μmol mol$^{-1}$, with a recovery to ~565 μmol

$mol^{-1}$ by the end of the lower interval. $Mn/Ca_M$ is very variable ($\sigma 1$ is around a third of the mean), so it is imprudent to try to pick out anything on a smaller scale.

The upper interval shows no clear trend until ~15.53 Ma, prior to which it varies by as much as 600 μmol $mol^{-1}$. At 15.53 Ma $Mn/Ca_M$ decreases from ~450 μmol $mol^{-1}$ to ~275 μmol $mol^{-1}$ at 15.48 Ma, followed by a recovery to ~480 μmol $mol^{-1}$ by 15.42 Ma. This, again, appears to coincide with the similar feature in $B/Ca_M$ (Figure 49b). After that there is a decrease to ~350 μmol $mol^{-1}$ by the end of the record.

#### *5.3.5.3 O. umbonatus*

The mean of Mn/Ca in *O. umbonatus* ($Mn/Ca_O$, Figure 50c) is 574 μmol $mol^{-1}$, with a $\sigma 1$ of 218 μmol $mol^{-1}$. With a $\sigma 1$ of ~38% of the mean, variability is much higher than $Mn/Ca_M$ (Figure 50b), and there is perhaps one clear feature that can be picked out in this record: From 15.48 Ma to 15.43 Ma, $Mn/Ca_O$ increases from ~450 μmol $mol^{-1}$ to ~910 μmol $mol^{-1}$, and then recovers back to hovering around the mean.

### *5.3.6 Sr/Ca*

#### *5.3.6.1 G. trilobus*

Sr/Ca in *G. trilobus* ($Sr/Ca_G$, Figure 51a) has a mean value of 1.23 mmol $mol^{-1}$ and has a $\sigma 1$ of 0.04 mmol $mol^{-1}$. $Sr/Ca_G$ begins at 1.22 mmol $mol^{-1}$, but there is a rapid rise to 1.36 mmol $mol^{-1}$ at 16.31Ma, followed by a sudden crash to 1.17 mmol $mol^{-1}$ by 16.28 Ma. There is then a 2-step increase at 16.26 Ma first to 1.22 mmol $mol^{-1}$, and then to 1.26 mmol $mol^{-1}$ by 16.22 Ma. At 16.18 Ma, there is a rapid decrease to 1.21 mmol $mol^{-1}$, followed by another rapid increase to 1.26 mmol $mol^{-1}$ by 16.14 Ma. By 16.09 Ma $Sr/Ca_G$ has decreased to 1.21 mmol $mol^{-1}$, but there is a rapid increase to 1.31 mmol $mol^{-1}$ by 16.07 Ma, followed by a rapid decrease to 1.23 mmol $mol^{-1}$ by the end of the lower interval.

The upper interval starts at ~1.28 mmol $mol^{-1}$, but there is a quick decrease to 1.23 mmol $mol^{-1}$ that is followed by a rapid increase to 1.34 mmol $mol^{-1}$ by 15.68 Ma. This pattern repeats again at 15.64 Ma, though the decrease is larger this time, with a trough of 1.19 mmol $mol^{-1}$ by 15.57 Ma. There is a gradual increase to 1.29 mmol $mol^{-1}$ by 15.49 Ma, though superimposed in this are oscillations of ~0.04 mmol $mol^{-1}$ in amplitude. At 15.49 Ma there is a very sudden drop to 1.17 mmol $mol^{-1}$. The upper interval ends with a two-stepped increase ~1.22 mmol $mol^{-1}$, though the end of the final step has one point with an $Sr/Ca_G$ of 1.30 mmol $mol^{-1}$.

#### *5.3.6.2 C. mundulus*

Sr/Ca in *C. mundulus* ($Sr/Ca_M$, Figure 51b) has a mean value of 1.15 mmol $mol^{-1}$, with a $\sigma 1$ of 0.069 mmol $mol^{-1}$. In the lower interval at ~16.26 Ma $Sr/Ca_M$ is ~1.11 mmol $mol^{-1}$ and gradually increases to 1.19 mmol $mol^{-1}$ by 16.23 Ma. There is then a stepped decrease, first to ~1.15 mmol $mol^{-1}$ by 16.21 Ma, then to ~1.12 mmol $mol^{-1}$ by 16.17 Ma. $Sr/Ca_M$ then stays around 1.14 until the end of the lower interval.

$Sr/Ca_M$ begins the upper interval at ~1.16 mmol $mol^{-1}$ and oscillates by between 0.01 and 0.1 mmol $mol^{-1}$ until 15.59 Ma. At this point there is a large drop to ~1.12 mmol $mol^{-1}$. Between 15.52 Ma and 15.44 Ma $Sr/Ca_M$ shows a gradual decrease from around 1.14 mmol $mol^{-1}$ to 1.08 mmol $mol^{-1}$, followed by a gradual increase to ~1.14 mmol $mol^{-1}$ by 15.39 Ma. This Sr/Ca shows similar behaviour to $B/Ca_M$ (Figure 49b) at this same point.

#### *5.3.6.3 O. umbonatus*

The mean of Sr/Ca in *O. umbonatus* ($Sr/Ca_O$, Figure 51c) is 0.93 mmol $mol^{-1}$, with a $\sigma 1$ of 0.050 mmol $mol^{-1}$. The lower interval starts at around a mean of 0.93 mmol $mol^{-1}$. There are three prominent decreases 16.25 Ma, 16.15 Ma, and 16.06 Ma to 0.85, 0.86, and 0.88 mmol $mol^{-1}$ respectively. This 100 kyr spacing

may correspond to Earth's short eccentricity cycle but the study interval is not long enough to confirm this.

The upper interval has a similar minimum at its start of 0.85 mmol $mol^{-1}$. The record stays between 0.89 and 0.97 mmol $mol^{-1}$ until ~15.51Ma, where there is a decrease to 0.80 mmol $mol^{-1}$ by 15.45 Ma. $Sr/Ca_O$ recovers to ~0.92mmol $mol^{-1}$ by 15.40, and again this gradual decrease followed by increase is similar to $B/Ca_M$ (Figure 49b).

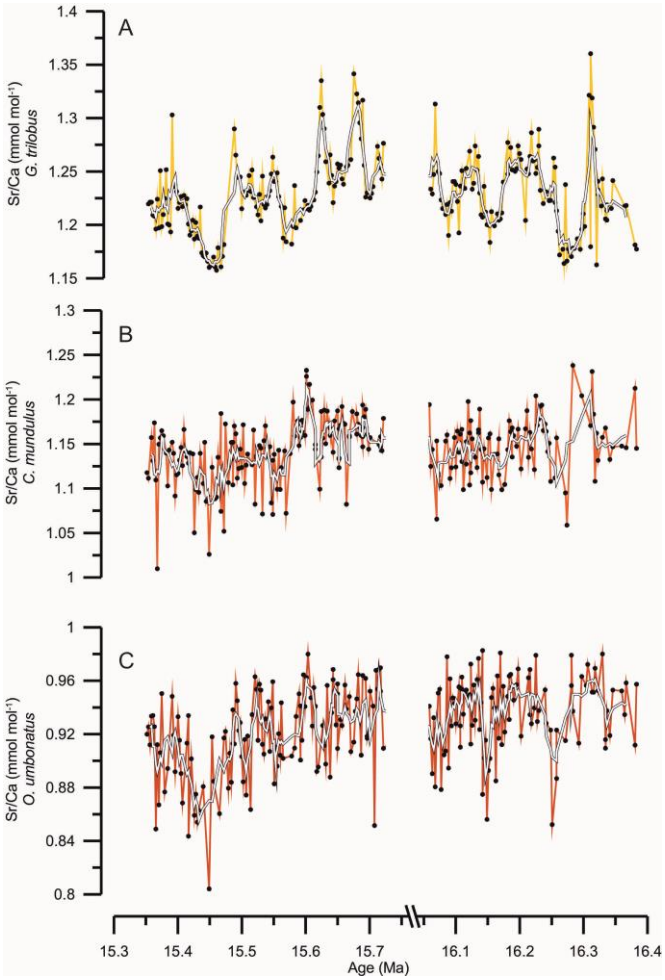


**Figure 51 – Sr/Ca at Site 926. A) *G. trilobus*. B) *C. mundulus*. C) *O. umbonatus*. Values outside of σ2 from the mean have been excluded from this figure.**

### *5.3.7 $\delta^{11}B$*

$\delta^{11}B$ was measured in five *G. trilobus* samples in order to estimate atmospheric $pCO_2^{ATM}$. The isotope ratio of boron is reported as $\delta^{11}B$ in parts per mil relative to the boric acid standard SRM 951 (Catanzaro et al., 1970). The mean value of $\delta^{11}B$ in the record is 15.98 ‰, with a minimum of 15.39 ‰ and a

maximum of 16.30 ‰ (Figure 52). Measured $\delta^{11}B$ in the lower interval begins at 16.25 Ma at ~16.07 ‰ and increases to 16.29 ‰ at 16.22 Ma. In the upper interval $\delta^{11}B$ begins at 15.52 Ma at 15.86 ‰ and increases to 16.30 ‰ by 15.48 Ma. It then decreases to 15.39 ‰ by 15.47 Ma. $\delta^{11}B$ in *G. trilobus* was used to calculate $pCO_2^{ATM}$ using the methodology of Foster et al. (2012) and Greenop et al. (2014) by S.M. Sosdian (2014, pers. comm.).

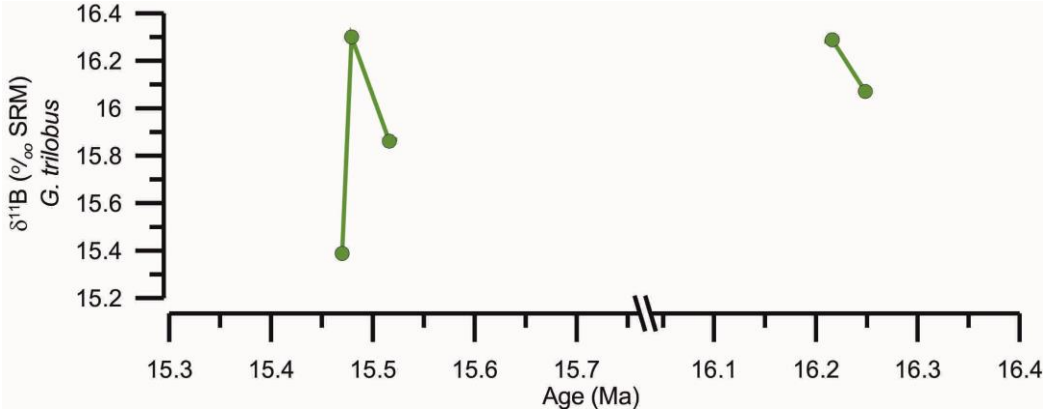


**Figure 52 – $\delta^{11}B$ in *G. trilobus*.**

## 5.4 Discussion

### *5.4.1 The Inorganic Carbon Cycle at Ceara Rise*

#### *5.4.1.1 $pCO_2^{ATM}$*

Figure 53 shows $pCO_2^{ATM}$ derived from *G. trilobus* $\delta^{11}B$ from ODP Site 926 and BWT derived from *C. mundulus* and *O. umbonatus* Mg/Ca. $pCO_2^{ATM}$ generally increases during the warming represented by T9. Prior to T9 $pCO_2^{ATM}$ is around 400 ppmv and it decreases to ~300 ppmv by the end of T9, though there is a sudden increase to ~560 ppmv which, given the close-spacing (~4 kyr) of this and the next measured value it appears as if $pCO_2^{ATM}$ varies rapidly. This agrees with the findings of Greenop et al. (2014) that $pCO_2^{ATM}$ varied rapidly during the MMCO. The close spacing of the $pCO_2^{ATM}$ data points in this study further suggests that $pCO_2^{ATM}$ may have varied more rapidly than the resolution of the study of Greenop et al. (2014) was capable of recording.

The increase in $pCO_2^{ATM}$ coincides with warmings in both the deep (Figure 53b) and shallow (Figure 53c) oceans, as evidenced by Mg/Ca. The increase in

$pCO_2^{ATM}$ is also associated with a decrease in global continental ice volume and an increase in surface seawater salinity, interpreted as a northwards shift in the ITCZ (Chapter 4). The limited resolution of the $\delta^{11}B$ record prevents further evaluation of the relative timings of changes in $pCO_2^{ATM}$ and temperature. Nevertheless, it seems likely that the changes in global ice volume and the consequent shift in locus of the ITCZ described in Chapter 4 were caused by variations in $pCO_2^{ATM}$.

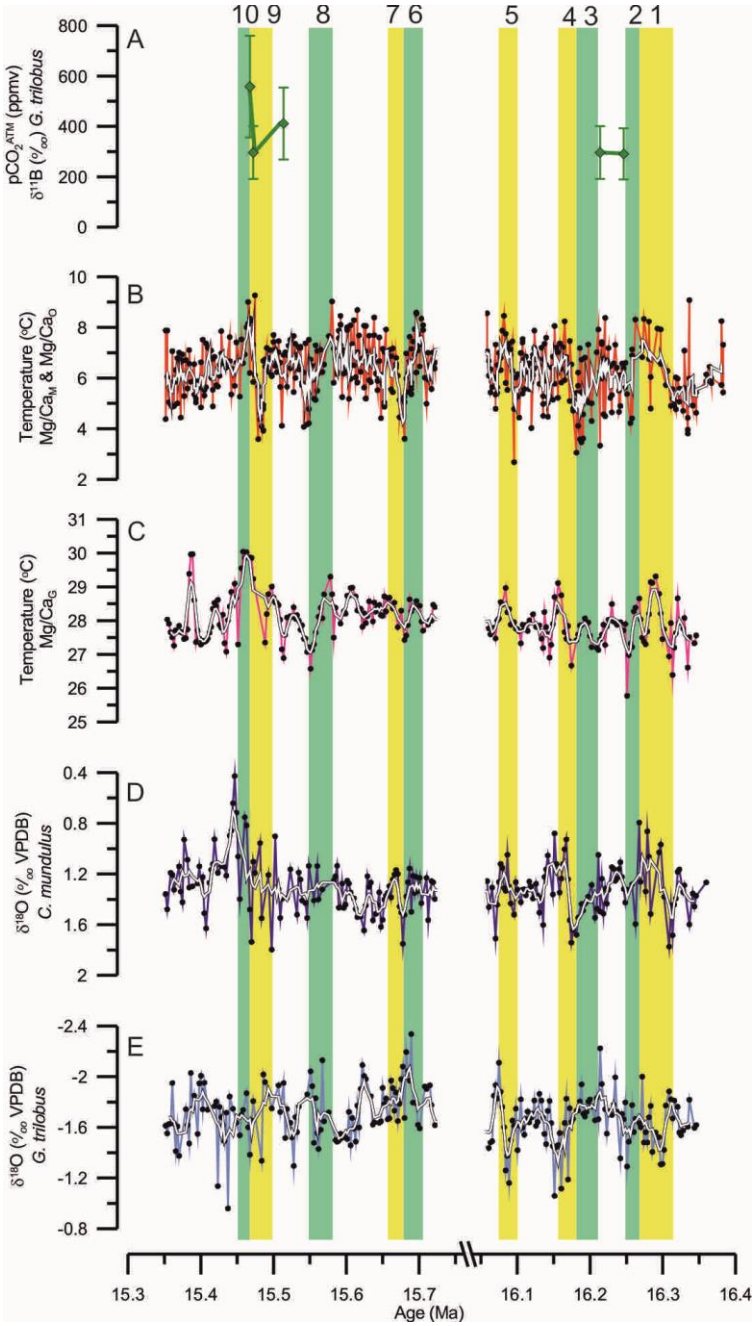


**Figure 53 – Changes in $pCO_2^{ATM}$, and temperature. A) $pCO_2^{ATM}$, measured from $\delta^{11}B$ in *G. trilobus* (Sosdian, S., pers. comm.). B) BWT. BWT were measured from $Mg/Ca_M$ and $Mg/Ca_O$ converted to be**

**equivalent to Mg/Ca$_M$ by multiplying the values by the quotient of the records' means (x0.73). C) SST measured from Mg/Ca$_G$ using the calibration of (Dekens et al., 2002). D) $\delta^{18}O_M$. E) $\delta^{18}O_G$.**

### *5.4.1.2 Carbonate saturation state ($\Delta[CO_3^{2-}]$) reconstructions*

#### 5.4.1.2.1 Interpretation of U/Ca variations

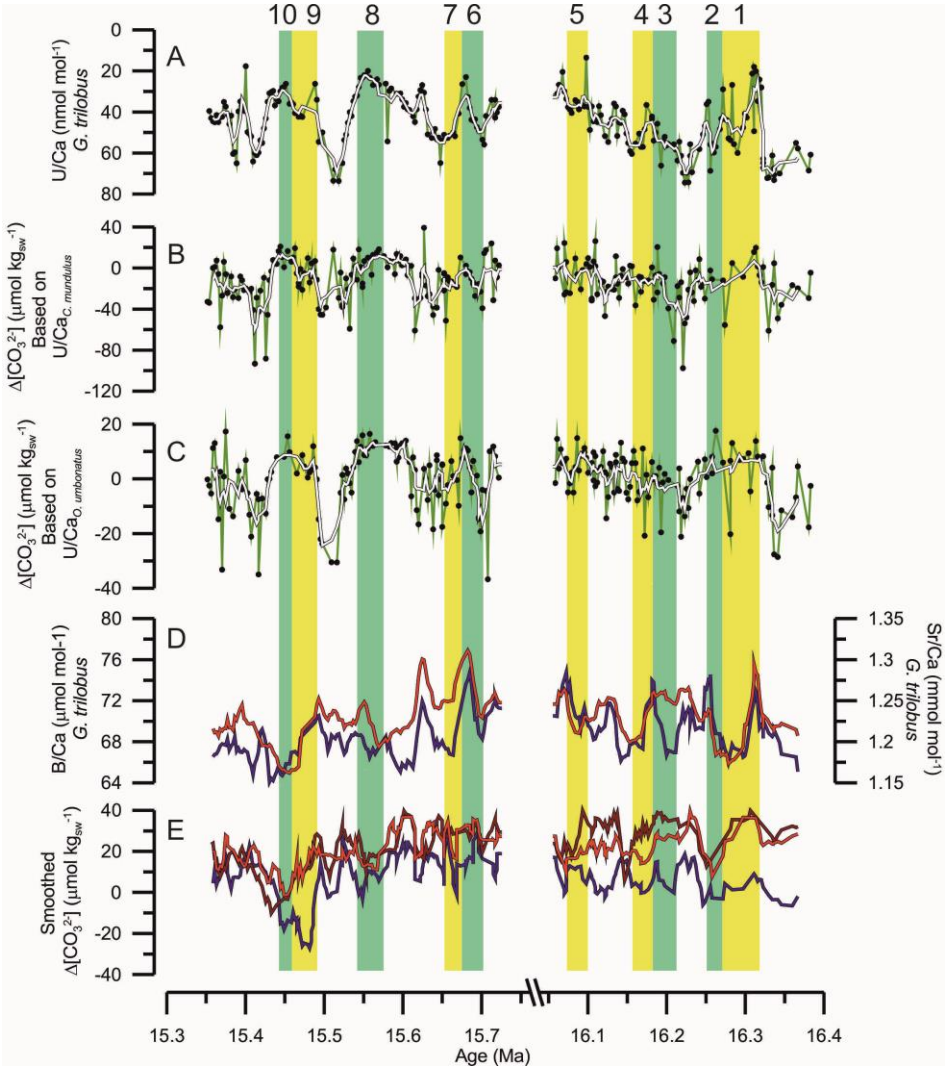


**Figure 54 – U/Ca as a $\Delta[CO_3^{2-}]$ proxy in Ceara Rise. Values higher than 80nmol mol$^{-1}$ have been omitted from the record as that is outside of the range of any published U/Ca calibration. A) U/Ca in *G. trilobus*. B) $\Delta[CO_3^{2-}]$ U/Ca in C. mundulus using the calibration of Raitzsch et al. (2011). C) U/Ca in O. umbonatus using the calibration derived in chapter 3. D) B/Ca and Sr/Ca from *G. trilobus*, same format as Figure 57. E) $\Delta[CO_3^{2-}]$ estimates from B/Ca$_M$, Sr/Ca$_M$ and Sr/Ca$_O$.**

U/Ca shows some promise as a proxy for $\Delta[CO_3^{2-}]$, with current calibrations suggesting that U/Ca in most foraminifera shows a negative relationship with $\Delta[CO_3^{2-}]$ (chapter 3, this thesis; Keul et al., 2013; Raitzsch et al., 2011). U/Ca$_G$ (Figure 54a), U/Ca$_M$ (Figure 54b), and U/Ca$_O$ (Figure 54c), all follow one another

very well. As *G. trilobus* is a planktonic species, this could be taken to mean that whatever is affecting U/Ca in the deep ocean is having an effect on the whole water column, or it may imply that post-depositional processes are affecting all three species. U/Ca does reflect bottom water oxygenation and precipitates out as part of authigenic coatings (Boiteau et al., 2012; Francois et al., 1993; McManus et al., 2005; Russell et al., 1996) and may explain why the three records look so similar.

The implied changes in $\Delta[CO_3^{2-}]$ as given by U/Ca do not agree with any changes in $\Delta[CO_3^{2-}]$ implied by Sr/Ca and B/Ca (Figure 54d & e). While U/Ca reflects changes in $\Delta[CO_3^{2-}]$ in some calibrations (Keul et al., 2013; Raitzsch et al., 2011), its disagreement with Sr/Ca and B/Ca (which are in generally good agreement with one another) suggests that it may be responding to something else. Uranium exists in oxygenated sea water as the soluble uranyl carbonate complex $[UO_2(CO_3)_3^{4-}]$, and precipitates out in sub-oxygenating conditions as uranite ($UO_2$, Chun et al., 2010). Therefore, in these samples, U/Ca appears to be responding to bottom water oxygenation. Redox variations will be discussed in section 5.4.2.2.

#### 5.4.1.2.2 Bottom water $\Delta[CO_3^{2-}]$

Figure 55 shows relative changes in bottom water $\Delta[CO_3^{2-}]$ estimated from the different proxies and different species studied. The relative changes in $\Delta[CO_3^{2-}]$ implied by the changes in $B/Ca_M$ and $Sr/Ca_M$ and $Sr/Ca_O$ are all in relatively good agreement in terms of the timings and magnitude of changes (Figure 55a-c). Stacking the smoothed records atop one another brings this out further (Figure 55d) and reveals two broad features in common. At the end of T2 at 16.25 Ma, $Sr/Ca_M$, $Sr/Ca_O$, and $B/Ca_M$ all record an increase in $\Delta[CO_3^{2-}]$, although the change in B/Ca is smaller than the change suggested by Sr/Ca. B/Ca shows an increase of ~-20 μmol $kg_{sw}^{-1}$ whereas both Sr/Ca records suggest an increase of ~30 μmol $kg_{sw}^{-1}$. In Sr/Ca this follows a drop in $\Delta[CO_3^{2-}]$ of the

same magnitude as the latter increase that begins at near the start of T1 at ~16.30 Ma, though this drop is not seen in B/Ca.

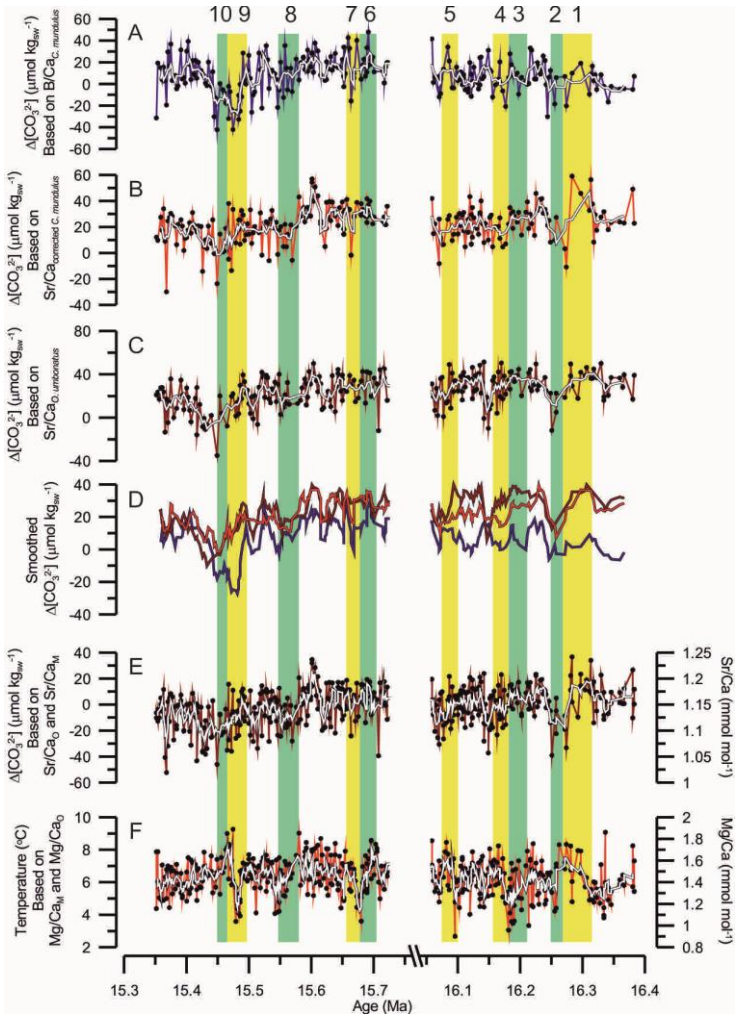


**Figure 55 – Relative changes in $\Delta[CO_3^{2-}]$ according to different proxies. A) B/Ca in C. mundulus using the calibration of Yu and Elderfield (2007). B) Sr/Ca in *C. mundulus*, using the equation of Dawber and Tripati (2012a) corrected to *O. umbonatus* values by comparison of the means C) Sr/Ca in O. umbonatus using the calibration of Dawber and Tripati (2012a). D) Smoothed $\Delta[CO_3^{2-}]$ stacked data to show the similarities between A-C. Blue is the smoothed B/Ca record, Light red is $Sr/Ca_M$ and dark red is $Sr/Ca_O$. E) $\Delta[CO_3^{2-}]$ from $Sr/Ca_M$ and $Sr/Ca_O$ using the calibration of Dawber and Tripati (2012a). $Sr/Ca_M$ was converted to $Sr/Ca_O$ using a conversion factor of x1.23, which was calculated by division of the means of the records of $Sr/Ca_M$ and $Sr/Ca_O$. F) Temperature from $Mg/Ca_M$ and $Mg/Ca_O$ using the calibration of Lear et al. (2002). $Mg/Ca_O$ was converted to $Mg/Ca_M$ using a conversion factor of x0.73, which was calculated by division of the means of the records of $Mg/Ca_M$ and $Mg/Ca_O$.**

There is another change in $\Delta[CO_3^{2-}]$ that occurs from ~15.50 Ma to approximately the youngest part of the record at ~15.35 Ma, coincident with T9 and T10. The decline begins sometime between 15.48 and 15.50 Ma and reaches its minimum sometime between 15.48 and 15.43 Ma. The timing and magnitude of the minima in the smoothed record (Figure 55d) is dependent on the proxy

being examined, with $B/Ca_M$ showing a minimum at ~15.48 Ma and $Sr/Ca_O$ showing a minimum of a lower magnitude at ~15.43Ma. The timing of the minimum in $Sr/Ca_M$ is intermediate between the two records at ~15.45Ma but the amplitude of the change (~20 μmol $kg_{sw}^{-1}$) is smaller than either $B/Ca_M$ (~50 μmol $kg_{sw}^{-1}$) or $Sr/Ca_O$ (~30 μmol $kg_{sw}^{-1}$). All three records have fully recovered from the minimum in $\Delta[CO_3^{2-}]$ by ~15.40 Ma (Figure 55). The differences in the magnitudes of the estimates of changes in $\Delta[CO_3^{2-}]$ in B/Ca and Sr/Ca cannot be put down solely to differences in the sensitivity of the calibrations. Both $Sr/Ca_M$ and $Sr/Ca_O$ use the same core-top calibration to calculate $\Delta[CO_3^{2-}]$ (Dawber and Tripati, 2012a). Species specific vital effects have been taken into account by correcting $Sr/Ca_M$ to $Sr/Ca_O$ by finding the quotient of the means of both records (1.23), and then multiplying $Sr/Ca_M$ by this quotient. In this case the two species may experience different magnitude changes in $\Delta[CO_3^{2-}]$ as *C. mundulus* is predominantly epifaunal and *O. umbonatus* is shallow infaunal (Rathburn and Corliss, 1994), however both species appear to show good agreement with one another (Figure 55d & e).

As for the differences in magnitude between $\Delta[CO_3^{2-}]$ (Figure 55d) calculated from Sr/Ca and from B/Ca, these may be down to the two proxies' sensitivities to other factors. Sr/Ca, for example, may respond to temperature as well as $\Delta[CO_3^{2-}]$ (Dawber and Tripati, 2012a), and its sensitivity to changes in $\Delta[CO_3^{2-}]$ was found to be lower than that of Mg/Ca, Li/Ca, and B/Ca by Dawber and Tripati (2012a). However, the change in $\Delta[CO_3^{2-}]$ over intervals T9 and T10 does not appear to follow the change in temperature implied by Mg/Ca (Figure 55f), and diagenetic effects on Mg/Ca and Sr/Ca were discounted in Section 4.4.1.

#### *5.4.1.2.2.1 Statistical analysis of relationships in Figure 55*

##### *5.4.1.2.2.1.1 Agreement between Sr/Ca and B/Ca*

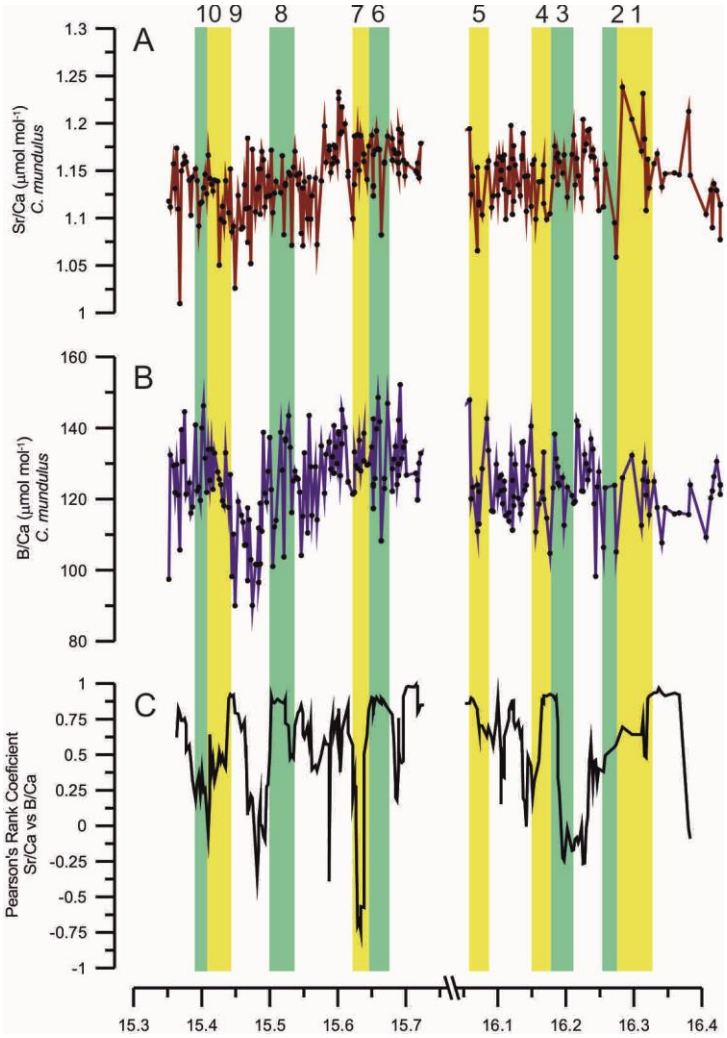


**Figure 56 – Correlation between Sr/Ca and B/Ca. A) Sr/Ca of *C. mundulus*. B) B/Ca of *C. mundulus*. C) Moving Pearson's Correlation coefficient of Sr/Ca and B/Ca.**

In general, B/Ca and Sr/Ca agree with one another. A moving Pearson's Correlation Coefficient gives a mean Pearson's rank of ~0.53, showing that in general the two records follow one another. The moving Pearson's rank coefficient (Figure 56c) shows a positive correlation across most of the record except between intervals 8 and 9, which I identify as showing a decrease in $\Delta[CO_3^{2-}]$ in Figure 55. An additional <0 correlation coefficients occurs during interval 7. This means that, in general, B/Ca and Sr/Ca are reflecting changes in the same parameter. This is most likely to be $\Delta[CO_3^{2-}]$ as both B/Ca (Rae et al., 2011; Yu and Elderfield, 2007; Yu et al., 2008; Yu et al., 2010b) and Sr/Ca

(Dawber and Tripati, 2012a; Raitzsch et al., 2010; Rathmann and Kuhnert, 2008; Rosenthal et al., 2006) have been shown to reflect changes in that parameter. However, while this shows that they do agree on the general direction of the trend, a mean Pearson's rank of 0.53 suggests that the magnitude of the changes are not consistent throughout, therefore the estimates of changes in $\Delta[CO_3^{2-}]$ are best left as qualitative.

#### 5.4.1.2.3 Surface water $\Delta[CO_3^{2-}]$

No core-top calibration currently exists for $B/Ca_G$ and $\Delta[CO_3^{2-}]$, though a study into the effects of growth rates on boron incorporation into the calcite test of *G. sacculifer* has recently been conducted (Gabitov et al., 2014), and several core-top calibrations with $[CO_3^{2-}]$ have been produced (Foster, 2008; Ni et al., 2007). A culture experiment performed by Allen et al. (2012) on *G. sacculifer* found a positive relationship between B/Ca and pH, $[CO_3^{2-}]$, salinity, and $[B(OH)_4^-]$. When $[CO_3^{2-}]$ was examined independently of other DIC parameters (primarily by controlling $[B(OH)_4^-]$), $[CO_3^{2-}]$ and B/Ca were found to have a negative relationship in *G. sacculifer*. This throws doubt on the viability of B/Ca as a proxy for $\Delta[CO_3^{2-}]$ and $[CO_3^{2-}]$ in planktonic foraminifera. Allen and Honisch (2012) caution that the environmental controls on B/Ca in planktonic foraminifera are not well constrained given that B/Ca appears to vary with various species of DIC, temperature, and salinity as well as $[B(OH)_4^-/[HCO_3^-]_{seawater}$. In some cases, B/Ca appears not to vary with any of these parameters, but the partition coefficient of B into calcite ($K_D = B/Ca_{calcite}/([B(OH)_4^-/[HCO_3^-]_{seawater})$) does (Foster, 2008). Past variation in $B/Ca_{seawater}$ are poorly constrained, limiting its use as an absolute $\Delta[CO_3^{2-}]$ proxy, though relative changes can still be calculated.

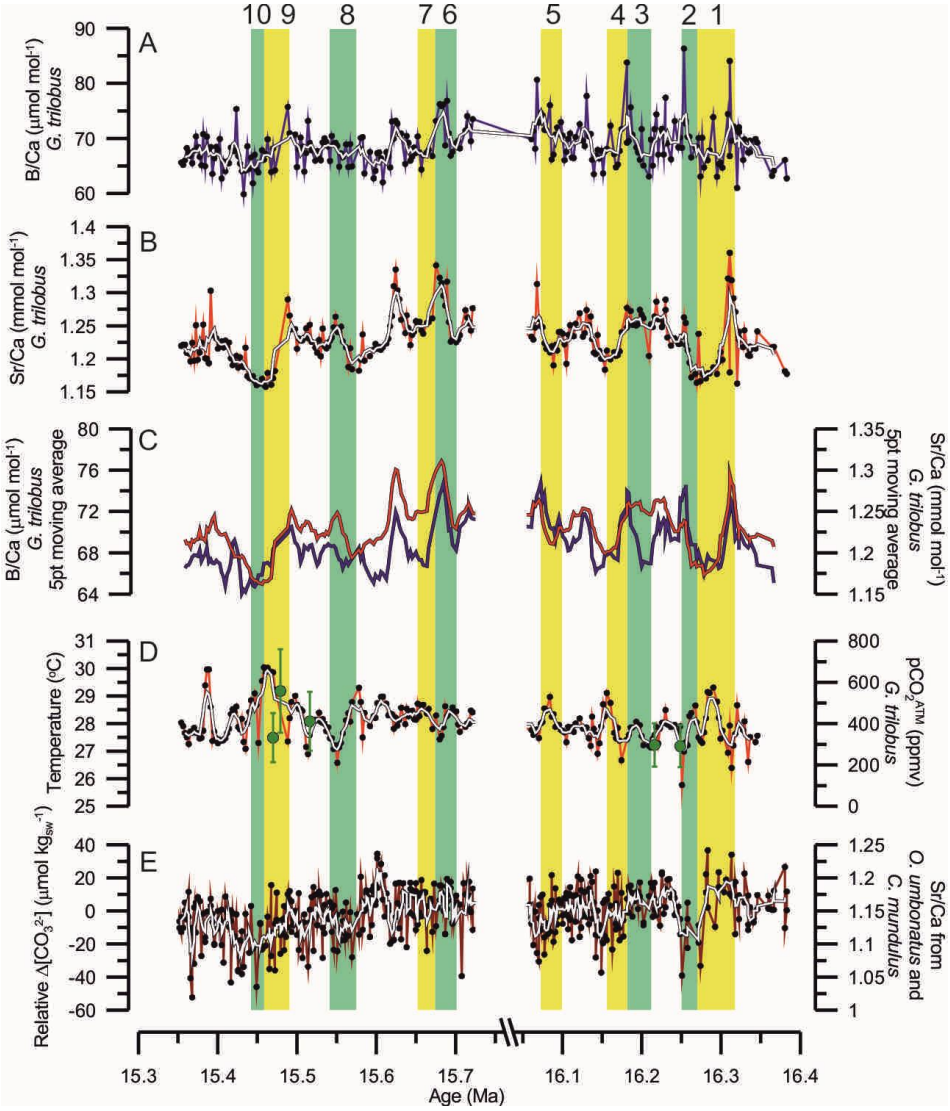


**Figure 57 – $\Delta[CO_3^{2-}]$ proxies from the surface ocean. A) $B/Ca_G$. B) $Sr/Ca_G$. C) $B/Ca_G$ and $Sr/Ca_G$ moving averages compared. D) Red line with white moving average: Temperature changes derived from $Mg/Ca_G$ using the temperature calibration of Dekens et al. (2002). Green points: $pCO_2^{ATM}$ derived from $\delta^{11}B$ from *G. trilobus* (Sosdian, S. 2014 pers. comm.). E) $\Delta[CO_3^{2-}]$ from $Sr/Ca_M$ and $Sr/Ca_O$ as Figure 55e.**

Similarly, core top studies into the relationship between Sr/Ca in *G. trilobus* ($Sr/Ca_G$) and $\Delta[CO_3^{2-}]$ have not been conducted but numerous temperature and $Sr/Ca_G$ calibrations do exist (Cleroux et al., 2008; Mortyn et al., 2005). Mortyn et al. (2005) examine the effect of $[CO_3^{2-}]$ on Sr/Ca, however $\Delta[CO_3^{2-}]$ is not looked at specifically. One culture calibration by Dueñas-Bohórquez et al. (2009) examined Ω (the saturation state) and $[CO_3^{2-}]$, however only three data points exist for *G. trilobus* within that calibration. As such, $B/Ca_G$ and $Sr/Ca_G$ are presented without quantification of the changes in surface $\Delta[CO_3^{2-}]$ that these may represent, and only a more qualitative approach is taken.

Figure 57 shows B/Ca (Figure 57a) and Sr/Ca (Figure 57b) from *G. trilobus* from Ceara Rise. As a planktonic foraminifera, *G. trilobus*' test is much more fragile than either *C. mundulus*' or *O. umbonatus*'. As such it is far more prone to diagenetic effects, including dissolution (e.g., Edgar et al., 2013). If $Sr/Ca_G$ and $B/Ca_G$ are affected by dissolution, then they would primarily reflect changes in bottom water $\Delta[CO_3^{2-}]$. However, as temperature from $Mg/Ca_G$ co-varies with neither $Sr/Ca_G$, nor $B/Ca_G$, a strong dissolution effect on the $\Delta[CO_3^{2-}]$ signal is discounted. None the less, $B/Ca_G$ and $Sr/Ca_G$ show similar features (Figure 57c). In addition, they show many similarities to Sr/Ca and B/Ca in the benthic record (Figure 57e), including the implied rise in $\Delta[CO_3^{2-}]$ at the end of T2, and the same drop and recovery over intervals T9 and T10. This suggests that major trends in all of the B/Ca and Sr/Ca records represent whole water-column changes in $\Delta[CO_3^{2-}]$.

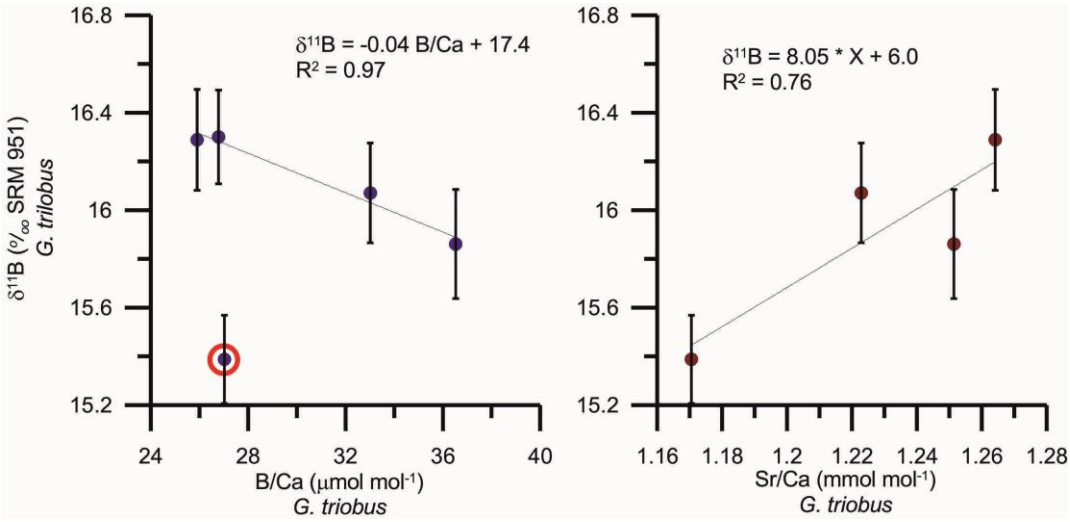


**Figure 58 – Attempt to correlate $\delta^{11}B$ in *G. trilobus* with B/Ca and Sr/Ca. The left panel shows the correlation with B/Ca for which there seems to be good agreement if the highlighted sample is ignored. The right panel shows the result of this with Sr/Ca for which one result was also ignored due it being a flier.**

The apparently good agreement between $\delta^{11}B_G$ and $B/Ca_G$ and $Sr/Ca_G$, suggests that the $Sr/Ca_G$ and $B/Ca_G$ records could be used as a high resolution stand-in for direct $\delta^{11}B$ measurements as trace element/Ca ratios are easier to generate than $\delta^{11}B$. If this were the case, it would allow for a more quantitative interpretation of the $B/Ca_G$ and $Sr/Ca_G$ records. To explore this possibility, the

$\delta^{11}B$ data were compared directly with the trace metal data from the same samples (Figure 58). In both cases, one result from $B/Ca_G$ and $Sr/Ca_G$ (representing 1/5 of the total data for each correlation) had to be ignored to produce a correlation. Despite the good agreement between $B/Ca_G$ and $Sr/Ca_G$ in the down-core record (Figure 57c) the correlations are of different signs. If $\delta^{11}B_G$ reflects pH, and $B/Ca_G$ and $Sr/Ca_G$ reflect $\Delta[CO_3^{2-}]$, then increased $\Delta[CO_3^{2-}]$ should correspond with lower pH. $B/Ca_G$ and $\delta^{11}B_G$ do show the negative correlation that would be expected in this case (flier notwithstanding), however $Sr/Ca_G$ does not. This may indicate that $Sr/Ca_G$ is a less reliable proxy for $\Delta[CO_3^{2-}]$ than $B/Ca_G$, but given the small sample size it is difficult to draw a strong conclusion. In this study therefore, interpretation of the planktonic $B/Ca_G$ and $Sr/Ca_G$ records remains qualitative.

#### 5.4.1.2.4 Whole Ocean Changes in Seawater $[CO_3^{2-}]$ During the Miocene Climatic Optimum

Ocean $[CO_3^{2-}]$, ALK, and DIC are controlled by changes in ocean circulation (Sigman and Boyle, 2000; Yu et al., 2010a), the rate of supply of ALK (e.g., from weathering) versus the rate of removal (e.g., the rate of burial of carbonates) to and from the oceans (Armstrong and Allen, 2011; Sigman and Boyle, 2000; Yu et al., 2010a), changes in export productivity and changes in the $CaCO_3$/Corg rain rate of biogenic carbon(Sigman and Boyle, 2000), and changes in sediment dissolution driven by organic matter remineralisation (Francois et al., 1997; Sigman and Boyle, 2000). Here I examine changes in the various $\Delta[CO_3^{2-}]$ proxies across three prominent warming events identified in chapter 4 (Mid-Miocene ITCZ Response to Changes in the Northern Hemisphere Ice Sheets) T1 (~16.30 Ma), T4 (~16.18 Ma), and T9 (~15.50 Ma). All three warmings are associated with a decrease in $\Delta[CO_3^{2-}]$ identified in both planktonic (*G. trilobus*) and benthic (*C. mundulus* and *O. umbonatus*) foraminiferal species.

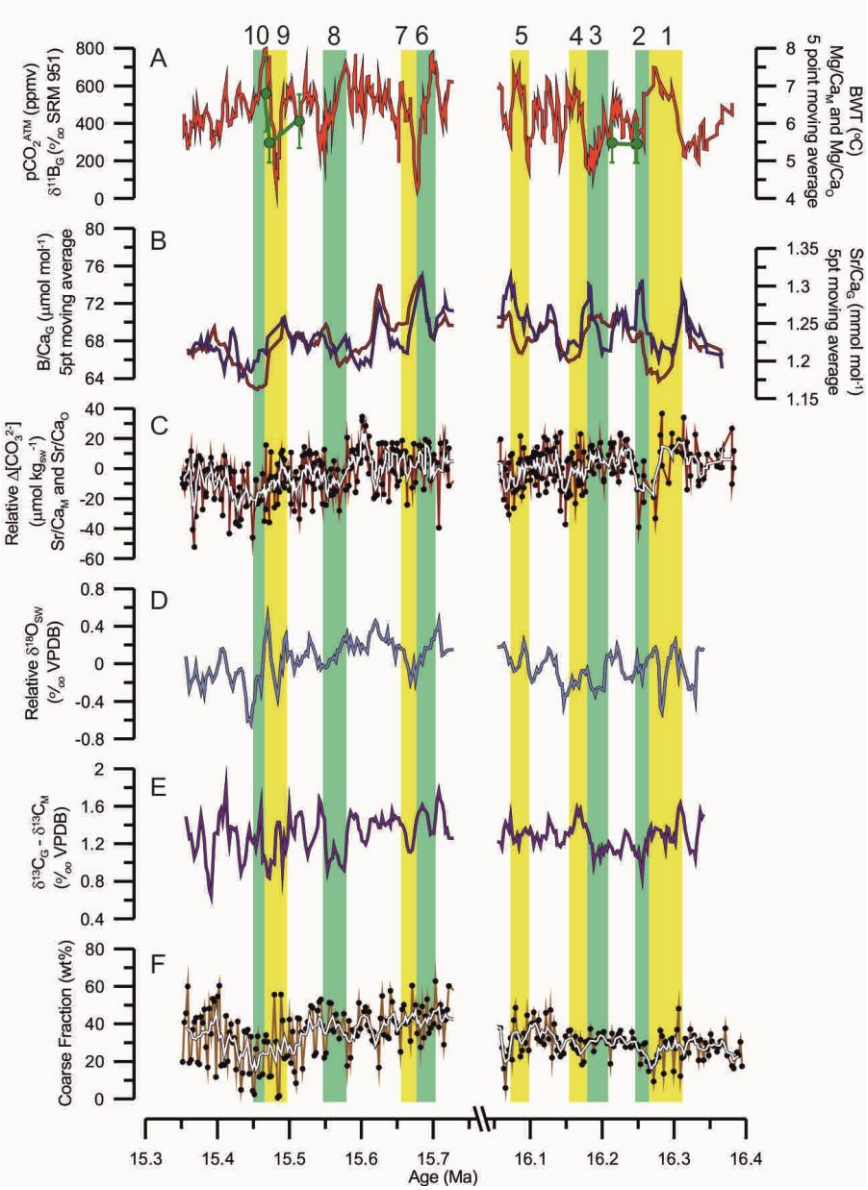


**Figure 59 – DIC changes at Ceara Rise. A) BWT (red line) from $Mg/Ca_M$ and $Mg/Ca_O$ and $pCO_2^{ATM}$ (green symbols). BWT is shown as the 5-point moving average. B) $B/Ca_G$ (blue line) and $Sr/Ca_G$ (dark red line) 5-point moving averages. $\Delta[CO_3^{2-}]$ as calculated from $Sr/Ca_O$ and $Sr/Ca_M$. D) $\delta^{13}C_{P\text{-}B}$, 5-point moving average $\delta^{13}C_G$ – 5-point moving average $\delta^{13}C_M$. E) $\delta^{13}C_M$. F) Coarse fraction (>63 μm) wt%.**

The change across T9 appears to be driven by changes in sea level and the rate of removal of carbonate from the oceans. The initial decrease in $pCO_2^{ATM}$ across T9 appears to coincide with the decrease in both surface and deep $\Delta[CO_3^{2-}]$ (Figure 59a, b, & c), although the exact timing is difficult to determine due to the lower resolution of the $pCO_2^{ATM}$ record compared to $\Delta[CO_3^{2-}]$. At the end of T9 $pCO_2^{ATM}$ increases, which coincides with the beginning of the increase in $\Delta[CO_3^{2-}]$, as would be expected from the relationship between $pCO_2^{ATM}$, and DIC and ALK (Sigman and Boyle, 2000). Across T1, surface $\Delta[CO_3^{2-}]$ decreases

rapidly and appears to mirror the increase in BWT (Figure 59a & b), which is consistent with a presumed increase in $pCO_2^{ATM}$ associated with the warming. Bottom water $\Delta[CO_3^{2-}]$ also decreases at this time (Figure 59c), though the decrease occurs later.

These changes in $\Delta[CO_3^{2-}]$ may be a result of the balance of ALK and DIC in the global ocean, and so may be associated with changes in sea level. Changes in sea level can affect ALK and DIC through shelf-basin partitioning of the deposition of $CaCO_3$ in the case of a fall in sea level (e.g., Merico et al., 2008), or through the "coral reef hypothesis" in the case of a rise in sea level (e.g., Opdyke and Walker, 1992; Vecsei and Berger, 2004). In essence, the coral reef hypothesis posits that an increase in sea levels would increase the shelf area available for growth of $CaCO_3$-producing organisms (such as corals). Through the process $2HCO_{3(aq)}^{2-} + Ca_{(aq)}^{2+} \leftrightarrow CaCO_{3(s)} + CO_{2(g)}$, $pCO_2^{ATM}$ rises and ALK decreases.

T9 is associated with a long decline in $\Delta[CO_3^{2-}]$ and an overall decrease in $\delta^{18}O_{sw}$ of ~0.4 ‰, equivalent to a drop in eustatic sea level of 20-40m (section 4.4.2.3). The drop in $\Delta[CO_3^{2-}]$ would imply a removal of $[CO_3^{2-}]$ from the oceans and thus an increase in $CaCO_3$ burial with respect to weathering (Sigman and Boyle, 2000) and could conceivably be caused by the growth of more calcite-producing organisms. The five-point-moving-average of the composite $Sr/Ca_M$ and $Sr/Ca_O$ $\Delta[CO_3^{2-}]$ suggests that the drop in $\Delta[CO_3^{2-}]$ was around 20 μmol $kg_{sw}^{-1}$. In the modern Atlantic, Ceara Rise has $\Delta[CO_3^{2-}]$ of ~-2.9 μmol $kg_{sw}^{-1}$ at ~4.5km depth to ~42 μmol $kg_{sw}^{-1}$ at ~2.5 km depth (Elderfield et al., 2006; Martin et al., 2002), so this change is the same $\Delta[CO_3^{2-}]$ change Site 926 (modern $\Delta[CO_3^{2-}]$ ~22 μmol $kg_{sw}^{-1}$ at ~3.6 km depth) would have experienced had the CCD shoaled by ~1 km.

The MMCO is associated with a ~500 m shallower CCD than the modern (Pälike et al., 2012), however the CCD shoaling from ~4.7 km to ~4.2 km below sea level occurred at ~17 Ma and remained there until ~16 Ma whereupon it

returned to its pre-MMCO level. The CCD does not appear to have been particularly dynamic between 16 and 13 Ma, though the resolution of this study may be picking up changes that could not be seen by Pälike et al. (2012). This is unlikely as their study is based on directly observable physical properties from oceanic cores around the globe. The relatively large changes in $\Delta[CO_3^{2-}]$ recorded here in the absence of evidence for associated changes in the CCD is intriguing, and may suggest at specific mechanisms for causing these changes such as variations in the $CaCO_3$:$C_{org}$ rain rate (Sigman and Boyle, 2000)

The total increase in $pCO_2^{ATM}$ implied by the $\delta^{11}B_G$ records across T9 (~150 ppmv, S.M. Sosdian, 2014, pers. comm.) is of equivalent size to that experienced since the last glacial maximum (~120 ppmv, Petit et al., 1999), the change in sea level implied by this record (20-40m) is much smaller (~100m at the LGM, Bard et al., 1990). This is perhaps unsurprising as ice sheets have a non-linear response to changes in $pCO_2^{ATM}$ (Pollard and DeConto, 2005; Rohling et al., 2013). Rohling et al. (2013) shows that there is a plateau between ~400 and 600 ppmv $pCO_2^{ATM}$ in which sea levels do not change much in response to changes in $pCO_2^{ATM}$. A change of 20-40m falls well within the envelope of uncertainties estimated by Rohling et al. (2013) for sea level changes in that $pCO_2^{ATM}$ range. As the estimates for $pCO_2^{ATM}$ from the MMCO fall within that range (Foster et al., 2012; Greenop et al., 2014; Kürschner and Kvaček, 2009; Zhang et al., 2013), a smaller response of sea level in the MMCO compared to the LGM for a given change in $pCO_2^{ATM}$ is to be expected.

The $\Delta[CO_3^{2-}]$ changes across the warmings T1, and T4, appear to be better explained by changes in export productivity. Figure 59d shows $\delta^{18}O_{sw}$ calculated using $\delta^{18}O_M$ and $Mg/Ca_M$ using the calibrations of Marchitto et al. (2014) and Lear et al. (2002), respectively. The change across T1 does not appear to coincide with any long-lasting changes in $\delta^{18}O_{sw}$. There is an increase of ~0.4‰ prior to T1 and a short-lived trough that bottoms out at ~-0.5 ‰ at 16.28 Ma, but nothing that appears to be affecting, or a response to, changes in

$\Delta[CO_3^{2-}]$. Similarly, the decrease in $\Delta[CO_3^{2-}]$ during T4 and the increase in $\Delta[CO_3^{2-}]$ at 15.62 Ma similarly show no strong coeval change in $\delta^{18}O_{sw}$.

From ~16.19 Ma to ~16.16 Ma $\delta^{13}C_{P\text{-}B}$ increases by ~0.6 ‰, implying reduced efficiency in export productivity. This is associated with an increase in temperatures, as would be expected from the relationship of export productivity to $pCO_2^{ATM}$ (Figure 46), but it is also associated with a decrease in $B/Ca_G$ and $Sr/Ca_G$. This is more or less the inverse of the scenario found by Kender et al. (2014), in which they saw an increase in ocean $[CO_3^{2-}]$ associated with a drop in sea level. They attributed this to an increase in continental wreathing increasing the supply of ALK to the oceans. A decrease in coarse fraction might be expected to accompany an increase in weathering rates as more clays are supplied to Ceara Rise, however no such change is seen (Figure 59f). Rather than an increase in the supply of ALK from weathering, this may indicate a decrease in the removal of ALK from carbonate burial. The reduction in efficiency of export productivity implied by $\delta^{13}C_{P\text{-}B}$ (Figure 59e) could explain this. The increased temperatures may be due to a reduction in $C_{org}$ burial that accompanies this and slowed the rate of draw-down of $pCO_2^{ATM}$.

The change at 15.62 Ma in which benthic records of $\Delta[CO_3^{2-}]$ show an increase and planktonic records of $\Delta[CO_3^{2-}]$ increase is harder to explain. There is no large change in $\delta^{13}C_{P\text{-}B}$ (Figure 59d) to accompany this change in $\Delta[CO_3^{2-}]$ and coarse fraction (~20%, based on the moving average) that is not much larger than the background variability (Figure 59f). This interval may represent a brief halt in ocean mixing, but a change in $\delta^{13}C_{G\text{–}M}$ might be expected to accompany it.

### *5.4.2 The Organic Carbon Cycle at Ceara Rise*

#### *5.4.2.1 Productivity Changes at Ceara Rise*

Productivity changes are best tracked in these records using BFAR (Figure 60a) as the Cd/Ca data are unreliable (Appendix 4, section 8.4). BFAR maxima occur at 16.31 Ma (at the start of T1), 16.21 Ma, 16.12 Ma, 15.67 Ma (at the end of

T6), 15.55 Ma (at the end of T8), and 15.48 Ma (during T9). The first three are associated with no significant changes in $\delta^{13}C_G$ (Figure 60b) and share no common features in $\delta^{13}C_{P-B}$ (Figure 60c).

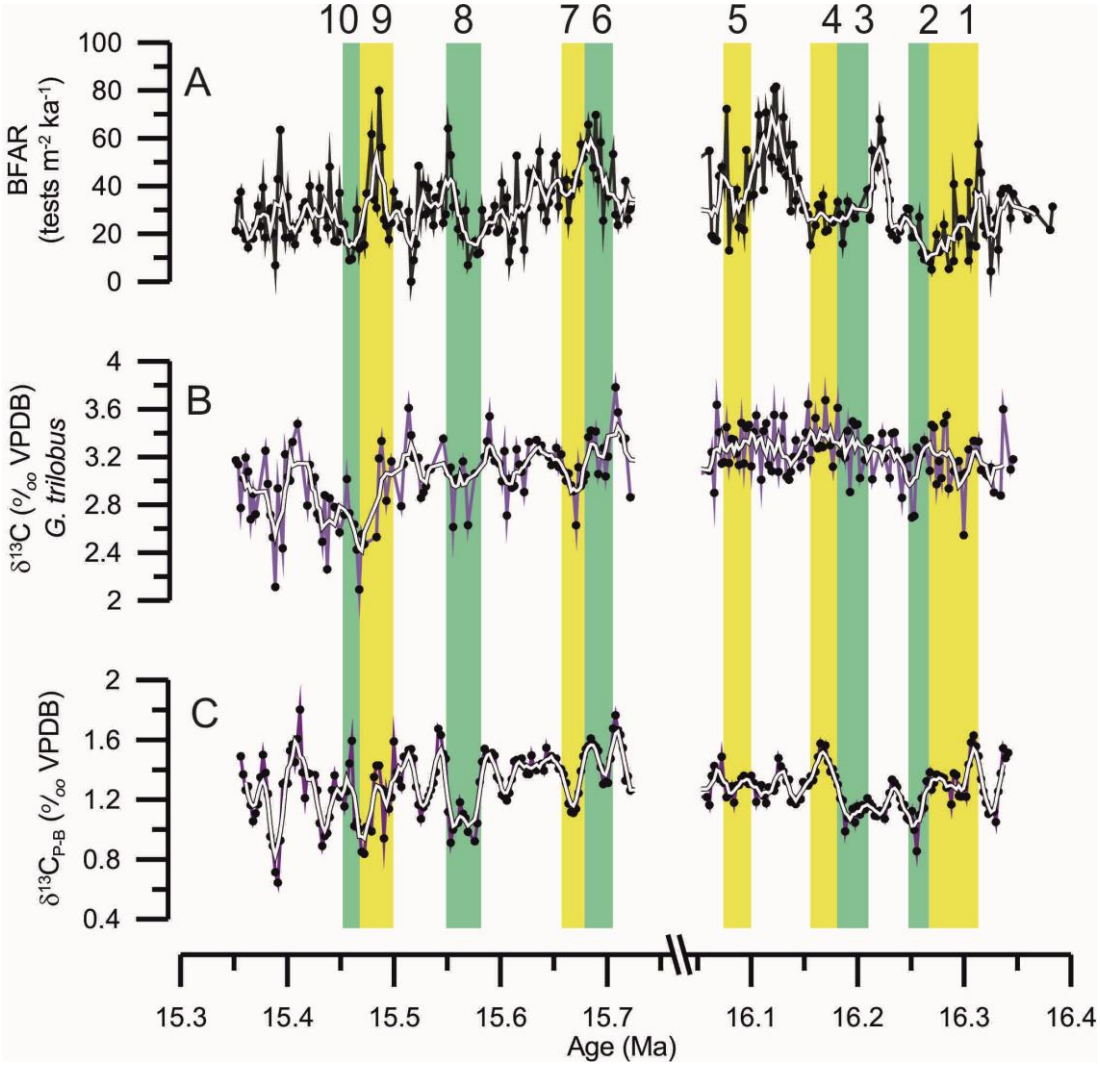


**Figure 60 – Productivity at Site 926. A) BFAR. Only tests >250 μm were counted as these were the tests used for trace metal analysis. B) $\delta^{13}C$ *G. trilobus*. C) $\delta^{13}C$ *G. trilobus* – $\delta^{13}C$ *C. mundulus* (planktonic-benthic).**

Within T9 there is a spike in BFAR of ~60 tests $m^{-2}$ $ka^{-1}$ and a trend towards lighter $\delta^{13}C_G$ (Figure 60b). The BFAR maximum suggests a maximum in productivity, though the trend towards lighter $\delta^{13}C_G$ may indicate a drop in PP as more $^{12}C$ becomes available to build carbonate. Alternatively, the increase in the lighter carbon isotope may coincide with upwelling which would bring nutrient rich waters to the surface and increased PP. The minimum in $\delta^{13}C_{P-B}$

(Figure 60c) associated with T9 suggests that export productivity was more efficient and corroborates the presence of increased upwelling. At the end of T9 BFAR decreases and $\delta^{13}C_G$ trends towards heavier values. This may indicate a cessation of stronger upwelling and thus reduced surface productivity.

BFAR is related to surface water PP but is a direct indication of the rate of growth of benthic populations. As increased rate of growth of benthic organisms is related to increased respiration rates, and thus utilisation of oxygen at the sea floor (Wilson et al., 2014). Maxima in BFAR should therefore coincide with minima in bottom water oxygenation as the organisms present scavenge the free oxygen for their own respiration.

### *5.4.2.2 Bottom water oxygenation*

Bottom water oxygenation at ODP Site 926 cannot easily be quantified, however a qualitative overview can be taken from U/Ca, Mn/Ca and a combination of both. Dissolved $Mn^{2+}$ is unstable in the presence of oxygen and is oxidised to insoluble $MnO_2$ (Calvert and Pedersen, 1996; Chun et al., 2010), and so Mn/Ca roughly follows the bottom water oxygenation state (Groeneveld and Filipsson, 2013). Conversely, uranium exists in oxygenated sea water as soluble $[UO_2(CO_3)_3^{4-}]$, and precipitates out in sub-oxygenating conditions as $UO_2$ (Chun et al., 2010). From this it can be seen that if oxygenation conditions are changing in the bottom waters, Mn/Ca and U/Ca should show an approximately negative relationship

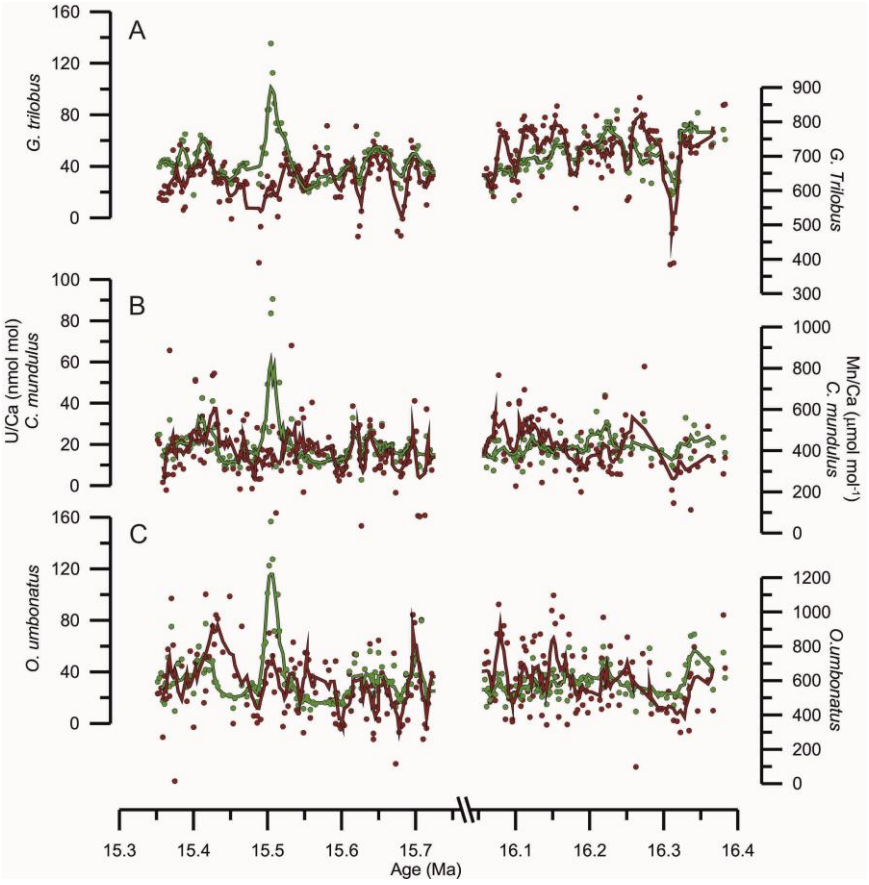


**Figure 61 – Mn/Ca versus U/Ca in the three species of foraminifera analysed in this study. Green points and lines are U/Ca (left axes), red points and lines are Mn/Ca (right axes). Data are displayed, but only the smoothed 5-point average of the data is shown for clarity to bring out the similar trends in both datasets. A) *G. trilobus*. B) *C. mundulus*. C) *O. umbonatus*. All three species display a generally positive correlation, which suggests that the uranium is associated with authigenic manganese coatings on the foraminiferal tests.**

What is instead seen is a generally positive correlation between the two metrics in all species (Figure 61 and Figure 62a), suggesting that Mn and U are related. Rather than following oxygenation, U may be forming in association with post-depositional manganese oxide coatings on the foraminiferal tests. These authigenic coatings are impossible to tell from lattice-bound uranium by whole-test analysis with ICP-MS, though U/Ca in authigenic coatings can be as high as 300 nmol $mol^{-1}$, whereas lattice-bound U is typically in the 1-15 nmol $mol^{-1}$ range (Boiteau et al., 2012). Values obtained in this study fall into the range of 20-160 nmol $mol^{-1}$ (Figure 48)., which may suggest alternating intervals of oxygenating and sub-oxygenating conditions The reducing step was used when cleaning the foraminiferal tests for trace metal analysis (Appendix 1, section 8.1), so the effect of coatings on the tests should have been minimal, none the less the U/Ca records in both the benthic and planktonic foraminifera show the same features, suggesting that either the U/Ca record shows a whole ocean signal or shows post-depositional effects. The latter is far more likely.

Those caveats in mind, and assuming that uranium and manganese bound in coatings are still strongly affected by the sea water oxygenation state, I propose that in addition to examining Mn/Ca and U/Ca ratios, the ratio of Mn/Ca to U/Ca in foraminiferal tests should give a qualitative estimate of significant changes in bottom water anoxia; a high Mn/Ca to U/Ca ratio should suggest more oxygenating conditions as conditions favour the precipitation of $MnO_2$ in authigenic coatings, and a low Mn/Ca to U/Ca ratio should indicate less oxygenating conditions as conditions favour the precipitation of $UO_2$. U/Ca also shows a strong negative relationship with $\Delta[CO_3^{2-}]$ (chapter 3, thesis; Keul et al., 2013; Raitzsch et al., 2011), but a $\Delta[CO_3^{2-}]$ effect on U/Ca has been ruled out in this record in favour of changes in redox chemistry (section 5.4.1.2.1, above).

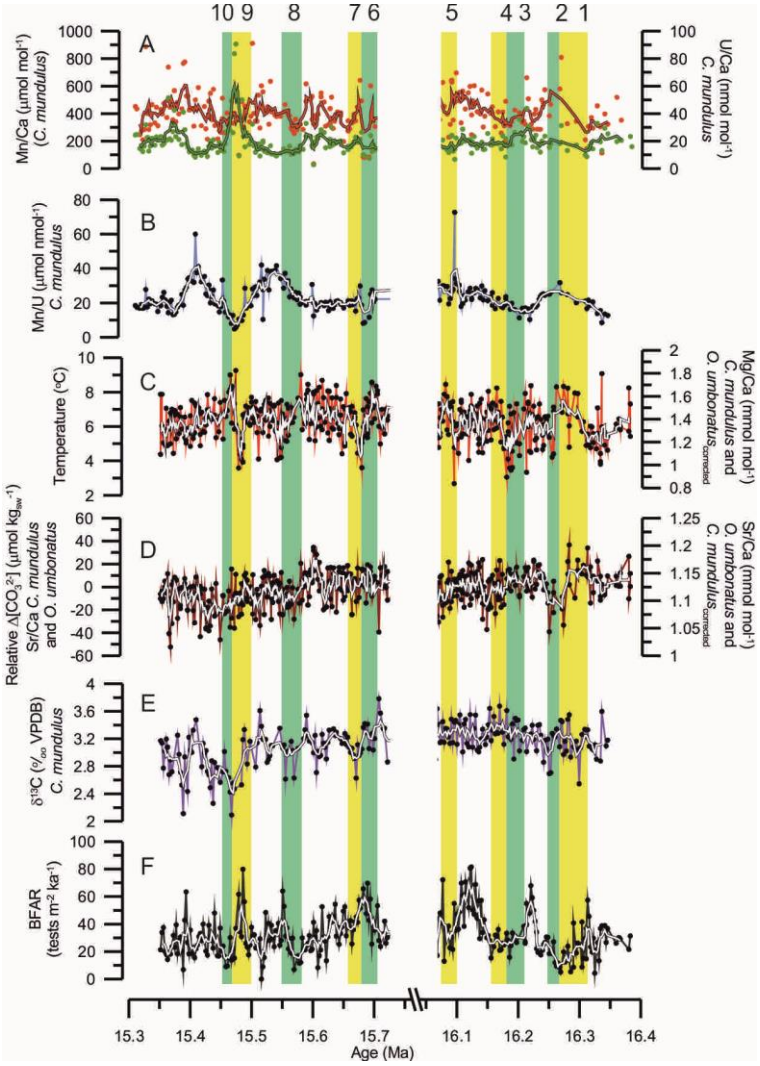


**Figure 62 – Changes in bottom water oxygenation. A) Mn/Ca$_M$ (orange) and U/Ca$_M$ (green). The line shown is the 5-point moving average. The age model for Mn/U has been adjusted to account for an assumed depth of the redox horizon of 45cm below the sediment-water interface (c.f. Francois et al., 1993) so that changes in Mn/U should appear coeval with changes in other proxies. B) Mn/U ratio in *C. mundulus*, calculated from Mn/Ca and U/Ca ratios. C) BWT changes calculated from a composite record of Mg/Ca$_M$ and Mg/Ca$_O$. Mg/Ca$_O$ has been corrected to Mg/Ca$_M$ using a correction factor of x0.73. The Mg/Ca temperature equation of Lear et al. (2002) was used. The value of Mg/Ca is shown on the second Y axis. D) Relative changes in Δ[$CO_3^{2-}$], calculated from a composite record of Sr/CaM and Sr/CaO. Sr/CaM has been corrected to Sr/CaO using a correction factor of x1.23. The Sr/Ca Δ[$CO_3^{2-}$] calibration of Dawber and Tripati (2012a) was used. The value of Sr/Ca is shown on the second Y axis. E) $\delta^{13}C$ in *C. mundulus*. F) BFAR, only including tests >250µm.**

Changes in the redox chemistry of the bottom waters at ODP Site 926 during the MMCO could be affected by a number of factors. Sedimentation rate is a potential candidate (Francois et al., 1993), however the sedimentation rate over the intervals studied appears to remain constant, or at least no indication of large changes in sedimentation rate are seen (Section 2.5), and so this is discounted. Changes in bottom water temperature may affect bottom water

oxidation state by increasing the metabolic rate of marine organisms and thus increasing their utilisation of oxygen (e.g., Wilson et al., 2014). In addition, oxygen is more soluble at lower temperatures, so a bottom water mass with a colder source region may initially have higher levels of dissolved oxygen. Thus we would expect to see a slight positive correlation between increased BWT and anoxia.

The lower interval has a very slight increase in Mn/U across T1 that appears to covary with a general trend towards warmer BWT (Figure 62b & c). This might suggest an increase in oxygenation as the bottom waters warmed. The solubility of oxygen decreases with increasing temperature, which suggests that other factors were responsible for the variations in oxygenation levels. In interval T3 an increase in Mn/U coincides with a decrease in BWT. A similar covariance is seen in T8 which shows a cooling of similar magnitude to T3 (~2$^{o}$C) but shows no response in Mn/U. Across T10 and T9 a minimum in Mn/U coincides with a maximum in BWT at ~ 15.46 Ma. Similarly, Mn/U increases steadily after T10, going from ~10 μmol nmol$^{-1}$ to more than 40 μmol nmol-1, though there is no clear change in BWT to accompany it. Therefore temperature can be ruled out as the dominant control on any variability recorded by Mn and U.

Another factor that may be affecting bottom water oxygenation is variations in the water mass that bathes ODP Site 926 during the MMCO. Periodic changes in the source waters may affect the redox conditions at the sea floor by bringing cold, oxygen rich waters with them, or older and more oxygen-depleted waters. A change in bottom water mass might also be expected to impact benthic $\delta^{13}C$ (Figure 62e) and $\Delta[CO_3^{2-}]$ (Figure 62d). In intervals T9 and T10 $\delta^{13}C_M$ shows a trend towards lighter values from ~1.8 to ~1.4 ‰ (Figure 62e) and $\Delta[CO_3^{2-}]$ from Sr/Ca appears to also show a steady decline of around ~20 μmol $kg_{sw}^{-1}$ (Figure 62d). If these redox changes were caused by changes in bottom water mass then we would expect to see coeval variability between $\delta^{13}C$

and Mn/U, but not BFAR. The decrease in Mn/U across T9 (Figure 62b) is coeval with an increase in BFAR (Figure 62f) and thus an increase in productivity is a far more likely mechanism to cause this change in oxygenation.

#### 5.4.2.2.1 The timing of Redox changes

Discerning the timing of signals within U/Ca and Mn/Ca relative to other proxies is problematic. The precipitation and mobilisation of uranium and manganese in sediments depends upon the depth of the boundary between oxidising and reducing conditions (the redox boundary). Finding the depth of that horizon is possible, but requires knowledge of the concentration of uranium in both sea water and the sediment (Francois et al., 1993). Francois et al. (1993) found the depth of the redox boundary of U in Indian Ocean sediments to have varied between 4.5 and 45cm over the Holocene, which amounts to an error in discerning the timing of the cause of any given change in Mn/U in this study of +2.6 ka to +26 ka.

Assuming the uranium redox horizon contemporaneous with changes in other proxies is always below the sediment-water interface, any changes in the redox conditions at the sea floor will be recorded deeper in the sediments and appear to be too old. Further assuming that the maximum depth of the redox horizon is 45cm, the maximum depth found by Francois et al. (1993), means that we can adjust the timescale of the Mn/U record by subtracting 45cm from the mbsf scale of the U/Ca and Mn/Ca results. This has been done for the whole record, however a strong caveat is that the redox horizon does not remain at a constant depth through time but instead depends on the sediment accumulation rate (S), the dry bulk density ($\varrho$), $[U]_{seawater}$, the pore water diffusion coefficient for U (D), and $[U]_{sediment}$ (Francois et al., 1993) by the relationship (21):

$$z_U = \frac{D \times C}{S \times \rho \times [U]_{sediment}} \quad (21)$$

S, ϱ, and D are known (Klinkhammer and Palmer, 1991; Shipboard Scientific Party, 1995c), $[U]_{seawater}$ for the Miocene can be estimated from models, but $[U]_{sediment}$ is not known and so the depth of the redox horizon for uranium cannot be calculated.

An assumed depth of 45cm appears to be sufficient for the upper interval, but not for the lower one (Figure 63). Changes in BFAR and U/Ca appear to occur coevally in the upper record and timings of maxima in U/Ca and BFAR appear to coincide with the adjusted timescale. Disagreement between the timings of changes in BFAR and U/Ca suggest that the depth of the redox boundary was more dynamic in the lower interval than in the upper one. The assumption of a 45cm deep redox horizon probably does not hold true in the lower interval.

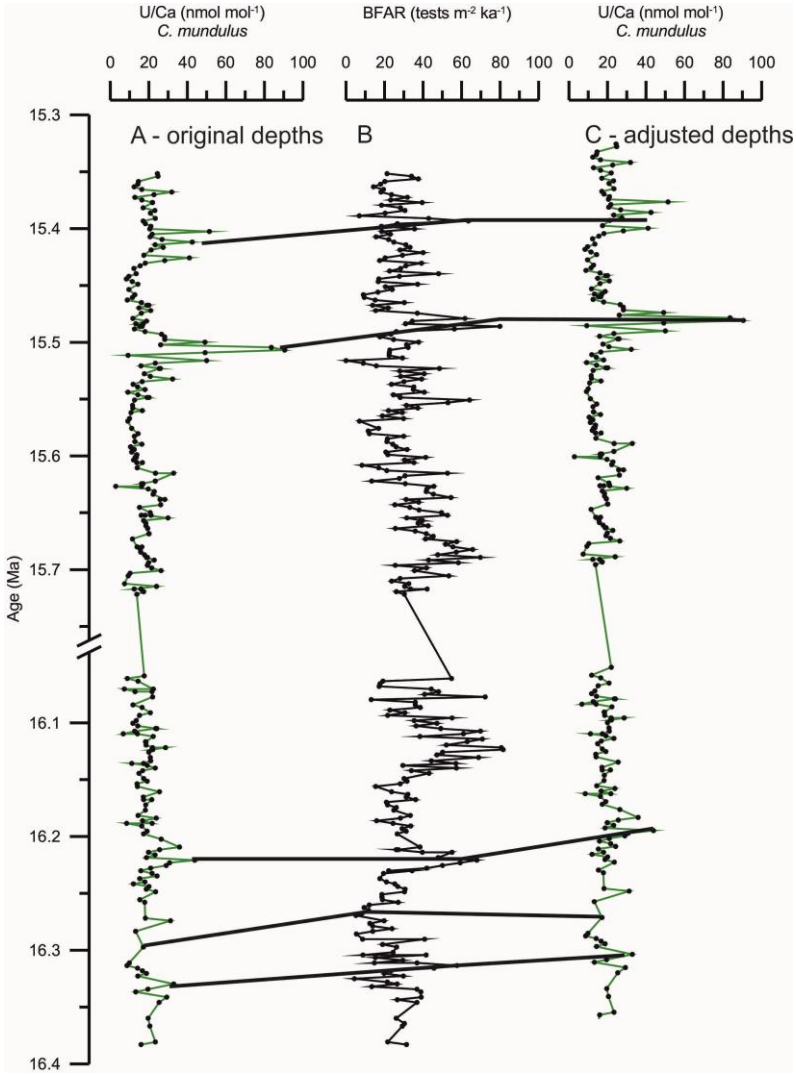


**Figure 63 – Adjusting the timing of U/Ca to account for changes in the depth of the redox horizon. A) U/Ca on the PPFI timescale. B) BFAR on the PPFI timescale. C) U/Ca on a timescale adjusted for a redox horizon at 45cm below the sediment-water interface (Francois et al., 1993). U/Ca appears to show better agreement in the timings of changes with BFAR on this later timescale, but the relationship breaks down in the lower part of the record. The redox horizon is not at a constant depth through time (Francois et al., 1993), and so the constant adjustment of the timescale by 45cm is insufficient for the whole record.**

### *5.4.2.3 Shifts in the Equatorial High Productivity Zone During the MMCO*

Increases in export productivity at Ceara Rise may be associated with increased upwelling of deep waters to the surface, caused by variations in the ITCZ. The ITCZ is a zone of lower salinities and increased ocean mixing. Its presence brings deep nutrient-rich waters to the surface which facilitates an increase in PP. In chapter 4, the position of the ITCZ was inferred to have moved based on reconstructed changes in surface salinity. Under this scenario, periods of low salinity would be expected to coincide with periods of efficient

export productivity and high PP due to increased mixing caused by upwelling associated with the ITCZ. This should also coincide with reduced oxygenation of the deep ocean. Figure 64 shows the methods used to track these metrics.

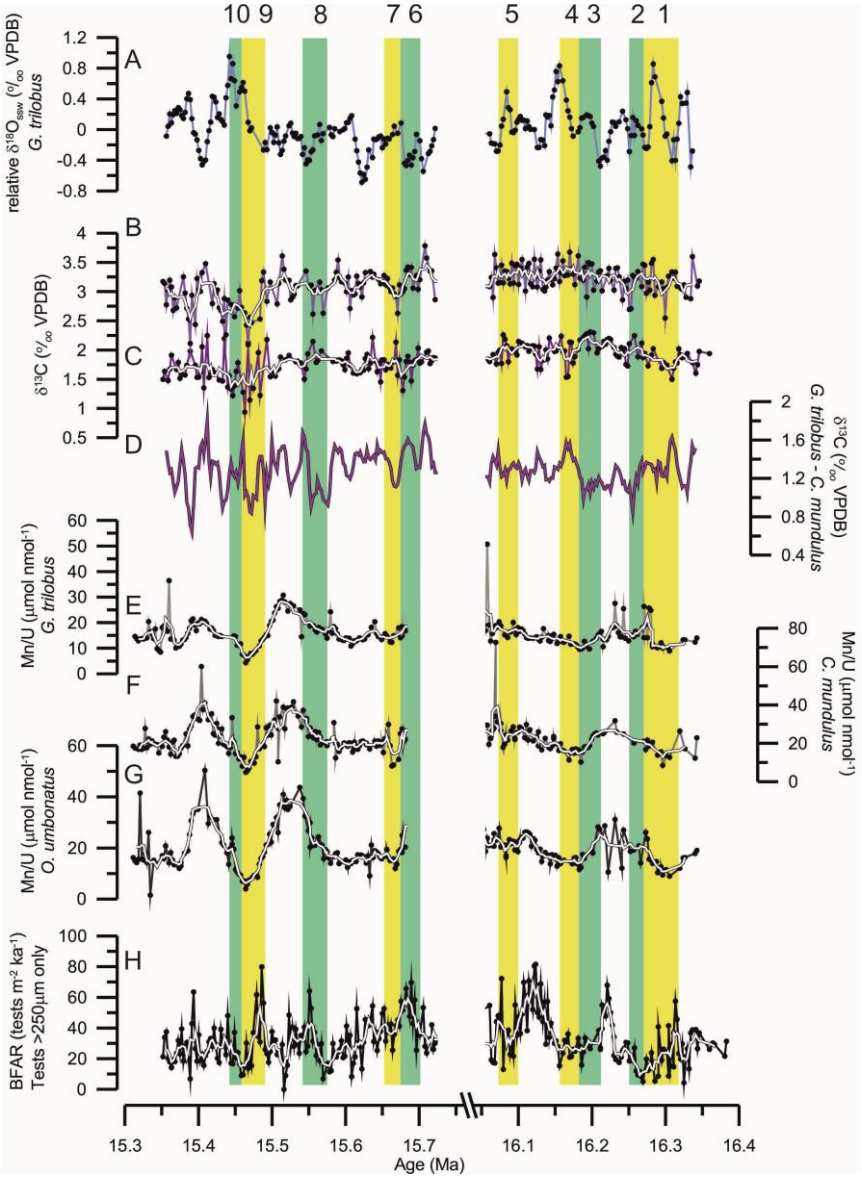


**Figure 64 – Productivity and the ITCZ. A) relative $\delta^{18}O_{ssw}$ B) $\delta^{13}C$ *G. trilobus* C) $\delta^{13}C$ *C. mundulus.* Note that B and C are displayed on the same axis. D) $\delta^{13}C$ *G. trilobus* – *C. mundulus*. E) Mn/U *G. trilobus*. F) Mn/U *C. mundulus*. F) Mn/U *O. umbonatus*. G) BFAR, only including tests >250µm.**

Maxima in $\delta^{18}O_{ssw}$ (Figure 64a) in the lower interval all occur coevally with low BFAR values and no strong changes in $\delta^{13}C_{P\text{-}B}$, which provides evidence for a distal ITCZ in all cases. Similarly, $\delta^{18}O_{ssw}$ minima in the lower interval appear to coincide with high BFAR values, which suggests that the increased mixing and lowered salinities associated with the ITCZ would be an explanation for both. Lower (higher) $\delta^{18}O_{sw}$ and higher (lower) $\delta^{18}O_{ssw}$ in the lower interval

appear to occur at the same time (chapter 4), and so it is likely that fluctuations in the northern hemisphere ice sheets are causing these movements of the ITCZ.

Minima in $\delta^{18}O_{ssw}$ in the upper interval in between T7 and T8 at 15.62 Ma could indicate low salinity and thus a proximal ITCZ. The $\delta^{18}O_{ssw}$ minimum at 15.41 Ma occurs with a maximum in the surface-deep gradient in $\delta^{13}C$ (Figure 64d). This suggests more efficient export productivity, but with no associated Mn/U minimum (Figure 64e-g) that would imply low oxygenation and no BFAR maximum (Figure 64h) that would imply increased deep ocean productivity. This may indicate that while the export productivity was more efficient, it may not have been particularly strong (Hilting et al., 2008), and so some other limiting factor in the surface was retarding PP. The other low in $\delta^{18}O_{ssw}$ that occurs at 15.62 Ma is not associated with any strong high in $\delta^{13}C_{P\text{-}B}$, nor any changes in Mn/U or highs in BFAR. In the lower interval there are three lows in $\delta^{18}O_{ssw}$ at ~16.13 Ma, ~16.21 Ma, and ~16.31 Ma. The first and third of these are all associated with maxima in $\delta^{13}C_{P\text{-}B}$ (Figure 64d) and all three are associated with elevated BFAR (Figure 64h). Mn/U appears to be consistently low at this point, which suggests that the bottom waters were poorly ventilated at the time (Figure 64e-g). The second $\delta^{18}O_{ssw}$ minima at 16.21 Ma is associated with a slight increase in Mn/U which may suggest a brief input of more oxygenated waters, or a drop in metabolic rate allowing for more free oxygen at the sea floor.

Maxima in $\delta^{18}O_{ssw}$ that could be associated with a more distal ITCZ occur in the upper interval at the end of T10 (~15.44 Ma), and in the lower interval during T5 at 16.09Ma, 16.16Ma and 16.28 Ma. In the upper interval, the maxima in $\delta^{18}O_{ssw}$ at ~15.44 Ma is not associated with any particular highs or low in any other metric. Though the increase leading up to it occurs approximately coevally with an increase in $\delta^{13}C_G$ (Figure 64b), and Mn/U, especially in *C. mundulus* and *O. umbonatus* (Figure 64f & g). This may suggest that surface productivity was increasing at the time which would argue for no strong effect

of the ITCZ on this $\delta^{18}O_{ssw}$ maximum, but there is no associated increase in BFAR (Figure 64h) to accompany the implied increased surface productivity.

#### *5.4.2.4 The Response of the Organic Carbon Cycle at Ceara Rise to Movement of the ITCZ*

Contrary to weathering and export productivity driving changes in $pCO_2^{ATM}$, $\Delta[CO_3^{2-}]$, and temperature (Section 5.4.1), changes in PP and bottom water oxygenation at Ceara Rise appear to be responding to changes in climate, rather than acting as a driver. PP seems to follow changes in surface salinity, as evidenced by $\delta^{18}O_{ssw}$ and BFAR. This suggests that the ITCZ is controlling ocean mixing at Ceara Rise; when the ITCZ is proximal to Ceara Rise, BFAR is elevated and Mn/U is depressed, suggesting that increased PP is causing a higher metabolic rate in the deep ocean.

### *5.4.3 Reliability of the Mg/Ca Temperature Signal*

Given that benthic foraminiferal Mg/Ca may respond more to changes in $\Delta[CO_3^{2-}]$ than to changes in temperature at low temperatures (<3°C) and low $\Delta[CO_3^{2-}]$ (<~25 μmol $kg_{sw}^{-1}$), care needs to be taken in analysing the temperature changes in this record (Elderfield et al., 2006). SST should be exempt from this as the surface ocean is well saturated with respect to $[CO_3^{2-}]$. The BWT estimates from this study fall within the range of 3-10°C, however changes in the H-value used to correct for changes in the partitioning of $Mg/Ca_{sw}$ to $Mg/Ca_{calcite}$ can cause large changes in the absolute temperatures thus calculated (Evans and Müller, 2012). H has no effect on relative temperature changes, and the direction of temperature changes implied by Mg/Ca and $\delta^{18}O$ are in good agreement throughout the record, even in T9 and 10 which experience the largest changes in $\Delta[CO_3^{2-}]$ (Figure 53, Figure 55, Figure 59).

There is good agreement between the direction of the major temperature changes in the records of *G. trilobus*, *C. mundulus,* and *O. umbonatus*. The magnitude of temperature changes implied by $Mg/Ca_O$ and $Mg/Ca_M$ are in good

agreement which at worst suggests that the temperature changes estimated from both species are at least biased by the same amount. If Mg/Ca in *O. umbonatus* does provide a more reliable temperature signal than in other *Cibicidoides spp.* (chapter 3, this thesis; Lear et al., 2010; Mawbey and Lear, 2013), then it suggests that large changes in $\Delta[CO_3^{2-}]$ have not biased the $Mg/Ca_M$ temperature signal.

## 5.5 Conclusions

Bottom water $\Delta[CO_3^{2-}]$ is quite variable over the interval studied, with swings of between 20 and 40 μmol $mol^{-1}$ $kg_{sw}^{-1}$ over relatively short (~10 ka) timescales. $pCO_2^{ATM}$ in general terms appears to change coevally with $\Delta[CO_3^{2-}]$, which is the expected behaviour if $\Delta[CO_3^{2-}]$ can be taken as an indicator of ALK. The longest lasting change in $\Delta[CO_3^{2-}]$ that begins at the start of T9 is associated with the increase in sea level that began at around the same time. It is likely that the sea level increase caused a change in the rate of removal of ALK from the oceans, perhaps through increased growth of calcite-producers, and helped to enhance the $pCO_2^{ATM}$ increase seen across T9. The sea level and $pCO_2^{ATM}$ changes seen are within the magnitudes that would be expected from the work of Rohling et al. (2013). In addition, enhanced export productivity at 15.50 Ma resulted in enhanced BFAR. The enhanced nutrient utilisation at the sea floor resulted in an oxygen minimum, as evidenced by the spike in U/Ca and low Mn/U ratios at this time.

Other changes in $\Delta[CO_3^{2-}]$ appear to be linked to changes in export productivity. BFAR maxima are closely associated in time with $\delta^{18}O_{ssw}$ minima, suggesting a close link between low sea surface salinities and high productivity. This increase in productivity is likely linked to the southern movement of the ITCZ speculated in chapter 4. Southern movements of the ITCZ tied to ice expansion in the northern hemisphere resulted in increased mixing that reduced the gradient in surface to deep $\delta^{13}C$ and decreased surface salinities

(chapter 4). Similarly, BFAR minima and $\delta^{18}O_{ssw}$ maxima are closely linked, further strengthening the tie between the position of the ITCZ and PP at Ceara Rise during the MMCO.

# 6 SYNTHESIS AND CONCLUSIONS

This thesis provides further insight into the response of benthic foraminiferal trace metal geochemistry to changes in bottom water $\Delta[CO_3^{2-}]$, as well as a high (~2ka) resolution examination of two intervals during the MMCO. In this closing chapter, the conclusions of the individual chapters will be re-examined and a "big picture" overview will be provided.

## 6.1 Outcome of the Study On Norwegian Sea Core Top Benthic Foraminifer Trace Metal Geochemistry

Chapter 3 (Core-Top Calibration of Trace Metal Ratios of Benthic Foraminifera From the Norwegian Sea) focused on a core-top analysis of benthic foraminifera from the Norwegian Sea. The deep waters of the Norwegian Sea are unsuited to examining changes in temperature as it is more-or-less holothermal; the range of temperatures examined in this study is far less than 0.1°C; from -0.86 to -0.82°C. The range of $\Delta[CO_3^{2-}]$ is far greater; from 12 to 28 μmol $mol^{-1}$ $kg_{sw}^{-1}$. The effects of this variation in $\Delta[CO_3^{2-}]$ without variation in temperature were examined in three species of benthic foraminifer: the epifaunal hyaline foraminifer *C. wuellerstorfi*, and the miliolite *P. murrhina*,; and the infaunal hyaline foraminifer *O. umbonatus*. The foraminifera were examined for their Mg/Ca, Li/Ca, B/Ca, and U/Ca ratios, though B/Ca was not presented in *O. umbonatus* due to the low concentration of boron in its test. In addition *C. wuellerstorfi* was split into sinistral and dextral morphotypes to examine any changes this might have on its test chemistry.

The main conclusions of this chapter were:

- The estimated relationship between $\Delta[CO_3^{2-}]$ and Mg/Ca in *C. wuellerstorfi* without the effects of temperature by Elderfield et al. (2006) holds true when the Norwegian sea datasets are combined. This allows the equation estimated in Elderfield et al. (2006) to be used to estimate $\Delta[CO_3^{2-}]$ changes essentially unaltered when changes in temperature are thought to be negligible or non-existent (Figure 20) .

- Mg/Ca in *O. umbonatus* shows a lower sensitivity to changes in $\Delta[CO_3^{2-}]$ than *C. wuellerstorfi*, which makes it suitable for cross-checking Mg/Ca-based temperature estimates made on *Cibicidoides* species (Figure 24).
- *P. murrhina* may either show little sensitivity to changes in temperature and instead may respond to changes in $\Delta[CO_3^{2-}]$, or may show no sensitivity to changes in temperature below 2°C, and enormous sensitivity to temperature above that threshold. If it is the former case, Mg/Ca in *P. murrhina* may be an excellent indicator of $\Delta[CO_3^{2-}]$ conditions in the deep ocean (Figure 26) .
- *P. murrhina*'s U/Ca sensitivity bears the opposite sign to *C. wuellerstorfi* and *O. umbonatus*. Whether this is specific to this study, to *P. murrhina* specifically, or miliolite foraminifera in general are not known or explored (Figure 27) .
- Coiling direction has no effect on trace element ratios in *C. wuellerstorfi (*Figure 17*),* though size fraction does (Figure 16). This means that it is unlikely that differently "handed" *C. wuellerstorfi* are unlikely to represent different species variants in the manner of Rae et al. (2011).

## 6.2 Outcomes of the Studies of Climate During the Mid Miocene Climatic Optimum

### *6.2.1 Ice volume*

Chapter 4 (Mid-Miocene ITCZ Changes in Response to Northern Hemisphere Ice Sheet Growth) focused on a high resolution geochemical analysis of two intervals from the MMCO: one from ~15.3-15.7 Ma, and the other from ~16-16.4Ma. These analyses were performed on three species of foraminifera: the epifaunal *C. mundulus*, the infaunal *O. umbonatus*, and the planktonic *G. trilobus*. Multiple proxies from each species were examined. The

stable isotope delta-ratios $\delta^{18}O$ and $\delta^{13}C$ were used, as well as the trace element ratios Mg/Ca, Li/Ca, and Sr/Ca.

The principal conclusions of this chapter were:

- BWT variability within the MMCO appears to be around 2°C on ~10ka time scales, though there is an interval where BWT appears to jump by 4°C in as much time. This is coeval with a decrease in $\delta^{11}B$ that implies that pH of the surface ocean was decreasing at this time, consistent with a general increase in $pCO_2^{ATM}$ (Figure 38, Figure 45).
- The aforementioned 4°C warming is coincident with a long-term decrease in $\delta^{18}O_M$ of around 0.3 ‰, though the largest change within that longer-term trend is a 1.2‰ decrease in $\delta^{18}O_M$ that is coeval with the largest change in $Mg/Ca_M$ and $Mg/Ca_O$. This overall trend is taken to represent a change $\delta^{18}O_{sw}$ that could be caused by a decrease in ice volume equivalent to a 30m eustatic increase in sea level (Figure 41). This is in line with previous estimates of sea level variability during the MMCO (Pekar and DeConto, 2006).
- The change in sea level inferred from the bottom-water signal is also coincident with changes in the planktonic realm as inferred from *G. trilobus*. Taking changes in $\delta^{18}O_{sw}$ and removing the ice volume signal allows us to infer changes in SSS that reveal an increase in SSS coincident with the implied drop in ice volume (Figure 43). This is taken to imply a northward movement of the ITCZ relative to Ceara Rise. This is consistent with a decrease in ice volume in the northern hemisphere (Chiang and Bitz, 2005; Philander et al., 1996), and so the retreat of (a) northern hemisphere continental ice sheet(s) is inferred (Figure 44).

### *6.2.2 Carbon cycling*

Chapter 5 (Carbon Cycling During the MMCO) focused on a high resolution geochemical analysis of the same two intervals from the MMCO that were examined in chapter 4. These analyses were performed on the same species of foraminifera: the epifaunal *C. mundulus*, the infaunal *O. umbonatus*, and the planktonic *G. trilobus*. Multiple proxies from each species were examined. The stable isotope delta-ratios $\delta^{18}O$, $\delta^{13}C$, and $\delta^{11}B$ were used, as well as the trace element ratios Mg/Ca, B/Ca, Sr/Ca, Mn/Ca and U/Ca.

The principal conclusions of this chapter were:

- Bottom water $\Delta[CO_3^{2-}]$ also varied during the MMCO, though small-scale trends are harder to determine. B/Ca and Sr/Ca agree in terms of the direction of changes in $\Delta[CO_3^{2-}]$, though not in magnitude. The 30m sea level change is coincident with a drop in bottom water $\Delta[CO_3^{2-}]$ between 20-50 μmol $mol^{-1}$ $kg_{sw}^{-1}$, based on $B/Ca_M$, $Sr/Ca_M$ and $Sr/Ca_O$ estimates. The cause of most of the changes in $\Delta[CO_3^{2-}]$ is most likely changes in export productivity, with less efficient export productivity resulting in a lessening of $pCO_2^{ATM}$ drawdown and thus warming. The largest change at 15.50 Ma is attributed to the rise in sea level implied by the $\delta^{18}O_{sw}$. I imply that the rise increased the rate of burial of $CaCO_3$, perhaps by increasing the area of shelf seas and providing more space for carbonate-producing organisms, which would serve to reduce ALK relative to DIC and thus decrease $\Delta[CO_3^{2-}]$ (Figure 55).
- Decreases in $\Delta[CO_3^{2-}]$ could be expected to bias the temperature change inferred from the Mg/Ca record towards underrepresenting the total change in temperature. The direction of temperature changes implied by Mg/Ca are agreed upon by all species studied in both the benthic and planktonic realms and in benthic $\delta^{18}O$ and so the changes seen are robust (Figure 34).

- U/Ca does not agree with B/Ca and Sr/Ca if its signal is assumed to represent $\Delta[CO_3^{2-}]$. The values of U/Ca are intermediate between typical foraminiferal test U/Ca and that found in authigenic coatings on foraminiferal tests, so this is taken as a sign that the reductive cleaning step has not been 100% effective in removing oxides. U/Ca and Mn/Ca show strong correlation to one another, suggesting that they may be bound in authigenic coatings. A Mn/U ratio was calculated on the assumption that it would reveal some information about bottom water oxidation states. The general form of the Mn/U trend matches that of $\delta^{13}C_M$, and so that is taken as a sign that it reveals something about the carbon cycle's relation to 926. In the absence of evidence, it is assumed that Mn/U is tracking with oxidation state as both U and Mn precipitation from sea water is strongly linked to redox conditions (Figure 54).
- Changes in productivity proxies (BFAR, $\delta^{13}C_G$) support the interpretation of movement of the ITCZ relative to Ceara Rise (Figure 64).

### *6.2.3 Synthesis*

Studied of ice volume retreat during the Cenozoic are extremely important as they provide a glimpse of what the world may become as a result of modern-day global warming. The Mid-Miocene Climatic Optimum provides an ideal period of geologic history to examine for this purpose, not least because $pCO_2^{ATM}$ was around the same values as it is today (c.f. Foster et al., 2012; IPCC, 2013). One of the inferences of this study has been that ice-volume retreat during at least one interval in the MMCO was centred on the Northern Hemisphere, which *a priori* requires ice sheets to have been present in the Northern Hemisphere. This may mean that the MMCO is more similar to

today's world, and thus more like the world of the not-too-distant future than has previously been thought.

$pCO_2^{ATM}$ reached the modelled threshold for Northern Hemisphere glaciation by ~20 Ma (DeConto et al., 2008; Foster et al., 2012). Assuming that this modelled threshold is accurate and that 20 Ma is the date for Northern Hemisphere ice sheet inception, this pushes the accepted age for the inception of Northern Hemisphere glaciation back by ~17Ma from 3 Ma in the Pliocene (Bartoli et al., 2005; Lunt et al., 2008; Zachos et al., 2001). This may help to enforce the strong links between $pCO_2^{ATM}$ and global ice volume. Continental configuration may not ultimately matter, except to "prime the pump" as DeConto and Pollard (2003) showed with their modelled opening of the Drake Passage, and provide a substrate for ice sheets to nucleate on.

There is some evidence of Northern Hemisphere ice during the Middle Miocene in the rock record (St John, 2008), and it is present in at least one model (Herold et al., 2012), but to my knowledge this is the first time that geochemical evidence has been used to imply as such. This interpretation relies somewhat on the assumption that Ceara Rise remained to the south of the ITCZ during the MMCO. Given its current position in relation to the ITCZ, its palaeo-position relative to modelled simulations of the ITCZ in the geologic past (Lunt, D., personal communication), and the fact that the ITCZ in the Atlantic showed the same behaviour in seasonality as it does today (Kaandorp et al., 2005) I do not feel that this is an unreasonable assumption.

## 6.3 Future Work

### *6.3.1 Development of Geochemical Proxies for $\Delta[CO_3^{2-}]$*

#### *6.3.1.1 Pyrgo murrhina Mg/Ca as $\Delta[CO_3^{2-}]$ Recorder*

The most surprising result, or at least most unexpected, was to find that it seemed that either Mg/Ca in *P. murrhina* does not respond to temperature changes at all, or that there is a threshold at around 2°C after which it becomes

the most sensitive palaeothermometer yet recorded. A sensitivity of ~20 mmol $mol^{-1}$ $^{o}C^{-1}$ is truly astounding and could mean that temperature changes on the order of 0.1°C could be incredibly easy to resolve. Assuming this fanciful scenario is false, we are left with an equally fanciful one: that Mg/Ca in *P. murrhina* does not respond much to changes in temperature and instead faithfully records $\Delta[CO_3^{2-}]$, which would make it the ideal companion to any palaeo-temperature record based on *Cibicidoides spp.*, *Planulina spp.*, *Oridorsalis spp.*, or any other previously-examined genus of benthic foraminifer.

There are a number of problems with this study, however, that need to be addressed: to begin with, *P. murrhina* does not tolerate temperatures much below 7°C, and thrives in cold waters <2.5°C (Gudmundsson, 1998; Murgese and De Deckker, 2005). In addition, its temporal range does not appear to go back much beyond the Oligocene (Shipboard Scientific Party, 2002), so it is completely unsuited to examining Eocene hyperthermals, or the much-studied PETM. It does have relatively global modern range, however, being that it is found in all three ocean basins (Gudmundsson, 1998; Murgese and De Deckker, 2005), which should make core-top calibrations relatively straight forward.

An additional problem with this study is the narrow range of temperatures and $\Delta[CO_3^{2-}]$ it covers. The above two fanciful scenarios are based on this dataset, which has a <0.1°C temperature range and a $\Delta[CO_3^{2-}]$ range of ~16 μmol $mol^{-1}$ and the dataset of Healey et al. (2008), which covers a range of temperatures of ~4°C (2°C for *P. murrhina*) and a $\Delta[CO_3^{2-}]$ range of ~35 μmol $kg_{sw}^{-1}$. This dataset serves to plug a gap in the range of $\Delta[CO_3^{2-}]$ that Healey et al. (2008) covers, but it does nothing to extend it. It extends the range of temperatures from 2°C to ~4°C, but leaves ~2°C gap in the -1 to 1°C range, so there is much to be done in extending, and improving the range of *P. murrhina* trace metal calibrations.

Furthermore, *P. murrhina* differs from previously examined foraminifer species in that it has a miliolite, rather than hyaline, test structure. The odd

behaviour displayed by *P. murrhina* in this study may be something unique to itself, or may be a feature of miliolite foraminifers' response to changes in $\Delta[CO_3^{2-}]$. Why the partitioning of Mg into its or their tests would be different enough to make it extremely (in?)sensitive to changes in temperature I could not even begin to hypothesise.

To those ends, I propose two experiments: the first is a culturing experiment. *P. murrhina* would be cultured in six climate controlled tanks; three with temperatures between 1 and 6°C to cover the range of *P. murrhina*'s extant habitats, and three with $\Delta[CO_3^{2-}]$ between 25 μmol $kg_{sw}^{-1}$ and 80 μmol $kg_{sw}^{-1}$ for much the same reason, but to remain above the threshold posited by Elderfield et al. (2006) below which foraminiferal Mg/Ca responds more to $\Delta[CO_3^{2-}]$ than to temperature. This precaution is to ensure that the sensitivities thus produced would not be exaggerated. This experiment would essentially act as a pilot experiment to see which variable Mg/Ca in *P. murrhina* responds to more, and may allow us to remove one or the other variable as a control on Mg/Ca in *P. murrhina*.

The second experiment is a global core-top calibration in the same vein as every global core top calibration that has come before, focussing on those sites examined by Gudmundsson (1998), Murgese and De Deckker (2005), Healey et al. (2008), and myself. In the sites off the South East and North West coasts of Iceland, labelled ATS (Atlantic Shallow) by Gudmundsson (1998). *P. murrhina* can be found there at depths of ~500-1500m, between temperatures of 3°C and 7°C. GEOSECS data from sites 15, 21, and 22 are in those areas. The range of $\Delta[CO_3^{2-}]$ values as calculated from that GEOSECS data is not calculable by me at this time as the GEOSECS data lacks the necessary carbonate system parameters to estimate it using CO2SYS_2011.xls (Lewis and Wallace, 1998).

In the Indian Ocean Deep Water, *P. murrhina* can be found over a depth range of 500 to 4500m (greatest abundance at 3500m), and in water temperatures of ~1.5-7°C (Murgese and De Deckker, 2005). The range of

carbonate saturation states, based on data from GEOSECS site 438 and CO2SYS_2011.xls (Lewis and Wallace, 1998) is -22 μmol $kg_{sw}^{-1}$ to 85 μmol $kg_{sw}^{-1}$.

I propose these sites because we know that *P. murrhina* already exists there, and so it obviates the need to search for new sites. Using sites from all of the previously mentioned studies has the added advantage that the material has already been gathered and picked, so it may not even need another cruise.

#### *6.3.1.2 Further development of U/Ca*

Currently, there are three studies on the use of U/Ca as a proxy for $\Delta[CO_3^{2-}]$ in benthic foraminifera: Keul et al. (2013), Raitzsch et al. (2011), and this thesis. Between the three studies, U/Ca has been examined in core tops using the species *C. wuellerstorfi* (Raitzsch et al., 2011; chapter 3 of this thesis), *C. mundulus* (Raitzsch et al., 2011), *O. umbonatus* (chapter 3 of this thesis), and *P. murrhina* (chapter 3 of this thesis), and in a culturing study using *Ammonia sp.* (Keul et al., 2013). Any additional expansion of these studies, either by increasing the range of $\Delta[CO_3^{2-}]$ examined, or increasing the number of species-specific calibrations would be beneficial to palaeoclimatology as a whole. Special attention needs to be given to the concentration of dissolved $O_2$ in the water column, however, as high U/Ca may also indicate reducing conditions as well as low $\Delta[CO_3^{2-}]$.

### *6.3.2 Mn/U as a Proxy for Redox Conditions*

Further examination of foraminiferal Mn/U ratios are warranted as it may hold some promise as a proxy for oxidation state, or perhaps even bottom water oxygen concentrations. Uranium precipitates out of sea water in reducing conditions as $UO_2$ (Chun et al., 2010), whereas $Mn^{2+}$ reacts quickly with oxygen and precipitates out as $MnO_2$ in oxygenating conditions (Calvert and Pedersen, 1996; Chun et al., 2010). It follows that, even in authigenic coatings, the concentration of U and Mn should approximately mirror one another (as [U] increases, [Mn] should decrease, and vice versa) in response to changing

oxygen levels, and so Mn/U of foraminiferal tests should provide an approximate record of how strongly reducing the waters they grew in were, or Mn/U of authigenic coatings on foraminifera should show how reducing the sediments they were deposited were.

Laser ablation can be used to examine the authigenic coatings and the test walls separately on the same foraminifera. The difference between the two may give an indication of the oxygen gradient between where the foraminifera grew and the redox horizon at which the authigenic coatings were laid down. The gradient in Mn/U between planktonic and benthic foraminiferal tests (not including any authigenic coatings) may give an indication of how stratified the water column was with respect to oxygen.

### *6.3.3 Ice Volume Changes in the Miocene*

#### *6.3.3.1 Hemisphere-Specific Analyses*

Given that Antarctic deglaciation would result in enhanced warming in the Southern Hemisphere (Justino et al., 2014), and that the same can be said for the Arctic and the Northern Hemisphere (Shakun and Carlson, 2010), an inter-hemispheric comparison of climate change during the MMCO would help to pin down the location of ice volume changes. The magnitude of warmings experienced by both hemispheres would need to be analysed. This analysis would need to be restricted to planktonic foraminifera as different depths may experience different magnitudes of warming or cooling in response to changes in ice volume. Similarly, latitude-equivalent sites would need to be used as different latitudes may warm by differing amounts. The Pacific ocean would be ideal for this, however the Southern Ocean and Southern Pacific are very sediment-poor, and so a comparison of a North Atlantic and South Atlantic site would have to be conducted.

#### *6.3.3.2 Tracking the ITCZ*

Another method to pin down the primary hemisphere of ice volume change would be to attempt to track the movements of the ITCZ across the MMCO. A high resolution study of a deglaciation in the Pacific, perhaps the largest one outlined in chapter 4 between 15.6 and 15.4 Ma would be conducted using both benthic and planktonic foraminiferal Mg/Ca, and $\delta^{18}O$ to allow for calculations of changes in BWT, $\delta^{18}O_{sw}$, SST and SSS. $\delta^{13}C$, BFAR, and perhaps Cd/Ca could be used as supporting analyses to examine changes in productivity that would accompany changes in the position of the ITCZ.

The PEAT sites of IODP Leg 320 (Pälike et al., 2009) offer an ideal solution, as they were already taken across the equator, and thus across the predominant locus for the ITCZ. They also have strong age control, which would allow for easy comparison of timings of changes of SSS, and the plate movements of the Pacific are well known which would allow them to be taken into account. In addition the ITCZ in the Pacific is less prone to dramatic movements as the temperature over the open ocean is seasonally more stable than on or near land, so its movement should merely be down to broad-scale climate effects. A site some distance either north or south of the Equator would need to be used, as changed in SSS in a site directly inside the ITCZ could not be attributed a direction. Ideally, two sites with good age control could be used so as to provide a better special component.

### *6.3.4 Ice Volume Retreats in the Wider Cenozoic*

#### *6.3.4.1 High Resolution Examination of End-Oligocene*

The original aim of this study was to examine a stable cold interval prior to a deglaciation and a warm interval after a deglaciation to examine variability in ice volume; the initial working hypothesis was that changes in ice volume would be larger and more frequent during a warm interval. This would be done during an interval after the EOCT but before the inception of northern hemisphere ice sheets so that any ice volume changes could be attributed to

Antarctica only so that the data thus gained would provide a framework for future ice volume modelling efforts: X temperature change causes Y ice volume change on Antarctica within a stable warm interval, and Z ice volume change within a stable cold interval. This has not been achieved.

On one front, the intervals chosen were supposed to be before (>17Ma) and just after (~16Ma) the onset of the MMCO, but problems with the age model used to select sample material has resulted in two intervals during the MMCO. On another front, it appears as if northern hemisphere ice sheets may have been present during the intervals studied, and if that is true then they were likely to have been there from ~20 Ma when $pCO_2^{ATM}$ became low enough for Northern Hemisphere ice sheet inception (Foster et al., 2012; Zhang et al., 2013). This means that for the initial aims of this study to be completed, the Oligocene seems like it may offer the best natural laboratory to study ice volume changes that only involve one ice sheet.

Zachos et al. (2001) noted a rapid warming towards the end of the Oligocene at ~26Ma he labelled the "Late Oligocene Warming". It was later noted that this was probably an artefact of the way the composite record was constructed: The composite record was constructed primarily from Pacific Sites prior to 26Ma, and primarily of Atlantic Sites after 26Ma so that warming may have just represented a seam of the two composites. ODP Site 1218 covered that entire interval in one Pacific site, and it is clear from Pälike et al. (2006b), where the $\delta^{18}O$ record is more-or-less presented in full, that there is a general trend towards lighter isotopes from ~27Ma to ~25Ma, with an overall change of ~0.5 ‰. This is consistent with a warming or a deglaciation, and meets the requirement of being prior to 20Ma, so unlikely to include the presence of anything but ephemeral Northern Hemisphere Glaciation.

The PEAT sites once again provide an ideal location. Their Mid-Equatorial-Pacific location should allow them to be globally representative in their bottom water signal; the Pacific is after all the largest ocean basin. Site 1334 covers the

required interval with no significant hiatuses, and offers a sedimentation rate of ~12-24 $mMa^{-1}$ during the Oligocene (Pälike et al., 2009), and the only reason it was not used in this thesis was that the sample material was still on moratorium when it was begun.

# 7 REFERENCES CITED

Algeo, T. J., Henderson, C. M., Tong, J. N., Feng, Q. L., Yin, H. F., and Tyson, R. V., 2013, Plankton and productivity during the Permian-Triassic boundary crisis: An analysis of organic carbon fluxes: Global and Planetary Change, v. 105, p. 52-67.

Allen, K. A., and Honisch, B., 2012, The planktic foraminiferal B/Ca proxy for seawater carbonate chemistry: A critical evaluation: Earth and Planetary Science Letters, v. 345, p. 203-211.

Allen, K. A., Honisch, B., Eggins, S. M., and Rosenthal, Y., 2012, Environmental controls on B/Ca in calcite tests of the tropical planktic foraminifer species Globigerinoides ruber and Globigerinoides sacculifer: Earth and Planetary Science Letters, v. 351, p. 270-280.

Allison, N., Austin, W., Paterson, D., and Austin, H., 2010, Culture studies of the benthic foraminifera Elphidium williamsoni: Evaluating pH Delta $CO_3^{2-}$ and inter-individual effects on test Mg/Ca: Chemical Geology, v. 274, no. 1-2, p. 87-93.

Anand, P., Elderfield, H., and Conte, M. H., 2003, Calibration of Mg/Ca thermometry in planktonic foraminifera from a sediment trap time series: Paleoceanography, v. 18, no. 2.

Anderson, R. F., 1982, Concentration, vertical flux, and remineralization of particulate uranium in sea-water: Geochimica Et Cosmochimica Acta, v. 46, no. 7, p. 1293-1299.

Arbuszewski, J. A., Demenocal, P. B., Cleroux, C., Bradtmiller, L., and Mix, A., 2013, Meridional shifts of the Atlantic intertropical convergence zone since the Last Glacial Maximum: Nature Geoscience, v. 6, no. 11, p. 959-962.

Armstrong, H. A., and Allen, M. B., 2011, Shifts in the Intertropical Convergence Zone, Himalayan exhumation, and late Cenozoic climate: Geology, v. 39, no. 1, p. 11-14.

Baker, P. A., Gieskes, J. M., and Elderfield, H., 1982, Diagenesis of Carbonates In Deep-Sea Sediments - Evidence from Sr/Ca Ratios and Interstitial Dissolved Sr2+ Data: Journal of Sedimentary Petrology, v. 52, no. 1, p. 71-82.

Báldi, K., 2006, Paleoceanography and climate of the Badenian (Middle Miocene, 16.4-13.0 Ma) in the Central Paratethys based on foraminifera and stable isotope (delta O-18 and delta C-13) evidence: International Journal of Earth Sciences, v. 95, no. 1, p. 119-142.

Bard, E., Hamelin, B., and Fairbanks, R. G., 1990, U-TH AGES OBTAINED BY MASS-SPECTROMETRY IN CORALS FROM BARBADOS - SEA-LEVEL DURING THE PAST 130,000 YEARS: Nature, v. 346, no. 6283, p. 456-458.

Barker, S., Greaves, M., and Elderfield, H., 2003, A study of cleaning procedures used for foraminiferal Mg/Ca paleothermometry: Geochemistry Geophysics Geosystems, v. 4.

Barnes, C. E., and Cochran, J. K., 1990, Uranium Removal in Oceanic Sediments and the Oceanic-U Balance: Earth and Planetary Science Letters, v. 97, no. 1-2, p. 94-101.

Bartoli, G., Sarnthein, M., Weinelt, M., Erlenkeuser, H., Garbe-Schonberg, D., and Lea, D. W., 2005, Final closure of Panama and the onset of northern hemisphere glaciation: Earth and Planetary Science Letters, v. 237, no. 1-2, p. 33-44.

Be, A. W. H., and Hutson, W. H., 1977, Ecology of planktonic foraminifera and biogeographic patterns of life and fossil assemblages in the Indian Ocean: Micropaleontology, v. 23, no. 4, p. 369-414.

Bentov, S., and Erez, J., 2006, Impact of biomineralization processes on the Mg content of foraminiferal shells: A biological perspective: Geochemistry Geophysics Geosystems, v. 7.

Berger, W. H., and Wefer, G., 1990, Export Production - Seasonality and Intermittency, and Paleoceanographic Implications: Global and Planetary Change, v. 89, no. 3, p. 245-254.

Berner, R. A., 2006, GEOCARBSULF: A combined model for Phanerozoic atmospheric $O_2$ and $CO_2$: Geochimica Et Cosmochimica Acta, v. 70, no. 23, p. 5653-5664.

Berner, R. A., and Kothavala, Z., 2001, GEOCARB III: A revised model of atmospheric $CO_2$ over phanerozoic time: American Journal of Science, v. 301, no. 2, p. 182-204.

Berner, R. A., Lasaga, A. C., and Garrels, R. M., 1983, The carbonate-silicate geochemical cycle and its effect on atmospheric carbon-dioxide over the past 100 million years: American Journal of Science, v. 283, no. 7, p. 641-683.

Billups, K., and Schrag, D. P., 2002, Paleotemperatures and ice volume of the past 27 Myr revisited with paired Mg/Ca and O-18/O-16 measurements on benthic foraminifera: Paleoceanography, v. 17, no. 1, p. 1003.

Bingham, F. M., Foltz, G. R., and McPhaden, M. J., 2010, Seasonal cycles of surface layer salinity in the Pacific Ocean: Ocean Science, v. 6, no. 3, p. 775-787.

-, 2012, Characteristics of the seasonal cycle of surface layer salinity in the global ocean: Ocean Sci., v. 8, no. 5, p. 915-929.

Bischof, B., Mariano, A. J., and Ryan, E. H., 2004a, "The North Equatorial Counter Current." Ocean Surface Currents.

Bischof, B., Rowe, E., Mariano, A. J., and Ryan, E. H., 2004b, "The North Equatorial Current." Ocean Surface Currents.

Bischoff, T., and Schneider, T., 2014, Energetic Constraints on the Position of the Intertropical Convergence Zone: Journal of Climate, v. 27, no. 13, p. 4937-4951.

Bohaty, S. M., Zachos, J. C., Florindo, F., and Delaney, M. L., 2009, Coupled greenhouse warming and deep-sea acidification in the middle Eocene: Paleoceanography, v. 24, p. PA2207.

Böhme, M., 2003, The Miocene Climatic Optimum: evidence from ectothermic vertebrates of Central Europe: Palaeogeography Palaeoclimatology Palaeoecology, v. 195, no. 3-4, p. 389-401.

Boiteau, R., Greaves, M., and Elderfield, H., 2012, Authigenic uranium in foraminiferal coatings: A proxy for ocean redox chemistry: Paleoceanography, v. 27.

Bonhoure, D., Rowe, E., Mariano, A. J., and Ryan, E. H., 2004, "The South Equatorial Sys Current." Ocean Surface Currents.

Bowen, G. J., 2013, Up in smoke: A role for organic carbon feedbacks in Paleogene hyperthermals: Global and Planetary Change, v. 109, p. 18-29.

Boyle, E. A., 1983, Manganese Carbonate Overgrowths on Foraminifera Tests: Geochimica Et Cosmochimica Acta, v. 47, no. 10, p. 1815-1819.

Boyle, E. A., and Keigwin, L. D., 1985/1986, Comparison of atlantic and pacific paleochemical records for the last 215,000 years - Changes in deep ocean circulation and chemical inventories: Earth and Planetary Science Letters, v. 76, no. 1-2, p. 135-150.

Brachfeld, S., Pinzon, J., Darley, J., Sagnotti, L., Kuhn, G., Florindo, F., Wilson, G., Ohneiser, C., Monien, D., and Joseph, L., 2013, Iron oxide tracers of ice sheet extent and sediment provenance in the ANDRILL AND-1B drill core, Ross Sea, Antarctica: Global and Planetary Change, v. 110, p. 420-433.

Broccoli, A. J., Dahl, K. A., and Stouffer, R. J., 2006, Response of the ITCZ to Northern Hemisphere cooling: Geophysical Research Letters, v. 33, no. 1.

Broecker, W. S., and Peng, T. H., 1982, Tracers in the Sea, Palisades, New York, Lamont-Doherty Geological Observatory, Columbia University.

Broecker, W. S., and Takahashi, T., 1978, Relationship between lysocline depth and insitu carbonate ion concentration: Deep-Sea Research, v. 25, no. 1, p. 65-95.

Brown, R. E., Anderson, L. D., Thomas, E., and Zachos, J. C., 2011, A core-top calibration of B/Ca in the benthic foraminifers Nuttallides umbonifera and Oridorsalis umbonatus: A proxy for Cenozoic bottom water carbonate saturation: Earth and Planetary Science Letters, v. 310, no. 3–4, p. 360-368.

Bryan, S. P., and Marchitto, T. M., 2008, Mg/Ca-temperature proxy in benthic foraminifera: New calibrations from the Florida Straits and a hypothesis regarding Mg/Li: Paleoceanography, v. 23, no. 2, p. PA2220.

Burton, E. A., and Walter, L. M., 1991, The effects of $pCO_2$ and temperature on magnesium incorporation in calcite in seawater and $MgCl_2$-$CaCl_2$ solutions: Geochimica Et Cosmochimica Acta, v. 55, no. 3, p. 777-785.

Calov, R., and Ganopolski, A., 2005, Multistability and hysteresis in the climate-cryosphere system under orbital forcing: Geophysical Research Letters, v. 32, no. 21.

Calvert, S. E., and Pedersen, T. F., 1996, Sedimentary geochemistry of manganese: Implications for the environment of formation of

manganiferous black shales: Economic Geology and the Bulletin of the Society of Economic Geologists, v. 91, no. 1, p. 36-47.

Carozza, D. A., Mysak, L. A., and Schmidt, G. A., 2011, Methane and environmental change during the Paleocene-Eocene thermal maximum (PETM): Modeling the PETM onset as a two-stage event: Geophysical Research Letters, v. 38, no. 5, p. L05702.

Catanzaro, E. J., Champion, C. E., Garner, E. L., Marienko, G., Sappenfield, K. M., and Shields, W. R., 1970, Boric Acid; Isotopic, and Assay Standard Reference Materials, *in* Research, I. f. M., ed., Volume Special Publication 260-17: National Bureau of Standards, Washington D.C. 20234, Department of Commerce, p. 70.

Chang, Y. P., Liao, C. C., and Wang, W. L., 2012, Reconstruction of oceanographic changes based on diatom records of the core MD012380 since Marine Isotopic Stage 11 in the Banda Sea: Journal of Quaternary Science, v. 27, no. 9, p. 873-883.

Chapman, M. R., Shackleton, N. J., Zhao, M., and Eglinton, G., 1996, Faunal and alkenone reconstructions of subtropical North Atlantic surface hydrography and paleotemperature over the last 28 kyr: Paleoceanography, v. 11, no. 3, p. 343-357.

Chave, K. E., 1954, Aspects of the biochemistry of magnesium 1. calcarious marine organisms: Journal of Geology, v. 62, p. 266-283.

Chiang, J. C. H., Biasutti, M., and Battisti, D. S., 2003, Sensitivity of the Atlantic Intertropical Convergence Zone to Last Glacial Maximum boundary conditions: Paleoceanography, v. 18, no. 4.

Chiang, J. C. H., and Bitz, C. M., 2005, Influence of high latitude ice cover on the marine Intertropical Convergence Zone: Climate Dynamics, v. 25, no. 5, p. 477-496.

Chun, C. O. J., Delaney, M. L., and Zachos, J. C., 2010, Paleoredox changes across the Paleocene-Eocene thermal maximum, Walvis Ridge (ODP Sites 1262, 1263, and 1266): Evidence from Mn and U enrichment factors: Paleoceanography, v. 25.

Cleroux, C., Cortijo, E., Anand, P., Labeyrie, L., Bassinot, F., Caillon, N., and Duplessy, J. C., 2008, Mg/Ca and Sr/Ca ratios in planktonic foraminifera: Proxies for upper water column temperature reconstruction: Paleoceanography, v. 23, no. 3.

Coggon, R. M., Teagle, D. A. H., Smith-Duque, C. E., Alt, J. C., and Cooper, M. J., 2010, Reconstructing Past Seawater Mg/Ca and Sr/Ca from Mid-Ocean Ridge Flank Calcium Carbonate Veins: Science, v. 327, no. 5969, p. 1114-1117.

Cooke, S., and Rohling, E. J., 2001, Stable isotopes in foraminiferal carbonate: Southampton University Internal Documents, v. 72, p. 56pp.

Corfield, R. M., and Cartlidge, J. E., 1992, OCEANOGRAPHIC AND CLIMATIC IMPLICATIONS OF THE PALEOCENE CARBON ISOTOPE MAXIMUM: Terra Nova, v. 4, no. 4, p. 443-455.

Coxall, H. K., and Wilson, P. A., 2011, Early Oligocene glaciation and productivity in the eastern equatorial Pacific: Insights into global carbon cycling: Paleoceanography, v. 26.

Coxall, H. K., Wilson, P. A., Palike, H., Lear, C. H., and Backman, J., 2005, Rapid stepwise onset of Antarctic glaciation and deeper calcite compensation in the Pacific Ocean: Nature, v. 433, no. 7021, p. 53-57.

Davies, B. J., Hambrey, M. J., Smellie, J. L., Carrivick, J. L., and Glasser, N. F., 2012, Antarctic Peninsula Ice Sheet evolution during the Cenozoic Era: Quaternary Science Reviews, v. 31, p. 30-66.

Dawber, C. F., and Tripati, A., 2012a, Relationships between bottom water carbonate saturation and element/Ca ratios in coretop samples of the benthic foraminifera Oridorsalis umbonatus: Biogeosciences, v. 9, no. 8, p. 3029-3045.

Dawber, C. F., and Tripati, A. K., 2012b, Exploring the controls on element ratios in middle Eocene samples of the benthic foraminifera Oridorsalis umbonatus: Climate of the Past, v. 8, no. 6, p. 1957-1971.

De Nooijer, L. J., Hathorne, E. C., Reichart, G. J., Langer, G., and Bijma, J., 2014, Variability in calcitic Mg/Ca and Sr/Ca ratios in clones of the benthic foraminifer Ammonia tepida: Marine Micropaleontology, v. 107, p. 32-43.

DeConto, R. M., and Pollard, D., 2003, Rapid Cenozoic glaciation of Antarctica induced by declining atmospheric $CO_2$: Nature, v. 421, no. 6920, p. 245-249.

DeConto, R. M., Pollard, D., Wilson, P. A., Palike, H., Lear, C. H., and Pagani, M., 2008, Thresholds for Cenozoic bipolar glaciation: Nature, v. 455, no. 7213, p. 652-U652.

Dekens, P. S., Lea, D. W., Pak, D. K., and Spero, H. J., 2002, Core top calibration of Mg/Ca in tropical foraminifera: Refining paleotemperature estimation: Geochemistry Geophysics Geosystems, v. 3.

Dickson, A. G., 1990, Thermodynamics of the dissociation of boric-acid in synthetic seawater from 273.15 K to 318.15 K: Deep-Sea Research Part a-Oceanographic Research Papers, v. 37, no. 5, p. 755-766.

Diester-Haass, L., Billups, K., and Emeis, K., 2011, Enhanced paleoproductivity across the Oligocene/Miocene boundary as evidenced by benthic foraminiferal accumulation rates: Palaeogeography Palaeoclimatology Palaeoecology, v. 302, no. 3-4, p. 464-473.

Donnadieu, Y., Godderis, Y., Pierrehumbert, R., Dromart, G., Fluteau, F., and Jacob, R., 2006, A GEOCLIM simulation of climatic and biogeochemical consequences of Pangea breakup: Geochemistry Geophysics Geosystems, v. 7.

Duckworth, D. L., 1977, Magnesium Concentration in the Tests of the Planktonic Foraminifer *Globorotalia-truncatulinoides*: Journal of Foraminiferal Research, v. 7, no. 4, p. 304-312.

Dueñas-Bohórquez, A., da Rocha, R. E., Kuroyanagi, A., Bijma, J., and Reichart, G. J., 2009, Effect of salinity and seawater calcite saturation state on Mg

and Sr incorporation in cultured planktonic foraminifera: Marine Micropaleontology, v. 73, no. 3-4, p. 178-189.

Edgar, K. M., Palike, H., and Wilson, P. A., 2013, Testing the impact of diagenesis on the delta O-18 and delta C-13 of benthic foraminiferal calcite from a sediment burial depth transect in the equatorial Pacific: Paleoceanography, v. 28, no. 3, p. 468-480.

Elderfield, H., Greaves, M., Barker, S., Hall, I. R., Tripati, A., Ferretti, P., Crowhurst, S., Booth, L., and Daunt, C., 2010, A record of bottom water temperature and seawater δ18O for the Southern Ocean over the past 440 kyr based on Mg/Ca of benthic foraminiferal Uvigerina spp: Quaternary Science Reviews, v. 29, no. 1–2, p. 160-169.

Elderfield, H., Yu, J., Anand, P., Kiefer, T., and Nyland, B., 2006, Calibrations for benthic foraminiferal Mg/Ca paleothermometry and the carbonate ion hypothesis: Earth and Planetary Science Letters, v. 250, no. 3-4, p. 633-649.

Erez, J., and Luz, B., 1982, Temperature control of oxygen-isotope fractionation of cultured planktonic foraminifera: Nature, v. 297, no. 5863, p. 220-222.

Evans, D., and Müller, W., 2012, Deep time foraminifera Mg/Ca paleothermometry: Nonlinear correction for secular change in seawater Mg/Ca: Paleoceanography, v. 27, no. 4, p. PA4205.

Fairbanks, R. G., and Matthews, R. K., 1978, Marine Oxygen Isotope Record in Pleistocene Coral, Barbados, West-Indies: Quaternary Research, v. 10, no. 2, p. 181-196.

Falkowski, P., Scholes, R. J., Boyle, E., Canadell, J., Canfield, D., Elser, J., Gruber, N., Hibbard, K., Högberg, P., Linder, S., Mackenzie, F. T., Moore Iii, B., Pedersen, T., Rosenthal, Y., Seitzinger, S., Smetacek, V., and Steffen, W., 2000, The Global Carbon Cycle: A Test of Our Knowledge of Earth as a System: Science, v. 290, no. 5490, p. 291-296.

Fantle, M. S., and DePaolo, D. J., 2006, Sr isotopes and pore fluid chemistry in carbonate sediment of the Ontong Java Plateau: Calcite recrystallization rates and evidence for a rapid rise in seawater Mg over the last 10 million years: Geochimica et Cosmochimica Acta, v. 70, no. 15, p. 3883-3904.

Feldberg, M. J., and Mix, A. C., 2002, Sea-surface temperature estimates in the Southeast Pacific based on planktonic foraminiferal species; modern calibration and Last Glacial Maximum: Marine Micropaleontology, v. 44, no. 1-2, p. 1-29.

Fielding, C. R., Browne, G. H., Field, B., Florindo, F., Harwood, D. M., Krissek, L. A., Levy, R. H., Panter, K. S., Passchier, S., and Pekar, S. F., 2011, Sequence stratigraphy of the ANDRILL AND-2A drillcore, Antarctica: A long-term, ice-proximal record of Early to Mid-Miocene climate, sea-level and glacial dynamism: Palaeogeography Palaeoclimatology Palaeoecology, v. 305, no. 1-4, p. 337-351.

Filipsson, H. L., Romero, O. E., Stuut, J. B. W., and Donner, B., 2011, Relationships between primary productivity and bottom-water

oxygenation off northwest Africa during the last deglaciation: Journal of Quaternary Science, v. 26, no. 4, p. 448-456.

Flower, B. P., and Kennett, J. P., 1993, Relations Between Monterey Formation Deposition and Middle Miocene Global Cooling - Naples-Beach Section, California: Geology, v. 21, no. 10, p. 877-880.

-, 1994, The Middle Miocene Climatic Transition - East Antarctic ice-sheet development, deep-ocean circulation and global carbon cycling: Palaeogeography Palaeoclimatology Palaeoecology, v. 108, no. 3-4, p. 537-555.

Flower, B. P., Zachos, J., and Martin, E., 1997, Latest Oligocene through early Miocene isotopic stratigraphy and deep-water paleoceanography of the western equatorial Atlantic: sites 926 and 929, *in* Shackleton, N. J., Curry, W. B., Richter, C., and Bralower, T. J., eds., Proceedings of the Ocean Drilling Program, Scientific Results, Volume 154: College Station, Texas, Ocean Drilling Program, p. 451-461.

Foster, G. L., 2008, Seawater pH, pCO2 and [CO2-3] variations in the Caribbean Sea over the last 130 kyr: A boron isotope and B/Ca study of planktic foraminifera: Earth and Planetary Science Letters, v. 271, no. 1-4, p. 254-266.

Foster, G. L., Lear, C. H., and Rae, J. W. B., 2012, The evolution of pCO(2), ice volume and climate during the middle Miocene: Earth and Planetary Science Letters, v. 341, p. 243-254.

Foster, G. L., Lunt, D. J., and Parrish, R. R., 2010a, Mountain uplift and the glaciation of North America - a sensitivity study: Climate of the Past, v. 6, no. 5, p. 707-717.

Foster, G. L., Pogge von Strandmann, P. A. E., and Rae, J. W. B., 2010b, Boron and magnesium isotopic composition of seawater: Geochemistry Geophysics Geosystems, v. 11.

Francois, R., Altabet, M. A., Yu, E. F., Sigman, D. M., Bacon, M. P., Frank, M., Bohrmann, G., Bareille, G., and Labeyrie, L. D., 1997, Contribution of Southern Ocean surface-water stratification to low atmospheric CO2 concentrations during the last glacial period: Nature, v. 389, no. 6654, p. 929-935.

Francois, R., Bacon, M. P., Altabet, M. A., and Labeyrie, L. D., 1993, Glacial Interglacial Changes in Sediment Rain Rate in the SW Indian Sector of Sub-Antarctic Waters as Recorded By $Th^{230}$, $Pa^{231}$, U, and $\delta^{15}N$: Paleoceanography, v. 8, no. 5, p. 611-629.

Gabitov, R. I., Rollion-Bard, C., Tripati, A., and Sadekov, A., 2014, In situ study of boron partitioning between calcite and fluid at different crystal growth rates: Geochimica Et Cosmochimica Acta, v. 137, p. 81-92.

Ganopolski, A., Calov, R., and Claussen, M., 2010, Simulation of the last glacial cycle with a coupled climate ice-sheet model of intermediate complexity: Climate of the Past, v. 6, no. 2, p. 229-244.

Gasson, E., Lunt, D. J., DeConto, R., Goldner, A., Heinemann, M., Huber, M., LeGrande, A. N., Pollard, D., Sagoo, N., Siddall, M., Winguth, A., and Valdes, P. J., 2014, Uncertainties in the modelled CO2 threshold for Antarctic glaciation: Climate of the Past, v. 10, no. 2, p. 451-466.

Godderis, Y., Donnadieu, Y., Tombozafy, M., and Dessert, C., 2008, Shield effect on continental weathering: Implication for climatic evolution of the Earth at the geological timescale: Geoderma, v. 145, no. 3-4, p. 439-448.

Goldner, A., Herold, N., and Huber, M., 2014, The challenge of simulating the warmth of the mid-Miocene climatic optimum in CESM1: Climate of the Past, v. 10, no. 2, p. 523-536.

Greenop, R., Foster, G. L., Wilson, P. A., and Lear, C. H., 2014, Middle Miocene climate instability associated with high amplitude CO2 variability: Paleoceanography, p. 2014PA002653.

Groeneveld, J., and Filipsson, H. L., 2013, Mg/Ca and Mn/Ca ratios in benthic foraminifera: the potential to reconstruct past variations in temperature and hypoxia in shelf regions: Biogeosciences, v. 10, no. 7, p. 5125-5138.

Gudmundsson, G., 1998, Distributional Limits of *Pyrgo* Species at the Biogeographic Boundaries of the Arctic and the North-Atlantic Boreal Regions: Journal of Foraminiferal Research, v. 28, no. 3, p. 240-256.

Hall, J. M., and Chan, L. H., 2004, Li/Ca in multiple species of benthic and planktonic foraminifera: Thermocline, latitudinal, and glacial-interglacial variation: Geochimica Et Cosmochimica Acta, v. 68, no. 3, p. 529-545.

Hallberg, R. O., 2004, Formation of eastern Mediterranean sapropels - What can be learnt from Baltic sea sapropels?, Amsterdam, Elsevier Science Bv, Geochemical Investigations in Earth and Space Science: A Tribute to Issac R. Kaplan, v. 9, 425-439 p.:

Hasiuk, F. J., and Lohmann, K. C., 2010, Application of calcite Mg partitioning functions to the reconstruction of paleocean Mg/Ca: Geochimica Et Cosmochimica Acta, v. 74, no. 23, p. 6751-6763.

Healey, S. L., Thunell, R. C., and Corliss, B. H., 2008, The Mg/Ca-temperature relationship of benthic foraminiferal calcite: New core-top calibrations in the < 4 degrees C temperature range: Earth and Planetary Science Letters, v. 272, no. 3-4, p. 523-530.

Herguera, J. C., 2000, Last glacial paleoproductivity patterns in the eastern equatorial Pacific: benthic foraminifera records: Marine Micropaleontology, v. 40, no. 3, p. 259-275.

Herold, N., Huber, M., Muller, R. D., and Seton, M., 2012, Modeling the Miocene climatic optimum: Ocean circulation: Paleoceanography, v. 27.

Hilting, A. K., Kump, L. R., and Bralower, T. J., 2008, Variations in the oceanic vertical carbon isotope gradient and their implications for the Paleocene-Eocene biological pump: Paleoceanography, v. 23, no. 3, p. PA3222.

Hodell, D. A., Curtis, J. H., Sierro, F. J., and Raymo, M. E., 2001, Correlation of late Miocene to early Pliocene sequences between the Mediterranean and North Atlantic: Paleoceanography, v. 16, no. 2, p. 164-178.

Hodell, D. A., and Woodruff, F., 1994, Variations in the strontium isotopic ratio of seawater during the Miocene - stratigraphic and geochemical implications: Paleoceanography, v. 9, no. 3, p. 405-426.

Hofmann, P., and Wagner, T., 2011, ITCZ controls on Late Cretaceous black shale sedimentation in the tropical Atlantic Ocean: Paleoceanography, v. 26.

Holbourn, A., Kuhnt, W., Lyle, M., Schneider, L., Romero, O., and Andersen, N., 2014, Middle Miocene climate cooling linked to intensification of eastern equatorial Pacific upwelling: Geology, v. 42, no. 1, p. 19-22.

Holbourn, A., Kuhnt, W., Regenberg, M., Schulz, M., Mix, A., and Andersen, N., 2010, Does Antarctic glaciation force migration of the tropical rain belt?: Geology, v. 38, no. 9, p. 783-786.

Holbourn, A., Kuhnt, W., Schulz, M., Flores, J. A., and Andersen, N., 2007, Orbitally-paced climate evolution during the middle Miocene "Monterey" carbon-isotope excursion: Earth and Planetary Science Letters, v. 261, no. 3-4, p. 534-550.

Holbourn, A., Kuhnt, W., Simo, J. A., and Li, Q. Y., 2004, Middle miocene isotope stratigraphy and paleoceanographic evolution of the northwest and southwest Australian margins (Wombat Plateau and Great Australian Bight): Palaeogeography Palaeoclimatology Palaeoecology, v. 208, no. 1-2, p. 1-22.

Horita, J., Zimmermann, H., and Holland, H. D., 2002, Chemical evolution of seawater during the Phanerozoic: Implications from the record of marine evaporites: Geochimica Et Cosmochimica Acta, v. 66, no. 21, p. 3733-3756.

Huang, J., and McElroy, M. B., 2014, Contributions of the Hadley and Ferrel Circulations to the Energetics of the Atmosphere over the Past 32 Years*: Journal of Climate, v. 27, no. 7, p. 2656-2666.

Hyeong, K., Lee, J., Seo, I., Lee, M. J., Yoo, C. M., and Khim, B. K., 2014, Southward shift of the Intertropical Convergence Zone due to Northern Hemisphere cooling at the Oligocene-Miocene boundary: Geology, v. 42, no. 8, p. 667-670.

Ichoku, C., 2004, Global Chlorophyll: Image of the Day, *in* Przyborski, P., ed.: NASA Goddard Space Flight Center, NASA Earth Observatory (http://earthobservatory.nasa.gov/IOTD/view.php?id=4097) accessed 2014-09-18.

International Hydrographic Organisation, 1953, Limits of Oceans and Seas (special publication number 28), Monte-Carlo, International Hydrographic Organisation.

IPCC, 2013, Climate Change 2013: The Physical Science Basis. Contribution of Working Group I to the Fifth Assessment Report of the Intergovernmental Panel on Climate Change, Cambridge, United Kingdom and New York, NY, USA, Cambridge University Press.

John, C. M., Karner, G. D., Browning, E., Leckie, R. M., Mateo, Z., Carson, B., and Lowery, C., 2011, Timing and magnitude of Miocene eustasy derived from the mixed siliciclastic-carbonate stratigraphic record of the northeastern Australian margin: Earth and Planetary Science Letters, v. 304, no. 3-4, p. 455-467.

Johnson, K., Key, R., Millero, F., Sabine, C., Wallace, D., Winn, C., L.Arlen, K.Erickson, Friis, K., Galanter, M., Goen, J., Rotter, R., Thomas, C., Wilke, R., Takahashi, T., and Sutherland, S., 2003, Carbon Dioxide, Hydrographic, and Chemical Data Obtained During the R/V Knorr Cruises in the North Atlantic Ocean on WOCE Sections AR24 (November 2 - December 5, 1996) and A24, A20, and A22 (May 30 - September 3, 1997), *in* A, K., ed.: Oak Ridge National Laboratory, U.S. Department of Energy, Oak Ridge, Tennessee.

Jordan, K. A., 2008, Evaluating carbonate saturation effects on magnesium calcium core top calibration in benthic foraminifera [Master of Science Graduate Program in Oceanography: Rutgers, 141 p.

Justino, F., Marengo, J., Kucharski, F., Stordal, F., Machado, J., and Rodrigues, M., 2014, Influence of Antarctic ice sheet lowering on the Southern Hemisphere climate: modeling experiments mimicking the mid-Miocene: Climate Dynamics, v. 42, no. 3-4, p. 843-858.

Kaandorp, R. J. G., Vonhof, H. B., Wesselingh, F. P., Pittman, L. R., Kroon, D., and van Hinte, J. E., 2005, Seasonal Amazonian rainfall variation in the Miocene Climate Optimum: Palaeogeography Palaeoclimatology Palaeoecology, v. 221, no. 1-2, p. 1-6.

Kaiho, K., 1998, Phylogeny of Deep-Sea Calcareous Trochospial Benthic Foraminifera: Evolution and Diversification: Micropaleontology, v. 44, no. 3, p. 291-311.

Karnauskas, K., and Ummenhofer, C., 2014, On the dynamics of the Hadley circulation and subtropical drying: Climate Dynamics, v. 42, no. 9-10, p. 2259-2269.

Katz, A., 1973, Interaction of magnesium with calcite during crystal-growth at 25-90 degrees C and one atmosphere: Geochimica Et Cosmochimica Acta, v. 37, no. 6, p. 1563-&.

Katz, M. E., Miller, K. G., Wright, J. D., Wade, B. S., Browning, J. V., Cramer, B. S., and Rosenthal, Y., 2008, Stepwise transition from the Eocene greenhouse to the Oligocene icehouse: Nature Geoscience, v. 1, no. 5, p. 329-334.

Kender, S., Yu, J. M., and Peck, V. L., 2014, Deep ocean carbonate ion increase during mid Miocene CO2 decline: Scientific Reports, v. 4.

Kennett, J. P., and Stott, L. D., 1991, Abrupt deep-sea warming, palaeoceanographic changes and benthic extinctions at the end of the Palaeocene: Nature, v. 353, no. 6341, p. 225-229.

Keul, N., Langer, G., de Nooijer, L. J., Nehrke, G., Reichart, G. J., and Bijma, J., 2013, Incorporation of uranium in benthic foraminiferal calcite reflects

seawater carbonate ion concentration: Geochemistry Geophysics Geosystems, v. 14, no. 1, p. 102-111.

Kim, J., Hyeong, K., Jung, H. S., Moon, J. W., Kim, K. H., and Lee, I., 2006, Southward shift of the Intertropical Convergence Zone in the western Pacific during the late Tertiary: Evidence from ferromanganese crusts on seamounts west of the Marshall Islands: Paleoceanography, v. 21, no. 4.

Kim, J. H., Schouten, S., Hopmans, E. C., Donner, B., and Damste, J. S. S., 2008, Global sediment core-top calibration of the TEX86 paleothermometer in the ocean: Geochimica Et Cosmochimica Acta, v. 72, no. 4, p. 1154-1173.

Kim, J. H., van der Meer, J., Schouten, S., Helmke, P., Willmott, V., Sangiorgi, F., Koc, N., Hopmans, E. C., and Damste, J. S. S., 2010, New indices and calibrations derived from the distribution of crenarchaeal isoprenoid tetraether lipids: Implications for past sea surface temperature reconstructions: Geochimica Et Cosmochimica Acta, v. 74, no. 16, p. 4639-4654.

King, T. A., Ellis Jr., W. G., Murray, D. W., Shackleton, N. J., and S., H., 1997, Miocene evolution of carbonate sedimentation at the Ceara Rise: a multivariate data/proxy approach, *in* Shackleton, N. J., Curry, W. B., Richter, C., and Bralower, T. J., eds., Proceedings of the Ocean Drilling Program, Scientific Results, Volume 154: College Station, Texas, Ocean Drilling Program, p. 349-365.

Klinkhammer, G. P., and Palmer, M. R., 1991, Uranium in the Oceans - Where it Goes and Why: Geochimica Et Cosmochimica Acta, v. 55, no. 7, p. 1799-1806.

Knorr, G., and Lohmann, G., 2014, Climate warming during Antarctic ice sheet expansion at the Middle Miocene transition: Nature Geoscience, v. 7, no. 5, p. 376-381.

Koziol, A. M., and Newton, R. C., 1995, Experimental determination of the reactions magnesite plus quartz equals enstatite plus $CO_2$ and magnesite equals periclase plus $CO_2$, and enthalpies of formation of enstatite and magnesite: American Mineralogist, v. 80, no. 11-12, p. 1252-1260.

Kroopnic.P, Weiss, R. F., and Craig, H., 1972, Total $CO_2$,$^{13}C$, and dissolved-oxygen - $^{18}O$ at Geosecs II in the North-Atlantic: Earth and Planetary Science Letters, v. 16, no. 1, p. 103-&.

Kucera, M., Weinelt, M., Kiefer, T., Pflaumann, U., Hayes, A., Weinelt, M., Chen, M. T., Mix, A. C., Barrows, T. T., Cortijo, E., Duprat, J., Juggins, S., and Waelbroeck, C., 2005, Reconstruction of sea-surface temperatures from assemblages of planktonic foraminifera: multi-technique approach based on geographically constrained calibration data sets and its application to glacial Atlantic and Pacific Oceans: Quaternary Science Reviews, v. 24, no. 7-9, p. 951-998.

Kürschner, W. M., and Kvaček, Z., 2009, Oligocene-Miocen $CO_2$ fluctuations, climatic and palaeofloristic trends inferred from fossil plant assemblages in central Europe: Bulletin of Geosciences, v. 84, no. 2, p. 189-202.

Kürschner, W. M., Kvaček, Z., and Dilcher, D. L., 2008, The impact of Miocene atmospheric carbon dioxide fluctuations on climate and the evolution of terrestrial ecosystems: Proceedings of the National Academy of Sciences of the United States of America, v. 105, no. 2, p. 449-453.

Langebroek, P. M., Paul, A., and Schulz, M., 2009, Antarctic ice-sheet response to atmospheric CO2 and insolation in the Middle Miocene: Climate of the Past, v. 5, no. 4, p. 633-646.

LaRiviere, J. P., Ravelo, A. C., Crimmins, A., Dekens, P. S., Ford, H. L., Lyle, M., and Wara, M. W., 2012, Late Miocene decoupling of oceanic warmth and atmospheric carbon dioxide forcing: Nature, v. 486, no. 7401, p. 97-100.

Lea, D. W., Mashiotta, T. A., and Spero, H. J., 1999, Controls on magnesium and strontium uptake in planktonic foraminifera determined by live culturing: Geochimica Et Cosmochimica Acta, v. 63, no. 16, p. 2369-2379.

Lear, C. H., 2007, Mg/Ca palaeothermometry: a new window into Cenozoic climate change, *in* Williams, M., Haywood, A. M., Gregory, F. J., and Schmidt, D. N., eds., Deep-Time Perspectives on Climate Change: Marrying the Signal from Computer Models and Biological Proxies. The Micropalaeontological Society, Special Publications: London, The Geological Society, p. 313-322.

Lear, C. H., Bailey, T. R., Pearson, P. N., Coxall, H. K., and Rosenthal, Y., 2008, Cooling and ice growth across the Eocene-Oligocene transition: Geology, v. 36, no. 3, p. 251-254.

Lear, C. H., Elderfield, H., and Wilson, P. A., 2000, Cenozoic deep-sea temperatures and global ice volumes from Mg/Ca in benthic foraminiferal calcite: Science, v. 287, no. 5451, p. 269-272.

Lear, C. H., Mawbey, E. M., and Rosenthal, Y., 2010, Cenozoic benthic foraminiferal Mg/Ca and Li/Ca records: Toward unlocking temperatures and saturation states: Paleoceanography, v. 25, no. 4, p. PA4215.

Lear, C. H., and Rosenthal, Y., 2006, Benthic foraminiferal Li/Ca: Insights into Cenozoic seawater carbonate saturation state: Geology, v. 34, no. 11, p. 985-988.

Lear, C. H., Rosenthal, Y., Coxall, H. K., and Wilson, P. A., 2004, Late Eocene to early Miocene ice sheet dynamics and the global carbon cycle: Paleoceanography, v. 19, no. 4, p. PA4015.

Lear, C. H., Rosenthal, Y., and Slowey, N., 2002, Benthic foraminiferal Mg/Ca-paleothermometry: A revised core-top calibration: Geochimica Et Cosmochimica Acta, v. 66, no. 19, p. 3375-3387.

Lear, C. H., Rosenthal, Y., and Wright, J. D., 2003, The closing of a seaway: ocean water masses and global climate change: Earth and Planetary Science Letters, v. 210, no. 3-4, p. 425-436.

Leider, A., Hinrichs, K. U., Mollenhauer, G., and Versteegh, G. J. M., 2010, Core-top calibration of the lipid-based U-37(K)' and TEX86 temperature proxies on the southern Italian shelf (SW Adriatic Sea, Gulf of Taranto): Earth and Planetary Science Letters, v. 300, no. 1-2, p. 112-124.

Levitus, S., 1982, Climatological Atlas of the World Ocean: Princeton, NJ, NOAA/ERL/GFDL.

Lewis, A. R., Marchant, D. R., Ashworth, A. C., Hemming, S. R., and Machlus, M. L., 2007, Major middle Miocene global climate change: Evidence from East Antarctica and the Transantarctic Mountains: Geological Society of America Bulletin, v. 119, no. 11-12, p. 1449-1461.

Lewis, E., and Wallace, D. W. R., 1998, Program Developed for $CO_2$ System Calculations. ORNL/CDIAC-105: Oak Ridge National Laboratory, US Department of Energy, Oak Ridge, Tennessee, Carbon Dioxide Information Analysis Centre.

Lisiecki, L. E., and Raymo, M. E., 2005, A Pliocene-Pleistocene stack of 57 globally distributed benthic δ18O records: Paleoceanography, v. 20, no. 1, p. PA1003.

Lombard, F., Labeyrie, L., Michel, E., Spero, H. J., and Lea, D. W., 2009, Modelling the temperature dependent growth rates of planktic foraminifera: Marine Micropaleontology, v. 70, no. 1-2, p. 1-7.

Lowenstein, T. K., Timofeeff, M. N., Brennan, S. T., Hardie, L. A., and Demicco, R. V., 2001, Oscillations in Phanerozoic seawater chemistry: Evidence from fluid inclusions: Science, v. 294, no. 5544, p. 1086-1088.

Lunt, D. J., Foster, G. L., Haywood, A. M., and Stone, E. J., 2008, Late Pliocene Greenland glaciation controlled by a decline in atmospheric CO(2) levels: Nature, v. 454, no. 7208, p. 1102-U1141.

Mackensen, A., 1987, Benthische Foraminiferen auf dem Island-Schottland Rücken: Umwelt-Anzeiger an der Grenze zweier ozeanischer Räume: Paläontologische Zeitschrift, v. 61, no. 3-4, p. 149-179.

Mackensen, A., Sejrup, H. P., and Jansen, E., 1985, The distribution of living benthic foraminifera on the continental-slope and rise off southwest Norway: Marine Micropaleontology, v. 9, no. 4, p. 275-306.

Majewski, W., and Bohaty, S. M., 2010, Surface-water cooling and salinity decrease during the Middle Miocene climate transition at Southern Ocean ODP Site 747 (Kerguelen Plateau): Marine Micropaleontology, v. 74, no. 1-2, p. 1-14.

Mangini, A., Jung, M., and Laukenmann, S., 2001, What do we learn from peaks of uranium and of manganese in deep sea sediments?: Marine Geology, v. 177, no. 1-2, p. 63-78.

Marchitto, T. M., Bryan, S. P., Curry, W. B., and McCorkle, D. C., 2007, Mg/Ca temperature calibration for the benthic foraminifer Cibicidoides pachyderma: Paleoceanography, v. 22, no. 1, p. PA1203.

Marchitto, T. M., Curry, W. B., Lynch-Stieglitz, J., Bryan, S. P., Cobb, K. M., and Lund, D. C., 2014, Improved oxygen isotope temperature calibrations for cosmopolitan benthic foraminifera: Geochimica Et Cosmochimica Acta, v. 130, p. 1-11.

Marchitto, T. M., and deMenocal, P. B., 2003, Late Holocene variability of upper North Atlantic Deep Water temperature and salinity: Geochemistry Geophysics Geosystems, v. 4.

Martin, P. A., and Lea, D. W., 2002, A simple evaluation of cleaning procedures on fossil benthic foraminiferal Mg/Ca: Geochemistry Geophysics Geosystems, v. 3.

Martin, P. A., Lea, D. W., Rosenthal, Y., Shackleton, N. J., Sarnthein, M., and Papenfuss, T., 2002, Quaternary deep sea temperature histories derived from benthic foraminiferal Mg/Ca: Earth and Planetary Science Letters, v. 198, no. 1-2, p. 193-209.

Mawbey, E. M., and Lear, C. H., 2013, Carbon cycle feedbacks during the Oligocene-Miocene transient glaciation: Geology, v. 41, no. 9, p. 963-966.

McConnell, M. C., and Thunell, R. C., 2005, Calibration of the planktonic foraminiferal Mg/Ca paleothermometer: sediment trap results from the Guaymas Basin, Gulf of California: Paleoceanography, v. 20, no. 2, p. PA2106.

McManus, J., Berelson, W. M., Klinkhammer, G. P., Hammond, D. E., and Holm, C., 2005, Authigenic uranium: relationship to oxygen penetration depth and organic carbon rain: Geochimica Et Cosmochimica Acta, v. 69, no. 1, p. 95-108.

Merico, A., Tyrrell, T., and Wilson, P. A., 2008, Eocene/Oligocene ocean de-acidification linked to Antarctic glaciation by sea-level fall: Nature, v. 452, no. 7190, p. 979-U976.

Miller, K. G., Kominz, M. A., Browning, J. V., Wright, J. D., Mountain, G. S., Katz, M. E., Sugarman, P. J., Cramer, B. S., Christie-Blick, N., and Pekar, S. F., 2005, The phanerozoic record of global sea-level change: Science, v. 310, no. 5752, p. 1293-1298.

Miller, K. G., Wright, J. D., Katz, M. E., Wade, B. S., Browning, J. V., Cramer, B. S., and Rosenthal, Y., 2009, Climate threshold at the Eocene-Oligocene transition: Antarctic ice sheet influence on ocean circulation: Late Eocene Earth: Hothouse Icehouse, and Impacts, v. 452, p. 169-178.

Mix, A. C., Morey, A. E., Pisias, N. G., and Hostetler, S. W., 1999, Foraminiferal faunal estimates of paleotemperature: Circumventing the no-analog problem yields cool ice age tropics: Paleoceanography, v. 14, no. 3, p. 350-359.

Monnin, E., Indermuhle, A., Dallenbach, A., Fluckiger, J., Stauffer, B., Stocker, T. F., Raynaud, D., and Barnola, J. M., 2001, Atmospheric CO2 concentrations over the last glacial termination: Science, v. 291, no. 5501, p. 112-114.

Mortyn, P. G., Elderfield, H., Anand, P., and Greaves, M., 2005, An evaluation of controls on planktonic foraminiferal Sr/Ca: Comparison of water column and core-top data from a North Atlantic transect: Geochemistry Geophysics Geosystems, v. 6.

Murgese, D. S., and De Deckker, P., 2005, The distribution of deep-sea benthic foraminifera in core tops from the eastern Indian Ocean: Marine Micropaleontology, v. 56, no. 1-2, p. 25-49.

Ni, Y. Y., Foster, G. L., Bailey, T., Elliott, T., Schmidt, D. N., Pearson, P., Haley, B., and Coath, C., 2007, A core top assessment of proxies for the ocean carbonate system in surface-dwelling foraminifers: Paleoceanography, v. 22, no. 3.

Nurnberg, D., 2000, Paleoclimate - Taking the temperature of past ocean surfaces: Science, v. 289, no. 5485, p. 1698-1699.

O'Neil, J. R., Clayton, R. N., and Mayeda, T. K., 1969, Oxygen isotope fractionation in divalent metal carbonates: Journal of Chemical Physics, v. 51, no. 12, p. 5547-&.

Oerlemans, J., 2002, On glacial inception and orography: Quaternary International, v. 95-6, p. 5-10.

Oomori, T., Kaneshima, H., Maezato, Y., and Kitano, Y., 1987, Distribution coefficient of $Mg^{2+}$ ions between calcite and solution at 10-50-degrees-C: Marine Chemistry, v. 20, no. 4, p. 327-336.

Opdyke, B. N., and Walker, J. C., 1992, Return of the coral reef hypothesis: basin to shelf partitioning of CaCO3 and its effect on atmospheric CO2: Geology, v. 20, no. 8, p. 733-736.

Ortiz, J. D., and Mix, A. C., 1997, Comparison of Imbrie-Kipp transfer function and modern analog temperature estimates using sediment trap and core top foraminiferal faunas: Paleoceanography, v. 12, no. 2, p. 175-190.

Pagani, M., Zachos, J. C., Freeman, K. H., Tipple, B., and Bohaty, S., 2005, Marked decline in atmospheric carbon dioxide concentrations during the Paleogene: Science, v. 309, no. 5734, p. 600-603.

Paillard, D., Labeyrie, L., and Yiou, P., 1996, Macintosh program performs time-series analysis: EOS Transactions of the American Geophysical Union, v. 77, p. 379.

Pälike, H., Frazier, J., and Zachos, J. C., 2006a, Extended orbitally forced palaeoclimatic records from the equatorial Atlantic Ceara Rise: Quaternary Science Reviews, v. 25, no. 23-24, p. 3138-3149.

Pälike, H., Laskar, J., and Shackleton, N. J., 2004, Geologic constraints on the chaotic diffusion of the solar system: Geology, v. 32, no. 11, p. 929-932.

Pälike, H., Lyle, M. W., Nishi, H., Raffi, I., Ridgwell, A., Gamage, K., Klaus, A., Acton, G., Anderson, L., Backman, J., Baldauf, J., Beltran, C., Bohaty, S. M., Bown, P., Busch, W., Channell, J. E. T., Chun, C. O. J., Delaney, M., Dewangan, P., Dunkley Jones, T., Edgar, K. M., Evans, H., Fitch, P., Foster, G. L., Gussone, N., Hasegawa, H., Hathorne, E. C., Hayashi, H., Herrle, J. O., Holbourn, A., Hovan, S., Hyeong, K., Iijima, K., Ito, T., Kamikuri, S., Kimoto, K., Kuroda, J., Leon-Rodriguez, L., Malinverno, A., Moore, T. C., Murphy, B. H., Murphy, D. P., Nakamura, H., Ogane, K., Ohneiser, C., Richter, C., Robinson, R., Rohling, E. J., Romero, O., Sawada, K., Scher, H., Schneider, L., Sluijs, A., Takata, H., Tian, J.,

Tsujimoto, A., Wade, B. S., Westerhold, T., Wilkens, R., Williams, T., Wilson, P. A., Yamamoto, Y., Yamamoto, S., Yamazaki, T., and Zeebe, R. E., 2012, A Cenozoic record of the equatorial Pacific carbonate compensation depth: Nature, v. 488, no. 7413, p. 609-+.

Pälike, H., Nishi, H., Lyle, M., Raffi, I., Klaus, A., Gamage, K., and Scientists, a. t. E., 2009, Pacific Equatorial Transect. IODP Prel. Rept., 320. , Integrated Ocean Drilling Program Management International, Inc.

Pälike, H., Norris, R. D., Herrle, J. O., Wilson, P. A., Coxall, H. K., Lear, C. H., Shackleton, N. J., Tripati, A. K., and Wade, B. S., 2006b, The heartbeat of the Oligocene climate system: Science, v. 314, no. 5807, p. 1894-1898.

Passchier, S., Browne, G., Field, B., Fielding, C. R., Krissek, L. A., Panter, K., Pekar, S. F., and Team, A.-S. S., 2011, Early and middle Miocene Antarctic glacial history from the sedimentary facies distribution in the AND-2A drill hole, Ross Sea, Antarctica: Geological Society of America Bulletin, v. 123, no. 11-12, p. 2352-2365.

Pearson, P. N., and Chaisson, W. P., 1997, Late Paleocene to Middle Miocene Planktonic Foraminifer Biostratigraphy of the Ceara Rise, *in* Shackleton, N. J., Curry, W. B., Richter, C., and Bralower, T. J., eds., Proceedings of the Ocean Drilling Program, Scientific Results, Volume 154: College Station, TX, Ocean Drilling Program, p. 33-68.

Pearson, P. N., Ditchfield, P. W., Singano, J., Harcourt-Brown, K. G., Nicholas, C. J., Olsson, R. K., Shackleton, N. J., and Hall, M. A., 2001, Warm tropical sea surface temperatures in the Late Cretaceous and Eocene epochs: Nature, v. 413, no. 6855, p. 481-487.

Pearson, P. N., Foster, G. L., and Wade, B. S., 2009, Atmospheric carbon dioxide through the Eocene-Oligocene climate transition: Nature, v. 461, no. 7267, p. 1110-1114.

Pearson, P. N., and Palmer, M. R., 2000, Atmospheric carbon dioxide concentrations over the past 60 million years: Nature, v. 406, no. 6797, p. 695-699.

Pearson, P. N., van Dongen, B. E., Nicholas, C. J., Pancost, R. D., Schouten, S., Singano, J. M., and Wade, B. S., 2007, Stable warm tropical climate through the Eocene Epoch: Geology, v. 35, no. 3, p. 211-214.

Pekar, S. F., Christie-Blick, N., Kominz, M. A., and Miller, K. G., 2002, Calibration between eustatic estimates from backstripping and oxygen isotopic records for the Oligocene: Geology, v. 30, no. 10, p. 903-906.

Pekar, S. F., and DeConto, R. M., 2006, High-resolution ice-volume estimates for the early Miocene: Evidence for a dynamic ice sheet in Antarctica: Palaeogeography Palaeoclimatology Palaeoecology, v. 231, no. 1-2, p. 101-109.

Pena, L. D., Calvo, E., Cacho, I., Eggins, S., and Pelejero, C., 2005, Identification and removal of Mn-Mg-rich contaminant phases on foraminiferal tests: Implications for Mg/Ca past temperature reconstructions: Geochemistry Geophysics Geosystems, v. 6.

Petit, J. R., Jouzel, J., Raynaud, D., Barkov, N. I., Barnola, J. M., Basile, I., Bender, M., Chappellaz, J., Davis, M., Delaygue, G., Delmotte, M., Kotlyakov, V. M., Legrand, M., Lipenkov, V. Y., Lorius, C., Pepin, L., Ritz, C., Saltzman, E., and Stievenard, M., 1999, Climate and atmospheric history of the past 420,000 years from the Vostok ice core, Antarctica: Nature, v. 399, no. 6735, p. 429-436.

Philander, S. G. H., Gu, D., Halpern, D., Lambert, G., Lau, N. C., Li, T., and Pacanowski, R. C., 1996, Why the ITCZ is mostly north of the equator: Journal of Climate, v. 9, no. 12, p. 2958-2972.

Pollard, D., and DeConto, R. M., 2005, Hysteresis in cenozoic antarctic ice-sheet variations: Global and Planetary Change, v. 45, no. 1-3, p. 9-21.

Pollard, D., Kump, L. R., and Zachos, J. C., 2013, Interactions between carbon dioxide, climate, weathering, and the Antarctic ice sheet in the earliest Oligocene: Global and Planetary Change, v. 111, p. 258-267.

Powers, L. A., Werne, J. P., Johnson, T. C., Hopmans, E. C., Damste, J. S. S., and Schouten, S., 2004, Crenarchaeotal membrane lipids in lake sediments: A new paleotemperature proxy for continental paleoclimate reconstruction?: Geology, v. 32, no. 7, p. 613-616.

Rae, J. W. B., Foster, G. L., Schmidt, D. N., and Elliott, T., 2011, Boron isotopes and B/Ca in benthic foraminifera: Proxies for the deep ocean carbonate system: Earth and Planetary Science Letters, v. 302, no. 3-4, p. 403-413.

Raffi, I., Backman, J., Fornaciari, E., Palike, H., Rio, D., Lourens, L., and Hilgen, F., 2006, A review of calcareous nannofossil astrobiochronology encompassing the past 25 million years: Quaternary Science Reviews, v. 25, no. 23-24, p. 3113-3137.

Raitzsch, M., Duenas-Bohorquez, A., Reichart, G. J., de Nooijer, L. J., and Bickert, T., 2010, Incorporation of Mg and Sr in calcite of cultured benthic foraminifera: impact of calcium concentration and associated calcite saturation state: Biogeosciences, v. 7, no. 3, p. 869-881.

Raitzsch, M., Kuhnert, H., Hathorne, E. C., Groeneveld, J., and Bickert, T., 2011, U/Ca in benthic foraminifers: A proxy for the deep-sea carbonate saturation: Geochemistry Geophysics Geosystems, v. 12.

Rathburn, A. E., and Corliss, B. H., 1994, The ecology of living (stained) deep-sea benthic foramnifera from the Sulu Sea: Paleoceanography, v. 9, no. 1, p. 87-150.

Rathmann, S., and Kuhnert, H., 2008, Carbonate ion effect on Mg/Ca, Sr/Ca and stable isotopes on the benthic foraminifera Oridorsalis umbonatus off Namibia: Marine Micropaleontology, v. 66, no. 2, p. 120-133.

Raymo, M. E., 1994, The Himalayas, Organic-Carbon Burial, and Climate in the Miocene: Paleoceanography, v. 9, no. 3, p. 399-404.

Retallack, G. J., 2002, Carbon dioxide and climate over the past 300 Myr: Philosophical Transactions of the Royal Society of London Series a-Mathematical Physical and Engineering Sciences, v. 360, no. 1793, p. 659-673.

-, 2009, Refining a pedogenic-carbonate CO2 paleobarometer to quantify a middle Miocene greenhouse spike: Palaeogeography Palaeoclimatology Palaeoecology, v. 281, no. 1-2, p. 57-65.

Rohling, E. J., Haigh, I. D., Foster, G. L., Roberts, A. P., and Grant, K. M., 2013, A geological perspective on potential future sea-level rise: Scientific Reports, v. 3.

Rosenthal, Y., Boyle, E. A., and Slowey, N., 1997, Temperature control on the incorporation of magnesium, strontium, fluorine, and cadmium into benthic foraminiferal shells from Little Bahama Bank: Prospects for thermocline paleoceanography: Geochimica Et Cosmochimica Acta, v. 61, no. 17, p. 3633-3643.

Rosenthal, Y., Field, M. P., and Sherrell, R. M., 1999, Precise determination of element/calcium ratios in calcareous samples using sector field inductively coupled plasma mass spectrometry: Analytical Chemistry, v. 71, no. 15, p. 3248-3253.

Rosenthal, Y., Lear, C. H., Oppo, D. W., and Linsley, B. K., 2006, Temperature and carbonate ion effects on Mg/Ca and Sr/Ca ratios in benthic foraminifera: Aragonitic species Hoeglundina elegans: Paleoceanography, v. 21, no. 1, p. PA1007.

Rosenthal, Y., Lohmann, G. P., Lohmann, K. C., and Sherrell, R. M., 2000, Incorporation and preservation of Mg in Globigerinoides sacculifer: Implications for reconstructing the temperature and O-18/O-16 of seawater: Paleoceanography, v. 15, no. 1, p. 135-145.

Rousselle, G., Beltran, C., Sicre, M. A., Raffi, I., and De Rafelis, M., 2013, Changes in sea-surface conditions in the Equatorial Pacific during the middle Miocene-Pliocene as inferred from coccolith geochemistry: Earth and Planetary Science Letters, v. 361, p. 412-421.

Russell, A. D., Emerson, S., Mix, A. C., and Peterson, L. C., 1996, The use of foraminiferal uranium/calcium ratios as an indicator of changes in seawater uranium content: Paleoceanography, v. 11, no. 6, p. 649-663.

Russell, A. D., Hönisch, B., Spero, H. J., and Lea, D. W., 2004, Effects of seawater carbonate ion concentration and temperature on shell U, Mg, and Sr in cultured planktonic foraminifera: Geochimica et Cosmochimica Acta, v. 68, no. 21, p. 4347-4361.

Sabine, C. L., Feely, R. A., Gruber, N., Key, R. M., Lee, K., Bullister, J. L., Wanninkhof, R., Wong, C. S., Wallace, D. W. R., Tilbrook, B., Millero, F. J., Peng, T. H., Kozyr, A., Ono, T., and Rios, A. F., 2004, The oceanic sink for anthropogenic CO(2): Science, v. 305, no. 5682, p. 367-371.

Schmidt, M. W., and Spero, H. J., 2011, Meridional shifts in the marine ITCZ and the tropical hydrologic cycle over the last three glacial cycles: Paleoceanography, v. 26.

Schouten, S., Forster, A., Panoto, F. E., and Damste, J. S. S., 2007, Towards calibration of the TEX86 palaeothermometer for tropical sea surface

temperatures in ancient greenhouse worlds: Organic Geochemistry, v. 38, no. 9, p. 1537-1546.

Schulz, M., and Mudelsee, M., 2002, REDFIT: estimating red-noise spectra directly from unevenly spaced paleoclimatic time series: Computers & Geosciences, v. 28, no. 3, p. 421-426.

Schwarz, T., 1997, Lateritic bauxite in central Germany and implications for Miocene palaeoclimate: Palaeogeography Palaeoclimatology Palaeoecology, v. 129, no. 1-2, p. 37-50.

Segev, E., and Erez, J., 2006, Effect of Mg/Ca ratio in seawater on shell composition in shallow benthic foraminifera: Geochemistry Geophysics Geosystems, v. 7.

Sepulcre, S., Vidal, L., Tachikawa, K., Rostek, F., and Bard, E., 2011, Sea-surface salinity variations in the northern Caribbean Sea across the Mid-Pleistocene Transition: Climate of the Past, v. 7, no. 1, p. 75-90.

Sexton, P. F., Wilson, P. A., and Pearson, P. N., 2006, Microstructural and geochemical perspectives on planktic foraminiferal preservation: "Glassy" versus "Frosty": Geochemistry Geophysics Geosystems, v. 7.

Shackleton, N. J., Crowhurst, S. J., Weedon, G. P., and Laskar, J., 1999, Astronomical calibration of Oligocene-Miocene time: Philosophical Transactions of the Royal Society of London Series a-Mathematical Physical and Engineering Sciences, v. 357, no. 1757, p. 1907-1929.

Shackleton, N. J., and Kennett, J. P., 1975, Paleotemperature history of the Cenozoic and the initiation of Antarctic glaciation: oxygen and carbon isotope analyses in DSDP Sites 277, 279, and 281, *in* Kennett, J. P., Houtz, R. E., and al., e., eds., Initial Retorts, DSDP, Volume 29: Washington, U.S. Govt. Printing Office, p. 743-755.

Shakun, J. D., and Carlson, A. E., 2010, A global perspective on Last Glacial Maximum to Holocene climate change: Quaternary Science Reviews, v. 29, no. 15-16, p. 1801-1816.

Shevenell, A. E., Kennett, J. P., and Lea, D. W., 2004, Middle Miocene Southern Ocean cooling and Antarctic cryosphere expansion: Science, v. 305, no. 5691, p. 1766-1770.

-, 2008, Middle Miocene ice sheet dynamics, deep-sea temperatures, and carbon cycling: A Southern Ocean perspective: Geochemistry Geophysics Geosystems, v. 9.

Shipboard Scientific Party, 1982, Site 588: Lord Howe Rise, 26°S, *in* Kennett, J. P., von der Borch, C. C., and al., e., eds., Intial Reports DSDP Volume 90: Washington, U.S. Govet. Printing Office, p. 139-252.

-, 1995a, Introduction, *in* Curry, W. B., Shackleton, N. J., Richter, C., and al., e., eds., Proceedings of the Ocean Drilling Program, Initial Reports, Volume 154: College Station, Texas, Ocean Drilling Program, p. 5-10.

-, 1995b, Site 925, *in* Curry, W. B., Shackleton, N. J., Richter, C., and al., e., eds., Proceedings of the Ocean Drilling Program, Initial Reports, Volume 154: College Station, Texas, Ocean Drilling Program, p. 55-152.

-, 1995c, Site 926, *in* Curry, W. B., Shackleton, N. J., Richter, C., and al., e., eds., Proceedings of the Ocean Drilling Program, Initial Reports, Volume 154: College Station, Texas, Ocean Drilling Program, p. 153-232.

-, 1995d, Site 927, *in* Curry, W. B., Shackleton, N. J., Richter, C., and al., e., eds., Proceedings of the Ocean Drilling Program, Initial Reports, Volume 154: College Station, Texas, Ocean Drilling Program, p. 233-279.

-, 2002, Site 1208, *in* Bralower, T. J., Premoli Silva, I., Malone, M. J., and al., e., eds., Proceedings of the Ocean Drilling Program, Initial Reports, 198: College Station, TX Ocean Drilling Program, p. 1-93.

Sigman, D. M., and Boyle, E. A., 2000, Glacial/interglacial variations in atmospheric carbon dioxide: Nature, v. 407, no. 6806, p. 859-869.

Skinner, L. C., and Elderfield, H., 2005, Constraining ecological and biological bias in planktonic foraminiferal Mg/Ca and delta $O^{18}$(cc): A multispecies approach to proxy calibration testing: Paleoceanography, v. 20, no. 1, p. PA1015.

Skinner, L. C., Shackleton, N. J., and Elderfield, H., 2003, Millennial-scale variability of deep-water temperature and delta O-18(dw) indicating deep-water source variations in the Northeast Atlantic, 0-34 cal. ka BP: Geochemistry Geophysics Geosystems, v. 4.

Spofforth, D. J. A., Agnini, C., Palike, H., Rio, D., Fornaciari, E., Giusberti, L., Luciani, V., Lanci, L., and Muttoni, G., 2010, Organic carbon burial following the middle Eocene climatic optimum in the central western Tethys: Paleoceanography, v. 25.

St John, K., 2008, Cenozoic ice-rafting history of the central Arctic Ocean: Terrigenous sands on the Lomonosov Ridge: Paleoceanography, v. 23, no. 1.

Stachnik, J. P., and Schumacher, C., 2011, A comparison of the Hadley circulation in modern reanalyses: Journal of Geophysical Research-Atmospheres, v. 116.

Stanley, S. M., and Hardie, L. A., 1998, Secular oscillations in the carbonate mineralogy of reef-building and sediment-producing organisms driven by tectonically forced shifts in seawater chemistry: Palaeogeography Palaeoclimatology Palaeoecology, v. 144, no. 1-2, p. 3-19.

Tachikawa, K., Timmermann, A., Vidal, L., Sonzogni, C., and Timm, O. E., 2014, CO2 radiative forcing and Intertropical Convergence Zone influences on western Pacific warm pool climate over the past 400 ka: Quaternary Science Reviews, v. 86, p. 24-34.

Thomas, E., 2007, Cenozoic mass extinctions in the deep sea: What perturbs the largest habitat on Earth?, Large Ecosystem Perturbations: Causes and Consequences: Geological Society of America Special Paper, Volume 424, p. 1-23.

Thomas, E., and Vincent, E., 1987, Equatorial Pacific Deep-Sea Benthic Foraminifera - Faunal Changes Before the Middle Miocene Polar Cooling: Geology, v. 15, no. 11, p. 1035-1039.

Tisserand, A. A., Dokken, T. M., Waelbroeck, C., Gherardi, J. M., Scao, V., Fontanier, C., and Jorissen, F., 2013, Refining benthic foraminiferal Mg/Ca-temperature calibrations using core-tops from the western tropical Atlantic: Implication for paleotemperature estimation: Geochemistry Geophysics Geosystems, v. 14, no. 4, p. 929-946.

Tripati, A., Backman, J., Elderfield, H., and Ferretti, P., 2005, Eocene bipolar glaciation associated with global carbon cycle changes: Nature, v. 436, no. 7049, p. 341-346.

Tripati, A., and Elderfield, H., 2005, Deep-Sea Temperature and Circulation Changes at the Paleocene-Eocene Thermal Maximum: Science, v. 308, no. 5730, p. 1894-1898.

Tripati, A. K., Roberts, C. D., and Eagle, R. A., 2009, Coupling of CO2 and Ice Sheet Stability Over Major Climate Transitions of the Last 20 Million Years: Science, v. 326, no. 5958, p. 1394-1397.

van de Wal, R. S. W., de Boer, B., Lourens, L. J., Köhler, P., and Bintanja, R., 2011, Reconstruction of a continuous high-resolution CO2 record over the past 20 million years: Clim. Past, v. 7, no. 4, p. 1459-1469.

Vecsei, A., and Berger, W. H., 2004, Increase of atmospheric CO2 during deglaciation: Constraints on the coral reef hypothesis from patterns of deposition: Global Biogeochemical Cycles, v. 18, no. 1, p. GB1035.

Verducci, M., Foresi, L. M., Scott, G. H., Tiepolo, M., Sprovieri, M., and Lirer, F., 2007, East Antarctic Ice Sheet fluctuations during the Middle Miocene Climatic Transition inferred from faunal and biogeochemical data on planktonic foraminifera (Kerguelen Plateau): Antarctica: A Keystone in a Changing World – Online Proceedings of the 10th ISAES, v. U.S. Geological Survey and The National Academics USGS OF-2007-1047, p. Short Research Paper 037.

von Langen, P. J., Pak, D. K., Spero, H. J., and Lea, D. W., 2005, Effects of temperature on Mg/Ca in neogloboquadrinid shells determined by live culturing: Geochemistry Geophysics Geosystems, v. 6.

Wade, B. S., Pearson, P. N., Berggren, W. A., and Pälike, H., 2011, Review and revision of Cenozoic tropical planktonic foraminiferal biostratigraphy and calibration to the geomagnetic polarity and astronomical time scale: Earth-Science Reviews, v. 104, no. 1-3, p. 111-142.

Wan, S. M., Kurschner, W. M., Clift, P. D., Li, A. C., and Li, T. G., 2009, Extreme weathering/erosion during the Miocene Climatic Optimum: Evidence from sediment record in the South China Sea: Geophysical Research Letters, v. 36.

Wang, P., Prell, W. L., Blum, P., and al., e., 2000, Site 1148, Proceedings of the Ocean Drilling Program, Initial Reports, Volume 184, p. 1-122.

Warny, S., Askin, R. A., Hannah, M. J., Mohr, B. A. R., Raine, J. I., Harwood, D. M., Florindo, F., and Team, S. M. S. S., 2009, Palynomorphs from a sediment core reveal a sudden remarkably warm Antarctica during the middle Miocene: Geology, v. 37, no. 10, p. 955-958.

Weldeab, S., Schneider, R. R., and Kolling, M., 2006a, Comparison of foraminiferal cleaning procedures for Mg/Ca paleothermometry on core material deposited under varying terrigenous-input and bottom water conditions: Geochemistry Geophysics Geosystems, v. 7.

-, 2006b, Deglacial sea surface temperature and salinity increase in the western tropical Atlantic in synchrony with high latitude climate instabilities: Earth and Planetary Science Letters, v. 241, no. 3-4, p. 699-706.

Wilson, J. M., Severson, R., and Beman, J. M., 2014, Ocean-Scale Patterns in Community Respiration Rates along Continuous Transects across the Pacific Ocean: Plos One, v. 9, no. 7.

Woodard, S. C., Rosenthal, Y., Miller, K. G., Wright, J. D., Chiu, B. K., and Lawrence, K. T., 2014, Antarctic role in Northern Hemisphere glaciation: Science, v. 346, no. 6211, p. 847-851.

Xie, S.-P., and Philander, S. G. H., 1994, A coupled ocean-atmosphere model of relevance to the ITCZ in the eastern Pacific: Tellus, v. 46A, p. 340-350.

Xie, S.-P., and Saito, K., 2001, Formation and Variability of a Northerly ITCZ in a Hybrid Coupled AGCM: Continental Forcing and Oceanic–Atmospheric Feedback*: Journal of Climate, v. 14, no. 6, p. 1262-1276.

You, Y., Huber, M., Muller, R. D., Poulsen, C. J., and Ribbe, J., 2009, Simulation of the Middle Miocene Climate Optimum: Geophysical Research Letters, v. 36.

Yu, J. M., Broecker, W. S., Elderfield, H., Jin, Z. D., McManus, J., and Zhang, F., 2010a, Loss of Carbon from the Deep Sea Since the Last Glacial Maximum: Science, v. 330, no. 6007, p. 1084-1087.

Yu, J. M., and Elderfield, H., 2007, Benthic foraminiferal B/Ca ratios reflect deep water carbonate saturation state: Earth and Planetary Science Letters, v. 258, no. 1-2, p. 73-86.

-, 2008, Mg/Ca in the benthic foraminifera Cibicidoides wuellerstorfi and Cibicidoides mundulus: Temperature versus carbonate ion saturation: Earth and Planetary Science Letters, v. 276, no. 1-2, p. 129-139.

Yu, J. M., Elderfield, H., and Piotrowski, A. M., 2008, Seawater carbonate ion-delta C-13 systematics and application to glacial-interglacial North Atlantic ocean circulation: Earth and Planetary Science Letters, v. 271, no. 1-4, p. 209-220.

Yu, J. M., Foster, G. L., Elderfield, H., Broecker, W. S., and Clark, E., 2010b, An evaluation of benthic foraminiferal B/Ca and delta B-11 for deep ocean carbonate ion and pH reconstructions: Earth and Planetary Science Letters, v. 293, no. 1-2, p. 114-120.

Yu, L. S., 2011, A global relationship between the ocean water cycle and near-surface salinity: Journal of Geophysical Research-Oceans, v. 116.

Zachos, J., Pagani, M., Sloan, L., Thomas, E., and Billups, K., 2001, Trends, rhythms, and aberrations in global climate 65 Ma to present: Science, v. 292, no. 5517, p. 686-693.

Zachos, J. C., Dickens, G. R., and Zeebe, R. E., 2008, An early Cenozoic perspective on greenhouse warming and carbon-cycle dynamics: Nature, v. 451, no. 7176, p. 279-283.

Zachos, J. C., and Kump, L. R., 2005, Carbon cycle feedbacks and the initiation of Antarctic glaciation in the earliest Oligocene: Global and Planetary Change, v. 47, no. 1, p. 51-66.

Zhang, Y. G., Pagani, M., Liu, Z. H., Bohaty, S. M., and DeConto, R., 2013, A 40-million-year history of atmospheric CO2: Philosophical Transactions of the Royal Society a-Mathematical Physical and Engineering Sciences, v. 371, no. 2001.

Ziegler, M., Nurnberg, D., Karas, C., Tiedemann, R., and Lourens, L. J., 2008, Persistent summer expansion of the Atlantic Warm Pool during glacial abrupt cold events: Nature Geosci, v. 1, no. 9, p. 601-605.

Zou, H. B., McKeegan, K. D., Xu, X. S., and Zindler, A., 2004, Fe-Al-rich tridymite-hercynite xenoliths with positive cerium anomalies: preserved lateritic paleosols and implications for Miocene climate: Chemical Geology, v. 207, no. 1-2, p. 101-116.

# 8 APPENDICES

## 8.1 Appendix 1 – Cleaning procedure

### *8.1.1 Fine Clay Removal*

The purpose of this step is to remove residual clay material that has not been removed by the sediment washing, or was inside the chambers of the foraminifera. The tubes are partially filled with 18.2 MΩ DI $H_2O$, agitated and ultrasonicated before being left to allow the foraminifera to settle for 30s or so and then the remainder siphoned off. This is repeated twice more with water, twice more again with methanol and then twice more again with DI $H_2O$. The procedure is varied slightly by siphoning a different tube at the start of each iteration to avoid systematic variation. At the end of the last iteration of this the tubes are siphoned as dry as possible without losing foraminiferal material.

### *8.1.2 Oxide Removal*

The purpose of this step is to remove the metal oxide coatings that can form on a foraminifer's test during diagenesis (Barker et al., 2003; Martin and Lea, 2002). If terriginous material has been deposited along with the foraminifera then this step can also remove any Mg/Ca signal that has been imposed upon the sediment from this source (Weldeab et al., 2006a).

A solution of ammonia, citric acid and hydrous hydrazine is added to the tubes, and the tubes are placed into a water bath at ~80-90$^{o}$C for 30 minutes. They are ultrasonicated for a few seconds every 2 minutes during this time. The hydrous hydrazine solution is then pipetted off and the tubes are cleaned of the hydrous hydrazine by filling with DI $H_2O$ and leaving in the hot water bath for 5 minutes. The water is then siphoned off, the tubes refilled and siphoned twice more and then once again refilled and placing in the water bath for five more minutes before the water is siphoned off once more. After this step, the material is then transferred into new tubes because the inner surfaces of the old tubes

become contaminated with metals adsorbed during this phase (Boyle and Keigwin, 1985/1986).

### *8.1.3 Removal of Organic Contaminants*

The purpose of this step is to remove any organic material that contaminates the samples. The samples are placed into a water bath at ~80-90$^{o}$C oxidised in a solution of 0.1 M NaOH and $H_2O_2$. The samples are left in there for five minutes before being ultrasonicated for a few seconds and then returned to the water bath for a further five minutes. The samples are then topped up with 18.2 MΩ DI $H_2O$ and the NaOH and $H_2O_2$ solution is siphoned off. The tubes are then topped up with DI $H_2O$ and re-siphoned twice more.

### *8.1.4 Dilute Acid Leach*

The purpose of this phase is to leach any contaminants that have become adsorbed onto the surfaces of the foraminifers' tests during the cleaning process (Boyle and Keigwin, 1985/1986). 0.002M $HNO_3$ is added to each tube and then they are ultrasonicated for 30 seconds. The foraminifera are left to settle for a few seconds and then the $HNO_3$ is siphoned off. This is quickly repeated four more times, changing the orientation of the rack in the ultrasonic bath, and which tube is siphoned first to avoid systematic variations. The tubes are then filled with 18.2 MΩ DI $H_2O$, ultrasonicated for a few seconds and then siphoned. This is repeated once more, after which all the remaining water is pipetted off.

## 8.2 Appendix 2 – Frequencies Present in Physical Properties

| | f1 | f2 | f3 | f4 | f5 | f6 | f7 | f8 | f9 | f10 | f11 | f12 | f13 | f14 | f15 | f16 | f17 | f18 | f19 | f20 |
|---|---|---|---|---|---|---|---|---|---|---|---|---|---|---|---|---|---|---|---|---|
| *A** | | | | | | | | | | | | | | | | | | | | |
| **frequency ($m^{-1}$)** | | | 0.042 | | | | | | | | | | 1.91 | 2.03 | | | | | | 4.71 |
| **period (ka) 13.7 $mMa^{-1}$** | | | 1735.22 | | | | | | | | | | 38.28 | 35.90 | | | | | | 15.49 |
| **new period (ka) 17.3 $mMa^{-1}$** | | | 1376.27 | | | | | | | | | | 30.26 | 28.47 | | | | | | 12.27 |
| *L** | | | | | | | | | | | | | | | | | | | | |
| **frequency ($m^{-1}$)** | | 0.023 | | | | | | | | | 1.40 | 1.75 | | 2.07 | 2.21 | | 3.45 | 3.63 | 4.08 | |
| **period (ka) 13.7 $mMa^{-1}$** | | 3185.06 | | | | | | | | | 52.21 | 41.63 | | 35.19 | 33.01 | | 21.16 | 20.10 | 17.89 | |
| **new period (ka) 17.3 $mMa^{-1}$** | | 2513.19 | | | | | | | | | 41.29 | 33.03 | | 27.92 | 26.16 | | 16.75 | 15.92 | 14.17 | |
| *B** | | | | | | | | | | | | | | | | | | | | |
| **frequency ($m^{-1}$)** | 0.013 | | | 0.066 | 0.093 | | | | | | 1.40 | | | 2.08 | | | 3.47 | | | 4.63 |
| **period (ka) 13.7 $mMa^{-1}$** | 5519.59 | | | 1103.92 | 788.52 | | | | | | 52.07 | | | 35.16 | | | 21.07 | | | 15.77 |
| **new period (ka) 17.3 $mMa^{-1}$** | 4446.42 | | | 875.81 | 621.54 | | | | | | 41.29 | | | 27.79 | | | 16.66 | | | 12.48 |
| *Bulk Density* | | | | | | | | | | | | | | | | | | | | |
| **frequency ($m^{-1}$)** | | | | | 0.087 | | | 0.44 | 0.54 | 0.63 | | | | | | | | | | |
| **period (ka) 13.7 $mMa^{-1}$** | | | | | 835.74 | | | 167.15 | 134.80 | 116.07 | | | | | | | | | | |
| **new period (ka) 17.3 $mMa^{-1}$** | | | | | 664.41 | | | 131.37 | 107.04 | 91.75 | | | | | | | | | | |
| *Magnetic Susceptibility* | | | | | | | | | | | | | | | | | | | | |
| **frequency ($m^{-1}$)** | | | | 0.061 | | 0.15 | 0.24 | | | | 1.40 | | | | | 3.11 | | | | |
| **period (ka) 13.7 $mMa^{-1}$** | | | | 1198.02 | | 479.21 | 299.51 | | | | 52.09 | | | | | 23.49 | | | | |
| **new period (ka) 17.3 $mMa^{-1}$** | | | | 947.60 | | 385.36 | 240.85 | | | | 41.29 | | | | | 18.59 | | | | |

**Table 6 - Prominent frequencies and their associated periods (assuming a 13.7 or 17.3 m $Ma^{-1}$ linear sedimentation rate over the whole interval) present in the different physical processes between 10 Ma and 16.4 Ma. Similar frequencies are grouped into columns labelled f1-20.**

## 8.3 Appendix 3 – Core Recovery and Images

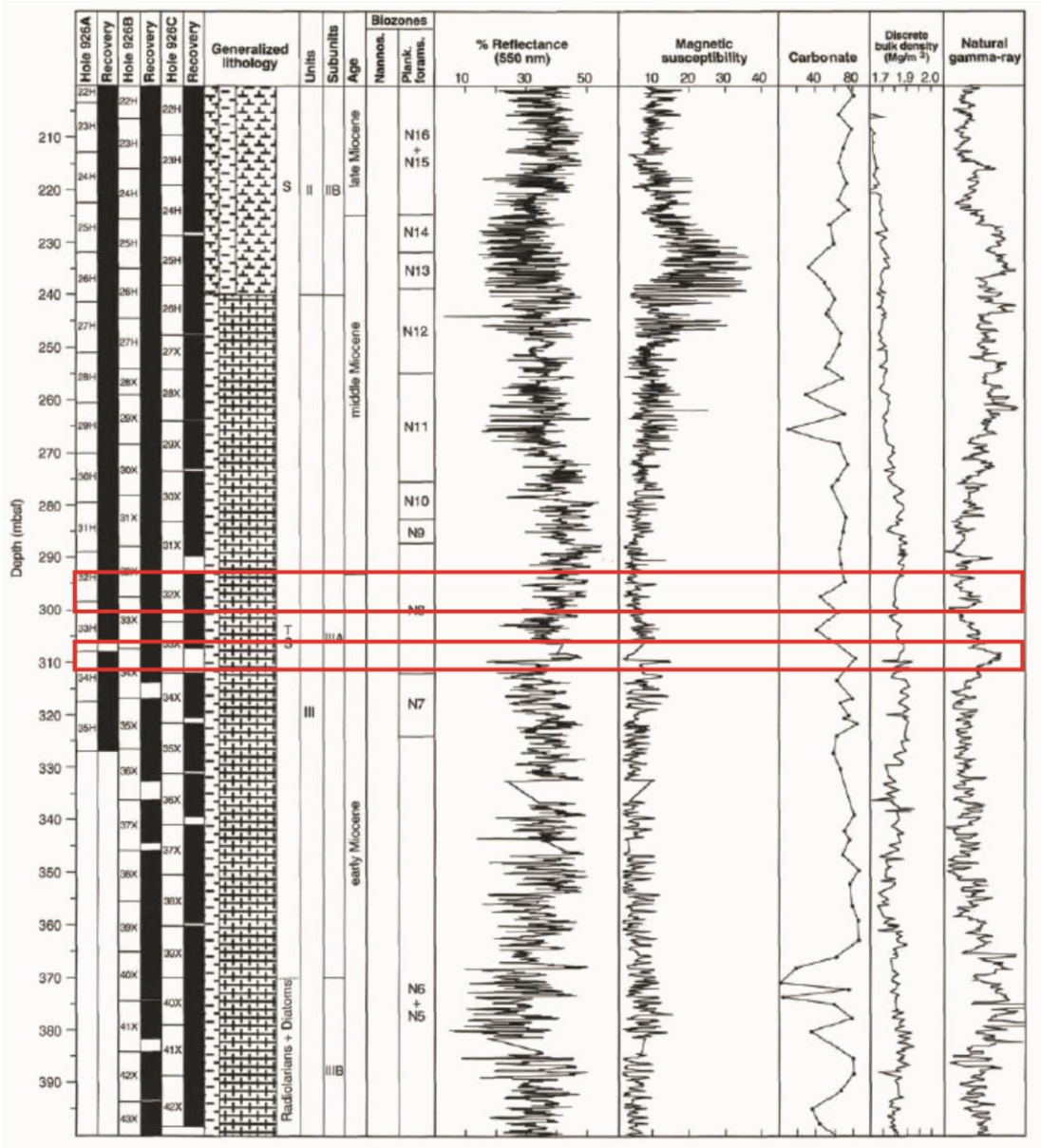


**Figure 65 – Core recovery from the studied intervals. The intervals studied in this thesis are highlighted in red and all sample material was taken from Hole 926B. Taken from Shipboard Scientific Party (1995c)**

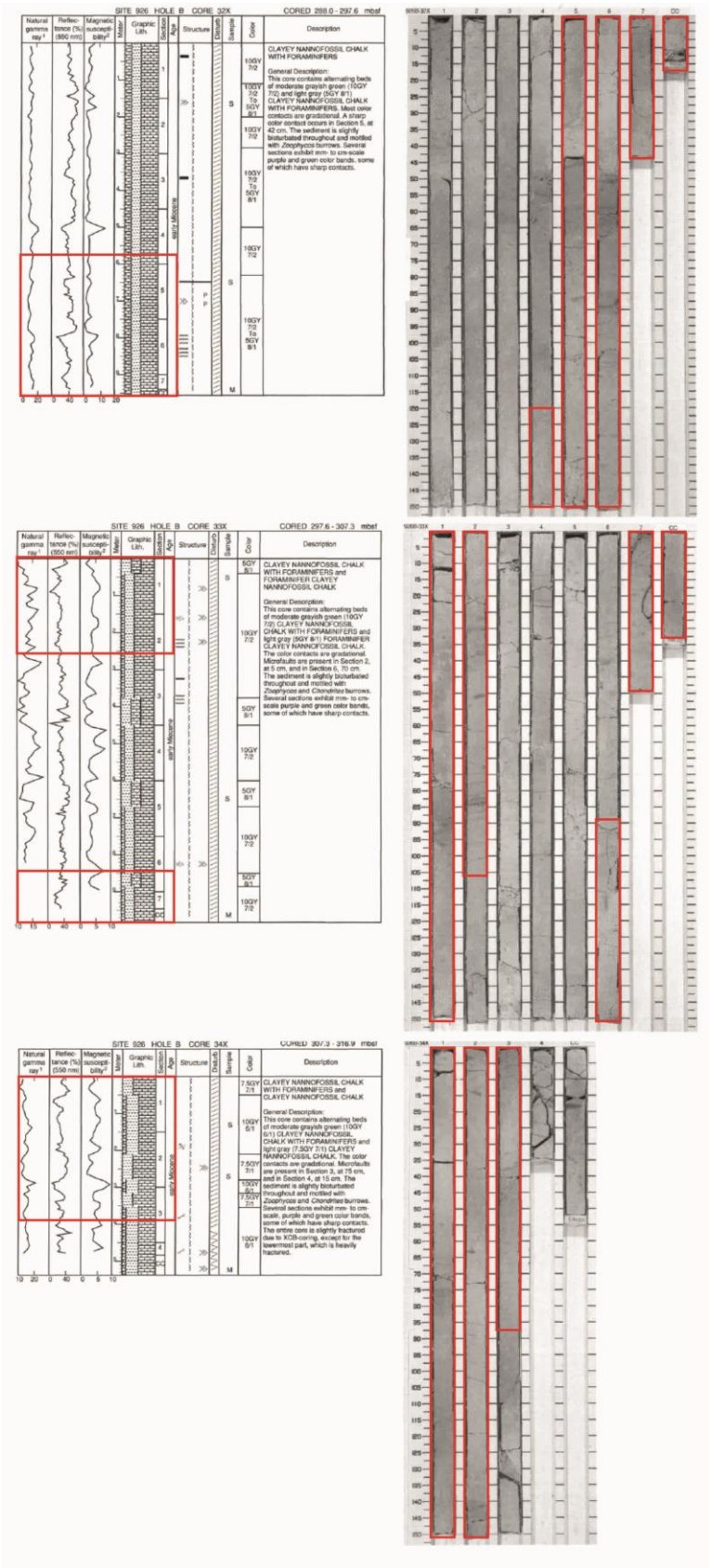

**Figure 66 – Core images of the studied intervals taken from Shipboard Scientific Party (1995c). Studied intervals are highlighted in red.**

## 8.4 Appendix 4 - Data

For all the raw data used in this thesis, please refer to the attached CD.

## 8.5 Appendix 5 – Poetry

### *8.5.1 The Foram*

In a lab so cold and dreary, as I worked a late night nearly
Driven mad by tiny fossils from some far bathyal floor
Suddenly there came a patter, pseudopodal tipper-tapper,
Some protozoan noise and clatter, clatter on the stage on my microscope's stage floor
"'Tis hallucination" I intoned "tapping on my microscope's stage floor"
"This it is and nothing more"

In the late night I was working to make up for all the shirking,
Procrastination, forum lurking, lurking I'd been doing years before,
My PhD was ending, and my health I had been spending,
Saneness torn from bloody rending, rent and shattered on the floor,
My accoutrements all scattered 'round laboratory floor.
Laying still for evermore

And the humming ever dimmer from some samples sitting on the spinner,
My frame growing ever thinner from countless meals skipped before,
My only nourishment from snacking, exercise from knuckles cracking, and the ever ceaseless tapping, tapping on my microscope's stage floor.
On the picking tray upon the microscope's stage floor.
"'Tis my madness, nothing more."

Presently my soul grew stronger, I could take the noise no longer,
"Figment" said I "or phantom, truly your silence I implore!"
"For you make a persistent clatter, though you may think it not matter,
But I need not a new distractor or I shall be here for evermore!"
Working in this accursed lab for evermore!"
Silence then, and nothing more.

I ceased my microscopal peering, ceased my wondering, started fearing,
For the silence even extended to the spinner by the door,
But the hush was 'ere long broken, in my desperation I had spoken,
spoken out against the silence so complete as ne'er before
"Mere coincidence, as before"
"The timer stopped it, nothing more."

Back into the eyepiece peering, heart a-flutter, eyes near-tearing,
Soon again I heard the tapping somewhat louder than before,
"Surely" said I "surely just my sleepy brain creating
Figments from some unholy mating of poor nutrition and films of gore
Poor diet, lack of sleep and films of gore,
Temporary madness, nothing more"

All at once, my mind now broken, all my explanations spoken,
A tiny fossil gave a token, a sign of life though it was long dead fifteen million years or more,
Its tiny chambers at once turning, its aperture seemed to be burning,
Staring up into the eyepiece I had often used before,
No eyes, but glared into the eyepiece often used before
It glared at me, and nothing more.

Tired of resisting this madness, I broke into a sudden gladness,
For such a microscopic cyclops could do no harm to me for sure
"Tell me true, oh tiny demon, surely with sinistral plots a-scheming,
For I'm sure that I'm not dreaming, asleep upon this laboratory floor,
Tell your name as you sit on my microscope stage floor"

Quoth the foram "Nevermore"

Much I marvelled this tiny plankton could be possessed of speech, I thanked him,
"A strange name for any creature, though it is one I've heard before."
"Have you met a man called Edgar? He called for his wife, he begged her,
Begged her name before he died, amongst his final words: 'Lenore'.
'Praps you recall a desperate man who cried out for his Lenore.
Were you the raven, Nevermore?"

But the foram staring at me did not agree or attack me,
Though his aperture stared at me, away my gaiety it bore,
For although it lay unmoving, all its malice it was proving,
All the silence never soothing, my fear growing more and more,
My terror of this tiny foram growing all the more,
An avatar of Nevermore.

I cried "what have I done to deserve thee, that you have come here to unnerve me,
And I'm sure a death you soon will serve me, my body cold upon the floor.
Is my procrastination a sin so deadly, my fear of work so wrong? I bid thee,
Leave me be, and I shall rid me of my sloth that has plagued me evermore,
Let me be in peace for evermore!"
Quoth the foram "Nevermore."

Some strength my resentment lent me for the hand that fate had dealt me,
"What right have you to come here from some far bathyal floor?
Seemingly just for my torment, my energy is far more than spent,
My shoulders hunched and spine far too bent from this microscope and more
From my computer, this accursed microscope and more"
Quoth the foram "Nevermore"

I turned away from the scope's eye piece, hoping I might win back all my peace,
For the evil from the foram was burning stronger than before,
I thought that if I could ignore it, as I'd failed to implore it,
Reality would cease to store it, and it would sail from my shore,
"Go back to the ancient ocean nearer to your plutonian shore"
Screamed the Foram "Nevermore"

Then methought the air grew denser, scented by some unseen censer,
Swung by devils, not the angles from Poe's poetry of yore,
"You wretches, oh you dandies, let me find solace in my brandies,
For I know not what is nepenthe, nor have Pallas ere to guard me from above laboratory door."
I flew in terror out of the laboratory door
"Please torment me nevermore!"

I came at once to the brass railing, guarding from the heights the steps were scaling,
I could feel my courage failing, as though torn out by some claw,
And I leapt into the open, fearing I would merely end up broken,
Ever mocked by words the foram spoken as I lay still breathing on the floor,
But my corpse crashed lifeless into the marble floor.
To awaken nevermore.

### *8.5.2 Mundulus*

I drifted like a plankton bloom,

That forms in spring without a fuss,

When I saw deep down in murky gloom,

*Cibicidoides mundulus;*

Upon the substrate in the deeps,
Pseudopod that slips and creeps,
Trochospiral, whirling test,

Biconvex and umbo proud,

Each chamber just like all the rest:

A solid, silent calcite shroud.

I saw just one sat all alone,
Atop a flat, well-rounded stone,
The currents like Aeolus played,

They swirled and lifted silt and sand,

But stoic foram clung and stayed,

And searched with cytoplasmic hand,

Such silent beauty, in waters hushed,
Its fate to be for data crushed
By some researcher drunk on fame,

Hoping for to proxy make,

The calcite test all cracked and maimed,

This innocent whose one mistake

Was chemistry worth a discuss.
So sorry, friend *C. mundulus.*